



UV studies of the Local Interstellar Medium

David Duncan Boyce

Supervisors:

Martin Barstow
Richard Jameson

A thesis submitted for the degree of
Doctor of Philosophy
at the University of Leicester

X-ray & Observational Astronomy Group
Department of Physics & Astronomy
University of Leicester

January 2009

Declaration

I hereby declare that no part of this thesis has been previously submitted to this or any other University as part of the requirement for a higher degree. The work described herein was conducted by the undersigned, except for contributions from colleagues as acknowledged in the text.

David Duncan Boyce
January 2009

©David Boyce (2009). This thesis is copyright material and no quotation from it may be published without proper acknowledgement

UV studies of the Local Interstellar Medium

David Duncan Boyce

ABSTRACT

We present new measurements of the spatial distribution of cool and hot gas in the local interstellar medium as a result of a search for O VI absorption in the FUV spectra of 100 white dwarfs at distances between 50 and 300 pc. We have carried out a detailed velocity analysis on the detected O VI lines to ascertain the degree of contamination from the background star. The position of the stars relative to the local cavity is calculated through cold gas phase column density measurements. Through curve of growth analysis we note that the local cavity is depleted in metals relative to hydrogen by a factor of 5-10 compared to the space beyond.

Whereas the O VI producing hot gas was originally thought to be observed in the interface regions between hot and cold gas, i.e. the cavity wall, our investigation finds no unambiguously hot gas in lines of sight that span such regions. We do, however, find hot gas at high galactic latitudes where there are no such walls. We discuss the wider context of this result by comparing the position of these detections to the soft X-ray background. This work ultimately changes our picture of the local interstellar environment and its processes by removing the ubiquitous million degree gas that was once thought to surround the solar system. One possible explanation worthy of further investigation is that the local cavity has recently begun to be inundated by hot gas spilling out of the loop 1 supernova remnant.

In support of this work there is an enclosed CD that contains the data and models used in this thesis. Examples of the information found on this CD can be found in the appendix. Explanations of the data, charts and graphs can be found in the body of the text when required.

Publications

David Boyce has made significant contributions to the following publications :

Boyce, D. D., Barstow, M. A., Dobbie, P. D., Aston, J. H., Booles, B. C., Preval, S. P., Laird, R. J. M., James, F. A., Barstow, J. K. and Forbes, A. E., "Post Iron Group Elements in DO Stars", *Hydrogen-Deficient Stars*, (2008), *Astronomical Society of the Pacific Conference Series*, 391, Werner, A. and Rauch, T., jul, 235-+

Boyce, D. D., Burleigh, M. R. and Barstow, M. A., "GALEX Search for Praesepe's White Dwarfs in Sirius Like Binary Systems", *15th European Workshop on White Dwarfs*, (2007), *Astronomical Society of the Pacific Conference Series*, 372, Napiwotzki, R. and Burleigh, M. R., sep, 103-+

Barstow, M. A., Boyce, D. D., Barstow, J. K., Forbes, A. E., Welsh, B. Y. and Lallement, R., "in the local interstellar medium", (2008), jul, 119-+,

Barstow, M. A., Dobbie, P. D., Forbes, A. E. and Boyce, D. D., "The Enigma of RE J0503-289 Revisited", *15th European Workshop on White Dwarfs*, (2007), *Astronomical Society of the Pacific Conference Series*, 372, Napiwotzki, R. and Burleigh, M. R., sep, 243-+

Dobbie, P. D., Napiwotzki, R., Burleigh, M. R., Barstow, M. A., Boyce, D. D., Casewell, S. L., Jameson, R. F., Hubeny, I. and Fontaine, G., "New Praesepe white dwarfs and the initial mass-final mass relation", *mnras*, (2006), jun, 369, 383-389,

Rol, E., Levan, A., Wiersema, K., Dobbie, P., Boyce, D. and Tanvir, N., "GRB060203: WHT z-band observations.", *GRB Coordinates Network*, (2006), 4680, 1-+

Acknowledgements

Though all the data reduction and data analysis for this work was carried out by myself the interpretation became a collaborative effort between myself and Professor Martin Barstow of the University of Leicester, Barry Welsh of Space Sciences Laboratory, University of California and Rosine Lallement of Service d'Aronomie du CNRS. I wish to thank these people for their involvement on this project. I also wish to to thank Dr Paul Dobbie, and Jo Barstow for their help in preparing and maintaining the data pipeline during the early stages of my PhD.

Though the author claims this work as his own, he does so with the acknowledgment that it only exists because of the considerable help and guidance of Professor Barstow. Without Professor Barstow's input the project would never have happened. The author would also like to thank Professor Barstow for investing in his development and bringing him up to the standard required to complete this work. Thanks Martin.

Dedication

For Anna

Contents

1	Introduction	1
1.1	Historical overview	1
1.2	What we know	7
1.2.1	A tail of two phases	8
1.2.2	Radiative environment	10
1.3	Composition of the ISM	11
1.3.1	The neutral gas phase	12
1.3.2	The molecular phase	18
1.3.3	Ionised atomic gas	22
1.3.4	Hot gas	25
1.3.5	Cosmic rays	26
1.3.6	Dust	27
1.4	Physical processes in the ISM	30
1.4.1	Heating and cooling	30

1.4.2	Photodissociation regions	32
1.4.3	Shocks	33
1.4.4	The local bubble	38
2	FUSE	41
2.1	FUSE	41
2.1.1	Introduction	41
2.1.2	FUSE data reduction	42
2.1.3	FUSE sample	46
2.1.4	Line velocity	47
2.1.5	Line selection	49
3	Cool gas in the LISM	59
3.1	The density of the LISM	59
3.1.1	Introduction	59
3.1.2	Creating synthetic spectra	61
3.1.3	Interstellar reddening	67
3.1.4	Binarity	77
3.2	Distance determination	77
3.3	Finding the amount of cold gas in the lines of sight used in this sample .	85
3.3.1	The volume density derived from different lines of the same species	92

3.3.2	Column density measurements of cold gas species	94
4	Hot gas in the LISM	115
4.1	Introduction	115
4.2	O VI measurement	117
4.3	O VI compared to the star's position	129
4.4	Velocity of the O VI line	136
4.5	Results of velocity analysis	142
4.5.1	Stars with no offset	144
4.5.2	Notes on candidate suitability	144
4.5.3	Stars with a positive line velocity	147
4.5.4	Stars with non photospheric v_{OVI} offset	147
5	Interpretation	148
5.1	Hot gas	148
5.2	Unambiguous ISM detections	151
5.3	Ambiguous ISM detections	156
5.3.1	Summary	167
5.4	The connection with the SXRb	170
5.5	Discussion	177
5.6	Speculation	180

6 Appendix	182
6.1 Introduction	182
6.2 Contents	182
6.2.1 WD0501+524	184
6.2.2 WD1314+293	199
6.3 Appendix B	210

Chapter 1

Introduction

1.1 Historical overview

Since prehistoric times mankind has been curious about the stars. Early man, free from the plague of artificial lights, lived his life to a backdrop of a million stars. "What are these lights in the night sky" he asked "and what is the inky blackness that separates them?" The idea that the stars were connected to the sky by some kind of interstellar framework was appealing to early astronomers as it seemed to explain why the stars were fixed in position and the planets were not. Indeed the earliest possible reference to the medium in which the stars are located comes from Genesis 1,14 in the Bible where it is reported that God said "Let there be lights in the firmament". Ideas along similar lines were developed by Plato (427 - 347BC) in his book 10 of The Republic. Plato described how the visible objects in the heavens were connected to an invisible framework called the Spindle of Necessity. Aristotle (384 - 322BC) later increased the complexity of this idea by suggesting that all the celestial bodies moved around the earth in concentric

Third party
copyright material

FIGURE 1.1. Left: The first human reference to the space between the stars is found in the bible. Moses (1393–1273BC) refers to the firmament in his description of creation. Image source: jesuswalk.com. Middle; Aristotle (384 BC–322 BC) first attempted to understand the properties of the firmament. He called the substance between the stars quintessence (meaning fifth element). Image source: empirecontact.com. Right; Ibn al-Haytham (965–1039). Whilst the works of the ancient Greek philosophers were lost during the western dark ages, Arabic philosophers preserved the early Greek works. When the texts of scholars such as Ibn al-Haytham reached European astronomers like Johannes Kepler in the 16th century it began the scientific revolution and the renaissance. The lack of evidence for an interstellar framework or firmament changed how mankind treated the space between the stars, and began the scientific study of the interstellar medium. Image source: tiger.uic.edu.

spheres made of a substance called the aether. The aether was renamed quintessence (meaning fifth element) and considered an element alongside earth, air, fire and water. Ptolemy (83 - 161AD) and later Greek philosophers became increasingly fixated by the movements of the planets and the idea of the firmament was almost forgotten. Slowly through the dark ages much of the early Greek work was lost to the west. See Figure 1.1.

It wasn't until a thousand years later that the works of Ptolemy and Aristotle were re-discovered and the development of the firmament idea recommenced. Ibn al-Haytham (965 - 1039) noticed that the cosmology of Ptolemy was lacking in its absence of a fixed environment for the stars. Since it was considered by Christian and Muslim philosophers that the firmament was the dwelling place of God it was inconceivable that the firmament did not exist and so was reinvented.

By the time of Nicolaus Copernicus (1473 - 1543) it was no longer believed that the firmament was a solid object. Tycho Brahe (1546 - 1601) observed the unhindered movement of a comet through the solar system and concluded that space was not in fact solid but was rather a fluid of some kind. Despite this, philosophers continued to describe the interstellar medium as a solid object for many years. Francis Bacon (1561 - 1626) first coined the term interstellar, but used it to describe a rigid and solid structure. The opposite extreme was taken by Robert Boyle (1627 - 1691) who decided that the interstellar medium was empty. See Figure 1.2. Christiaan Huygens (1629 - 1695) hypothesized that light propagating through space required some kind of luminiferous aether. Isaac Newton (1643 - 1727), like Tycho before him, rejected this idea, since such a substance would

Third party
copyright material

FIGURE 1.2. Left; Tycho Brahe (1546-1601) observed that the space between the stars was not a solid structure. Image source: nada.kth.se. Middle; Francis Bacon (1561-1626) coined the term interstellar. Image source: wikipedia.org. Right; Robert Boyle (1627-1691) presumed that the interstellar medium was empty. Image source: wikipedia.org.

be seen to retard comets. Newton began the scientific investigation into the interstellar medium with the comment "there is no evidence for its existence, and therefore it ought to be rejected." (Opticks 1704) Despite this definitive statement physicists continued to speculate about the luminiferous aether until the special theory of relativity and the MichelsonMorley experiment explained all the observed problems with the propagation of light.

Whilst physicists chased the invisible, astronomers began to notice diffuse patches of light in the night sky. Emanuel Swedenborg (1688 - 1772) suggested that these objects were in fact clouds of gas between the stars. Immanuel Kant (1724 - 1804) developed these ideas by suggesting that these were stars in the process of forming. William Parsons, 3rd Earl of Rosse (1800 - 1867) having observed the spiral arms of galaxies refuted this by suggesting that nebula were in fact compact unresolved populations of distant stars. John Herschel (1792 - 1871) challenged this claim by showing how the Orion nebula seemed to be illuminated by nearby stars.

With the invention of photography, long exposure photographs of the night sky could be taken. Barnard (1895) produced the first images of dark nebulae and came to the conclusion that along with the illuminated gas and dust there was also significant quantities of dust and gas not directly illuminated. This gas and dust could only be seen in the absorption of starlight from more distant stars. Alongside the invention of photography came along the invention of spectroscopy. Huggins & Miller (1863) observed the spectrum of the orion nebula and found that its emission spectrum was characteristically gas

Third party
copyright material

FIGURE 1.3. Left; Edward Emerson Barnard (1857-1923) discovered dark nebulae through the first extensive use of photography in astronomy. Image source; wikipedia.org. Middle; Johannes Franz Hartmann (1865-1936) fathered interstellar medium spectroscopy with the discovery of stationary lines in stellar spectra. Image source: aip.de. Right; Mary Lea Heger (1887-1983) discovered interstellar sodium. Image source: library.ucsc.edu.

like. However the galaxies of the Earl of Rosse looked distinctly like combined spectra of millions of stars.

The greatest step in the history of ISM studies came when Hartmann (1904) observed the spectrum of Delta Orionis. The regular velocity shifts in the absorption lines of the star confirmed that it was a spectroscopic binary. Hartmann then went on to add that "quite surprising result that the calcium line at 393.4 nm does not share in the periodic displacements of the lines caused by the orbital motion of the spectroscopic binary star"

This K line of calcium had originated from the interstellar medium and was observed only through its absorption of the light of Delta Orionis. Heger (1918) followed this by reported the presence of the stationary D lines of sodium in the spectroscopic binaries, Beta Scorpii and Delta Orionis. See Figure 1.3.

1.2 What we know

The interstellar medium is a very broad term. It is generally used to describe the matter in the regions of space between the stars. By volume, the interstellar medium makes up most of the galaxy, by mass it is almost negligible. Despite this, the interstellar medium forms the immediate environment of the Solar System. For a majority of isolated stars the strongest external influence is that of the local interstellar medium. The processes which occur in the ISM could be argued to be the most important processes of the whole galaxy. The subtle conglomeration of atoms into dust grains is the first step in star formation

and thus one of the reasons we are here today. Despite the importance of the process, the difficulties faced in detecting the tenuous gases have resulted in it being one of the least understood processes of the stellar life cycle. Presented here is a broad overview of the interstellar medium. The disjointed nature of the discussion is a reflection of our understanding of the field at present. Different wavelength regimes offer different components of the ISM and the resultant big picture remains unclear.

1.2.1 A tail of two phases

The interstellar medium consists of two distinct phases. The gas phase consists of atomic, molecular and ionised gas at various temperatures. The grain phase consists of dust grains made from the conglomeration of molecules and atoms. Gas phase depletion is the process that is responsible for the growth of grains that have been produced in the atmospheres of evolved stars. Grain phase depletion is the inverse process. Gas phase depletion is responsible for selectively removing the heavier elements out of the gas phase and into the grain phase.

The dust grains play important roles in the interstellar medium. They absorb a large fraction of the light emitted by stars and re-emit this as infrared radiation. Grains also provide a surface that enables the formation of molecules and complex chemistry.

The gas in the interstellar medium is created by supernovae, winds from massive stars and from planetary nebulae. Stars can then form from this gas. This link results in the

gas and the stars occupying the same regions of the galaxy. Most of the ISM is confined to the galactic disk with some spilling out into the halo.

The total mass contribution of the ISM is approximately 5% of the baryonic mass and 0.5% of the galaxy's total mass. The most abundant ISM element is hydrogen, 70%, with helium contributing 28% and heavier elements making up the final 2% by mass. In molecular clouds, and with the exception of the noble gases, this 2% arrange themselves into molecules and dust grains.

The ISM is also affected by the radiation environment. The electromagnetic component of the cold neutral phase, like that closest to the Sun, consists of an average energy density of 1.26 eVcm^{-3} (Habing 1968), though this varies from location to location. The magnetic fields within the galactic disk are irregular but can provide an additional energy density of 1 eVcm^{-3} . A final radiative component comes from cosmic rays which provide an energy density of 1 eVcm^{-3} .

The ISM is subject to continual enrichment in heavier elements from the synthesis within stars. The chemical evolution of the galaxy is subject to the continual cycle of star production from the interstellar medium followed by the production of an enriched interstellar medium from the supernova of more massive stars.

The distribution of interstellar gas can be calculated by looking at the distance to stars that are both in front of the gas and those partially obscured by it. This method is valid for the distance to nearby stars but doesn't work over long distances due to the increased

complexity of distant star fields. At kpc distances a kinematic distance can be calculated by observing how quickly the gas is observed to be rotating around the galaxy. For gas in the line of sight of the galactic centre it would be expected that its radial velocity would be zero relative to the galaxy itself. Gas moving directly towards or away from us at the quadrature points would have the most non zero radial velocity. Observing how the radial velocity of the gas compares to the gases projected position in the galaxy can indicate its distance. This is limited in accuracy by the additional random motions of the gas clouds to about 0.5 kpc. This accuracy is acceptable for measuring galactic distances and has been used to trace the shape of the galaxy by observing the 21 cm H I line.

1.2.2 Radiative environment

The energy supplied to the interstellar medium comes from a range of sources. Radiative contributions from photons and cosmic rays energise the gas alongside mechanical energy from supernova and stellar wind shocks.

The UV, visible and near-IR radiation environment is important in ISM studies since it is these wavelengths that are responsible for a large fraction of the ionisation that converts atoms into ions. UV radiation is also responsible for the photodissociation of molecules in the grain phase. Ionisation of hydrogen occurs throughout the UV and optical with the most dramatic example at the Lyman edge where hydrogen absorbs nearly all of the flux from 911.7 \AA into the soft X-ray. Partial transparencies and the fortunate location of the sun in a low hydrogen density region enable some unabsorbed light to reach us from

nearby stars in these EUV wavelengths (Barstow et al. 1994a).

Mid and far-infrared radiation such as the blackbody radiation of the universe have no large effects on the gas phase but it is of sufficient energy to excite some of the rotational and vibrational states of molecules in the grain phase. Though > 1 keV X-rays do not play an important role in the ISM radiation environment the sub-keV X-rays are easily absorbed. Indeed both the hot gas in the galactic halo and hot gas from nearby sources such as the hot local bubble both contribute to the soft X-ray background.

Interstellar magnetic fields have a very important effect on galactic scales by adding to the thermal pressure that balances the gravitational attraction of the galactic disk. It is the measurement of Faraday rotation in distant clouds of interstellar matter that allow us to study galactic scale magnetic fields. Rand & Lyne (1994) show that galactic magnetic fields orientate along the spiral arms, often in opposite directions between adjacent spiral arms. On smaller scales there is a large superimposed random magnetic field (Rand & Kulkarni 1989) that plays a major role in the physics of gravitational instability in the molecular clouds that are undergoing star formation. This local field is responsible for the optical polarisation of the light from nearby stars (Leroy 1999).

1.3 Composition of the ISM

The interstellar medium comprises several different types of material that exist in a complex radiation environment. The simplest of these and the most numerous are the atoms

and molecules that have some degree of ionisation (or none at all). This is described as the gas phase. The presence of some gas phase species can act as indicators of the thermal environment of a region. The presence of these species allow us to sub-categorise the gas phase into cold, warm and hot gas regions. Existing alongside the gas phase is the grain phase. This dusty material constantly adds to the gas phase by evaporation and is removed from the gas phase by condensation. Cosmic rays are basically gas phase atoms accelerated to relativistic speeds by violent processes that propagate through the ISM, e.g. supernova shock waves. Together this mix of particles seed space with the building blocks of stars and planets, from which we originate.

1.3.1 The neutral gas phase

The neutral medium is defined by the presence of non ionised hydrogen and other species. The three main methods of measuring the neutral medium are through the 21 cm hydrogen line, fine structure lines and gas phase absorption lines. Absorption line analysis also allows study of ionised species and so is our most powerful tool in probing the ISM.

The 21-cm hydrogen line

The 21-cm hydrogen line corresponds to the transitions between hyperfine sublevels of neutral hydrogen. These hyperfine sublevels arise from the difference in energy between states where the spins of the proton and the electron are aligned and when they are in opposite directions. The temperature required to populate these levels is often called

Third party copyright material

FIGURE 1.4. The emission at 21cm indicates the presence of interstellar neutral hydrogen. This plot is a celestial coordinate projection of 21 cm emission. The yellow sinusoid through the plot is the plane of the galaxy. Image source: J. Dickey (UMn), F. Lockman (NRAO), SkyView

the spin temperature. These energy transitions are not normally allowed by the selection rules of quantum mechanics and so are called forbidden lines. They are observed in space because of the extreme low density environment ($20\text{-}50\text{ atoms/cm}^3$) prevents collisional de-excitation of the atom for several hours. This line can be observed in absorption against a background continuum radio source or in front of more distant 21-cm emission. So long as the background continuum varies slowly with frequency an optical depth can be measured and a column density can be calculated. By subtracting the modeled spectra of the background source the kinetic temperature of the gas can also be derived. See Figure 1.4. The 21-cm line can thus be used to measure the mass, the kinematics and the distribution of atomic gas in our galaxy. Studying the 21-cm line has revealed that neutral hydrogen within the galactic disk is extremely inhomogeneous. The structures

observed by Hartmann & Burton (1997) using the 25m radio telescope at Dwingeloo in the Netherlands show that the gas is dominated by filament structures and bubbles. Another surprising result is that the atomic interstellar medium consists of two distinct phases. The phase that is easier to detect is the dominant cold (60-100K) phase which is dense enough to show up strongly in absorption. The significantly less dense warm (2000K) gas is barely seen in absorption, though Mebold & Hills (1975) have detected it. Whereas both phases contain similar amounts of matter the inhomogeneities are only observed in the cold phase. Outside of the disk of the galaxy there are high velocity clouds of neutral interstellar gas that could be extragalactic in origin (Spitzer 1956).

Fine structure lines in the FIR

The fundamental energy levels of an atom can be split by the fine structure interaction between the orbital momentum of the electrons and the spin of the electrons. These transitions are forbidden and therefore the upper levels are in most cases only populated by collisional processes. De-excitation occurs both through collision and emission. When the density is large the former process dominates. In the far infra red there are numerous fine structure lines which indicate the cooling processes of the diffuse interstellar medium.

Gas phase absorption lines

Large numbers of atomic, ionic and molecular lines are observed in the optical and UV. The two dominant species in these spectra are the lines due to the hydrogen Lyman series and those due to molecular hydrogen. Alongside these absorption lines there are often many weaker lines from heavier elements. These lines can be measured directly and the column density between the observer and the background inferred.

The curve of growth method (see chapter 3.3) can describe the amount of material along a line of sight at a given ionisation. If there are lines for the same species that are of different ionisation state then the ratio of the volume densities can be used to estimate the temperature. For example at optical wavelengths there is a neutral calcium line at 4226 \AA and there are the H and K calcium lines at 3933 and 3968 \AA that come from singularly ionized calcium. The ionisation equilibrium between these two states can be calculated with Equation 1.1 .

$$n(\text{CaI})\Gamma = n(\text{CaII})n_e\alpha \quad (1.1)$$

Where Γ is the ionisation probability per second of Ca I, α is the recombination probability per second and n_e is the electron density. Γ can be estimated from the UV radiation field, α can be estimated from $\alpha \propto T_e^{-0.7}$ where T_e is the electron temperature (which is essentially the same as the kinetic temperature). From the measured column densities we can estimate the electron density, n_e .

Within H I regions, the relative amount of carbon in the excited fine-structure levels

is governed by the local gas pressure and temperature. The fine structure levels are populated primarily by collisions and depopulated by radiative decay. The fraction in the $N(\text{C I}^*)$ state compared to the fraction in the $N(\text{C I}^{**})$ state describes the conditions of the line forming region (Where the * annotation corresponds to the first excited state of given ionisation and N is the column density). The gas pressure $P = nkT_K$ is determined from the density of the dominant collision partner, atomic hydrogen, and the kinetic temperature. Jenkins & Shaya (1979) produce model curves of the ratio of (C II^*) to (C I^*) for a range of different temperatures and pressures.

The relationship between the column densities of different species

Where there is more neutral potassium there is more neutral sodium. Neutral hydrogen, however does not exist in a linear relationship with any of these metals. In fact, the dependence of $N(\text{Na I})$ and $N(\text{K I})$ with $N(\text{H I})$ is roughly quadratic (Hobbs 1974). Those species that are greatly depleted can be detected because they do not obey this relationship. Calcium for example is highly depleted to below solar abundance. Jenkins & Shaya (1979) highlight the interesting case of neutral carbon. Unlike the relationship between $N(\text{Na I})$ and $N(\text{K I})$ the relationship between $N(\text{C I})$ to either $N(\text{Na I})$ and $N(\text{K I})$ is steeper. Correcting $N(\text{C I})$ for differences in abundances, recombination rates and average ionisation rates result in relationship between $N(\text{Na I})$ or $N(\text{K I})$ with $N(\text{C I})$ though proportional has a proportionality constant that is greater than 1. They conclude by saying that in certain conditions the ionisation rate of different species is suppressed by different amounts depending on the conditions in the line forming region.

Elemental abundances relative to hydrogen

The elemental abundance of a species can be found through comparison with the hydrogen column density along a line of sight. In most cases the hydrogen column density is found by applying a theoretical line profile to the Lyman alpha line. In cases where there is also hydrogen bonded to itself (molecular hydrogen or H_2), calculating the hydrogen column density becomes non trivial and requires modeling of the H_2 region. To measure the abundance of a given species it is necessary to include all the occupied ionisation states for that species in the calculation. The majority of species in the ISM exist in a single ionised state. In the case where only one line is present, to measure an elemental abundance, requires us to factor in the possible amount of the other ionisation states that could remain unobserved due to noise in the spectrum and instrumental limitations. The non detection of some species may be due to a weak oscillator strength (see chapter 3.3) of the line or it may be that the line has an equivalent width of the same order of magnitude as the random noise in the spectra. In both cases the upper limit of the column density of the non-detections can be summed into the total elemental abundance of that element.

Studies of the lines of sight toward ζ Ophiucus (Savage & Sembach 1996, Snow & Witt 1996) show that most elements are underabundant in the diffuse interstellar medium with respect to the solar system. One suggestion is that our solar system formed from dust in a chemically enriched region of space, and drifted into this chemically poor region since its formation. Another explanation is that the missing elements of the interstellar

medium have been depleted by formation of dust grains and thus are no longer available to absorb the incident radiation in the same characteristic wavelengths in the gaseous phase. Though both processes are likely to have contributed to the underabundance there is direct evidence for gas phase depletion in some species and so this is considered to be the dominant process. Of the elements measured towards ζ Ophiucus the most under-abundant are those that have the larger condensation temperatures. The reverse is observed in warm regions where it is thought that grains are evaporating back into the gas phase.

1.3.2 The molecular phase

Wright (1918) observed an unidentified line at 6283 \AA in the spectrum of Deneb. He mistakenly concluded that the line was photospheric in origin. At the same time Mary Heger at the Lick Observatory measured two lines at 5780 \AA and 5797 \AA in the spectra of several B-type stars. Again an identification was sought but none found. In this case however Heger noticed that these unidentified lines were stationary compared to the star lines and thus originated in the interstellar medium. These unidentified lines continued to be observed in the spectra of other stars for several years before Merrill & Wilson (1938) described them as being "somewhat diffuse" or "not sharply defined" and William Wright described them as being "a trifle hazy". Several years before, Russell (1935) made the connection between molecular lines and the broad indistinct as yet unidentified lines in sunspots. Russell noted that "If the temperature of the gas is low enough - more precisely if the rotation of the molecules is little excited - only a few of the band

lines observed at room temperature might appear". What Russell was suggesting was that as well as broad lines from molecules you could, in certain conditions, get narrow lines as well. Adams (1941) at the Mount Wilson observatory made the first positive identification of molecules in the interstellar medium with the discovery of the basic hydrocarbon CH and basic cyanide CN.

In 1965 the number of known molecular species more than doubled as hydroxy OH (Gundermann et al. 1965), ammonia NH_3 (Cheung et al. 1968) and water H_2O (Barrett 1969) were discovered through radio observations. By the turn of the century 120 different molecules had been observed in the interstellar medium including long chain hydrocarbons and possibly one of the building blocks of life itself, the amino acid glycine (Kuan et al. 2003).

There are many different ways in which a molecule could absorb or emit energy and many different energy states the molecule could exist in. This large number of very similar states often results in the broadening or splitting of any given line into many. The simplest transitions that a molecule can undergo are the analog of those we observe from atoms. The electronic transitions of molecular hydrogen for example can be observed in the FUV alongside carbon monoxide CO and hydroxy OH. The hydrocarbon CH, CH^+ and the cyanide CN can be observed at slightly longer wavelength in the NUV. Several molecules are observable from the ground including molecular carbon C_2 and cyanide CN. Both of these have absorption lines in the near IR.

The electronic absorption lines of molecules can at high resolution be split into a whole

series of lines that correspond to the different vibrational levels and further into rotational sublevels. For low resolution instruments on spacecraft ($R < 20,000$) the lines are unresolved and could potentially be dominated by their damping wings. The abundance of such molecules can thus be found by the damping section of the curve of growth (See Chapter 3.3).

$$N = \frac{m_e c^3 W^2}{e^2 \lambda^4 f \gamma} \quad (1.2)$$

Equation 1.2 shows how the column density becomes a function of both the equivalent width (see chapter 3.3) and the damping constant γ .

As well as the many electronic transitions that a molecule could have there are also a large number of vibrational states that a molecule could occupy. The most common, the stretching modes, correspond to a variation in the distances between the atoms that make up the molecule. Molecules with more than two atoms can also have bending and deforming modes. These transitions are normally weaker than the electronic transitions and so the absorption and emission lines are significantly smaller.

Smaller still are the lines that arise from rotational transitions. These states are made up of rigid polar molecules rotating in different orientations and thus absorbing light of energy specific to the angle between the axis of rotation and that of the incident light. More peculiar transitions can occur from the more complex molecules. For example, ammonia NH_3 can turn itself inside out by passing the fourth atom of the tetrahedral through the triangle made by the other three atoms. This is known as an inversion transition. Further splitting can occur due to the interaction between orbital motion of an unpaired electron



FIGURE 1.5. A molecular cloud in front of the Carina Nebula. Image source: HST, Space Telescope Science Institute

and the rotation of the molecule.

The study of molecules in the interstellar medium is important because the locations that are dominated by molecules are often very different in terms of environment to that dominated by neutral atomic gas. Molecular hydrogen in the interstellar medium is often a tracer for warm gas as it indicates that the region has been disturbed by non-dissociative shocks. See Figure 1.5.

Though the molecular transitions of 120 molecules have been identified there is evidence that a great deal more exist in the interstellar medium. For example, the lines that Merrill & Wilson (1938) observed have identities that are still a mystery. These diffuse interstellar bands are thought to be from a very abundant material since they are observed in the optical towards nearby and low column density sight lines.

1.3.3 Ionised atomic gas

H II regions are clouds of hydrogen that have been ionised by the UV radiation of hot stars. These regions are often referred to as gaseous nebulae because of their visibility in the optical wavelengths. Ionisation within such a cloud is known as a Stromgren Sphere. In a given region the density of the gas peaks in a central location and in this location the density is either high enough or close enough to an ionisation source for the gas to be completely ionised. As we move away from that central position and the gas density drops and a radius is reached where the gas becomes neutral once more.

Calculating the abundance of materials in H II regions is often difficult because the recombination lines produced by H II involve different physics to that which produces the ionised lines of other species. Further more, problems arise from the emission of metal lines from the photodissociation regions at the interface between the H II regions and the neutral medium. Since these elements give off brighter emission from the interface than from within the region itself it is impossible to probe the H II region for these species. See Figure 1.6.

Outside of the H II regions and amongst the neutral medium there is a quantity of ionised gas that is called diffuse ionised gas. The production mechanisms for such gas include spillages from the H II region due to the hydraulic process known as the champagne effect (Bodenheimer et al. 1979) or ionisation of the neutral medium by hot stars. The amount of ionised material spread thinly throughout the galactic disk by mass outnumbers that inside the localised H II regions.

The observation of the diffuse ionised medium can be accomplished via a number of different methods. Primarily, there is the dispersion of the radio radiation from pulsars by the interstellar medium that is known as the interstellar scintillation (Narayan 1993, Taylor & Cordes 1993). Radio emission from the diffuse ionised gas is also observed at very low frequency. There are also some absorption lines of these species at higher frequencies such as in the microwave and in the FUV and optical recombination lines.

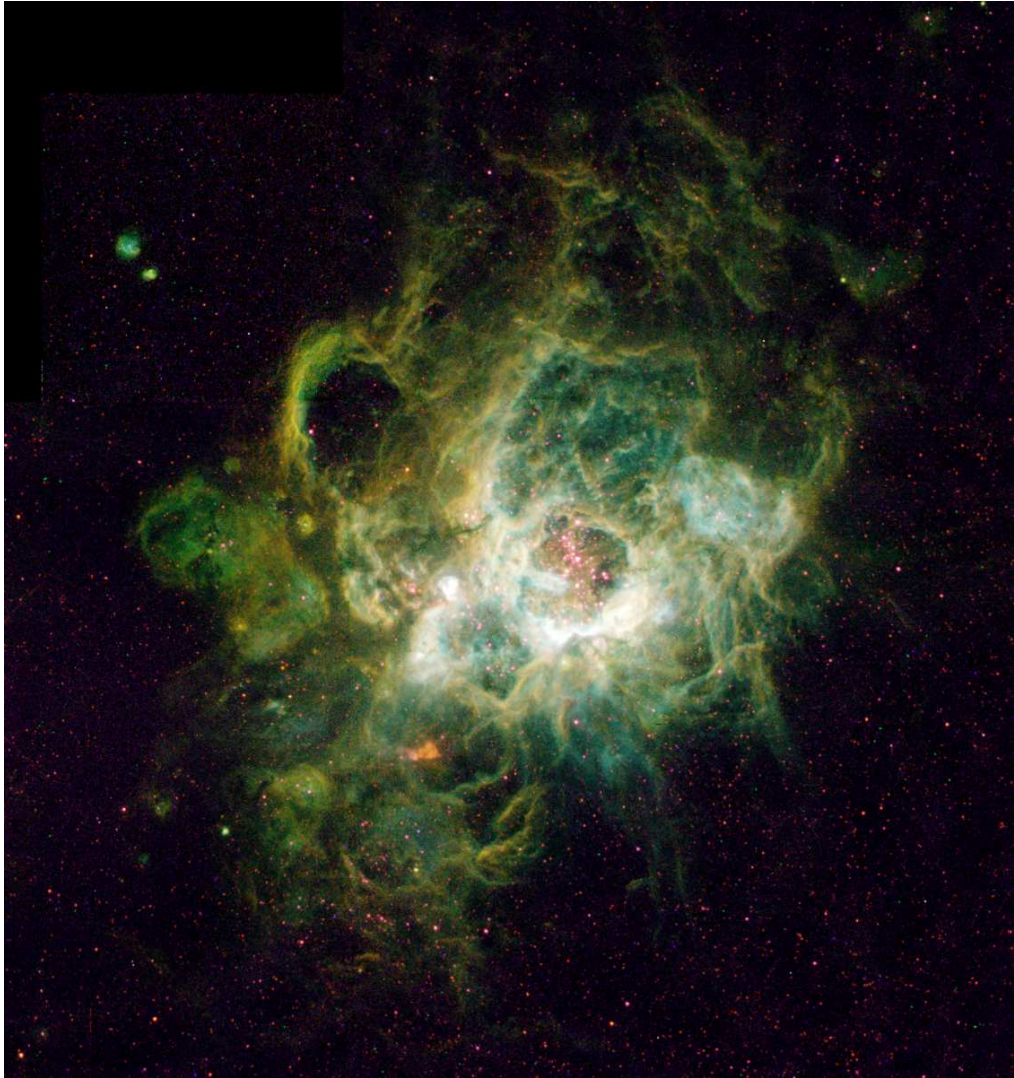


FIGURE 1.6. NGC 604, a giant H II region in the Triangulum Galaxy. Image source: HST, Space Telescope Science Institute

1.3.4 Hot gas

From the pressure equilibrium that was observed to exist between high density clouds of H I moving through the halo of the galaxy and the halo itself, Spitzer (1956) inferred that the temperature of the halo must itself be 10^6K . The first direct evidence for this hot gas came from observations of the soft X-ray background by Bowyer, Field & Mack (1968). After O VI was detected in the spectra of B stars (Rogerson et al. 1973), Jenkins & Meloy (1974) concluded that this too was further evidence of hot gas. This detection was not considered to be circumstellar or stellar in origin because there was no correlation between the radial velocity of star with that of O VI line. The reported detection of other high ionisation interstellar species, such as N V and C IV, by Jenkins & Meloy (1974) and the detections of interstellar O VII and O VIII by Inoue et al. (1979), Schnopper et al. (1982) and Sanders et al. (1998) would indicate that part of the interstellar medium is hotter (10^6K) than the stars that exist within it.

Ionising the interstellar oxygen five times would require the incident light to have an energy of 114 eV. Due to the relative scarcity of photons of this energy, and the low intrinsic density of the interstellar medium, photoionised O VI would only exist at very low volume density. This O VI could become visible over very long lines of sight despite the low volume density due to the extreme distances over which the light has traveled. O VI observed in the lines of sight to nearby stars, however, requires an alternative explanation. For example, the original stars observed by Rogerson et al. (1973) in which spectra O VI was first detected, all lie within 100 pc.

One explanation is that the gas is ionised through collisional processes. A hot gas under the right conditions will spontaneously ionise itself. The electrons liberated in this way add to the thermal background and increase the likelihood of spontaneous ionisation of further electrons. The recombination cross-sections of atoms ionised through collision can be used as an indicator of the interstellar temperature. For example O VI would require temperatures of $3 \times 10^5 \text{K}$ and O VIII would require temperatures greater than 10^6K (Schmutzler & Tscharnuter 1993). Thus the presence of spectral lines created by hot gas in short lines of sight is used as a tracer or indicator of the conditions required to produce it (McKee & Ostriker 1977).

1.3.5 Cosmic rays

Cosmic rays are atomic nuclei and electrons that have been accelerated to relativistic velocities. The most energetic of which include 10^{20} eV particles that, upon hitting the atmosphere of the earth, create showers of secondary particles that are detectable from the ground. The history of cosmic ray research starts with Victor Hess, who in 1912 measured the rate of ion production inside a hermetically sealed container that was carried to an altitude of 5300 meters by balloon. He noted that since the electrometer was discharging at a rate proportional to the altitude of the balloon that the ionising radiation must originate from space. Though the origin of cosmic rays is disputed, some agreement has been reached on the distances from which they originate. What is certain is that at the source, hadrons and leptons are accelerated to relativistic speeds by violent processes in or near our galaxy. The Earth-bound particles then travel mostly unimpeded

through the interstellar medium interacting predominantly with magnetic fields. Within the ISM the magnetic fields experienced by the particles are mostly weak with very little global direction. Only once a cosmic ray has entered the heliopause of a star does its trajectory become significantly modified. The lower energy cosmic rays, however, can ionise the matter in the interstellar medium and thus contribute to the ionisation balance.

1.3.6 Dust

Dust grain processes are an important part of interstellar chemistry. The production of dust from gas marks the first step in star formation. Though dust makes up less than one hundredth of the mass of the ISM the presence of dust had been observed long before any of the gas phase ingredients. When the first reflection nebulae were identified as interstellar objects it was considered that what was observed was dust rather than gas. This was because dust characteristically reflects optical light whereas gas does not. To directly observe dust requires illumination from a nearby star and for the dust to be concentrated enough to be optically thick. Both of these criteria are satisfied by the formation of stars and, therefore, it was the presence of dust that provided the first indicator of star formation. See Figure 1.7.

Dust can also be directly observed in the infrared. The possible photon energies that a dust grain could absorb are relatively large as a result of the many shapes and sizes of the individual grains. This absorbed energy is then re-emitted in the mid and far infrared. It is estimated that up to half of all the energy emitted by stars in a galaxy is absorbed



FIGURE 1.7. The Omega Nebula, with dust illuminated by reflection. HST, Space Telescope Science Institute

by dust. Dust along the line of sight to a star will decrease the observed brightness of the star. This process is known as extinction. Extinction occurs both through the absorption and scattering of photons by dust. It is dependent on the composition, shape, size and distribution of the dust grains. Since the extinction is dependent on wavelength, shorter wavelengths are scattered more than longer ones, resulting in the reddening of star light. Which can be used to quantify the amount of material along a line of sight. Extinction curves vary noticeably from star to star indicating that the structure of dust in the local interstellar medium is variable in density and in grain size. The method by which grains scatter light is via the induced motion in the weakly bound electrons in the atoms rather than the atoms themselves. The dust grain contains many chemical bonds and forms a much more rigid structure than a molecule allowing for very few of the bending, flexing and wobbling modes. Any given electron will respond slightly differently depending on the frequency and polarisation of the incoming light. Upon interaction with an electron the light gains a phase difference that is dependent on the degree of interaction. A complex grain therefore modifies the incoming light in such a way that the emitted light consists of many different phases at the same frequency.

The angle by which the radiation is scattered is dependent on the wavelength of the incident radiation. X-rays for instance have a wavelength smaller than the grain and so are not scattered at large angle. Light from a distant X-ray source will scatter through the intervening dust but continue along the direction of the incident light. The result is observed halos around X-ray sources (Smith & Dwek 1998).

1.4 Physical processes in the ISM

The identification of the constituent ingredients of the ISM has been predominantly the work of the astronomer. Knowledge of what species we know to exist in the ISM comes from direct observational evidence and these observations are often in different wavelength regimes. This makes the study of the physical processes that occur in the ISM a difficult and complex task. The study also crosses into the domain of theoretical physics.

1.4.1 Heating and cooling

The dominant processes that occur in the ISM are heating and cooling. The simplest way that the matter experiences heating, or the gain of kinetic energy, is by the removal of an electron by a photon. This is called photoionisation. Atoms and molecules can also be ionised by high energy particles such as cosmic rays. Cooling occurs via the inverse process. The free electron if caught inelastically by an ion will de-thermalise it by emission of radiation. Low mass particles such as protons can also be captured in this way.

There are many other ways in which the interstellar gas can be heated or cooled and these mechanisms depend strongly upon the species being heated. The predominant mechanism involves the electrons liberated by photoionisation. These along with some light weight ions are known as suprathermal particles. These particles are thermalised via Coulomb interactions with thermal electrons. The heated electron gas then brings the

ion gas back into equilibrium. The timescale in which this occurs is very short compared to the timescale of the evolution of the interstellar medium (Spitzer 1978).

The presence of the neutral interstellar medium makes our picture of the heating processes rather more complex. The gain of kinetic energy without photoionisation requires there to be additional heating processes. The dominant process for neutral medium heating comes from the interactions with low energy cosmic rays (Goldsmith et al. 1969). These non relativistic cosmic rays also interact with the electron gas via the coulomb interaction.

Another heating mechanism comes from the removal of electrons from dust grains by the absorption of UV photons. Having insufficient energy to further ionise the medium the free electrons will thermalise with the electron gas. What remains of the photon energy heats the grain. Another mechanism comes from the irradiation by X-rays. This can remove K shell electrons from the interstellar gas resulting again in the release of electrons. Chemical reactions within the interstellar medium can heat the gas. The most important chemical reaction in the ISM comes from the formation of molecular hydrogen. Since this reaction is strongly exothermic a large amount of energy is released with each association. Direct collisions between the particles in the interstellar medium can transfer some energy, though this mechanism is weak at low densities. Macroscopic motions of the gas such as hydrodynamic and magnetohydrodynamic heating can also modify the individual kinetic energies of the constituent particles.

The cooling of the interstellar medium is dominated by two main mechanisms. The first

is that of fine structure cooling. Since a given transition co-exists with many possible fine structure levels of similar energy the odds of the excited electron de-exciting into one of these states is large. This process is the dominant process for all but the hottest gas. At higher temperatures there exist many other levels that can be populated by collisions with electrons. The radiative de-excitation following the collisional excitation of the $n=2$ level in hydrogen for example results in the Lyman Alpha line of hydrogen.

Cooling mechanisms within molecular clouds involve the de-excitation of rotational states and maser effects. In high temperature plasmas the recombination of a free electron with an ion can also contribute to the cooling of the gas.

1.4.2 Photodissociation regions

Photodissociation regions are defined as the interfaces of molecular clouds. These photon dominated regions can also describe any situation where the UV radiation is strong enough to photodissociate molecules. These regions are characterised by strong lines of C II at 158 microns and O I at 63 microns. These regions can also be identified due to the presence of the strong vibrational lines of molecular hydrogen. In the mid infra-red these regions are characterised by strong aromatic band emission. In these regions the ultraviolet radiation field decreases with distances into the cloud itself. The rate at which the radiation field drops off is linked to the visual extinction of the cloud and thus its density. The transition from UV transparent cloud to UV opaque cloud comes in the form of stratified layers of ionisation. The molecular hydrogen within is surrounded by

atomic hydrogen which is itself surrounded with ionised hydrogen. A similar stratification exists with the carbon content that inside the clouds forms carbon monoxide, only to be disassociated at the boundary.

A photodissociation region is observed through the strong molecular hydrogen, carbon and oxygen lines in the infrared to submillimetre range. In the dense gas clouds that surround star forming regions most of the energy emitted from the young stars is reabsorbed by the surrounding nebula. The re-emission of this light dominates the line and continuum emission of the galaxy.

1.4.3 Shocks

Shocks occur in the interstellar medium as a result of a violent increase in pressure. This increase in pressure pushes material faster than the speed of sound in that material. Though the observed material velocity within a H II region is in the order of the sound velocity, the material in the neutral medium exists at highly super sonic velocity. The gas that makes up a supernova remnant has often been expelled at velocities much greater than the neutral medium velocity. Protostars and young stars also blow bubbles and jets of supersonic material. When this material intercepts the neutral medium material a discontinuity forms. The simplest physical description of a shock is one that occurs in the absence of a magnetic field. These are called J shocks. As with all shock fronts momentum and energy are conserved either side of the shock.

The presence of a shock front moving through the interstellar medium will, due to the rapid changes in the physical conditions, leave a lasting effect on the medium itself. The sudden increase in temperature will result in an outbreak of collisional ionisation. Additionally the shocked medium will emit radiation due to the collisional excitation of the atoms. This will result in the medium having lost energy after the shock and thus shocks are a cooling mechanism. However, this newly emitted light will propagate through space faster than the shock front and thus irradiate the un-shocked region. Though this process, known as the radiative precursor, is a heating mechanism its effects are generally smaller than the cooling mechanism. This results in their being a net cooling of the interstellar medium near shocks. The temperature profile across a shock front begins with this radiative precursor followed by a sharp rise in temperature that is the shock front itself. The shock front is considered radiative due to the thermalisation of the gas both in front and behind it. The pressure profile across a shock starts with a sudden increase in pressure at the shock front that persists as a high pressure region after the shock front moved on.

Magnetic fields in the interstellar medium add to the thermal pressure of the gas across a shock front with magnetic pressure. The magnetic energy of which changes across the shock front. In cases where the magnetic field is anti parallel to the direction of the shock the tangential velocity will change direction across the shock front. Other complications coming from modifications to a magnetic fluid include the propagation of low frequency ion oscillation waves such as Alfvén Waves. Also the existence of slow, intermediate and fast magnetosonic waves complicate the magnetohydrodynamic picture. Generally

speaking fast shocks have the effect of amplifying the magnetic field after the shock, whilst slow shocks have the effect of diminishing it. For a full review of this area of physics see Shaikh, Zank & Pogorelov (2008).

The ionised medium interacts differently with the shock front due to its charge. Direct collision between atoms of the neutral medium and ions of the ionised medium are relatively rare and so the two media can be considered two distinct dynamically isolated fluids. Indeed the magnetic field of the interstellar medium is anchored to the ions and it is through this medium that magnetosonic waves propagate. These waves carry information about the shock front to unaffected ions at a different velocity than between particles in the neutral medium. This difference is called ambipolar diffusion. The result of these high velocity plasma waves is that within the neutral medium there is a magnetic precursor to the shock front. In the two fluid scenario the subalfvenic ionised medium reacts to the incoming shock front before the supersonic neutral medium. If the velocity of the media varies constantly than the shock is called a C type (C for continuous). If there is a discontinuity in the velocity of one of the media, for example if the supersonic neutral medium becomes subsonic, then the shock is called a J type (J for jump). After the shock front has moved on the two fluids will gradually return to the same velocity. See Figure 1.8.

Shocks that originate from supernova and young stars expand away from the scene of the supernova or from the young star. This movement of the shock front will affect the rate at which the interstellar medium can return back to normal after the incursion of a

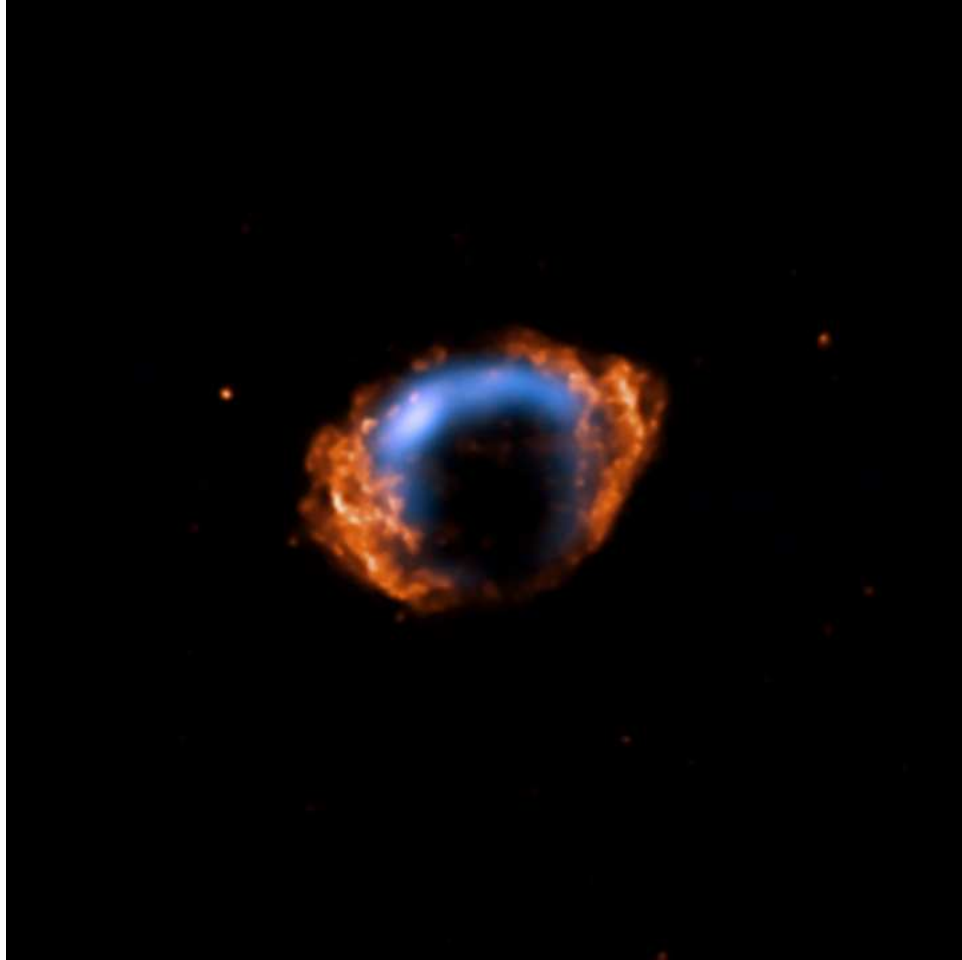


FIGURE 1.8. The shock wave of supernova G1.9+0.3 is the youngest known supernova remnant (SNR) in the Milky Way. Image source: Chandra X-ray and VLA

shock. (Chieze et al. 1998) calculated that for a shock propagating at ten km/s through a non magnetic medium the time scale before the medium returns to its stationary state is roughly 2000 years. In the case of the magnetic C shock the stationary state is reached after about 10,000 years.

A high velocity shock can create such extremes of temperature that it both destroys and creates a broad range of chemicals and dust grains. The high temperatures of the shock often overcome the activation energies required for certain endothermic reactions to occur and thus seed the interstellar medium with a rich chemistry of molecules and grains. The condensation of atoms into molecules and grains forms the first stage of the collapse of the interstellar medium required to produce stars. Hence, shocks moving through the interstellar medium act as the primary trigger of star formation.

The temperatures produced by a shock can be in the order of a million Kelvin and are thus emitters of X-rays. In fact shocks release photons of a broad range of energy including optical and ultraviolet photons. These wavelengths are largely unobserved because they are rapidly absorbed by the gas and dust close to the shock front. In H II regions shocks can be observed via the emission of recombination lines and forbidden lines in the optical wavelengths and general enhancements of sets of infrared lines. Some species such as iron tends to be liberated from dust by a passing shock waves and so the presence of ionised Iron is generally higher close to shock fronts (Nozawa et al. 2006).

The expansion of the spherical shock front from a supernova or new star will eventually lose its symmetry and become a broken shell. The shock wave becomes broken because

of the growing effect of slight differences in the shock path, known as Rayleigh-Taylor Instabilities. The broken shock front sections then propagate through space becoming more turbulent. Different shock front sections can also travel at different velocities. This instability at the interface of two fluids of different density is known as a Kelvin-Helmholtz instability.

1.4.4 The local bubble

The interstellar medium contains large low density bubbles which range from hundreds of parsecs to several thousand parsecs in size that are believed to be the result of ancient supernova explosions (Heiles 1987). These bubbles can be easily seen in other galaxies through observations of H alpha. Within our own galaxy these bubbles are harder to observe because of our perspective. One additional problem in our observations of galactic bubbles comes from our apparent position in the center of one. This bubble is known as the local bubble. It is not clear if a bubble the size of the local bubble was created by a single supernova or by several that went off in quick succession. The evidence that suggests that the local bubble was created by a single supernova comes from the low likelihood of several supernova going off in a small region of space in a galaxy as inactive as our own. Though it is noted by McClure-Griffiths et al. (2003) that in external galaxies the number of bubbles observed is only barely reconcilable with star formation rates.

The low expansion velocity, the large size and low x-ray luminosity indicates that the

local bubble is very old. Some estimates place the age at 10 million years. One theory is that though many of the observed bubbles have evolved from supernova the local bubble has not. Wada & Norman (1999) suggest that the local bubble is the natural result of a thermally and gravitationally unstable galactic disc.

Whatever the origin, these bubbles often become elongated in the galactic plane due to the radius of the bubble reaching the scale height of the gas and thus encountering lower and lower densities in the polar directions. Eventually the bubble will break out of the galactic disc and seed the halo with both high velocity clouds and hot gas. This is known as the fountain model. A another effect that influences bubble morphology is the deformation that occurs due to the differential rotation of the disk (Tenorio-Tagle & Palous 1987). This process requires at least 10 million years and so is not observed in the structure of the local bubble. It is however observed in other galaxies where bubbles are elongated and aligned with the rotation of the spiral arms. Finally, the most dramatic morphological change that a bubble can experience comes through the interaction with other bubbles. The result is that the high density gas between the bubbles becomes a dense wall of material (Yoshioka & Ikeuchi 1990). UV and X-ray absorption measurements and the observation of the 21 cm line indicates that due to its unusually large size the local bubble is interacting with other bubbles (Egger & Aschenbach 1995).

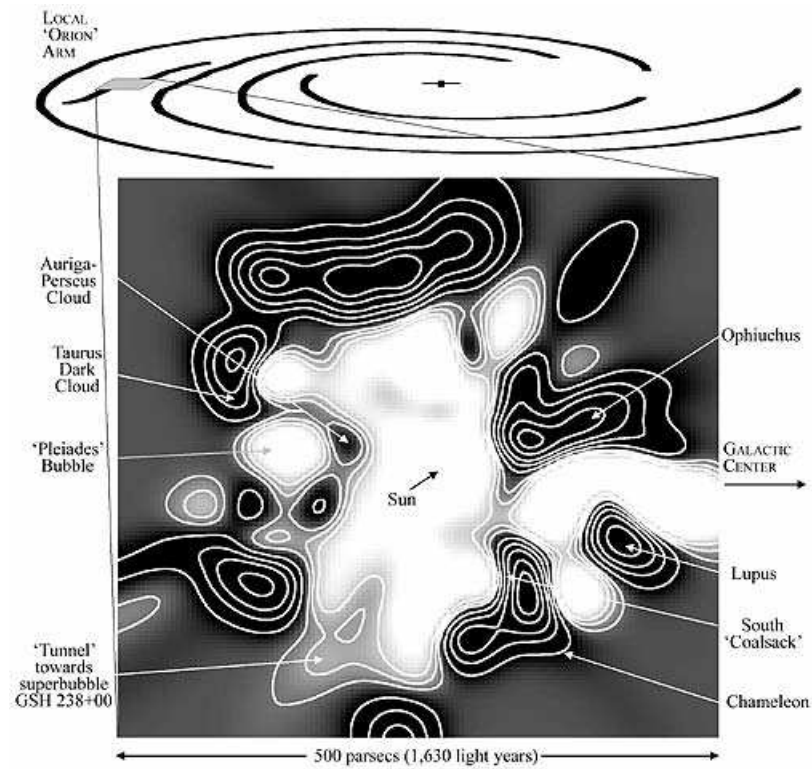


FIGURE 1.9. Lallement et al (2003) plot of cool gas in galactic latitudes

Chapter 2

FUSE

2.1 FUSE

2.1.1 Introduction

Ultraviolet absorption lines in the spectra of white dwarf stars present good opportunities for studying the Local Interstellar Medium (LISM). The white dwarf spectrum provides a simple continuum by which to observe the superimposed absorption lines from interstellar space however confusion can occur between interstellar and white dwarf spectral features. Most white dwarfs within the brightness range of the Far Ultraviolet Spectroscopic Explorer (Moos et al. 2000) lie at distances that are within, on the edge or just outside of the "Local Bubble". Having a collection of background stars that occupy positions within this short distance scale provides a way of quantifying the gas over these short distances. Critically these white dwarfs allow us to probe the most important interstellar environment, that which makes up the local neighborhood of the Sun.

The absorption lines of the ISM supply important information on the chemical composition and the physical conditions in the diffuse interstellar medium. Study of the ISM has often been limited by the inability to differentiate between the absorption lines of the interstellar medium and the absorption lines intrinsic to the star. Studies have previously used the movement of the photospheric lines in close binaries, or the widening of the photospheric lines in P-Cygni systems to identify the non-stellar lines. This limits the lines of sight available for study to a small number and often to stars that are very distant.

Hot white dwarfs have a complicated absorption pattern within the range 920-1180Å that makes distinguishing stellar lines from LISM lines very difficult. In many cases the width and depth of the stellar lines are extremely similar to those of the ISM lines. Thus the line profile cannot be used as an indicator of a line's origin.

2.1.2 FUSE data reduction

The FUSE satellite was launched on June 24 1999 and placed into a low Earth orbit. After the usual check out and calibration activities, science operations began that December. For eight years the satellite observed thousands of targets before finally failing in July 2007. The mission is described in detail by Moos et al. (2000) and its in-orbit performance has been published by Sahnou et al. (2000). What follows is a description of the data acquisition and reduction.

All of the public and proprietary FUSE data is stored in the Multimission Archive¹,

¹<http://archive.stsci.edu/mast.html>

Table 2.1. Wavelength ranges (\AA) of the fuse detector segments.

Channel	Segment A	Segment B
SiC 1	1090.9-1003.7	992.7-905.0
LiF 1	987.1-1082.3	1094.0-1187.7
SiC 2	916.6-1005.5	1016.4-1103.8
LiF 2	1181.9-1086.7	1075.0-979.2

hosted by the Space Telescope Science Institute. Over the eight years of the spacecraft's operation most of the proprietary data has become public. This study is the first to include all WD targets observed by the spacecraft and thus represents the first complete sample of a broad spectrum of degenerate objects.

The optics of the FUSE spectrographs are based on a Rowland circle design and consists of four separate co-aligned optical paths. Each optical path consists of a mirror, a focal plane assembly, a diffraction grating and a segment of a detector. Light from the star enters all of the optical paths simultaneously. Two of the mirrors and two of the gratings are coated with Lithium Fluoride (LiF) over a layer of aluminium. Since the reflectivity of AL+LiF is low below 1020 \AA the detectors that cover this region are coated in Silicon Carbide (SiC). FUSE has two microchannel plate detectors (1 and 2), each divided into two individual segments (A and B). Light from the two channels falls onto each detector resulting in eight individual spectra. See Table 2.1 for a list of the wavelength ranges for each detector segment.

The apertures available for use are small, medium and large, which deliver high, medium and low resolution spectroscopy, though inaccuracies in pointing and thermal instabilities often result in the target being missed when the high resolution aperture is used. The high

resolution aperture suffers the most from thermal changes that rotate the mirrors slightly. In this study most observations have been carried out using the largest aperture (LWRS, 30 x 30 arcsec). The nominal spectral resolution for the LWRS is $(20\,000)^2$ though this may have degraded with time due to source drift.

The data recording modes Time Tag (TTAG) and Histogram (HIST), are selected for targets depending on how bright it is. The brighter targets use the histogram mode since time tagging photons becomes meaningless when the arrival of two photons can not be resolved.

The particle and radiation environment of low earth orbit is quite severe. Radiation from cosmic rays is unavoidable but does not affect the spectra too badly. Radiation from earth's radiation belts is avoided by allowing the spacecraft to enter safe mode as it transits the region known as the South Atlantic Anomaly. Escaping atoms from earth's atmosphere are observed by the spacecraft as emission superimposed on the observations. This geocoronal emission is sun angle dependent and is absent whilst the spacecraft is shaded by the earth. These lines are often the result of the same atomic transitions that are observed in the interstellar medium. The result is that the ISM lines can be contaminated by emission. Occasionally the geocoronal emission is offset in velocity compared to the ISM lines and by infilling part of the absorption feature skews the measured line velocity. Luckily this effect seems to contaminate only the hydrogen lines and the 1134 N I multiplex so which are not essential in our analysis.

²The FUSE observers guide see <http://fuse.pha.jhu.edu/>

Another problem with FUSE spectra is the presence of a decrease in flux known as "the worm", of the spectra where a shadow cast by the electron repeller grid located above the detector surface blocks some of the light. It can be seen as a dip in flux by up to 50 per cent, particularly in the LiF 1B segment. Since this only disturbs data analysis for those lines that fall in this region and very few lines actually fall in this region its effects can be described as negligible.

The data were fed through calibration pipeline CALFUSE V3.2. (Dixon et al. 2007) which produces eight separate sections of spectra. This was designed so that a detector failure would not result in the loss of full wavelength coverage. This adds a redundancy of multiple exposures for each segment are then co-added and rebinned from 0.006 \AA to 0.04 \AA to minimise the random noise. The edges of the spectra sections are normally the noisiest and so these are removed. Each segment is then weighted according to the exposure time. This enables the cross correlation and stitching together of different sections using common features to assign the correct overlap. There are some instances where the weighting is miscalculated because the star has drifted off one of the detectors. The flux is then divided by too high an exposure time. These are visible as sudden discontinuities in the level of the flux continuum. Reliably stitching the middle section to the final section requires a measure of the velocity of interstellar features each side of the divide since the overlap contains no lines that can be cross correlated. Spectral fluxes are shifted by a constant factor to line up with the LiF 1A segment, which is the segment used in the pointing of the satellite and should have the best flux and wavelength calibrations. The result of these shifts is that each spectrum is displaced in wavelength

space. The absolute positions of spectral features are not consistent across repeated observations of the same target and, therefore, the absolute position of a feature does not yield any scientific information. However, the position of features relative to each other is consistent across multiple observations.

2.1.3 FUSE sample

Our sample consists of 123 white dwarfs that were observed by FUSE in its 8 year lifetime. Stars with spectra of very poor quality were removed resulting in a final sample that contained 97 stars. Literature coverage of these objects is patchy and ranges from several hundred references for some stars to fewer than five references for others. The surface temperature and gravities have been estimated for a large fraction of the sample. There is not complete coverage by any single survey, but the combined coverage of all the surveys gives some estimation of surface conditions for most stars. Systematic differences, do however, exist between these surveys. These are largely the result of differing models used, the quality of the observations and which series of hydrogen lines the models were compared to. These results have for some stars been used to ascertain the distance to the star by comparing the predicted flux, calculated from the fitted model, to the observed flux and deriving a distance modulus.

The sample ranges in temperature from 16,000K to 69,000K with an average of 42,000K. Surface gravity ranges from $10^{7.2} \text{cm s}^{-2}$ to $10^{9.2} \text{cm s}^{-2}$ with an average of $10^{8.0} \text{cm s}^{-2}$. The mass ranges from 0.4 solar mass to 1.3 solar mass with an average of 0.6 solar mass.

The distances to the stars in the sample range from 10 pc to 360 pc with an average of 110 pc.

2.1.4 Line velocity

FUSE data is not accompanied by a standard star spectrum and so some velocity information is lost. Whereas the relative velocity separation between lines is accurate, the whole spectrum may be shifted relative to the heliocentric velocity. Since there is no real benefit in doing so we have not shifted the spectrum so that the average interstellar medium line velocity coincides with the default 0 km/s. This means that when comparing the velocities deduced from this work to velocities previously deduced or deduced in other works, it may be different. However the relative separation between the photospheric and interstellar lines will remain constant.

The Doppler Effect describes how the wavelength of light changes when the source is moving towards or away from the observer. If a star has a large radial velocity, the features in its spectrum will be shifted in wavelength space by an amount that is characteristic of the star's velocity. This is given by Equation 2.1

$$v = \frac{c\lambda - c\lambda_o}{\lambda_o} \quad (2.1)$$

Where v is the stellar velocity as measured from a spectral feature. In this work v is given in units of km/s. The measured wavelength of a feature λ and its unshifted wavelength or lab wavelength λ_o is given in Angstroms.

The radial velocity of a star describes its space motion in the line of sight. Proper motion is a velocity vector formed from the apparent shift in position of the star in the sky. Since white dwarfs are fainter than main sequence stars those white dwarfs we have detected are typically closer. This proximity can result in a large proper motion. Since radial velocities are independent of distance the radial velocity distribution of white dwarfs is the same as the rest of the stellar population. If the space motion of the Sun was the same as the average of the space motions of the local stars, then the radial velocity distribution would peak at exactly 0 km/s. Since the sun does have a measurable velocity vector relative to this average the radial velocity distribution of stars is skewed away from the direction in which the Sun is moving. This effect is minor for a small sample since the individual space motions of the stars are normally orders of magnitude greater than the Sun's movement vector. This is the result of the large possible dispersion in space motions of other stars and the coincidentally small solar vector.

The radial velocity of a star is inferred from the blue or red shifting of the stars spectral features. Lines that form in the photosphere of the star all share a common velocity due to space motion. Small scale movements of material in the stellar atmospheres have negligible effects on the velocity of the star lines. Mass loss and strong out flowing winds can blue shift absorption lines. Circumstellar shells and the ionisation of the surrounding interstellar medium can also create blue and red shifted components of certain species. Rapid rotation of the star can broaden the lines but do not create separate components unless large features like star spots are present. If the star is a close binary there could, depending on the orientation of the system, be a periodic oscillation in the radial velocity.

Another factor that affects the spectral line velocity is the global reddening of the emergent light due to gravitational red shift. This was first measured in Sirius B by Greenstein et al. (1971) and was followed by Dupree & Raymond (1982) and Vennes & Thorstensen (1994a) for the binary star Feige 24. More recently Silvestri et al. (2001) determined the gravitational red shifts for 41 DA white dwarfs and found a distribution of red shifts extending from 8.8 to 132.3 km/s. Savage & Lehner (2006) find that the average gravitational red shift for their sample of white dwarfs is 33 km/s. The redshift obeys the following relation.

$$\frac{\lambda - \lambda_0}{\lambda} = \frac{GM}{c^2 r} \quad (2.2)$$

Where G is the universal constant of gravitation, M is the stellar mass, r is the radius of the star. Circumstellar shells exist at a different value of r and so are less red shifted than the lines associated with the star (Bannister et al. 2003).

The line velocity will be a combination of the gravitational red shift and the radial velocity of the star. Savage & Lehner (2006) and others do not take full account of the possible space motion contribution to the observed line velocity and thus stumble into the assumption that the line velocity is always approximately 33 km/s. A simple examination of a sample of stars shows that this is not the case.

2.1.5 Line selection

The two main sources of information from which one could compile a line list in order to measure the ISM and photospheric velocities is either laboratory experiment derived

line databases or from previous studies of the ISM and white dwarfs. Line databases are often less than ideal since they are rarely complete and often overcrowded with weak lines. In some instances a line in the observation can coincide with multiple lines in the line database. Using past literature is equally perilous due to the number of unnoticed misidentified lines. Before any definitive line list is created for the purpose of measuring the ISM and photospheric velocity a careful and critical evaluation of each literature line is required.

For this investigation several diagnostic techniques were developed in order to identify which lines were likely to be misidentified in the literature. For this a review of all the ISM literature that covers this spectral range was undertaken. The first technique used is to attempt to observe the line in our sample. If the line is absent then it can not be used as a velocity reference. If a line is present, a return to the literature is made to check that all published material is in agreement with the identification of the line. In several cases the line is labeled as a misidentification because several proposed identities exist for it.

Assuming that the range of the interstellar velocities is small compared to the width of the lines we can assume a single value for the interstellar medium velocity. Though some telescopes with better spectral resolution, observing longer lines of sight, can resolve several velocity components, FUSE is unable to do so over such short distances. This enables us to employ a third test that looks at how the line positions change between two stars of different radial velocities. Where the lines moved positions by a detectable amount, a diagnosis of interstellar could be made, and where they moved a

distance comparable with the difference of the radial velocities of the two stars then a diagnosis of stellar could be made. This final test showed that many Interstellar lines were photospheric in origin and therefore misidentified.

Table 2.2 displays all the literature identifications that fail at least one of these tests. If these lines are misidentifications then they will give an incorrect line velocity. It is worth rejecting these lines to avoid contaminating the average velocity derived for the interstellar medium.

Table 2.2: Literature identifications that fail at least one of the three tests of identity developed in this work

Species	Wavelength	Reference	Our conclusion	Notes
Ar II	919.781 Å	Jenkins et al. (2000)	Misidentification	Likely to be a misidentification of the 919.66 Å O I line.
O I	922.2 Å	Morton (1978)	Misidentification	Misidentification of photospheric 921.994 Å N IV line
O I	930.257 Å	Morton (1978)	Unresolvable	Coincident with hydrogen Lyman line
Al II	935.275 Å	Morton (1978)	Absent	
Fe II	935.783 Å	Morton (1978)	Absent	See Friedman et al. (2000)
O I	937.84 Å	Morton (1978)	Unresolvable	Coincident with hydrogen Lyman line
S VI	944.523 Å	Sembach et al. (2001)	Not ISM	Photospheric under velocity test
Ni II	944.633 Å	Barstow et al. (2002)	Misidentification	Misidentification of photospheric 944.53 Å S VI line
C I	945.34 Å	Herald & Bianchi (2002)	Absent	
N I	951.079 Å	Morton (1978)	Absent	
FI	951.871 Å	Snow & York (1981)	Absent	See Lauroesch et al. (2004), Federman et al. (2005) and Snow et al. (2007)
N I	952.303 Å	Morton (1978)	Absent	
N I	952.303 Å	Jenkins et al. (2000)	Misidentification	Photospheric under velocity test. See also Herald & Bianchi (2002), Wood et al. (2002), Froning et al. (2001), Wolff et al. (2001)
N I	952.415 Å	Morton (1978)	Absent	
FI	954.827 Å	Morton (1978)	Absent	
N I	954.827 Å	Morton (1978)	Absent	
N I	960.201 Å	Morton (1978)	Absent	
P II	961.04 Å	Morton (1978)	Absent	Possibly in longer lines of sight
O I	990.2 Å	Herald & Bianchi (2002)	Misidentification	Misidentification of NIII and Si II merged line at 989 Å
P III	998 Å	Morton (1978)	Absent	
Continued on next page				

Table 2.2 – continued from previous page

Species	Wavelength	Reference	Our conclusion	Notes
Cl III	1005.28 Å	Morton (1978)	Absent	
Cl III	1008.777 Å	Morton (1978)	Absent	
Cl III	1015.023 Å	Morton (1978)	Absent	
O I	1025.762 Å	Morton (1978)	Unresolvable	Coincident with hydrogen Lyman line
O I	1026.475 Å	Morton (1978)	Unresolvable	See Froning et al. (2001), Lemoine et al. (2002) and Froning et al. (2003)
O VI	1031.926 Å	Various	Not ISM	Photospheric under velocity test
Cr III	1033.35 Å	Morton (1975)	Absent	See Morton (1978)
O VI	1037.617 Å	Various	Not ISM	Photospheric under velocity test
Fe II	1055.262 Å	Wolff et al. (2001)	Absent	See Hoard et al. (2003). Possibly in wd2116+736 and wd2043-635
Fe II	1055.269 Å	Morton (1978)	Absent	See Friedman et al. (2000)
Fe II	1063.18 Å	Wolff et al. (2001)	Not ISM	Photospheric under velocity test, See also Hoard et al. (2003)
Cl II	1063.831 Å	Morton (1978)	Absent	See Morton (1978)
Fe II	1063.97 Å	Hoard et al. (2003)	Absent	Possibly in wd2111+498
Fe II	1063.982 Å	Morton (1978)	Absent	See Friedman et al. (2000)
Ar I	1066.66 Å	Morton (1978)	Misidentification	Misidentification of photospheric Si IV 1066.614 Å . See Oegerle et al. (2000), Welsh et al. (2001), Sembach et al. (2001), Richter et al. (2001), Lehner et al. (2002), Herald & Bianchi (2002) and Froning et al. (2003)
Cl II	1071.036 Å	Morton (1975)	Absent	See Morton (1978)
N II**	1085.545 Å	Morton (1975)	Absent	See Morton (1978)
N II**	1085.701 Å	Morton (1975)	Absent	See Morton (1978)
Cl I	1088.062 Å	Morton (1975)	Absent	See Morton (1978)
Continued on next page				

Table 2.2 – continued from previous page

Species	Wavelength	Reference	Our conclusion	Notes
Cl I	1094.769 Å	Morton (1975)	Absent	See Morton (1978)
Cl I	1097.369 Å	Morton (1975)	Absent	See Morton (1978)
Ge II	1098.71 Å	Morton (1978)	Absent	
Fe II	1112.048 Å	Friedman et al. (2000)	Not ISM	Photospheric under velocity test. See also Sembach et al. (2001) and Richter et al. (2001)
Cl I	1121.52 Å	Morton (1975)	Absent	See Morton (1978)
Cl I	1121.713 Å	Morton (1975)	Not ISM	Photospheric under velocity test
Fe II	1121.975 Å	Friedman et al. (2000)	Absent	Possibly in wd2116+736, wd1725+586, wd1611-084, wd1337+701, wd0937+505 and wd0416+402
Fe II	1121.987 Å	Morton (1978)	Absent	See Friedman et al. (2000)
Fe II	1121.987 Å	Morton (1978)	Not ISM	Photospheric under velocity test
Cl I**	1122.26 Å	Morton (1978)	Misidentification	Misidentification of photospheric Si IV 1122.500 Å line.
Cl I**	1122.33 Å	Morton (1978)	Misidentification	Misidentification of photospheric Si IV 1122.500 Å line.
Cl I	1122.447 Å	Morton (1975)	Not ISM	Photospheric under velocity test
Cl I	1122.518 Å	Morton (1975)	Not ISM	Photospheric under velocity test
Fe III	1122.526 Å	Morton (1978)	Misidentification	Misidentification of photospheric Si IV 1122.500 Å line. See also Sembach et al. (2001), Richter et al. (2001), Lehner et al. (2002) and Danforth et al. (2002)
Cl I*	1122.75 Å	Morton (1978)	Absent	
Cl I**	1123.065 Å	Morton (1978)	Absent	
V III	1123.53 Å	Morton (1975)	Absent	See Morton (1978)
Fe III	1125.448 Å	Oegerle et al. (2000)	Not ISM	Photospheric under velocity test. See also Friedman et al. (2000), Wolff et al. (2001), Sembach et al. (2001), Richter et al. (2001), Lehner et al. (2002) and Danforth et al. (2002)
Continued on next page				

Table 2.2 – continued from previous page

Species	Wavelength	Reference	Our conclusion	Notes
Fe II	1127.098 Å	Friedman et al. (2000)	Absent	See Sembach et al. (2001) and Danforth et al. (2002)
C I	1128.075 Å	Morton (1975)	Misidentification	Misidentification of photospheric P V 1128.008 Å
C I	1128.171 Å	Morton (1975)	Misidentification	Misidentification of photospheric P V 1128.008 Å
C I*	1128.27 Å	Morton (1975)	Misidentification	Misidentification of photospheric P V 1128.008 Å
C I	1128.477 Å	Morton (1975)	Misidentification	Misidentification of photospheric P V 1128.008 Å
C I*	1128.686 Å	Morton (1975)	Misidentification	Misidentification of photospheric P V 1128.008 Å
C I*	1129.078 Å	Morton (1978)	Absent	
C I	1129.196 Å	Morton (1975)	Absent	See Morton (1978)
C I	1129.318 Å	Morton (1975)	Absent	See Morton (1978)
C I*	1129.749 Å	Morton (1978)	Absent	
Fe II	1133.665 Å	Friedman et al. (2000)	Absent	Possibly in wd2116+736, wd2111+498 and wd2004-605
Fe II	1133.678 Å	Morton (1978)	Absent	See Friedman et al. (2000)
C I*	1138.595 Å	Morton (1978)	Absent	
C I*	1139.3 Å	Morton (1978)	Absent	
C I	1139.792 Å	Morton (1975)	Absent	See Morton (1978)
C I	1139.8 Å	Welsh et al. (2001)	Absent	
C I	1140.01 Å	Morton (1975)	Absent	See Morton (1978)
Fe II	1142.366 Å	Morton (1978)	Absent	See Friedman et al. (2000)
Fe II*	1148.295 Å	Morton (1978)	Absent	
P II	1152.818 Å	Morton (1978)	Absent	See Oegerle et al. (2000), Friedman et al. (2000), Wolff et al. (2001), Welsh et al. (2001), Sembach et al. (2001), Richter et al. (2001), Lehner et al. (2002) and Danforth et al. (2002)
V III	1153.18 Å	Morton (1975)	Absent	Possibly in wd2013+400, wd2116+736 and wd2004-605 See Morton (1978)
Continued on next page				

Table 2.2 – continued from previous page

Species	Wavelength	Reference	Our conclusion	Notes
CI	1155.809 Å	Morton (1975)	Absent	See Morton (1978)
CI*	1156 Å	Morton (1978)	Absent	
CI**	1156.386 Å	Morton (1978)	Absent	
CI**	1156.56 Å	Morton (1978)	Absent	See Morton (1978)
CI**	1156.765 Å	Morton (1978)	Absent	
CI	1157.186 Å	Morton (1975)	Absent	
CI*	1157.405 Å	Morton (1978)	Absent	See Morton (1978)
CI*	1157.77 Å	Morton (1978)	Absent	
CI	1157.91 Å	Morton (1975)	Absent	
CI*	1158.035 Å	Morton (1978)	Absent	See Morton (1978)
CI*	1158.13 Å	Morton (1978)	Absent	
CI	1158.324 Å	Morton (1975)	Absent	
CI**	1158.397 Å	Morton (1978)	Absent	See Morton (1978)
CI*	1158.544 Å	Morton (1978)	Absent	
CI**	1158.967 Å	Morton (1978)	Absent	
Ge II	1164.273 Å	Morton (1978)	Absent	

These criteria leave a series of lines that can be used to form a list (see Table 2.3) for the measurement of the average velocity for the ISM and photosphere.

Table 2.3: Absorption lines used in this investigation

λ	Species	Origin
919.66	O I	ISM
921.857	O I	ISM
921.994	N IV	Star
922.519	N IV	Star
922.519	N IV	Star
923.676	N IV	Star
924.284	N IV	Star
924.950	O I	ISM
925.446	O I	ISM
929.517	O I	ISM
933.376	S VI	Star
936.629	O I	ISM
944.525	S VI	Star
948.686	O I	ISM
953.415	N I	ISM
953.655	N I	ISM
953.97	N I	ISM
954.104	N I	ISM
963.801	P II	ISM
963.990	N I	ISM
964.626	N I	ISM
965.041	N I	ISM
971.738	N I	ISM
976.448	O I	ISM
977.03	C III	Star
1020.699	Si II	ISM
1030.515	P IV	Star
1031.912	O VI	Star
1035.516	P IV	Star
1036.337	C II	ISM
1037.018	C II	ISM
1039.23	O I	ISM
1048.22	Ar I	ISM
1072.996	S IV	Star
1066.636	Si IV	Star
1083.99	N II	ISM
1096.877	Fe II	ISM

Table 2.3

λ	Species	Origin
1128.008	P V	Star
1128.325	Si IV	Star
1134.165	N I	ISM
1134.415	N I	ISM
1134.980	N I	ISM
1143.226	Fe II	ISM
1144.938	Fe II	ISM
1152.81	P II	ISM
1174.933	C III	Star
1175.263	C III	Star
1175.7110	C III	Star
1175.987	C III	Star
1176.37	C III	Star

Chapter 3

Cool gas in the LISM

3.1 The density of the LISM

3.1.1 Introduction

The amount of cool gas in the interstellar medium can be calculated from the measured ISM column density and the length of the line of sight over which it is measured. Stellar distance determinations via the parallax method are not always possible for white dwarfs because of their low apparent brightness and so other methods are required. The stellar distance can be found by comparing the observed flux to the absolute stellar flux at a given wavelength. The absolute flux can be determined from synthetic spectra calculated for each star so that the surface temperature and gravities of the model produce the same hydrogen line profiles as the observed spectrum.

The FUV region contains both cold and warm gas absorption lines from neutral and ionised species. The column density can be calculated from the measured equivalent

widths of these lines using equation 3.28. The FUV region also contains the hydrogen Lyman lines from which T_{eff} and $\log g$ can be determined and the distance inferred. In short, observing white dwarfs in the FUV gives us all the information required to map the local interstellar medium from a single observation.

The hydrogen Balmer line series is a major feature of the optical spectra of white dwarfs and as such has been extensively used to calculate the properties of these stars. The measures of distance calculated from stellar properties ascertained this way are valid only for single star systems. If the white dwarf has a main sequence companion the observed optical flux may, depending on the companions spectral type, be dominated by the companion. Comparisons between the observed and the Eddington flux (the first order moment of flux at the stellar surface $H=f/4\pi$) becomes a comparison of the contributions from two different objects. This results in the distance being grossly underestimated. Binarity decreases the reliability of measurements. A search of the literature suggests that at least 40 per cent of our sample are binary stars or show some symptoms of binarity. This large binary fraction is the result of the favored selection of binary white dwarfs as observing candidates for FUSE. In the FUV the white dwarf dominates over most main sequence companions. The observed flux at these wavelengths can be safely compared to the absolute flux at these wavelengths to give an accurate measure of distance.

3.1.2 Creating synthetic spectra

The technique of obtaining the T_{eff} and $\log g$ from the shape and strength of the hydrogen recombination lines was pioneered by Holberg et al. (1985) and extended to a large sample of white dwarfs by Bergeron et al. (1992). Subsequent studies have looked at the effect of thin layers of non degenerate H and He in the atmospheres and for the prior evolution of the white dwarf (Bloeker 1995, Driebe et al. 1998).

In this work, a variable helium abundance model was used to produce a grid of synthetic spectra. For the majority of the white dwarfs the helium abundance was set at the default zero. *tlusty/synspec* (Hubeny & Lanz 1995) was employed to generate a grid of synthetic spectra for a range of temperatures and gravities. These were individually compared to the data by *XSPEC* and the closest fitting model selected by chi square minimization (See Barstow et al. (2003)).

The data were cropped around the Lyman lines. Data within absorption lines and the deep interstellar hydrogen Lyman cores was also removed. Any geo-coronal emission was cropped from the spectrum and what remained was compared to a model. In most cases the model was fitted simultaneously to the Lyman Beta, Gamma, Delta and Epsilon lines. In some cases where the quality of the spectra was too poor only Lyman Beta was used. An independent normalization constant was applied to each line to ensure that the result was independent of the local slope of the continuum, and reducing the effect of systematic errors in the flux calibration.

The accuracy of the Lyman $\text{Log } g$ and T_{eff} is dependent on several factors. The presence of elements in the stellar atmosphere could slightly change the calculated parameters if not taken into account. The effective temperature discrepancy between temperatures derived from Lyman line fitting and Balmer line fitting does pose a more serious problem for this analysis. For stars above 50000K the model temperature that best fits the Lyman lines becomes increasingly greater than the model temperature that best fits the Balmer lines (Barstow et al. 2003). The most likely explanation for this is that the assumption of homogeneous atmospheric structure breaks down at higher temperatures. The difficult to quantify stratification factor makes it impossible at this stage to determine if the Lyman line temperature is more or less accurate than the Balmer line temperature. What is certain is that the temperatures are not in agreement with each other. If indeed the problem is the Lyman line fitting then the hot stars in this sample could be mistaken for stars of even greater temperature and thus be placed further away than they really are. In this case the volume density will appear to be lower along these lines of sight compared to those of the cooler stars of the same actual distance. Though it is unlikely that the effect is large (in the most extreme cases the distance discrepancy is no larger than a factor of two), the value of volume density from the 8 stars in our sample that are hot enough to be potential problems, will be subject to closer scrutiny.

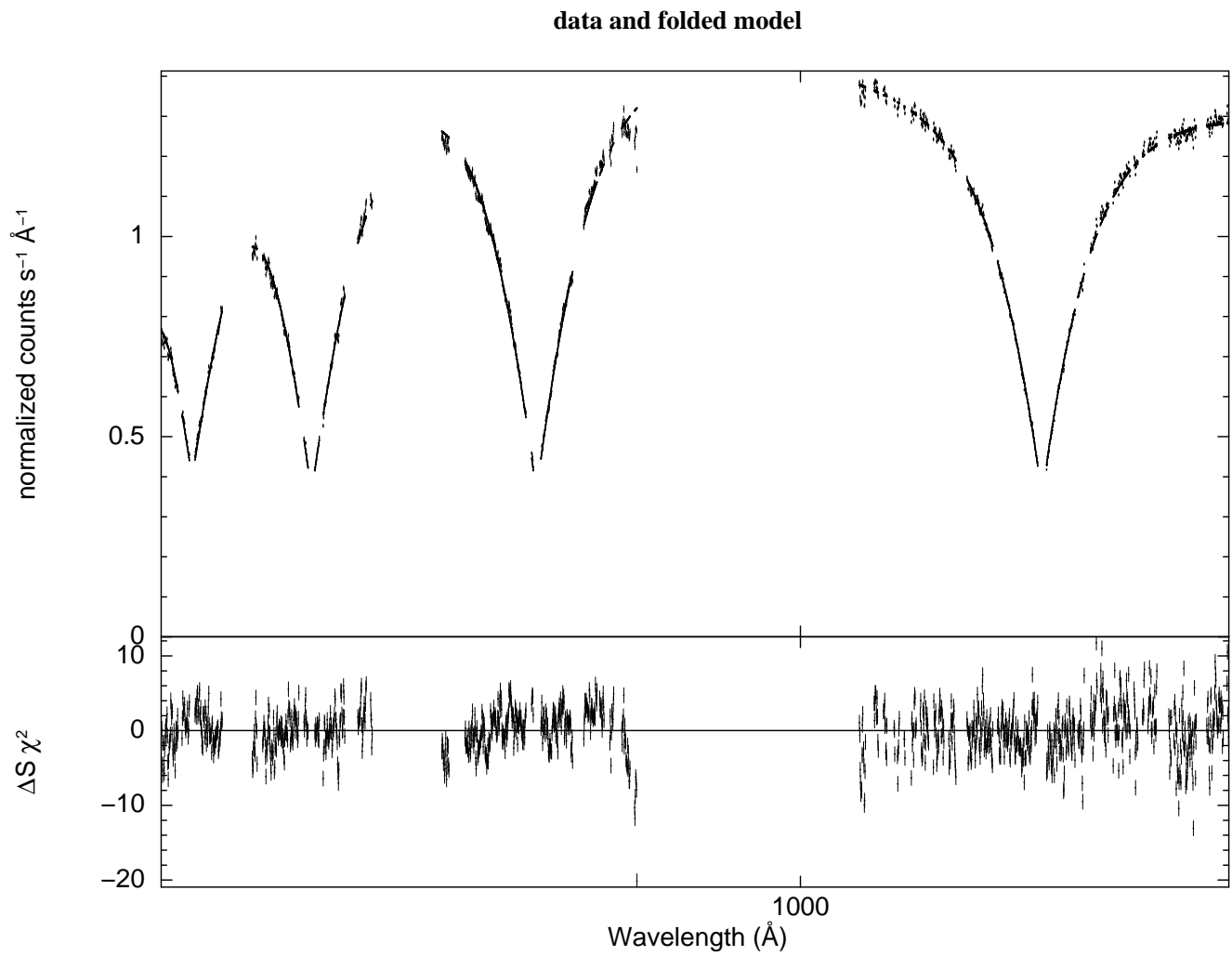


FIGURE 3.1. Data and folded model for WDO501+524

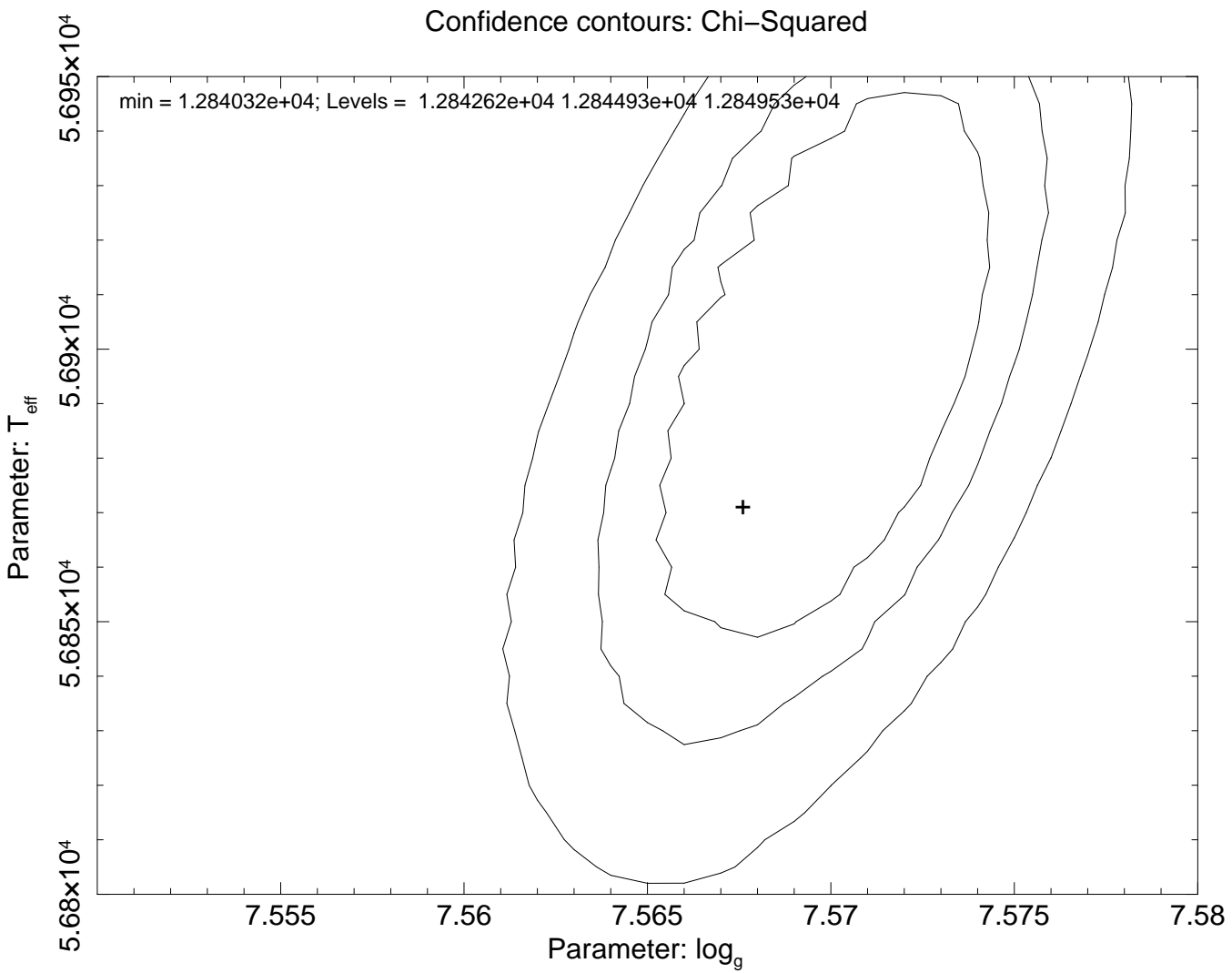


FIGURE 3.2. Confidence contours for WD0501+524

On the accompanying CD that can be found at the back of this thesis each star is displayed in an independent subsection. Examples of this data is given in Figure 3.1 and 3.2. In these subsections there are plots of the data points that go into the model and the fitted model. Stars WD0501+524 and WD0004+330 are good examples of stars where the residual between the data and the models is very small. Below the plot the residual is also plotted. After this diagram there is a standard confidence contour plot displaying the chi square minimum and 68, 90 and 99 per cent confidence levels. The location of a contour line between grid points is designated using a linear interpolation. Since the fit statistic surface is often quadratic, a linear interpolation will result in the lines being drawn inside the true location of the contour. In most stars this takes the form of three smooth concentric ellipses. In some stars the chi square surface is uneven and the resulting confidence plot takes on a more unpredictable shape. Examples of this include WD0236+498 and WD0353+284.

For each star, the value of $\log g$ and T_{eff} measured here (labelled "Boyce") is compared to literature values in the Figure 3.3. In these figures the literature values come from a range of indicators including Balmer line and Lyman line fits as well as fits to EUV continuum. Full details of the temperature determination method used as well as the results can be found in the included "physical parameters" table for each star. In most stars the result from this work is close enough to other estimates to suggest that the modeled parameters are correct within their uncertainties.

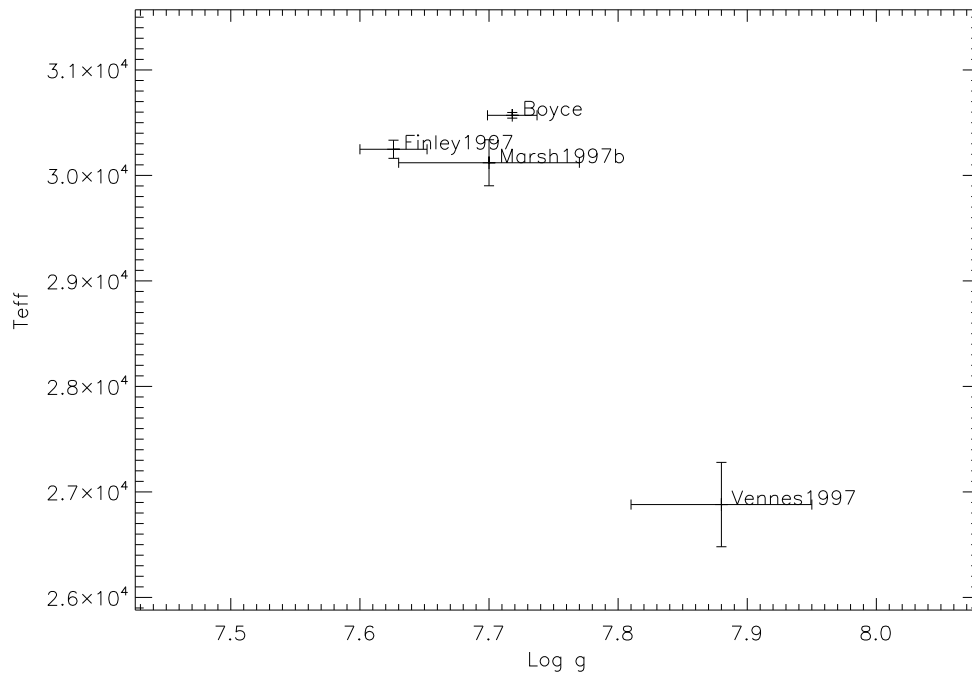


FIGURE 3.3. Example of $\log g$ and T_{eff} compared to literature values for WD0147+674

3.1.3 Interstellar reddening

Comparing the observed flux to the absolute flux will give a distance modulus only in the absence of interstellar dust. Since we are actively measuring the interstellar material it is assumed that the FUV spectra will be reddened by material along the line of sight. The effect on the FUV is a net decrease in the observed flux that becomes more pronounced towards the EUV. If the amount by which the net flux has been decreased can be quantified then the observed flux measurement used in our distance determination can be offset by this amount. There are many ways to quantify the interstellar reddening (E_{B-V}) and several were investigated for this study. Seaton (1979) characterized the effect of interstellar extinction throughout the UV region and through the Seaton reddening function we can calculate from the observed flux and the model flux the value of E_{B-V} through the equation 3.1.

$$E_{B-V} = \frac{1.08574 \log \frac{F_0}{F_H}}{X} \quad (3.1)$$

Where $X=13.92$ at 1000 \AA and 11.67 at 1100 \AA . However the result is dependent on knowing both the model absolute flux F_H and the observed absolute flux F_0 .

A different approach uses the model spectra to give an extrapolated value of flux at the central wavelengths for the B and V band filters and after passing this through the filter

response and converting to magnitude gives theoretical values of the absolute B and V band magnitudes.

$$M_V = -2.5 \log \frac{\int_0^\infty R^2 H_\lambda S_V(\lambda) d\lambda}{\int_0^\infty S_V(\lambda) d\lambda} + 73.6484 \quad (3.2)$$

For example, the V band magnitude can be calculated from the Eddington flux H_λ via Equation 3.2 (Holberg & Bergeron 2006). Where R is the radius of the white dwarf calculated from the $\log g$ and T_{eff} and described by Wood (1995) and Fontaine et al. (2001) as the mass radius relation. $S_V(\lambda)$ is the total system response including atmospheric transmission corresponding to an air mass of 1.3, mirror reflectance and detector quantum efficiency.

Equation 3.2 is used to construct a photometric grid for the absolute B and V band magnitudes. Since $B - V$ calculated this way becomes independent of distance, it can be directly compared to the observed $B - V$. In this sample large discrepancies between $E_{B-V_{obs}}$ and $E_{B-V_{syn}}$ will result from stars that are companions to main sequence stars. This is because the main sequence companion will dominate the optical colour. In single star systems and those white dwarfs that have a substellar companion the discrepancy between $E_{B-V_{obs}}$ and $E_{B-V_{syn}}$ will be the result of interstellar reddening, error of measurement of $E_{B-V_{obs}}$, inaccuracy in modeling, or systematic problems that arise from extrapolating down a synthetic spectrum. Either way, the discrepancy will indicate the uncertainty on the measurement and also may reveal those white dwarfs that have as yet an undiscovered companion.

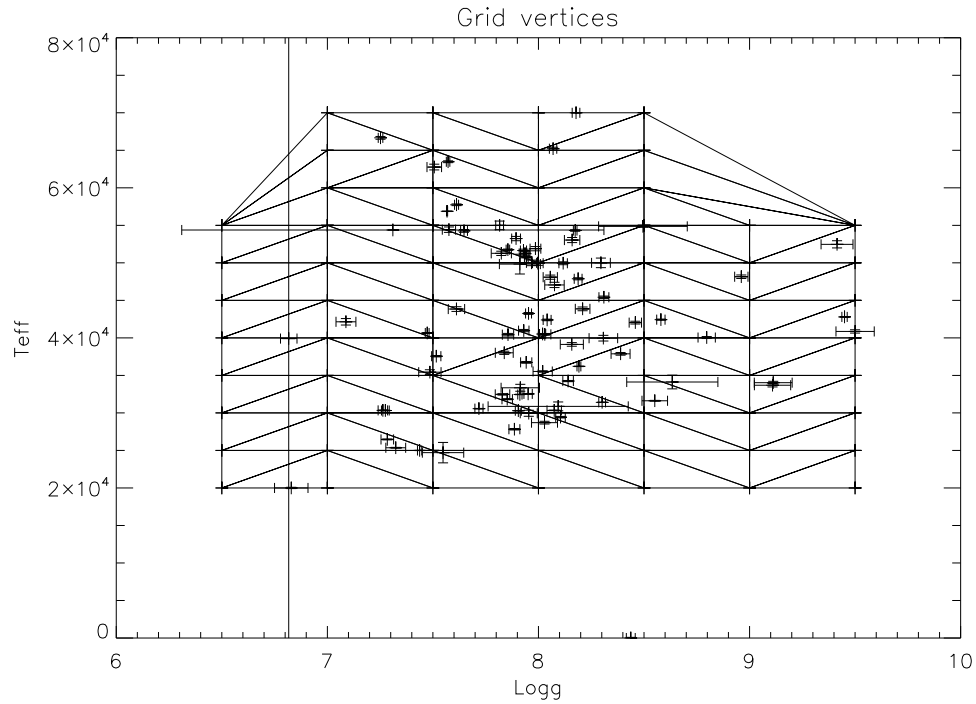


FIGURE 3.4. The positions of the stars in this sample plotted over the synthetic grid (represented by the linear interpolation splines). The distance between the interpolation splines is set at this value (e.g. 500K) because the uncertainty in the temperature across our sample averages around this number.

The grid of model spectra employed to deduce T_{eff} and $\log g$ of our stars was used to provide the Eddington flux H_λ for 68 points in T_{eff} and $\log g$ space. A surface was then linearly interpolated over the grid so that for every point in T_{eff} and $\log g$ space a value of H_λ could be found. See Figure 3.4.

These values of H_λ were fed through Equation 3.2 and a $M_{V_{syn}}$ and $M_{B_{syn}}$ was calculated for each star. $E_{B-V_{syn}}$ was thus obtained and compared to $E_{B-V_{obs}}$ calculated from $M_{B_{obs}} - M_{V_{obs}}$ taken from Simbad ¹.

¹<http://simbad.u-strasbg.fr/simbad/>

Figures 3.6 and 3.7, are plots of theoretical optical colour against observed optical colour. Figure 3.6 is a zoomed in portion of Figure 3.7 showing in more detail those points unlabeled on Figure 3.7.

Figure 3.7 shows that the discrepancy between the observed optical colour and the theoretical optical colour is quite large for some stars and yet very small for others. The line of $E_{B-V_{obs}} = E_{B-V_{syn}}$ or where the star appears to be exactly the colour that the models predict runs almost horizontally through this plot just below 0 on the Y axis. Figure 3.6 shows those stars clustered around the $E_{B-V_{obs}} = E_{B-V_{syn}}$ line.

Figure 3.8 and Figure 3.9 show the same but labeling those stars that are binary. The binary status (if any) of each star collected from literature is listed in the accompanying CD.

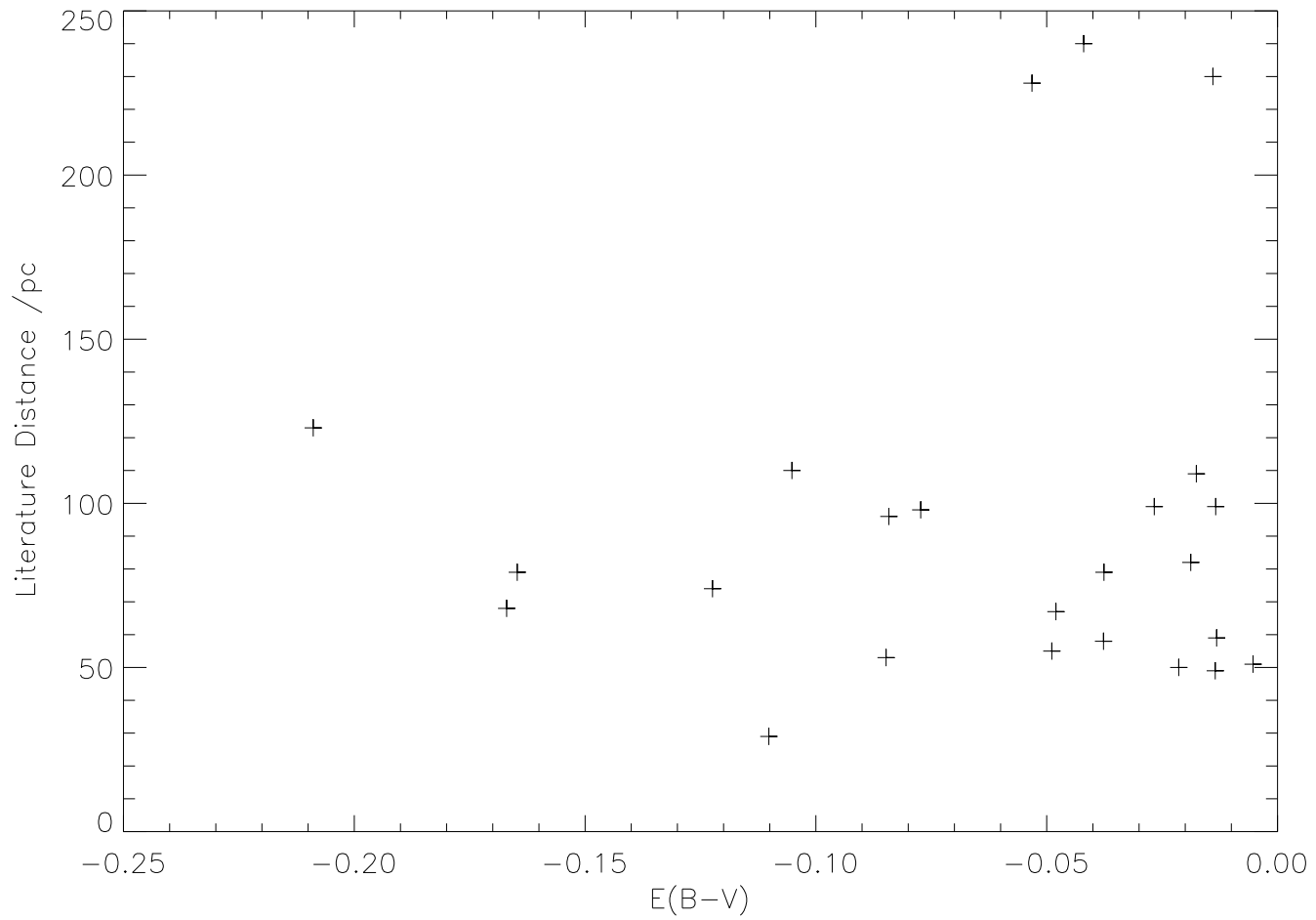


FIGURE 3.5. The derived E(B-V) values for our sample compared to literature distance estimates

Those stars that fall close to the $E_{B-V_{obs}} = E_{B-V_{syn}}$ are those where the amount of interstellar reddening can be quantified. Figure 3.11 shows that subset of stars plotted against a value of distance taken from literature. Though only a small number of stars can be compared this way it is clear from those that can be compared that interstellar reddening is not a major factor in these observations. Figure 3.11 shows that the measured reddening of the stars does not correlate with distance. The spread of E_{B-V} is more likely, therefore, to be the result of systematic errors rather than interstellar reddening.

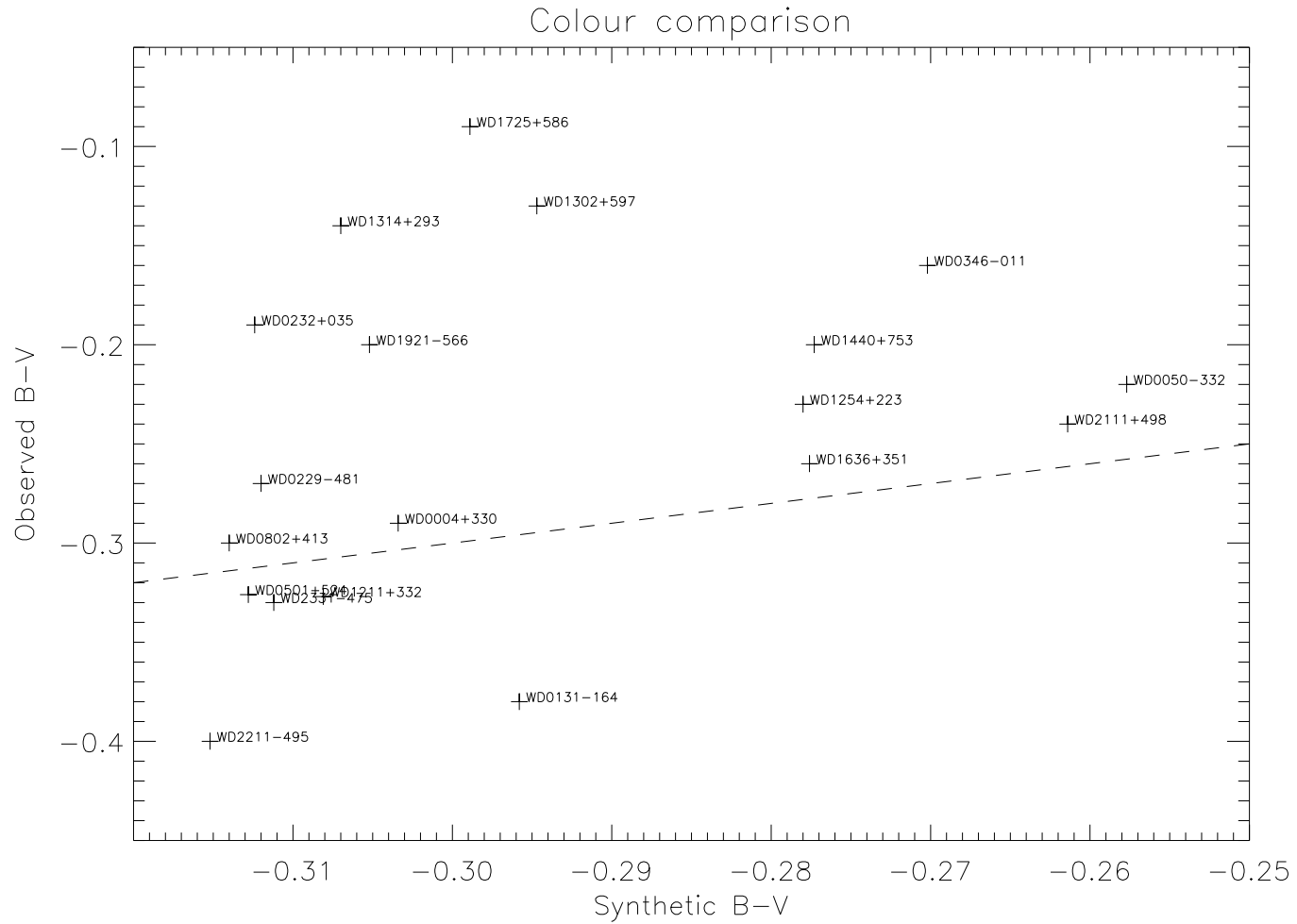


FIGURE 3.6. A comparison between the observed colour of the stars with a theoretical colour found by assuming the star a single star system. Discrepancy between the two indicates the presence of a companion dominating the optical part of the spectrum. Errors typically 0.05 in observed B-V (though on some individual cases this can be much higher) and 0.01 in synthetic B-V. Showing those where $E_{B-V_{obs}} - E_{B-V_{syn}} = 0$

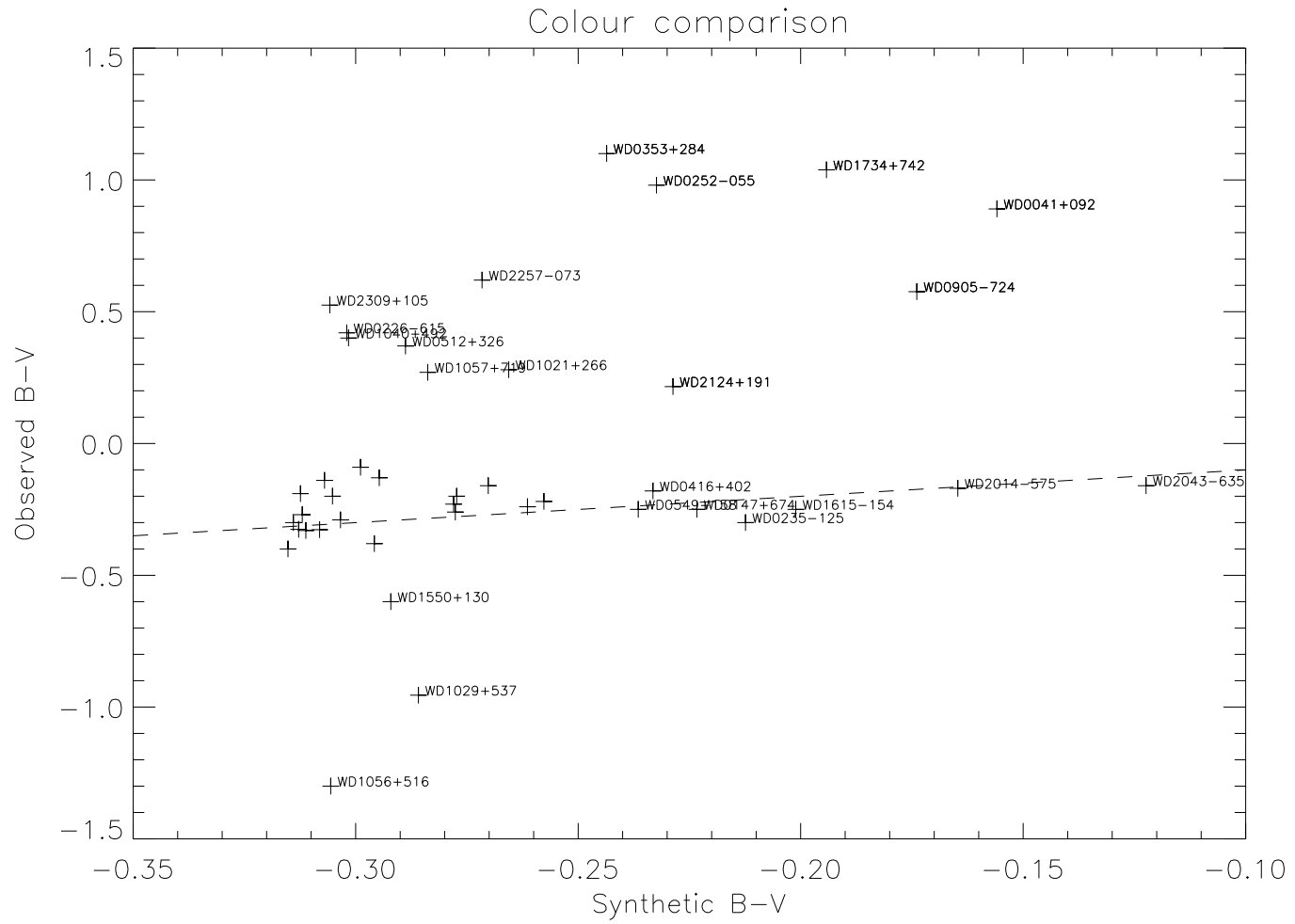


FIGURE 3.7. $E_{B-V_{obs}}$ plotted against $E_{B-V_{syn}}$. Showing the outliers

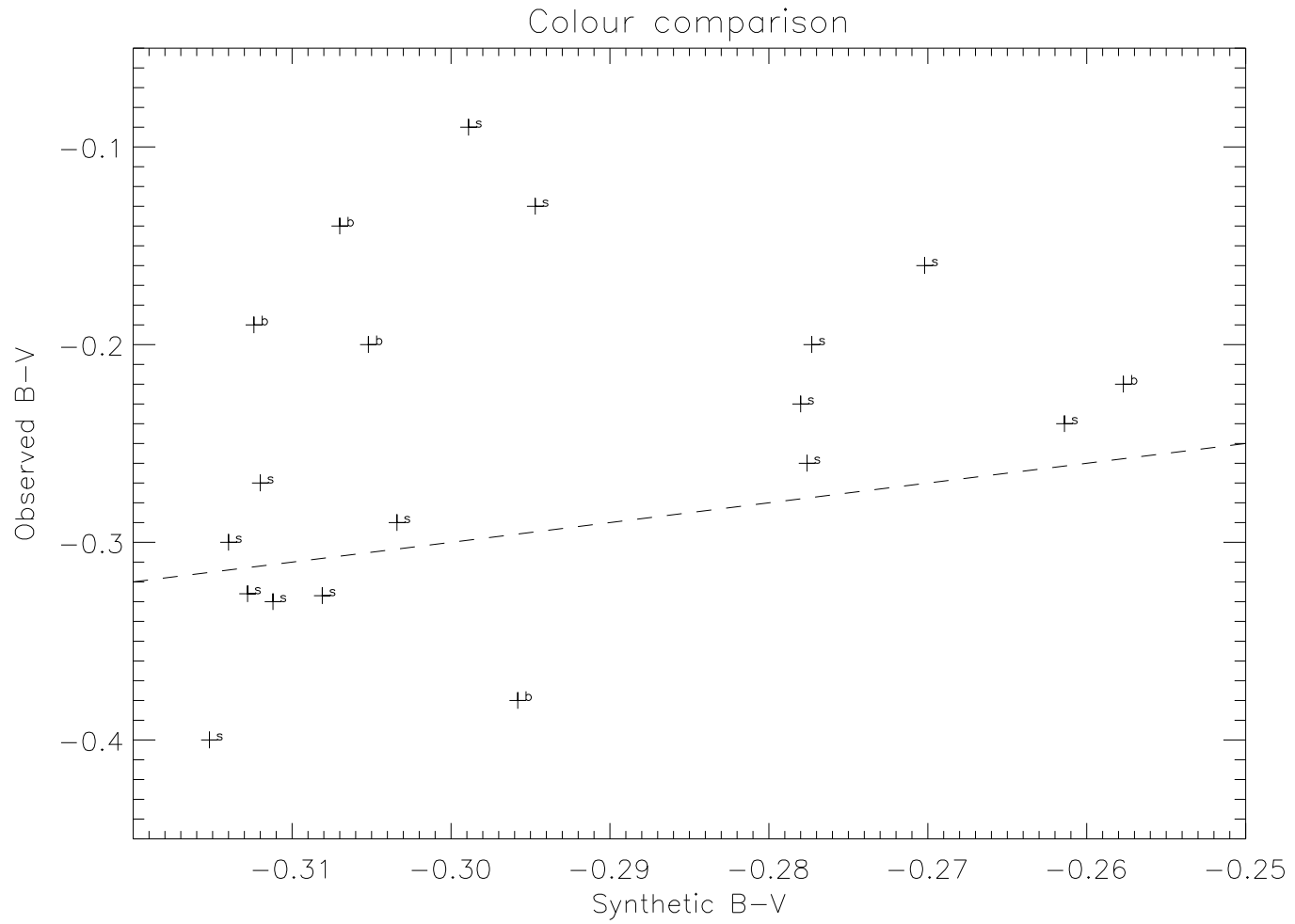


FIGURE 3.8. $E_{B-V_{obs}}$ plotted against $E_{B-V_{syn}}$. Showing those where $E_{B-V_{obs}} - E_{B-V_{syn}} = 0$ Known binaries labeled

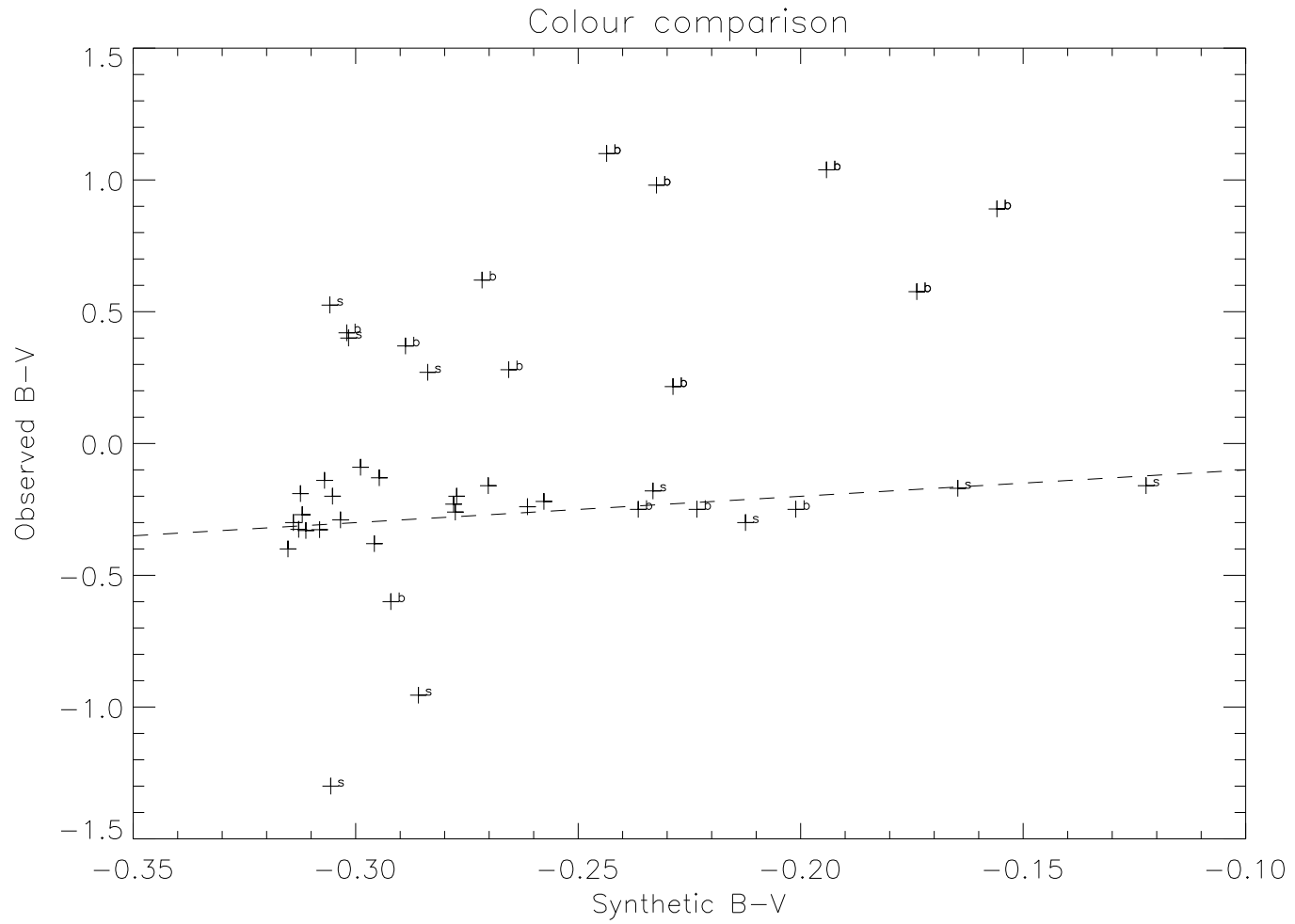


FIGURE 3.9. $E_{B-V_{obs}}$ plotted against $E_{B-V_{syn}}$. Showing the outliers. Known binaries labeled

3.1.4 Binarity

Those stars with no evidence of binarity, that have observed and model optical B-V in agreement are either isolated systems, a white dwarf with a substellar companion or a pair of white dwarfs of similar temperature and gravity. Though the isolated condition is the most likely, some stars with known substellar companions exist within this sample. Stars that exhibit symptoms of binarity, such as radial velocity variations, are probably white dwarfs with low mass and hence low luminosity companions. These stars would not necessarily exhibit the wrong colour since the contribution of the companion is negligible. Isolated white dwarfs that are too red in the optical most likely have undiscovered companions. Our sample does contain stars that are too red or blue for the white dwarf to be isolated and so in these cases the literature distance estimates, derived from optical properties, are not reliable.

3.2 Distance determination

The distance to the star is also the column length of the interstellar medium towards that star. As described previously this distance can be calculated by comparing the observed flux to the Eddington flux, calculated from synthetic spectra for a given stellar radius. Comparing the flux at 1000 angstroms removes flux contamination from most companion stars and potentially gives an uncontaminated measure of distance.

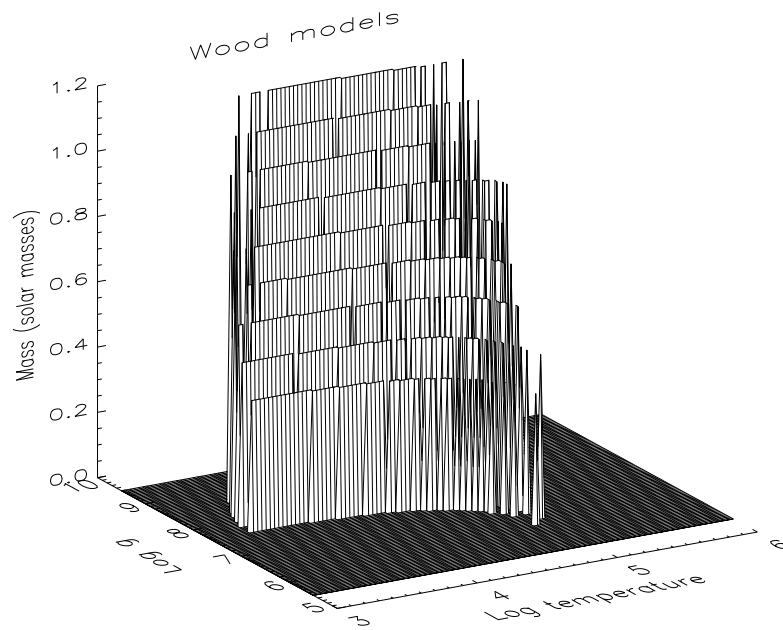


FIGURE 3.10. The Wood evolutionary models. This plot shows the gridded log g and temperature range before extrapolation. The extrapolated point on the surface is used to derive a mass for the star.

The Mass M and σ_M of the star is calculated from the extrapolated point on the $\log g$, T_{eff} and M surface of the (Wood 1995) evolutionary model (see Figure 3.10). The Radius R and the σ_R is then calculated with a mass radius relation.

$$R = \frac{\left(\frac{MM_{sun}}{10^{\log g}}\right)^{1/2}}{R_{sun}} \quad (3.3)$$

The Eddington flux H_r is taken for each star at 1000 Angstroms from the synthetic spectra. The measured flux f_r is taken from the average of four nearby points within 5 Angstroms of 1000 Angstroms. This prevents the flux being lowered by an unfortunately placed absorption feature. Using H_r , f_r and R then gives a distance. The uncertainty of this measurement is preserved at all times and includes the flux uncertainty from the f_r measurement.

$$d = \left(R^2 \frac{H_r}{f_r}\right)^{1/2} \quad (3.4)$$

Where R is the radius of the white dwarf, H_r is the Eddington flux at a given wavelength and f_r is the observed flux at a given wavelength. Table 3.1 and Figure 3.11 compares distances measured using this method to literature measurements. Figure 3.12 shows the locations of the stars in galactic coordinates.

Table 3.1: Distance measurements

<i>Name</i>	<i>l</i>	<i>b</i>	<i>d</i>	σ_d	<i>Litd</i>	<i>Ref f</i>
WD0001+433	113.9	-18.44	76	6		
WD0004+330	112.48	-28.69	101	1	98.8	(Vennes et al. 1997a)
WD0027-636	306.98	-53.55	176	7	236	(Vennes et al. 1997a)
WD0041+092	20.7	-48.3	90	7		
WD0050-332	299.14	-84.12	50	1	58	(Holberg et al. 1998)
WD0106-358	280.88	-80.81	85	3		
WD0131-164	167.26	-75.15	82	2	96	(Vennes et al. 1997a)
WD0147+674	128.58	5.44	102	4	99	(Dupuis et al. 2005)
WD0226-615	284.2	-52.16	138	6	199.2	(Perryman et al. 1997)
WD0229-481	266.62	-61.59	181	8		
WD0232+035	165.97	-50.27	71	1	74.4	(Perryman et al. 1997)
WD0235-125	187.4	-61.12	74	5		
WD0236+498	140.15	-9.15	61	7	96	(Vennes et al. 1997a)
WD0252-055	181.86	-53.47	114	6	104.4	(Perryman et al. 1997)
WD0320-539	267.3	-51.64	128	7		
WD0346-011	188.95	-40.1	24	1	29	(Vennes et al. 1997a)
WD0353+284	165.08	-18.67	122	10		
WD0354-368	238.64	-49.98	375	48		
WD0416+402	160.2	-6.95	409	43	228	(Vennes et al. 1997a)
WD0455-282	229.29	-36.17	106	2	102	(Oegerle et al. 2005)
WD0501+524	155.95	7.1	48	0	59	(Vennes et al. 1997a)
WD0512+326	173.3	-3.36	70	3	25.1	(Perryman et al. 1997)
WD0549+158	192.03	-5.34	49	1	49	(Vennes et al. 1997a)
WD0603-483	255.78	-27.36	187	12	178	(Vennes et al. 1997a)
WD0621-376	245.41	-21.43	59	1	78	(Holberg et al. 1998)
Continued on next page						

Table 3.1 – continued from previous page

<i>Name</i>	<i>l</i>	<i>b</i>	<i>d</i>	σ_d	<i>Litd</i>	<i>Ref</i>
WD0659+130	202.51	8.2	108	10		
WD0715-704	281.4	-23.5	98	3	94	(Vennes et al. 1997a)
WD0802+413	179.22	30.94	921	69	230	(Dupuis et al. 2005)
WD0809-728	285.82	-20.42	126	7	121	(Vennes et al. 1997a)
WD0830-535	270.11	-8.27	88	5	82	(Vennes et al. 1997a)
WD0905-724	287.82	-16.77	144	14	139.3	(Perryman et al. 1997)
WD0937+505	166.9	47.12	121	9	218	(Dupuis et al. 2005)
WD1019-141	256.48	34.74	102	5		
WD1021+266	205.72	57.21	163	11	250	(Burleigh et al. 1997)
WD1024+326	194.52	58.41	409	63		
WD1029+537	157.51	53.24	153	7	116	(Vennes et al. 1997a)
WD1040+492	162.67	57.01	264	10	230	(Vennes et al. 1997a)
WD1041+580	150.12	52.17	95	4	93	(Vennes et al. 1997a)
WD1056+516	156.33	57.82	525	90		
WD1057+719	134.48	42.92	124	4	141	(Savage & Lehner 2006)
WD1109-225	274.78	34.54	90	3	81.6	(Perryman et al. 1997)
WD1211+332	175.04	80.02	137	5	115	(Oegerle et al. 2005)
WD1234+481	129.81	69.01	138	4	129	(Vennes et al. 1997a)
WD1254+223	317.25	84.75	64	1	67	(Vennes et al. 1997a)
WD1302+597	119.82	57.59	436	29		
WD1314+293	54.11	84.16	52	1	68	(Finley et al. 1997)
WD1342+442	94.3	69.92	398	35		
WD1440+753	114.1	40.12	127	6	98	(Vennes et al. 1997a)
WD1528+487	78.87	52.72	130	4	140	(Vennes et al. 1997a)
WD1550+130	23.65	45.34	940	104		
WD1603+432	68.22	47.93	120	5	114	(Dupuis et al. 2005)
Continued on next page						

Table 3.1 – continued from previous page

<i>Name</i>	<i>l</i>	<i>b</i>	<i>d</i>	σ_d	<i>Litd</i>	<i>Ref</i>
WD1611-084	4.3	29.3	101	4	93	(Vennes 1999)
WD1615-154	358.79	24.18	47	1	55	(Oegerle et al. 2005)
WD1620+647	96.61	40.16	196	9	174	(Dupuis et al. 2005)
WD1631+781	111.3	33.58	67	1	67	(Vennes et al. 1997a)
WD1636+351	56.98	41.4	136	6	109	(Vennes et al. 1997a)
WD1648+407	64.64	39.6	178	13	200	(Vennes et al. 1997a)
WD1711+668	97.2	34.57	137	13		
WD1725+586	87.17	33.83	172	11		
WD1734+742	105.49	31.35	90	7	103	(Perryman et al. 1997)
WD1800+685	98.73	29.78	193	13	159	(Vennes et al. 1997a)
WD1819+580	87	26.76	48	2		
WD1844-223	12.5	-9.25	48	1	62	(Vennes et al. 1997a)
WD1845+683	98.81	25.65	265	20	125	(Vennes et al. 1997a)
WD1917+599	91.03	20.04	122	5	105	(Vennes et al. 1997a)
WD1921-566	340.63	-27.01	119	7		
WD1942+499	83.08	12.75	94	2	105	(Vennes et al. 1997a)
WD1950-432	356.51	-29.09	146	6	140	(Dupuis et al. 2005)
WD2000-561	341.78	-32.25	74	4	198	(Dupuis et al. 2005)
WD2004-605	336.58	-32.86	42	1	58	(Vennes et al. 1997a)
WD2011+398	77	3.18	123	3	141	(Vennes et al. 1997a)
WD2014-575	340.2	-34.25	68	2	51.0	(Vennes et al. 1997a)
WD2020-425	358.36	-34.45	144	12		
WD2043-635	332.36	-36.92	223	45		
WD2111+498	91.37	1.13	378	1	50	(Vennes et al. 1997a)
WD2116+736	109.39	16.92	161	4	177	(Dupuis et al. 2005)
WD2124+191	70.43	-21.98	37	3	46	(Vennes et al. 1998)
Continued on next page						

Table 3.1 – continued from previous page

<i>Name</i>	<i>l</i>	<i>b</i>	<i>d</i>	σ_d	<i>Litd</i>	<i>Reff</i>
WD2146-433	357.18	-50.13	337	17	362	(Dupuis et al. 2005)
WD2152-548	340.5	-48.7	119	7		
WD2211-495	345.79	-52.62	63	1	53	(Vennes et al. 1997a)
WD2257-073	65.17	-56.93	155	10	88.5	(Vennes 1999)
WD2309+105	87.26	-45.12	72	1	79.0	(Vennes et al. 1997a)
WD2321-549	326.91	-58.21	139	6	192	(Dupuis et al. 2005)
WD2331-475	334.84	-64.81	101	2	82	(Vennes et al. 1997a)

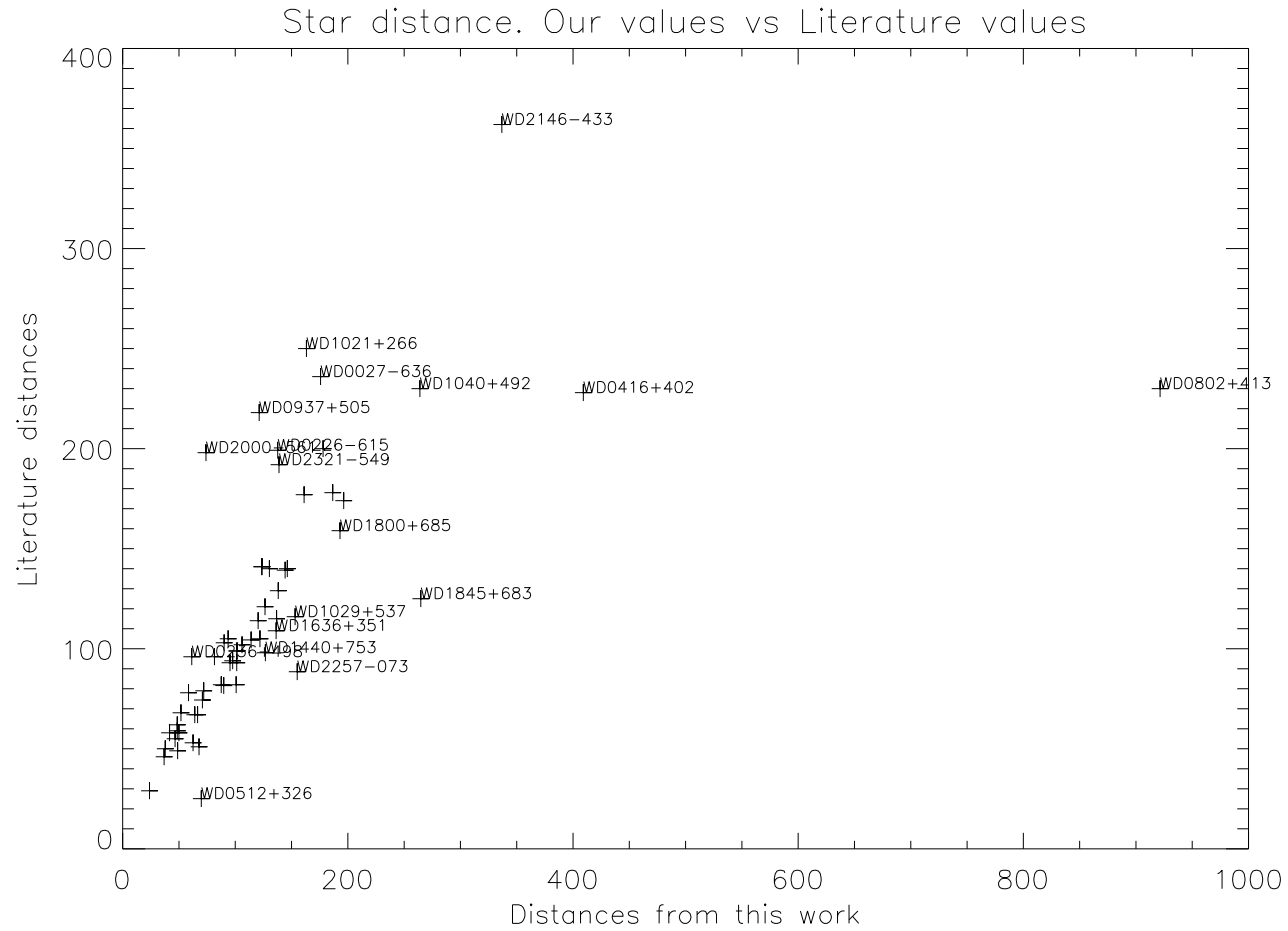


FIGURE 3.11. A figure showing the star distances measured in this work compared to those from literature. Stellar distance uncertainties are typically about 11 pc. In most cases there is good agreement. In some cases such as WD0802+413 we get a much larger distance due to our result being derived from an FUV flux where contamination from a companion star is unlikely.

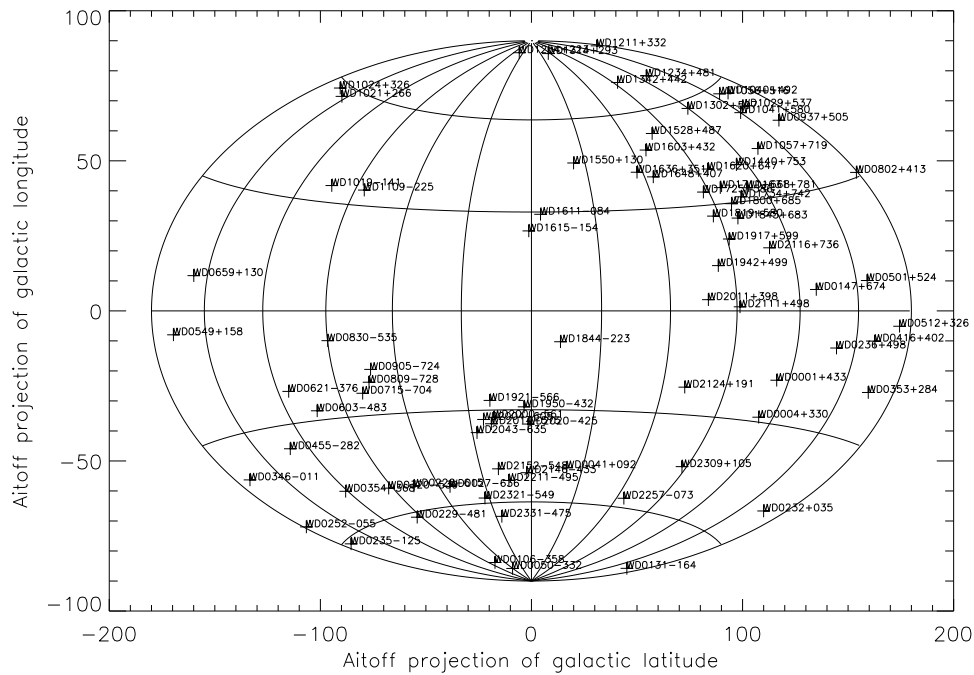


FIGURE 3.12. Distribution of stars in galactic coordinates (Note: Axis incorrectly labeled)

3.3 Finding the amount of cold gas in the lines of sight used in this sample

This investigation involves the measurement of absorption lines and calculating the amount of material required to produce such lines. The column density can be calculated from the equivalent width of the line using the curve of growth analysis. Though the derivation of these relationships are quite standard and can be found widely in the literature they are necessary for this investigation and so have been reproduced in this section. In order to quantify the amount of absorbing material in the interstellar medium we need first to derive the equations of radiative transfer. This basic derivation (Spitzer et al. 1974)

defines a property of matter called the absorption coefficient which is a measure of the extent to which a material absorbs energy. This basic property of matter is important to interstellar medium physics because it allows us to gage the amount of material along a line of sight.

The probability R_{lu} per unit time of a radiative excitation (a transition from a low energy state to a high one) is the result of spontaneous absorption at a given frequency.

$$R_{lu} = B_{lu} \frac{cu_\nu}{4\pi} \quad (3.5)$$

u_ν is the energy density at a single frequency ν (unit; $\text{ergcm}^{-3}\text{Hz}^{-1}$) and B_{lu} is Einstein's absorption coefficient that defines the extent to which a material absorbs energy. In a situation where the radiation is isotropic then the energy density can be expressed as a function of the specific intensity I_ν (unit; $\text{erg s}^{-1}\text{cm}^{-2}\text{sterad}^{-1}$) at a given frequency. Since $u_\nu = 4\pi I_\nu/c$ then this simplifies to Equation 3.6.

$$R_{lu} = B_{lu} I_\nu \quad (3.6)$$

The probability R_{ul} per unit time of a radiative de-excitation (a transition from a high energy state to a low one) is the result of both spontaneous emission and stimulated emission.

$$R_{ul} = A_{ul} + B_{ul} \frac{cu_\nu}{4\pi} \quad (3.7)$$

A_{ul} is Einstein's spontaneous emission probability and B_{ul} is Einstein's stimulated emission coefficient. Again for the isotropic energy density this expression can be simplified.

$$R_{ul} = A_{ul} + B_{ul} I_\nu \quad (3.8)$$

The number of atoms multiplied by the probability of them existing in a certain state gives the total number in each state. The difference between the number emitting and absorbing gives us the rate of change of specific intensity with length ds . This is known as the radiative transfer equation

$$\frac{dI_\nu}{ds} = \frac{h\nu}{4\pi} (n_u(\nu) A_{ul} - [n_l(\nu) B_{lu} - n_u(\nu) B_{ul}] I_\nu). \quad (3.9)$$

The total amount of absorption can be calculated by subtracting the total spontaneous emission from the total spontaneous absorption

$$\kappa_\nu = \frac{h\nu}{4\pi} [n_l(\nu) B_{lu} - n_u(\nu) B_{ul}]. \quad (3.10)$$

The optical depth can then be defined as the amount of absorption integrated over the length ds

$$\tau_\nu = \int \kappa_\nu ds. \quad (3.11)$$

We now consider that if a medium is in local thermal equilibrium then the population of its levels can be described by Boltzmann's law

$$\frac{n_u(\nu)}{n_l(\nu)} = \frac{g_u}{g_l} \exp\left(-\frac{h\nu_0}{kT}\right). \quad (3.12)$$

g_u and g_l are the number of sub-levels of the upper and lower states respectively. When the optical depth is very large the specific intensity tends to the blackbody intensity. In this case the source function, which describes the ratio of the emission coefficient to the absorption coefficient, simply equates to the plank function

$$\frac{n_u(\nu) A_{ul}}{n_l(\nu) B_{lu} - n_u(\nu) B_{ul}} = \frac{2h\nu_o^3}{c^2} \frac{1}{e^{\frac{h\nu_0}{kT}} - 1}. \quad (3.13)$$

This brings us to Einstein's relations between the probabilities of emission and absorption

$$A_{ul} = \frac{2h\nu_0^3}{c^2} B_{ul} \quad (3.14)$$

and

$$g_l B_{lu} = g_u B_{ul} \quad (3.15)$$

Finally we can express the absorption coefficient k_ν in terms of the number n of atoms in each state.

$$k_\nu = \frac{c^2 n_l(\nu) g_u}{8\pi\nu_0^2 g_l} A_{ul} \left[1 - \frac{g_l n_u(\nu)}{g_u n_l(\nu)} \right] \quad (3.16)$$

This relation shows that the absorption coefficient k_ν is proportional to the density of material and thus the density can be calculated from the amount of absorption observed.

To obtain the the total intensity in a spectral line, then we have to integrate the absorption coefficient over all frequencies ν . We define the normalised spectral distribution function $\phi_{ul}(\nu)$ as the following.

$$\int_{line} \phi_{ul}(\nu) d\nu = 1 \quad (3.17)$$

The absorption coefficient then can be written to describe the total integrated intensity.

$$k_\nu = \frac{c^2 n_l(\nu) g_u}{8\pi\nu_0^2 g_l} A_{ul} \left[1 - \frac{g_l n_u}{g_u n_l} \right] \phi_{ul}(\nu) \quad (3.18)$$

We can then equate the $\frac{g_l n_u}{g_u n_l}$ of the absorption coefficient to that in Equation 3.12 to write the absorption coefficient in terms of temperature.

$$k_\nu = \frac{c^2 n_l(\nu) g_u}{8\pi\nu_0^2 g_l} A_{ul} \left[1 - \exp\left(\frac{-h\nu_0}{kT}\right) \right] \phi_{ul}(\nu) \quad (3.19)$$

The second part of the derivation relates a measured property of the line, its equivalent width, to the strength of the transition and the amount of material undertaking this

transition.

Initially the line strength must be calculated from the equivalent width of the line.

$$W = \int_{line} \frac{I_0 - I_\lambda}{I_0} d\lambda \quad (3.20)$$

The equivalent width W is given as the integrated ratio of, the difference between the stellar continuum I_0 and the line intensity I_λ , to the stellar continuum I_0 . The units of equivalent width is the Angstrom. The equivalent width of the line can also be defined in terms of optical depth. Integrating the transfer equation (Equation 3.9) along the line of sight and neglecting the spontaneous and stimulated de-excitations gives the relation that equates equivalent width to optical depth.

$$W = \int (1 - e^{-\tau}) d\lambda \quad (3.21)$$

If we now consider a low density gas, such as the atomic gas in the ISM then we can approximate Equation 3.21 since $\tau \ll 1$.

$$W = \int \tau_\nu d\lambda = \int \tau_\nu \lambda^2 \frac{d\nu}{c} \quad (3.22)$$

Similarly in Equation 3.19 since the $-h\nu_0/kT \ll 1$ the equation can be integrated with depth ds (See Equation 3.11) and approximating so that the $\left[1 - \exp\left(\frac{-h\nu_0}{kT}\right)\right] = 1$. The results is an optical depth.

$$k_\nu = \frac{c^2 N_l(\nu) g_u}{8\pi\nu_0^2 g_l} A_{ul} \phi_{ul}(\nu) \quad (3.23)$$

This can be substituted into Equation 3.22.

$$W = \int \frac{c^2 N_l(\nu) g_u}{8\pi\nu_0^2 g_l} A_{ul} \phi_{ul}(\nu) \lambda^2 \frac{d\nu}{c} \quad (3.24)$$

Equation 3.17 shows how this can be integrated with respect to frequency.

$$W = \frac{\lambda^2 N_l(\nu) g_u}{8\pi g_l} A_{ul} \frac{\lambda^2}{c} \quad (3.25)$$

We define the oscillator strength f of the transition as Equation 3.26. This dimensionless quantity expresses the strength of the transition.

$$f = \frac{m_e c^3}{8\pi \nu^2 e^2} A_{ul} \frac{g_u}{g_l} \quad (3.26)$$

Rearranging around the spontaneous emission probability A_{ul} and then substituting into Equation 3.27 gives the equivalent width in terms of the oscillator strength.

$$W = \frac{\pi e^2}{m_e c^2} N_l \lambda^2 f \quad (3.27)$$

This expression is numerically Equation 3.28. Where W and λ are given in Angstroms.

$$W = 8.85 \times 10^{-21} N_l \lambda^2 f \quad (3.28)$$

For small equivalent widths the $W \propto N$ relationship can be realistically employed to find the column density N of the line of sight. As larger line profiles are considered the linear relationship breaks down and is superseded by a $W \propto (\log N)^{1/2}$ where the equivalent width depends very little on the column density. On a curve of growth diagram, where $\log \frac{W_\lambda}{\lambda}$ is plotted against $\log N f \lambda$ this region is described as the doppler plateau. In this region the line profile, dominated by doppler broadening becomes dependent on the linear and turbulent velocities of clouds of matter along the line of sight. At even greater line strength the equivalent width is dominated by damping and obeys the relationship $W_\lambda \propto N^{1/2}$.

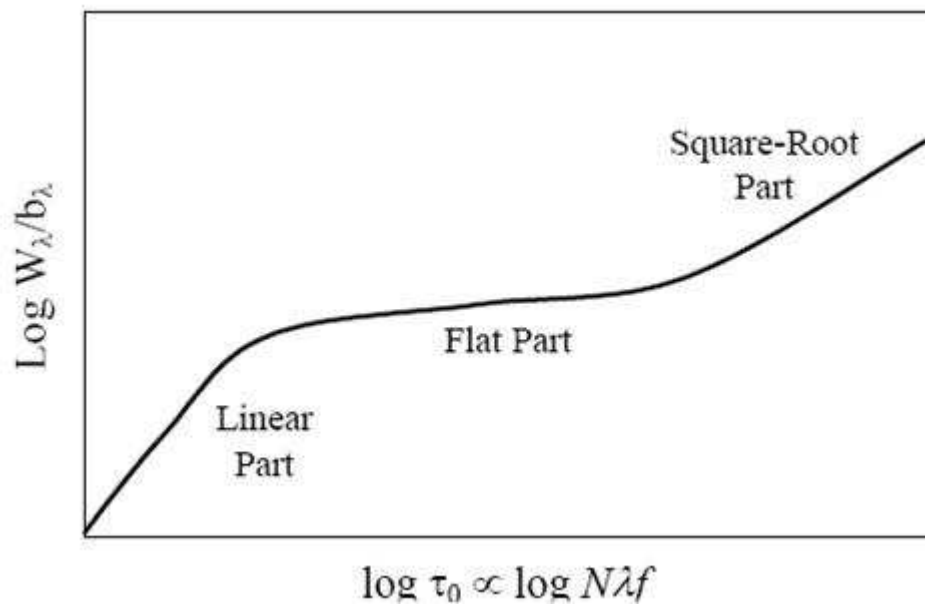


FIGURE 3.13. The curve of growth

The application of these relationships are useful since they can indicate the density of matter directly from the line profile. Since most lines measured in a long line of sight are of the strength that places them on the Doppler plateau this analysis requires the comparison of the data to a model. In cases where clouds of gas at different velocities occupy the line of sight, multiple curves of growth may be required to successfully reproduce the line profiles. For distances (50-300pc) used in this study the line strengths are weaker allowing more lines to be studied in the linear section of the curve of growth. For FUSE data the individual cloud velocities are not observed since the velocity resolution is poorer than the average difference between cloud velocities.

The species measured include the 30 species which were used in other parts of this thesis to calculate V_{ism} . The measured properties of these lines can be found on the data CD. These measurements include the equivalent width measurements from which the column density is calculated.

3.3.1 The volume density derived from different lines of the same species

The equivalent widths folded through the oscillator strength of a given species divided through by the distance produces a value of volume density. In any given star multiple lines of the same species should produce, within errors, similar values of volume density. In the FUV region the species O I and N I have multiple lines enabling the testing on a line by line basis of the values of volume density. Upon comparison with measurements of column density made in other works, but including some of the same stars, we find

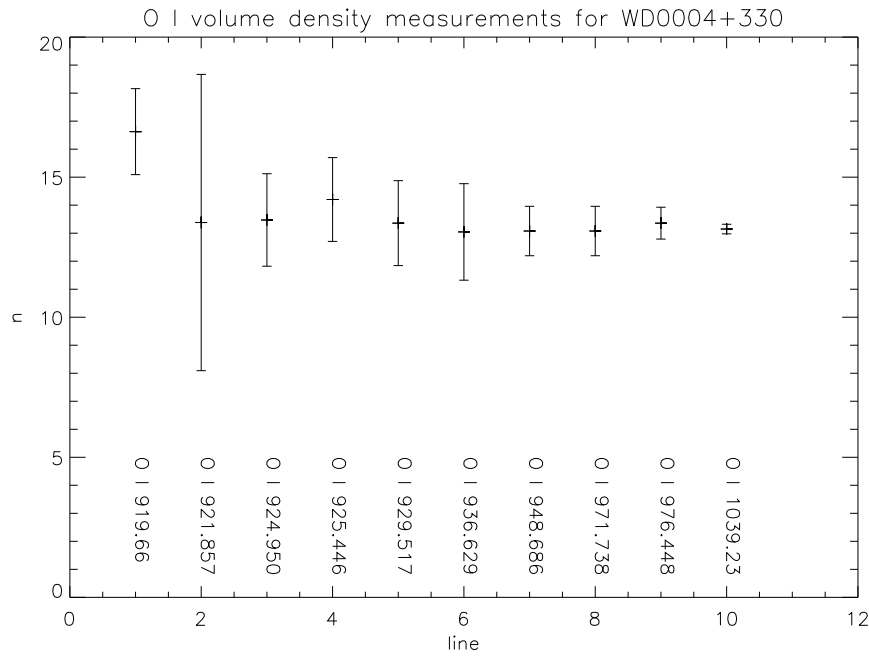


FIGURE 3.14. Example of O I volume density (measured in $cm^{-2}pc^{-1}$) measurements for WD0004+330

that our values are in agreement. See Figure 3.14.

O I and N I volume density measurements from multiple lines are roughly consistent with each other. Some lines do produce different values of volume density. In the weak line, O I 919.66, contamination with the nearby hydrogen line inflates the n value. In fact, the vast difference between the volume density consistently calculated from this line suggests that the Lyman line was measured instead of the O I line. The breakdown of the linear relationship between the equivalent width and column density results in a slight underestimation of those n values deduced from stronger lines such as O I 1039.23. Geocoronal emission in the 1134 N I multiplex can produce under estimated volume densities since the emission feature fills in the absorption feature somewhat.

3.3.2 Column density measurements of cold gas species

Inhomogeneities in the cold gas can be observed from a plot of column density against distance. In some of the presented column density against distance charts the number of observed lines is quite small and therefore inhomogeneities are difficult to see. In the stronger lines such as the 1144.938 Å Fe II line the boundary of the local cavity can be easily observed.

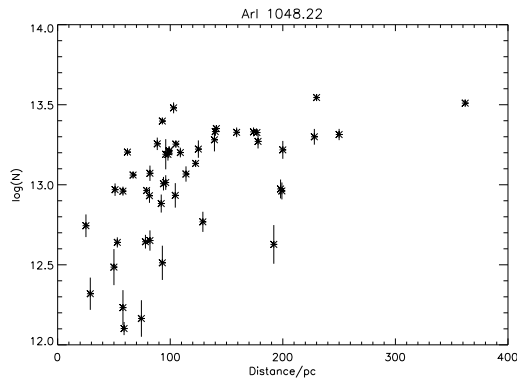


FIGURE 3.15. Column density of 1048.22 Å Ar I plotted against distance

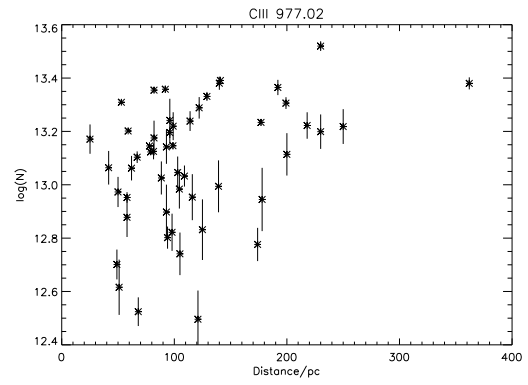


FIGURE 3.18. Column density of 977.02 Å C III plotted against distance

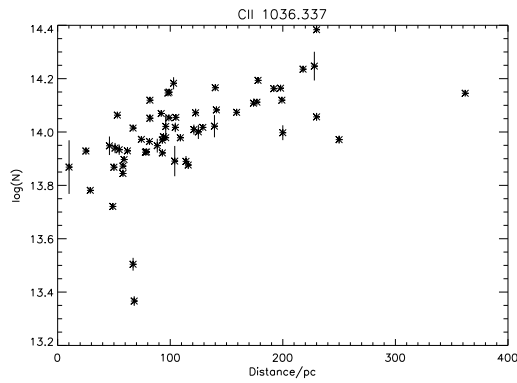


FIGURE 3.16. Column density of 1036.337 Å C II plotted against distance

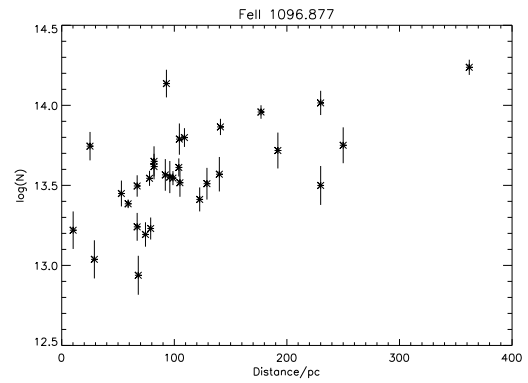


FIGURE 3.19. Column density of 1096.877 Å Fe II plotted against distance

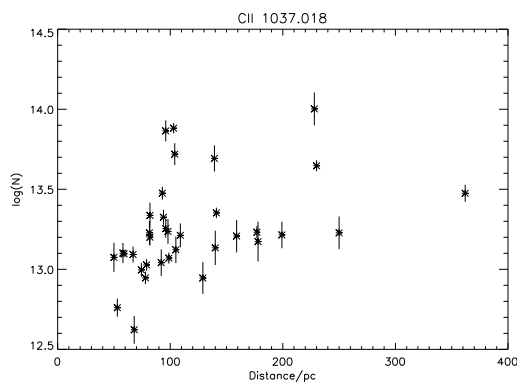


FIGURE 3.17. Column density of 1037.018 Å C II plotted against distance

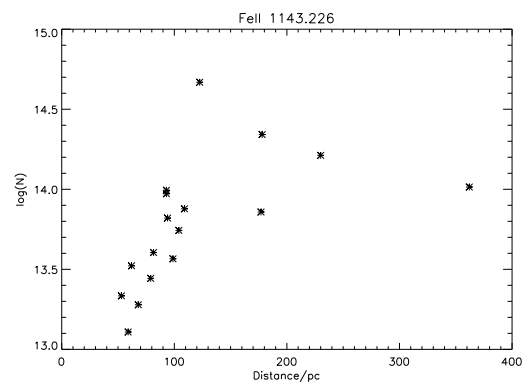


FIGURE 3.20. Column density of 1143.226 Å Fe II plotted against distance

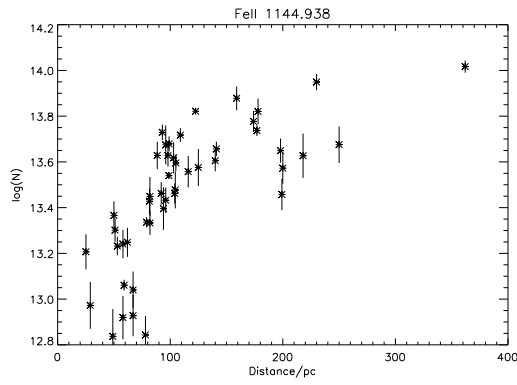


FIGURE 3.21. Column density of 1144.938 Å Fe II plotted against distance

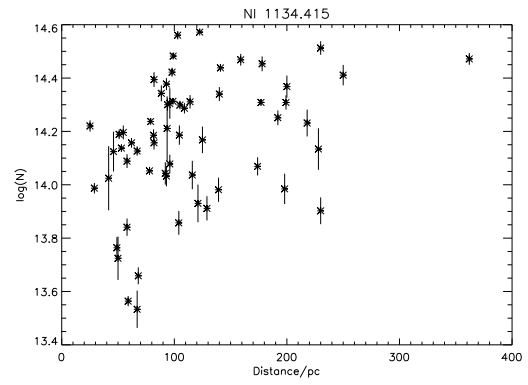


FIGURE 3.24. Column density of 1134.415 Å N I plotted against distance

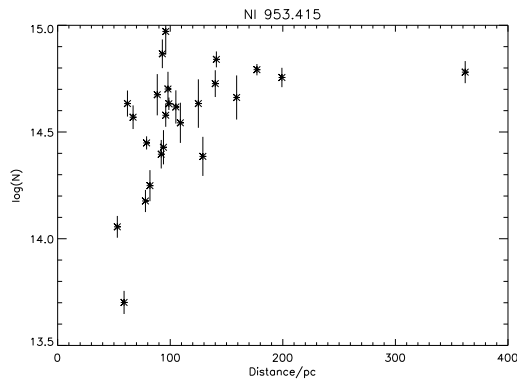


FIGURE 3.22. Column density of 953.415 Å N I plotted against distance

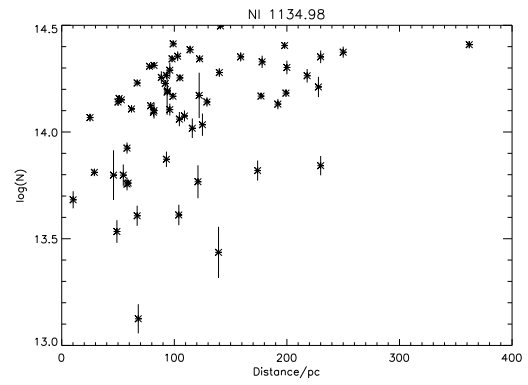


FIGURE 3.25. Column density of 1134.98 Å N I plotted against distance

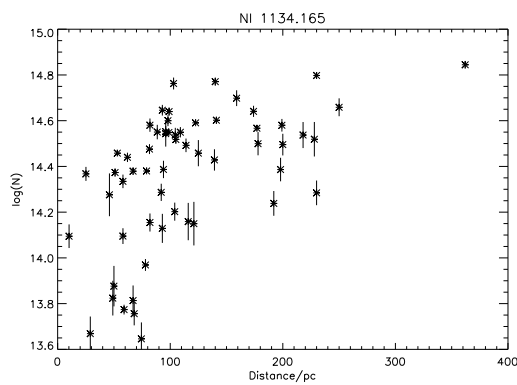


FIGURE 3.23. Column density of 1134.165 Å N I plotted against distance

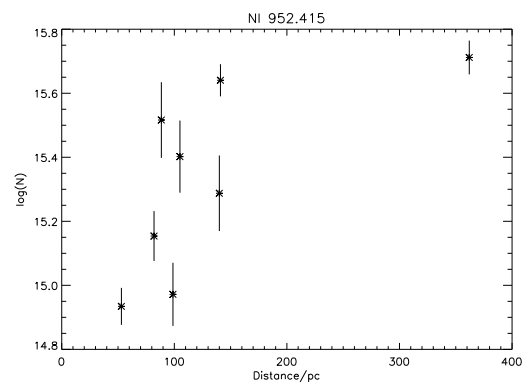


FIGURE 3.26. Column density of 952.415 Å N I plotted against distance

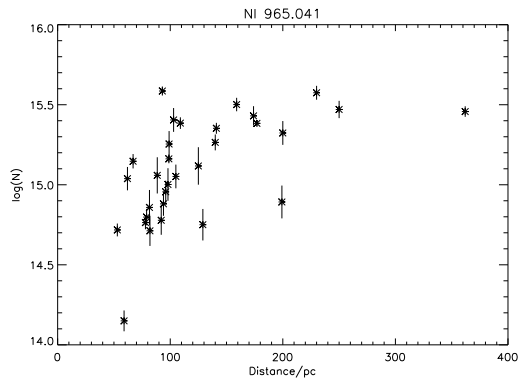


FIGURE 3.27. Column density of 965.041 Å N I plotted against distance

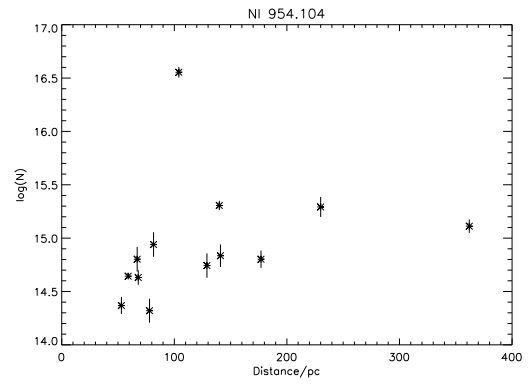


FIGURE 3.30. Column density of 954.104 Å N I plotted against distance

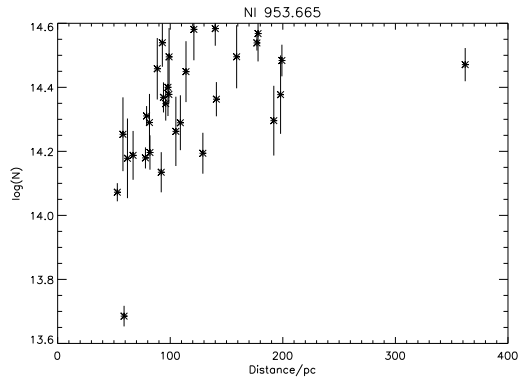


FIGURE 3.28. Column density of 953.665 Å N I plotted against distance

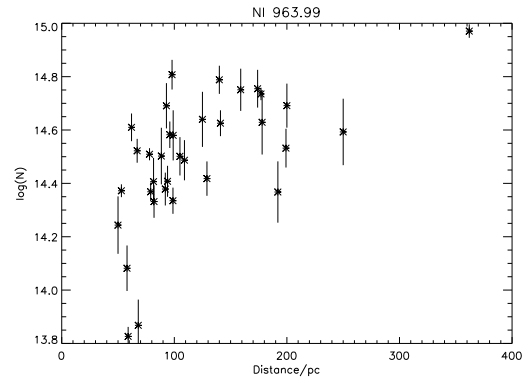


FIGURE 3.31. Column density of 963.99 Å N I plotted against distance

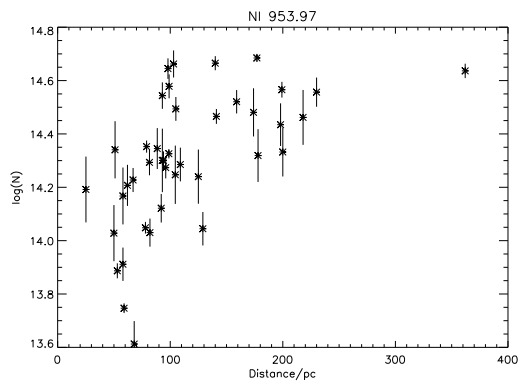


FIGURE 3.29. Column density of 953.97 Å N I plotted against distance

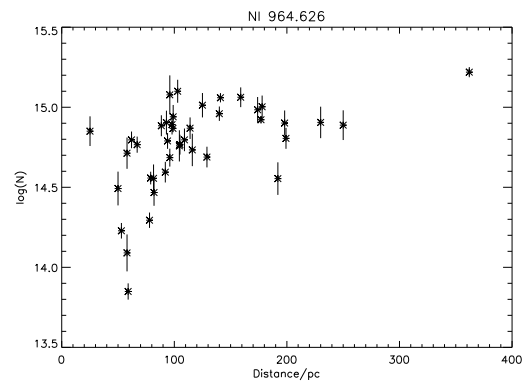


FIGURE 3.32. Column density of 964.626 Å N I plotted against distance

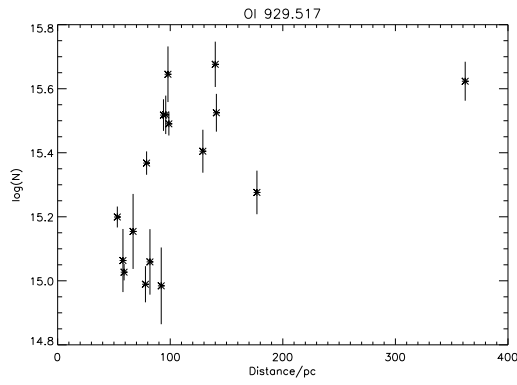


FIGURE 3.33. Column density of 929.517 Å O I plotted against distance

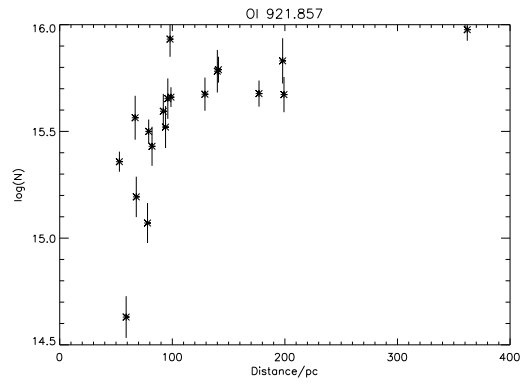


FIGURE 3.36. Column density of 921.857 Å O I plotted against distance

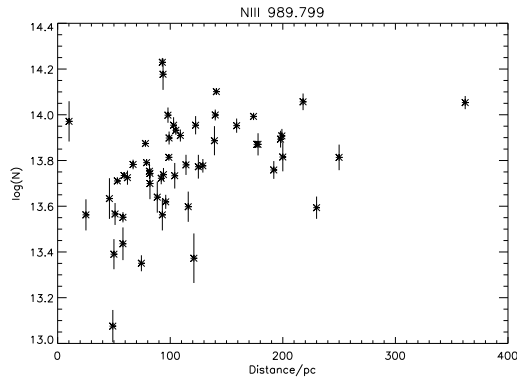


FIGURE 3.34. Column density of 989.799 Å N III plotted against distance

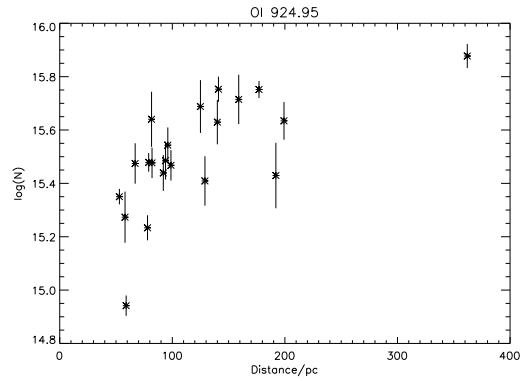


FIGURE 3.37. Column density of 924.95 Å O I plotted against distance

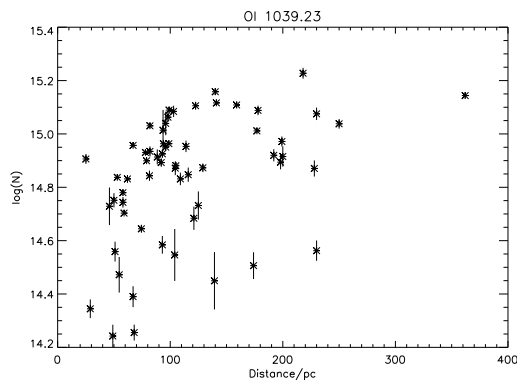


FIGURE 3.35. Column density of 1039.23 Å O I plotted against distance

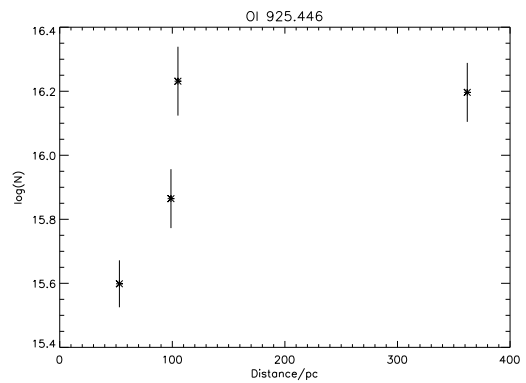


FIGURE 3.38. Column density of 925.446 Å O I plotted against distance

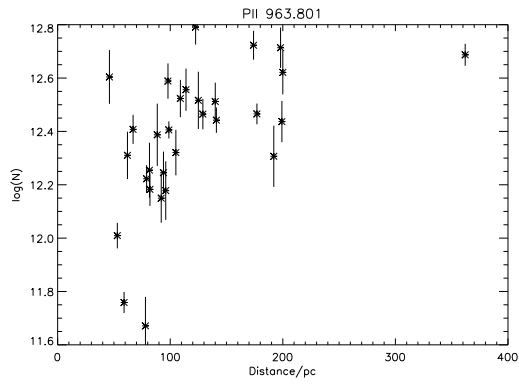


FIGURE 3.39. Column density of 963.801 Å P II plotted against distance

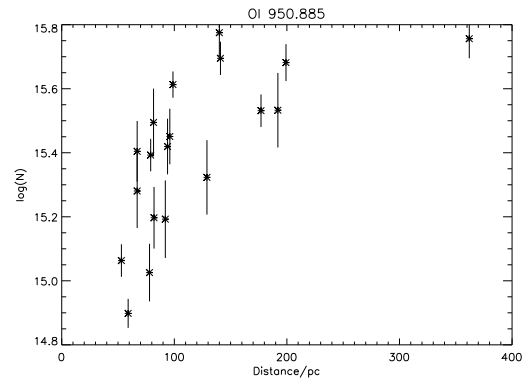


FIGURE 3.42. Column density of 950.885 Å O I plotted against distance

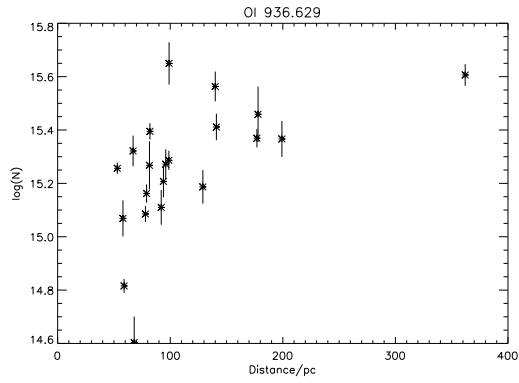


FIGURE 3.40. Column density of 936.629 Å O I plotted against distance

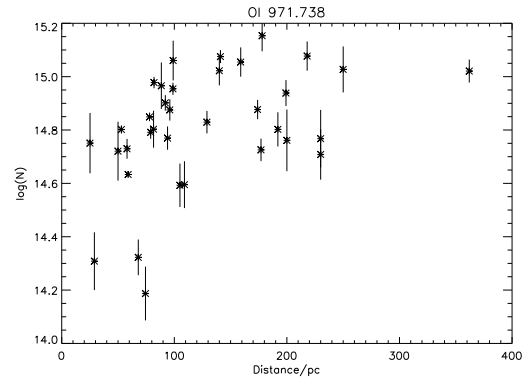


FIGURE 3.43. Column density of 971.738 Å O I plotted against distance

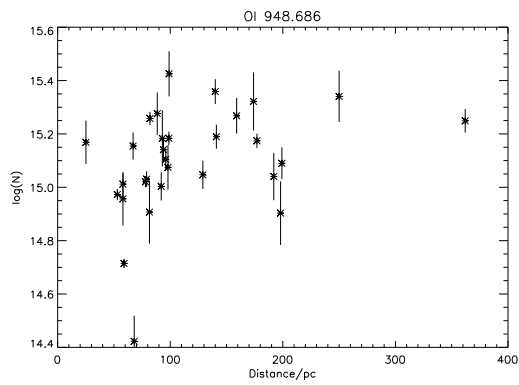


FIGURE 3.41. Column density of 948.686 Å O I plotted against distance

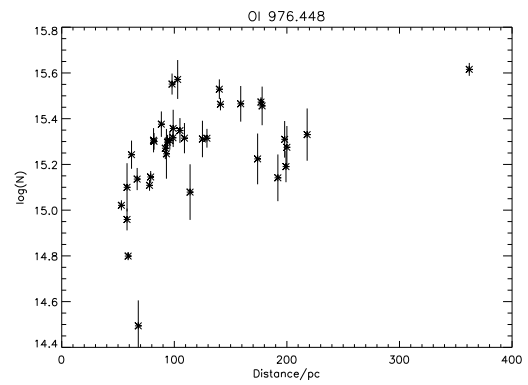


FIGURE 3.44. Column density of 976.448 Å O I plotted against distance

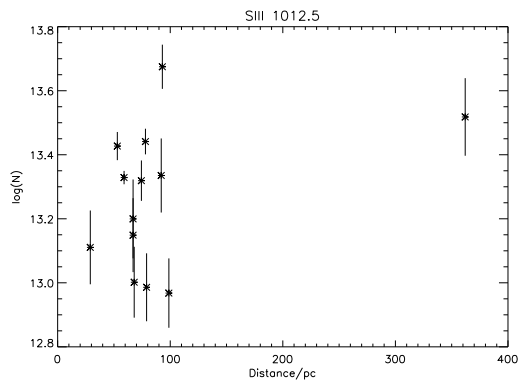


FIGURE 3.45. Column density of 1012.5 Å Si II plotted against distance

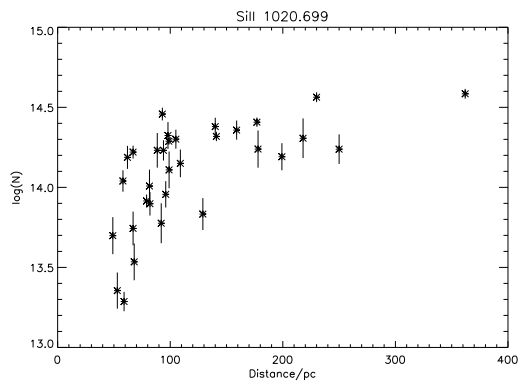


FIGURE 3.46. Column density of 1020.699 Å Si II plotted against distance

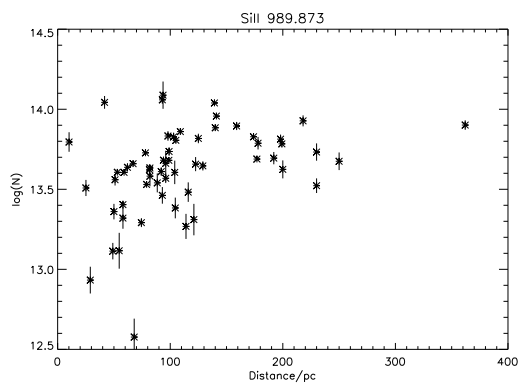


FIGURE 3.47. Column density of 989.873 Å Si II plotted against distance

The column density picture of the ISM can often appear different depending on the species that is measured. Figures 3.15 to 3.47 show the column densities for a series of measured lines. The most obvious trend is the increase in column density with distance. This is because more material is able to occupy the line of sight if the star is further away. The logarithmic y axis and the linear x axis would, in a uniformly dense region, result in a graph that resembles $y=\log x$ however in these lines of sight a slight discontinuity can be seen at roughly 100 pc. For some lines of sight the relationship differs at short distance due to a change in the gas density. These low values of column density arise because the star is within the local cavity. Some stars at these distances, however, display high column densities. This scatter is the result of the direction dependent distance to the boundary wall. The plots appear to flatten after 100 pc because the density changes more gradually beyond the wall. Though the densities do continue to rise beyond the wall, this effect is almost lost in the scatter. The cold gas absorption lines can therefore be used to identify the gas environment of the star itself. If the column density is characteristically low then the star is probably within the local cavity. This method of determining the environment of the star is more accurate than any comparison to the Lallement et al (2003) density map of the ISM.

Using the 1144.938 Å Fe II line as an example (Figure 3.21) we could define a threshold density as an indicator of the ISM environment of the star. For example, if the column density was measured to be less than this threshold, the star would be considered to be within the cavity. Savage & Lehner (2006) attempt to do this with O I. Since their sample is rather small, they get two discrete populations of column densities. They find

a collection of lines of sight that have high column densities and a few that have low densities but then draw the threshold arbitrarily at 15.8 dex. Though it is not clear how Savage & Lehner (2006) came to a value of 15.8 dex it is quite likely that they used the measured neutral hydrogen boundary density 19.3 cm^{-2} (Sfeir et al. 1999) and scaled it to the abundance of oxygen ($\text{O}/\text{H} = 3.45 \times 10^{-4}$) in the ISM. Evidence from this work and from an analysis of B stars (Welsh by private communication) suggests that this value is incorrect by a factor of 5 to 10.

One possible explanation for this discrepancy is that their value of oxygen abundance relative to hydrogen is obtained through the analysis of very long lines of sight, and so is heavily averaged. When applied to very short lines of sight the oxygen abundance may well be different. Since O I and the other gas species measured in this investigation follow the same basic pattern, there will be a deficiency of all these species compared to hydrogen within the bubble. It is, therefore, likely that the local divergence away from the H/O relationship is evidence of the local cavity being different to normal space by being especially devoid of metals. This finding independently verifies that of Lallement (2007) who find the local cavity depleted in oxygen and nitrogen.

One explanation could be that the heavier elements were selectively swept away by the creation of the local bubble. Another possibility is that the shock created by the formation of the local cavity collapsed the gas phase into dust. To test if the latter is true would require a follow up examination of the dust in the local cavity using the Indo-Israeli Ultraviolet Imaging Experiment, TAUVE X since the interstellar dust band at 217.4 nm falls

within the two TAUVEK filters SF2 and NBF3. If dust is more abundant in the bubble than outside of it then it is quite likely that depletion has caused the under-abundance.

Since the post boundary densities are seen to decrease towards shorter and shorter distances and because the boundary lies at different distance along the different lines of sight the discontinuity between pre boundary and post boundary densities is hard to observe. In the example of Fe II (Figure 3.21) there is a population of pre boundary lines of sight that can be seen within 100 pc. There are also, in this first part of the diagram, some lines of sight with slightly higher density that appear to follow the trend of decreasing density with distance indicative of a post boundary environment. However, these lines of sight are still considerably less dense than those that are obviously post boundary. If we set the threshold at $\log N=13.4$ (the point where the density becomes proportional to distance and thus in the high density region) then we include all the stars within 100 pc to be within the bubble. Though close comparison with Lallement et al. (2003) indicates that it is quite unlikely that all the stars within 100 pc are pre boundary this threshold serves as a best guess. Using this threshold the environments of the stars can then be categorized as pre or post boundary. See Table 3.3.

Table 3.2: Measurement of Fe II 1144.938 Å line. The wall threshold enables a judgment to be made on whether the star is within or outside the boundary. Iron is used because it appears in most lines of sight.

<i>Name</i>	W/λ	σ_W/λ	log N	$\sigma_{\log N}$	Location
WD0001+433	16.45	7.51	13.23	0.46	Inside cavity
WD0004+330	33.39	1.11	13.54	0.03	Outside cavity
WD0041+092	9.64	8.85	13.00	0.92	Inside cavity
WD0050-332	7.99	1.95	12.92	0.24	Inside cavity
WD0106-358	7.71	2.70	12.90	0.35	Inside cavity
WD0114-027	6.27	16.97	12.81	2.71	Inside cavity
WD0131-164	26.04	3.55	13.43	0.14	Outside cavity
WD0147+674	45.96	3.62	13.68	0.08	Outside cavity
WD0226-615	27.62	4.73	13.46	0.17	Outside cavity
WD0229-481	37.49	4.87	13.59	0.13	Outside cavity
WD0232+035	2.43	1.23	12.40	0.51	Inside cavity
WD0235-125	26.48	8.21	13.44	0.31	Outside cavity
WD0236+498	45.49	9.86	13.67	0.22	Outside cavity
WD0252-055	28.92	5.91	13.48	0.20	Outside cavity
WD0310-688	4.35	3.35	12.65	0.77	Inside cavity
WD0320-539	34.32	6.36	13.55	0.19	Outside cavity
WD0325-857	7.26	3.20	12.88	0.44	Inside cavity
WD0346-011	9.04	2.40	12.97	0.27	Inside cavity
WD0353+284	23.93	12.98	13.40	0.54	Inside cavity
WD0354-368	63.86	19.31	13.82	0.30	Outside cavity
WD0416+402	12.90	8.98	13.13	0.70	Inside cavity
WD0421+336	28.24	19.00	13.47	0.67	Outside cavity
Continued on next page					

Table 3.2 – continued from previous page

<i>Name</i>	W	σ_W	log N	$\sigma_{\log N}$	Location
WD0457-103	4.36	3.57	12.66	0.82	Inside cavity
WD0501+524	11.08	0.62	13.06	0.06	Inside cavity
WD0512+326	15.51	2.98	13.21	0.19	Inside cavity
WD0549+158	6.62	2.10	12.84	0.32	Inside cavity
WD0603-483	63.75	8.81	13.82	0.14	Outside cavity
WD0621-376	6.71	1.41	12.84	0.21	Inside cavity
WD0659+130	24.63	15.32	13.41	0.62	Inside cavity
WD0715-704	23.95	5.72	13.40	0.24	Inside cavity
WD0802+413	85.68	7.30	13.95	0.09	Outside cavity
WD0809-728	10.46	5.57	13.04	0.53	Inside cavity
WD0830-535	27.06	5.87	13.45	0.22	Outside cavity
WD0905-724	23.44	8.15	13.39	0.35	Inside cavity
WD0937+505	40.79	10.19	13.63	0.25	Outside cavity
WD1019-141	12.17	4.69	13.10	0.39	Inside cavity
WD1021+266	45.59	9.20	13.68	0.20	Outside cavity
WD1024+326	10.59	20.69	13.04	1.95	Inside cavity
WD1029+537	34.75	5.99	13.56	0.17	Outside cavity
WD1040+492	12.49	7.06	13.11	0.57	Inside cavity
WD1041+580	7.54	5.63	12.89	0.75	Inside cavity
WD1056+516	18.99	58.02	13.29	3.06	Inside cavity
WD1057+719	7.55	5.62	12.89	0.74	Inside cavity
WD1109-225	25.80	3.46	13.43	0.13	Inside cavity
WD1234+481	2.63	3.20	12.44	1.21	Inside cavity
WD1254+223	8.15	1.88	12.93	0.23	Inside cavity
WD1302+597	21.46	10.22	13.35	0.48	Inside cavity
WD1314+293	2.58	1.09	12.43	0.42	Inside cavity
Continued on next page					

Table 3.2 – continued from previous page

<i>Name</i>	W	σ_W	log N	$\sigma_{\log N}$	Location
WD1337+701	27.90	2.95	13.46	0.11	Outside cavity
WD1342+442	56.56	7.23	13.77	0.13	Outside cavity
WD1440+753	40.87	4.83	13.63	0.12	Outside cavity
WD1550+130	20.49	14.17	13.33	0.69	Inside cavity
WD1603+432	10.15	4.53	13.02	0.45	Inside cavity
WD1611-084	51.58	4.24	13.73	0.08	Outside cavity
WD1620+647	57.62	6.40	13.78	0.11	Outside cavity
WD1631+781	10.56	2.14	13.04	0.20	Inside cavity
WD1635+529	63.83	1.33	13.82	0.02	Outside cavity
WD1636+351	50.24	3.59	13.72	0.07	Outside cavity
WD1648+407	35.99	6.11	13.57	0.17	Outside cavity
WD1711+668	55.47	8.01	13.76	0.14	Outside cavity
WD1725+586	35.77	4.97	13.57	0.14	Outside cavity
WD1734+742	39.95	6.78	13.62	0.17	Outside cavity
WD1736+134	14.38	30.57	13.17	2.13	Inside cavity
WD1800+685	72.73	9.18	13.88	0.13	Outside cavity
WD1819+580	26.01	4.62	13.43	0.18	Outside cavity
WD1844-223	17.05	2.68	13.25	0.16	Inside cavity
WD1845+683	36.24	7.41	13.58	0.20	Outside cavity
WD1917+599	32.01	4.10	13.52	0.13	Outside cavity
WD1921-566	20.54	6.28	13.33	0.31	Inside cavity
WD1942+499	37.94	3.29	13.60	0.09	Outside cavity
WD1950-432	38.79	4.36	13.61	0.11	Outside cavity
WD2000-561	42.94	5.56	13.65	0.13	Outside cavity
WD2004-605	16.76	2.57	13.24	0.15	Inside cavity
WD2013+400	43.69	3.30	13.66	0.08	Outside cavity
Continued on next page					

Table 3.2 – continued from previous page

<i>Name</i>	W	σ_W	log N	$\sigma_{\log N}$	Location
WD2014-575	19.29	2.40	13.30	0.12	Inside cavity
WD2020-425	0.63	7.56	11.82	11.93	Inside cavity
WD2043-635	33.29	12.22	13.54	0.37	Outside cavity
WD2111+498	22.38	3.40	13.37	0.15	Inside cavity
WD2116+736	52.55	2.96	13.74	0.06	Outside cavity
WD2123-226	17.65	23.57	13.26	1.34	Inside cavity
WD2124+191	20.75	10.27	13.33	0.49	Inside cavity
WD2146-433	100.10	6.33	14.02	0.06	Outside cavity
WD2156-546	16.39	5.88	13.23	0.36	Inside cavity
WD2211-495	16.43	1.61	13.23	0.10	Inside cavity
WD2257-073	40.91	6.07	13.63	0.15	Outside cavity
WD2309+105	20.87	1.09	13.34	0.05	Inside cavity
WD2321-549	11.93	4.92	13.09	0.41	Inside cavity
WD2331-475	20.73	2.65	13.33	0.13	Inside cavity
WD2350-706	27.91	3.36	13.46	0.12	Outside cavity

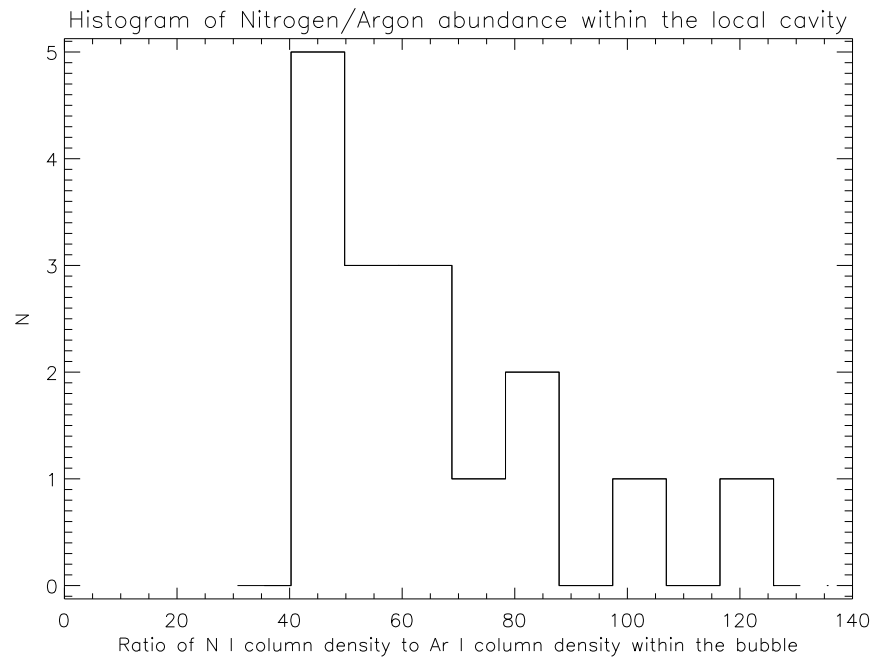


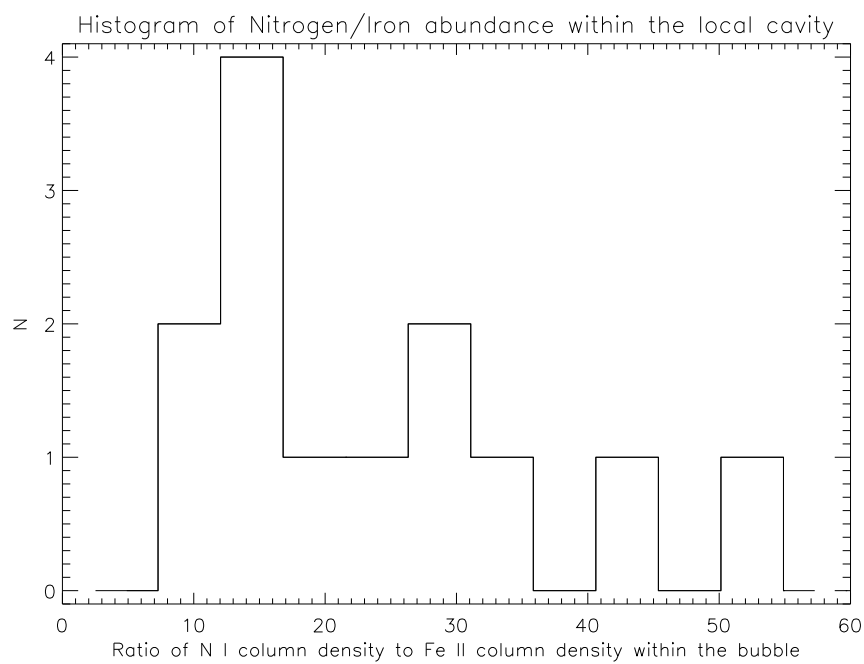
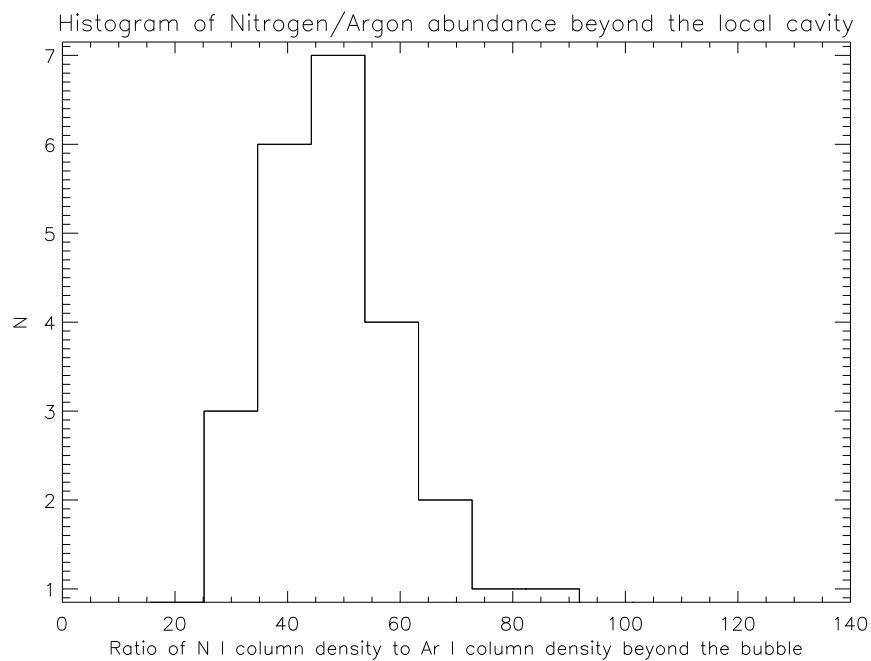
FIGURE 3.48.

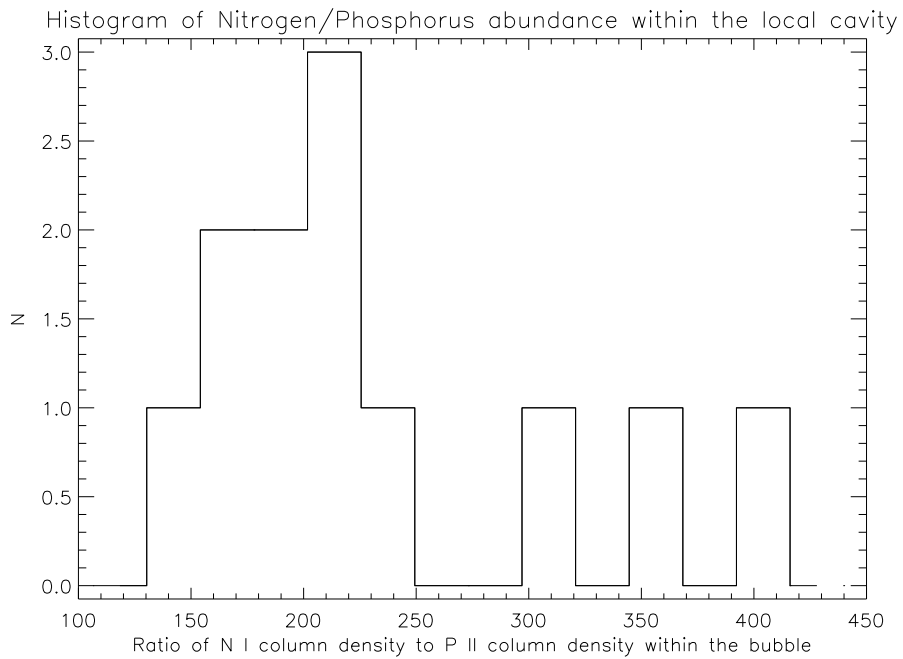
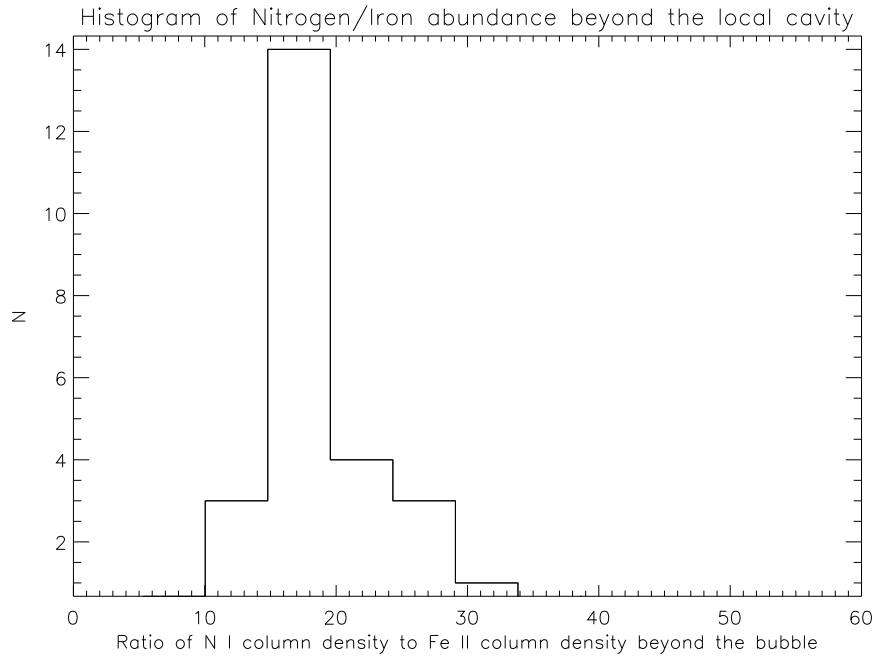
An average can be calculated from those lines without any obvious contamination, however, only species with multiple lines present can be tested this way, and care must be taken in the analysis of species only represented by a single line.

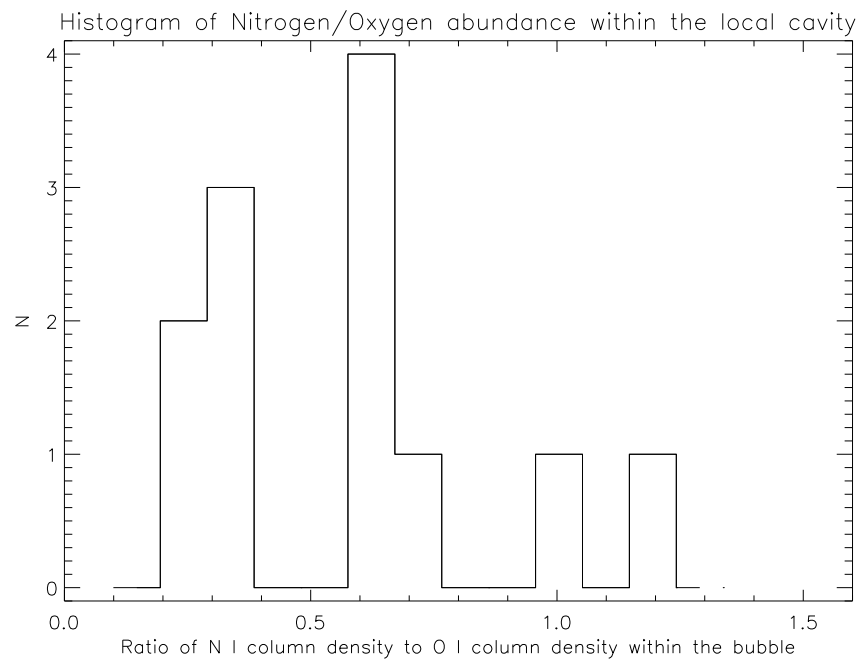
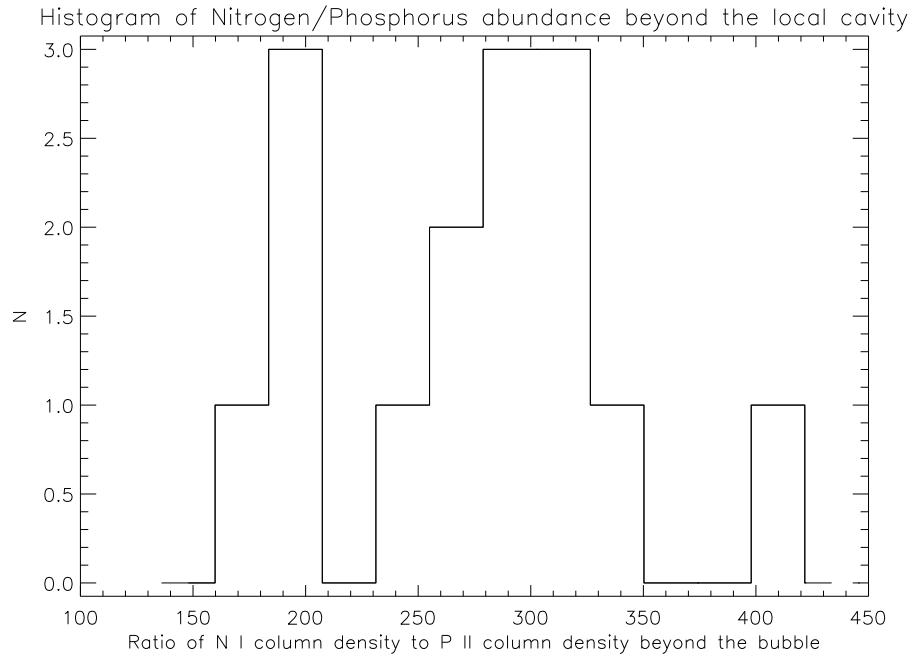
Table 3.3: Histogram peak location for abundance ratios

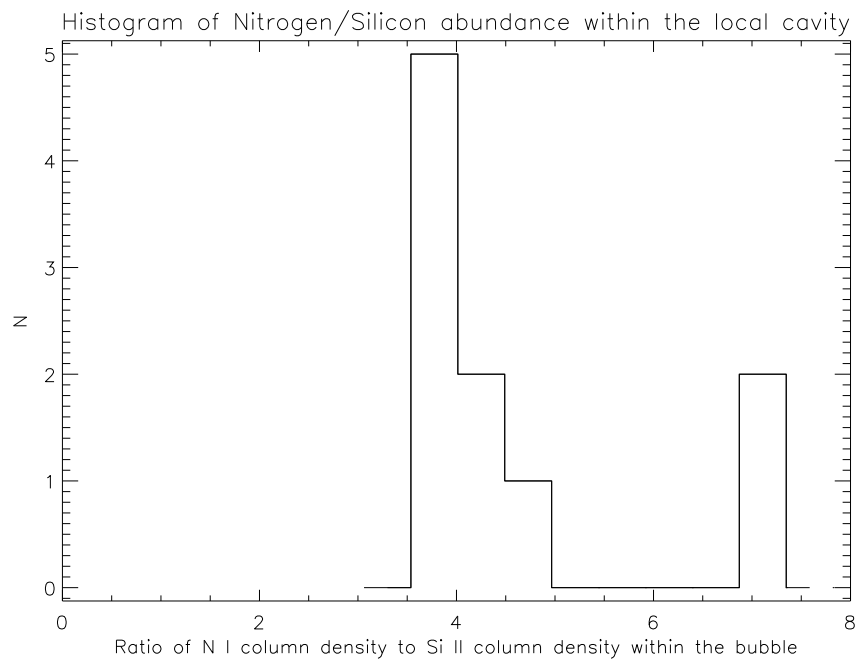
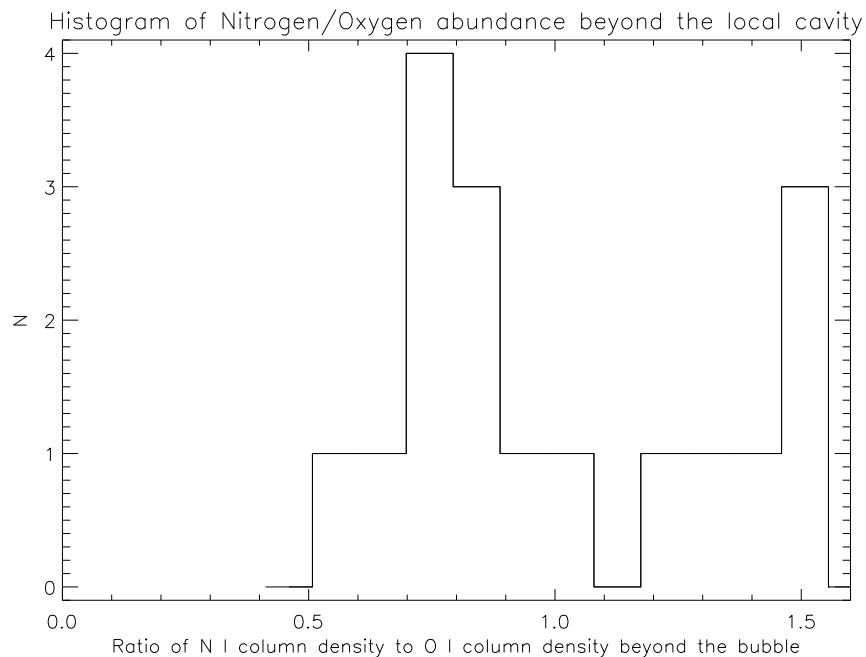
Species	Inside bubble	Outside bubble
N(N I)/N(Ar I)	45	47
N(N I)/N(Fe II)	14	17
N(N I)/N(P II)	215	300
N(N I)/N(O I)	0.65	0.72
N(N I)/N(Si II)	3.75	4.3

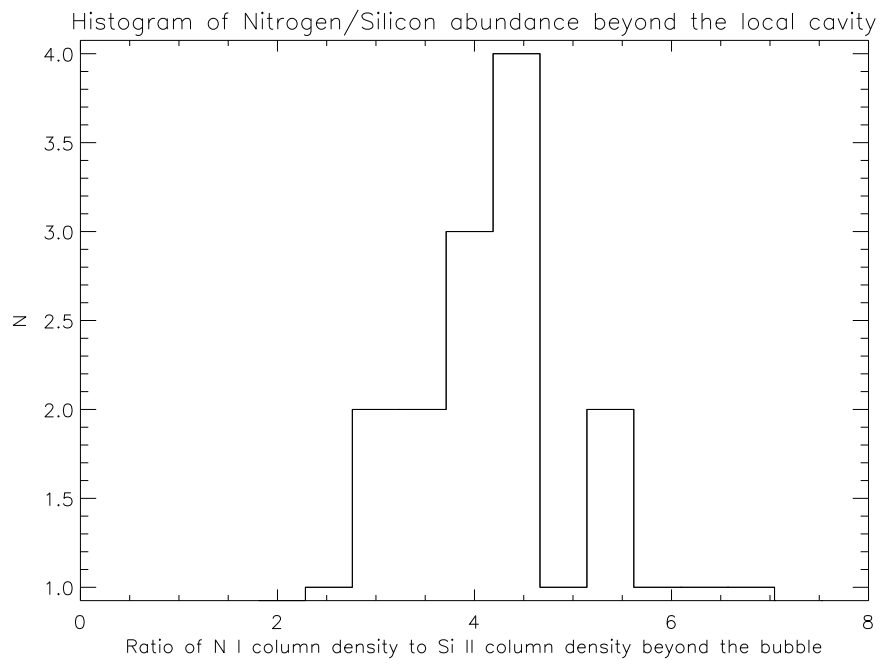
Figure 3.48 shows that argon, oxygen and silicon have similar values of abundance relative to nitrogen irrespective of environment. Figure 3.48 also shows that iron and phosphorus have abundances relative to nitrogen that change noticeably across the boundary of the local cavity.











the cosmic abundance ratio is 1 : 0.28. In this case some of the iron may have formed molecules on the surface of dust grains or could exist in the Fe I or Fe III states. Within the bubble the measured ratio of N I to O I is 1 : 1.53 whereas the cosmic abundance ratio is 1 : 0.11 suggesting that though most of oxygen is in the O I state a large fraction of nitrogen must exist in the N II state. Within the bubble the measured ratio of N I to Si II is 1 : 0.27 whereas the cosmic abundance ratio is 1 : 0.31 suggesting that most of it is accounted for in the interstellar medium.

The volume density and the volume density uncertainty for each detected species present in each line of sight can be found in the accompanying CD on a star by star basis.

Chapter 4

Hot gas in the LISM

4.1 Introduction

From the pressure equilibrium observed between high density clouds of H I in the galactic halo, Spitzer (1956) inferred that the temperature of the halo must be 10^6K . The first direct evidence for hot gas in the ISM came from observations of the soft X-ray background by Bowyer et al. (1968). O VI, a tracer of hot gas, was then detected in the spectra of B stars (Rogerson et al. 1973). Jenkins & Meloy (1974) concluded that this located a component of the hot gas in the local interstellar medium. The detection of high ionisation interstellar species, such as N V and C IV, by Jenkins & Meloy (1974) and the detections of interstellar O VII and O VIII by Inoue et al. (1979), Schnopper et al. (1982) and Sanders et al. (1998) all indicate that hot gas is present in the interstellar medium.

Five fold photoionisation of interstellar oxygen requires the incident light to have an

energy of 114 eV. Due to the relative scarcity of photons of this energy, and the low intrinsic density of the interstellar medium, photoionised O VI should only exist at very low volume density. This O VI becomes visible over very long lines of sight. O VI observed in the lines of sight of nearby stars, for example Rogerson et al. (1973)'s B Stars, requires an alternative explanation.

McKee & Ostriker (1977) and Cowie et al. (1979) suggested that the O VI observed in Copernicus observations was hot gas from supernovae running into cold gas ISM. They argued that the narrow line profile of the O VI suggested very little variation with temperature and concluded that the absorption was not coming from the hot gas itself. The interface theory also helped explain the Cowie et al. (1979) result that the cold gas and the hot gas changed similarly from one line of sight to another, suggesting a link between the two components. Slavin (1989) and Borkowski et al. (1990) found general agreement between the observed and the predicted column densities.

Further evidence of hot gas was the presence of the soft X-ray background (Snowden et al. 1998). Non zero flux found in the shadows of nearby gas clouds suggested that the SXRb was local. More recent work suggests, however, that a fraction of the soft X-ray background flux varies with the solar cycle. Given that the solar wind has no influence on interstellar gases outside of the heliosphere, this finding locates the origin of a large fraction of the soft X-ray background to the solar system. It is now believed that soft X-ray photons are produced from the charge exchange of heavy solar wind ions and the neutral species of the ISM at the heliopause. Modeling the X-ray emission Koutroumpa

et al. (2008) find that the 3/4 keV band emission is entirely heliospheric, while in the 1/4 keV band, the heliospheric component seems to be the primary contributor. A component of X-rays from hot gas is still observed towards the galactic poles and where supernova structures such as the Loop 1 bubble are seen.

The non detection of the EUV background and the results from the Cosmic Hot Interstellar Plasma Spectrometer (CHIPS) (Hurwitz et al. 2005) cast doubt on the amount of local hot gas since the then accepted amount of hot gas would have produced an EUV flux detectable by these instruments. These non detections can only be explained by significantly reducing the assumed amount of hot gas.

4.2 O VI measurement

The most thorough studies to date of the spatial distribution of O VI in the local interstellar medium are by Oegerle et al. (2005) and Savage & Lehner (2006) who studied the lines of sight of 25 and 39 white dwarfs respectively. Our sample contains all of these stars. One of the main findings of these papers is that O VI appears in some lines of sight and not in others, leading the authors to the conclusion that the distribution of hot gas is patchy. Cox & Helenius (2003) provide a theoretical explanation for this result based upon tangential magnetic quenching of the thermal environment. In this the presence of a magnetic field prevents thermal conduction by the movement of ions. The amount of quenching would be dependent on the local orientation of the interstellar magnetic field and so would result in detections along some lines of sight and non detections in others.

One of the largest problems that these investigations face is contamination with photospheric O VI. Phenomenological investigations into the variation of O VI equivalent width with both stellar distance and stellar temperature could give some qualitative insights into the amount of contamination. The strictly a posteriori test and the only one to deliver a definitive measure of contamination is the measurement of the velocity of the line compared with that of the star. This method will be employed later.

Since white dwarfs are dense objects, their emitted light is subject to a gravitational redshift. This, along with the space motion of the star, can move photospheric absorption features by as much as 60 km/s. Savage & Lehner (2006) recognize that the average difference between photospheric velocity and the interstellar medium velocity is about 35 km/s. What is not discernible from the size of their sample is that the random space motion in the line of sight adds an almost random scatter to this average velocity.

The expected effect of this random scatter is that some stars will have a space motion that cancels out the gravitational redshift. This renders some stars useless in a test of line velocity because the two velocities can not be differentiated. The photospheric and interstellar medium velocities will be too similar to differentiate from which component the O VI line originated.

In this investigation the average photospheric and interstellar line velocities are calculated from the measured photospheric and interstellar lines respectively (see table 2.2). Figure 4.1 shows the resulting comparison of photospheric velocity to interstellar medium velocities. The error bars are typically larger for the photospheric velocity

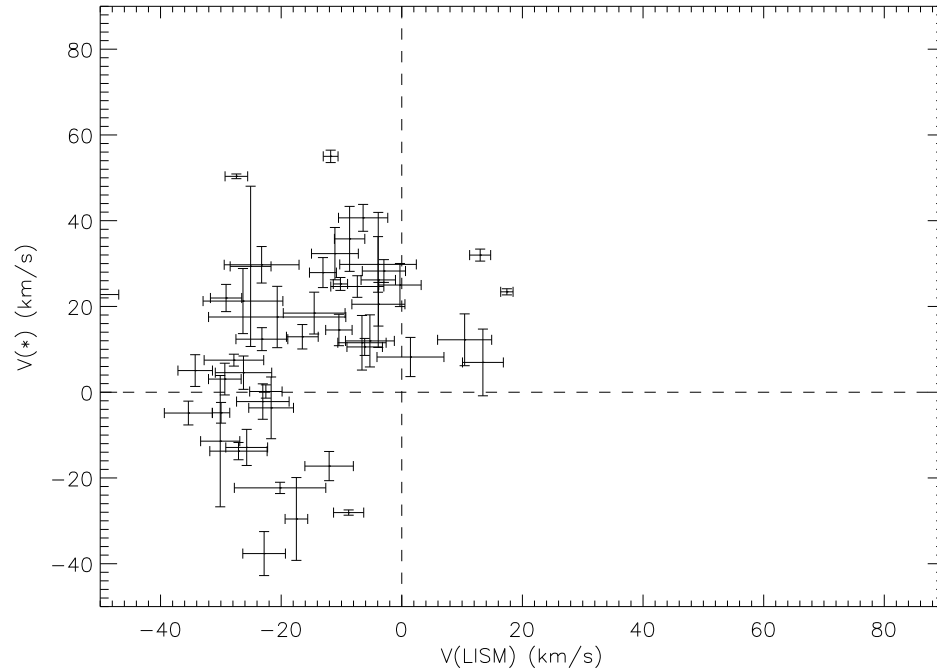


FIGURE 4.1. Photospheric velocity against interstellar medium velocity for this sample

because there are normally fewer lines from which to gauge the average. Some stars do not exhibit any photospheric lines and so can not be displayed on this Figure. Figure 4.2.

Table 4.1: Measured Photospheric and ISM velocity

Name	$V_{ism}/\text{km/s}$	$\sigma_{V_{ism}}/\text{km/s}$	$V_*/\text{km/s}$	$\sigma_{V_*}/\text{km/s}$
WD0001+433	-3.94	6.35	29.80	6.49
WD0004+330	-11.79	1.23	55.01	1.45
WD0027-636	-7.37	4.4	24.65	2.52
WD0041+092	-25.07	3.39	29.35	18.69
WD0050-332	-14.53	5.12	18.45	4.88
WD0106-358	-23.2	4.3	12.37	2.68
WD0111+002	-29.14	2.6	21.97	3.17
WD0114-027	-8.02	3.29		
WD0131-164	-6.15	2.94	10.56	1.99
WD0147+674	-15.47	3.12		
WD0226-615	-8.65	2.52	35.76	7.58

Table 4.1

Name	V_{ism}	$\sigma_{V_{ism}}$	V_*	σ_{V_*}
WD0229-481	-0.31	3.52	24.99	5.03
WD0232+035	-8.81	2.5	-28.08	0.62
WD0235-125	13.73	2.52		
WD0236+498	-4.49	7.17		
WD0252-055	10.42	4.49	12.22	6.04
WD0310-688	36.46	2.91		
WD0320-539	6.23	4.35		
WD0325-857	-10.15	4.49		
WD0346-011	15.29	2.62		
WD0353+284	8.41	6.7		
WD0354-368	8.67	4.56		
WD0416+402	-0.05	5.33		
WD0421+336	49.98	2.04		
WD0455-282	38.66	1.42		
WD0457-103	-5	3.68		
WD0501+524	17.42	1.02	23.41	0.71
WD0512+326	-3.87	4.4	20.51	5.09
WD0549+158	1.44	5.55	8.21	4.57
WD0603-483	18.58	3		
WD0621-376	12.99	1.74	31.98	1.4
WD0659+130	-0.29	4.76		
WD0715-704	-4.8	2.71		
WD0802+413	13.45	3.39	6.94	7.78
WD0809-728	-6.34	2.22		
WD0830-535	9.36	3.87		
WD0905-724	12.63	4.68		
WD0937+505	-5.07	5.17		
WD1019-141	-6.6	4	11.53	6.37
WD1021+266	-5.28	4.05	11.96	6.08
WD1024+326	-13.96	3.98		
WD1029+537	-16.49	2.63	12.93	2.85
WD1040+492	-21.66	3.71	-3.65	7.2
WD1041+580	-10.43	3.56		
WD1056+516	-12.72	6.72		
WD1057+719	-16.14	3.52		
WD1109-225	-4.85	5.1		
WD1234+481	-9.59	3		
WD1254+223	-11.78	4.21		
WD1302+597	23.87	4.67		
WD1314+293	-16.13	3.12		
WD1337+701	-12.05	4.02	-17.23	3.41
WD1342+442	-25.71	3.47	-12.88	4.21

Table 4.1

Name	V_{ism}	$\sigma_{V_{ism}}$	V_*	σ_{V_*}
WD1440+753	-13.73	3.76		
WD1528+487	-27.33	2.97		
WD1550+130	-9.89	5.05		
WD1603+432	-51.32	4.39	22.77	2.55
WD1611-084	-22.83	3.54	-37.64	5.13
WD1615-154	-68.31	1.61		
WD1620+647	-28.82	3.38		
WD1631+781	-6.9	2.5		
WD1634-573	-29.97	1.45	-4.80	2.42
WD1635+529	-22.54	2.69	0.17	1.55
WD1636+351	-31.08	2.55		
WD1648+407	-28.66	4.46		
WD1711+668	-26.33	6.62	21.26	7.59
WD1725+586	-16.6	4.19		
WD1734+742	-23.04	4.36	-2.18	4.13
WD1736+134	12.07	6.2		
WD1800+685	-35.38	3.99	-4.86	-2.77
WD1819+580	-27.08	4.75	-13.74	2.01
WD1844-223	-34.25	2.86	5.04	3.71
WD1845+683	-28.16	5.06		
WD1917+599	-29.34	2.71	3.06	3.7
WD1921-566	-30.1	3.25	-11.42	15.31
WD1942+499	-27.84	4.94	7.48	1.39
WD1950-432	-3.9	2.85	26.18	15.75
WD2000-561	-26.24	4.68	4.55	3.89
WD2004-605	-27.79	4.25		
WD2011+398	-10.43	2.19	14.51	3.66
WD2014-575	-29.81	4.13		
WD2020-425	-25.39	5.06		
WD2043-635	-36.91	6.9		
WD2111+498	-20.18	7.58	-22.32	1.31
WD2116+736	-17.47	1.87	-29.57	9.66
WD2123-226	50.88	6.85		
WD2124+191	-23.24	6.2	29.71	4.26
WD2124-224	-28.42	2.89		
WD2146-433	-13.07	2.23	27.90	3.5
WD2152-548	-3.92	5.78		
WD2211-495	-10.17	1.19	25.25	1.51
WD2257-073	-11.08	3.88	32.32	6.11
WD2309+105	-27.43	1.87	50.35	0.55
WD2321-549	-20.66	11.38	17.54	7.15
WD2331-475	-2.96	3.58	28.26	2.65

Table 4.1

Name	V_{ism}	$\sigma_{V_{ism}}$	V_*	σ_{V_*}
WD2350-706	-6.41	4.09	40.66	3.13

We present the line profiles of the 1031.912 O VI line compared to the C II 1036 and O I 1039 lines in the same format as Savage & Lehner (2006). An example of which is Figure 4.3. A local linear continuum was fit to each of the three lines independently. This treatment was repeated for the entire sample and can be seen on a star by star basis on the accompanying data CD. The average photospheric and interstellar medium line velocities are also plotted. The ISM line velocity is represented by the unlabeled line and the photospheric line velocity is annotated with a * symbol.

For each O VI line two positions were marked that defined the continuum and the horizontal extent of the absorption feature. To the data points bound by these two positions a single Gaussian curve was fitted. The properties of this Gaussian is listed in table 4.2. Gaps in the data indicate the absence of the O VI line.

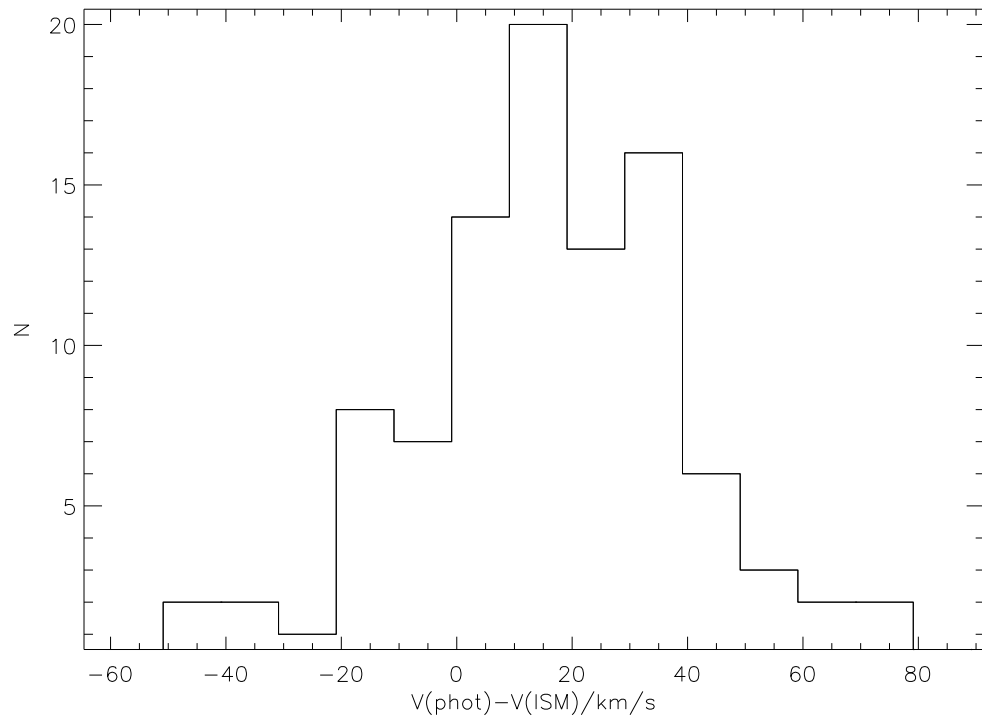


FIGURE 4.2. Histogram of $V_{phot} - V_{ISM}$ for those stars that have a measured V_{phot} and V_{ISM}

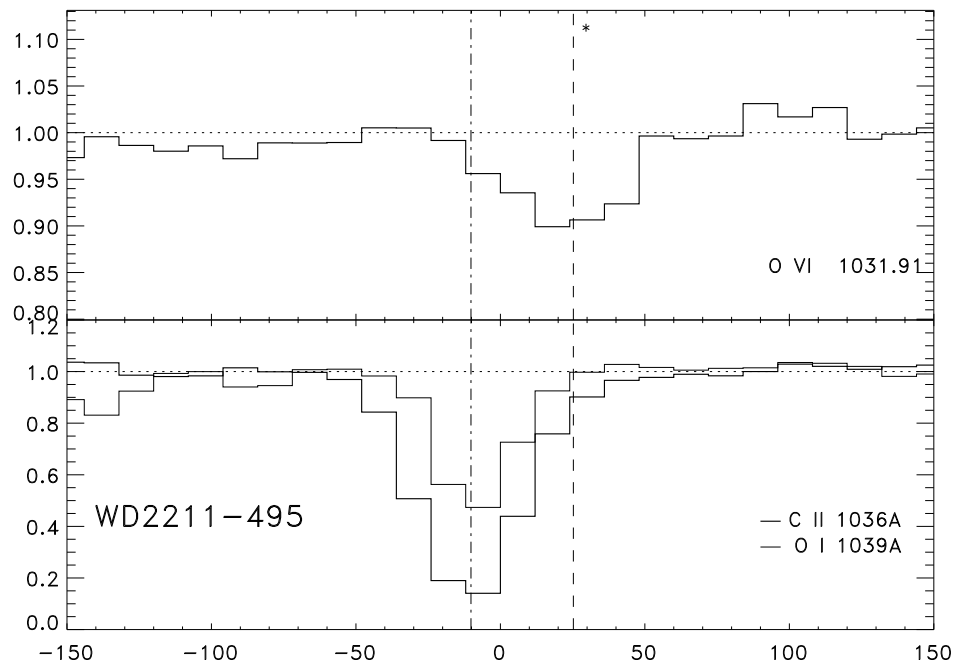


FIGURE 4.3. Example of O VI line profile plot. O VI line above, compared to O I and C II lines below. This graph indicates a photospheric O VI line. The vertical dashed line is the measured interstellar medium velocity for this line of sight and the vertical dashed line labeled with a * is the measured photospheric velocity for this star.

Table 4.2: Measured O VI properties. Blank lines indicate where no O VI line was observed

Name	λ_0/λ	$\sigma_{\lambda_0}/\lambda$	$V/km/s$	$\sigma_V/km/s$	V/σ_V	W/λ	σ_W/λ	W/σ_W
WD0001+433								
WD0004+330	1031.8741	0.0114	-11.0108	3.3150	-3.3215	6.1000	1.2200	5.0000
WD0027-636	1031.9137	0.0135	0.4960	3.9360	0.1260	28.5600	4.6100	6.1952
WD0041+092								
WD0050-332	1031.9590	0.0131	13.6545	3.7970	3.5961	6.2600	1.6600	3.7711
WD0106-358								
WD0111+002								
WD0114-027								
WD0131-164	1031.9790	0.0052	19.4649	1.5060	12.9249	43.1600	2.9800	14.4832
WD0147+674	1031.8300	0.0322	-23.8227	9.3430	-2.5498	32.7634	8.6779	3.7755
WD0226-615	1031.9440	0.0175	9.2967	5.0960	1.8243	16.3600	4.5400	3.6035
WD0229-481	1031.9325	0.0302	5.9557	8.7840	0.6780	6.1000	3.9700	1.5365
WD0232+035	1031.9000	0.0117	-3.4863	3.4108	-1.0221	8.3608	1.4200	5.8879
WD0235-125								
WD0236+498								
WD0252-055	1031.9679	0.0167	16.2401	4.8520	3.3471	23.8600	6.6500	3.5880
WD0310-688								
WD0320-539								
WD0325-857								
WD0346-011								
WD0353+284	1032.0000	0.0229	25.5659	6.6400	3.8503	69.9154	11.3100	6.1817
WD0354-368	1031.9475	0.0311	10.3135	9.0450	1.1402	44.9200	14.8400	3.0270
WD0416+402								
WD0421+336								
Continued								

Table 4.2

Name	λ_0	σ_{λ_0}	V	σ_V	V/σ_V	W	σ_W	W/σ_W
WD0455-282	1032.1160	0.0150	59.2600	4.3490	13.6261	11.2900	2.2500	5.0178
WD0457-103								
WD0501+524	1031.9822	0.0064	20.3946	1.8460	11.0480	4.8200	0.4500	10.7111
WD0512+326	1031.9979	0.0219	24.9558	6.3620	3.9226	14.3800	4.3600	3.2982
WD0549+158								
WD0603-483								
WD0621-376	1032.0302	0.0127	34.3396	3.6890	9.3087	4.7100	1.0400	4.5288
WD0659+130								
WD0715-704	1031.8730	0.0159	-11.3303	4.6050	-2.4604	11.5500	3.1300	3.6901
WD0802+413								
WD0809-728								
WD0830-535	1031.9054	0.0361	-1.9174	10.4970	-0.1827	12.6500	7.1600	1.7668
WD0905-724								
WD0937+505								
WD1019-141								
WD1021+266	1031.9580	0.0094	13.3640	2.7280	4.8988	36.3600	5.5900	6.5045
WD1024+326								
WD1029+537	1032.0004	0.0062	25.6821	1.7900	14.3475	63.6000	4.3500	14.6207
WD1040+492	1032.0669	0.0099	45.0018	2.8630	15.7184	30.2500	3.6700	8.2425
WD1041+580								
WD1056+516								
WD1057+719								
WD1109-225	1031.8846	0.0167	-7.9603	4.8560	-1.6393	13.7700	3.9500	3.4861
WD1211+332	1031.8856	0.0229	-7.6600	6.6410	-1.1534	8.3500	3.2800	2.5457
WD1234+481								
WD1254+223	1031.9718	0.0202	17.3732	5.8560	2.9667	5.2200	2.2800	2.2895
Continued								

Table 4.2

Name	λ_0	σ_{λ_0}	V	σ_V	V/σ_V	W	σ_W	W/σ_W
WD1302+597								
WD1314+293								
WD1337+701								
WD1342+442	1031.8699	0.0087	-12.2309	2.5320	-4.8305	72.3200	7.9800	9.0627
WD1440+753								
WD1528+487	1031.7938	0.0164	-34.3290	4.7540	-7.2211	23.7800	4.0900	5.8142
WD1550+130								
WD1603+432								
WD1611-084	1031.8287	0.0067	-24.2004	1.9470	-12.4296	53.0500	3.9900	13.2957
WD1615-154	1032.0728	0.0266	46.7060	7.7380	6.0359	7.2500	4.0100	1.8080
WD1620+647								
WD1631+781	1031.8846	0.0173	-7.9603	5.0130	-1.5879	6.8500	2.0600	3.3252
WD1634-573	1031.8765	0.0088	-10.3200	2.5690	-4.0171	8.1800	0.9900	8.2626
WD1635+529								
WD1636+351								
WD1648+407								
WD1711+668								
WD1725+586	1031.9763	0.0075	18.6805	2.1710	8.6046	53.0500	5.1800	10.2413
WD1734+742								
WD1736+134								
WD1800+685								
WD1819+580								
WD1844-223								
WD1845+683								
WD1917+599								
WD1921-566								
Continued								

Table 4.2

Name	λ_0	σ_{λ_0}	V	σ_V	V/σ_V	W	σ_W	W/σ_W
WD1942+499	1031.9340	0.0089	6.3915	2.6000	2.4583	15.7400	3.0800	5.1104
WD1950-432	1031.9132	0.0212	0.3486	6.1610	0.0566	17.4800	4.9500	3.5313
WD2000-561	1031.8595	0.0231	-15.2524	6.7170	-2.2707	25.4200	6.9300	3.6681
WD2004-605	1031.8500	0.0170	-18.0123	4.9501	-3.6388	9.4331	2.7782	3.3954
WD2011+398	1031.9598	0.0069	13.8869	2.0050	6.9261	62.6000	3.4800	17.9885
WD2014-575								
WD2020-425								
WD2043-635								
WD2111+498	1031.9570	0.0153	13.0735	4.4320	2.9498	20.1200	4.1600	4.8365
WD2116+736								
WD2123-226								
WD2124+191								
WD2124-224	1031.8556	0.0214	-16.3840	6.2070	-2.6396	20.1000	4.6600	4.3133
WD2146-433	1031.9479	0.0131	10.4297	3.7920	2.7505	20.2500	4.4500	4.5506
WD2152-548	1031.9030	0.0086	-2.6147	2.5040	-1.0442	89.9500	6.5700	13.6910
WD2211-495	1031.9741	0.0052	18.0414	1.4980	12.0436	15.3900	1.1500	13.3826
WD2257-073	1032.0179	0.0154	30.7662	4.4800	6.8675	19.0500	6.1800	3.0825
WD2309+105								
WD2321-549	1031.9065	0.0168	-1.5979	4.8850	-0.3271	44.4500	6.3300	7.0221
WD2331-475	1031.9224	0.0132	3.0214	3.8210	0.7907	13.2000	2.3700	5.5696
WD2350-706	1031.9486	0.0088	10.6331	2.5430	4.1813	45.0900	3.6100	12.4903

4.3 O VI compared to the star's position

The simplest analysis that can be conducted is to compare the O VI line properties to such things as stellar temperature and stellar distance. If O VI behaved in a similar fashion to the cold gas then we would expect an increase in equivalent width with distance. Deviations from this relationship would be the result of inhomogeneities in the gas. The volume densities of the hot gas and the cold gas and the orientation of the interstellar magnetic field are all factors that would effect the amount of absorption observed. Since the only tracer for both the hot gas and the magnetic fields is the O VI line itself it is impossible to quantify the two conditions independently. The presence of the cold gas can be quantified since cold gas absorption is visible in the FUV range and studied in the cool gas chapter of this thesis.

The largest change from one line of sight to another that is measurable from volume density will be whether or not the line of sight has intersected with the local cavity boundary. Due to the morphology of the local cavity (Lallement et al. 2003) lines of sight at a high galactic latitude will not encounter the cavity wall, whereas galactic latitude lines of sight will. Galactic latitude lines of sight (Figure 4.4) are of high density compared to the polar latitude lines of sight (Figure 4.5). Those lines of sight that occupy intermediate latitudes contain a mixture of both high and low density as some stars fall inside and outside the cavity depending on their relative position.

In Figure 4.4 the data points represent the stars of this sample. Those that are of low

galactic latitudes are highlighted with a diamond shape and labeled. In Figure 4.5 again all the stars are plotted and this time only those stars with a high galactic latitude are highlighted with triangle symbols and labeled. The two figures show that there is a tendency for higher galactic latitude stars to occupy the lower volume density regions of the plot and conversely the galactic latitude plots occupy the higher volume density regions.

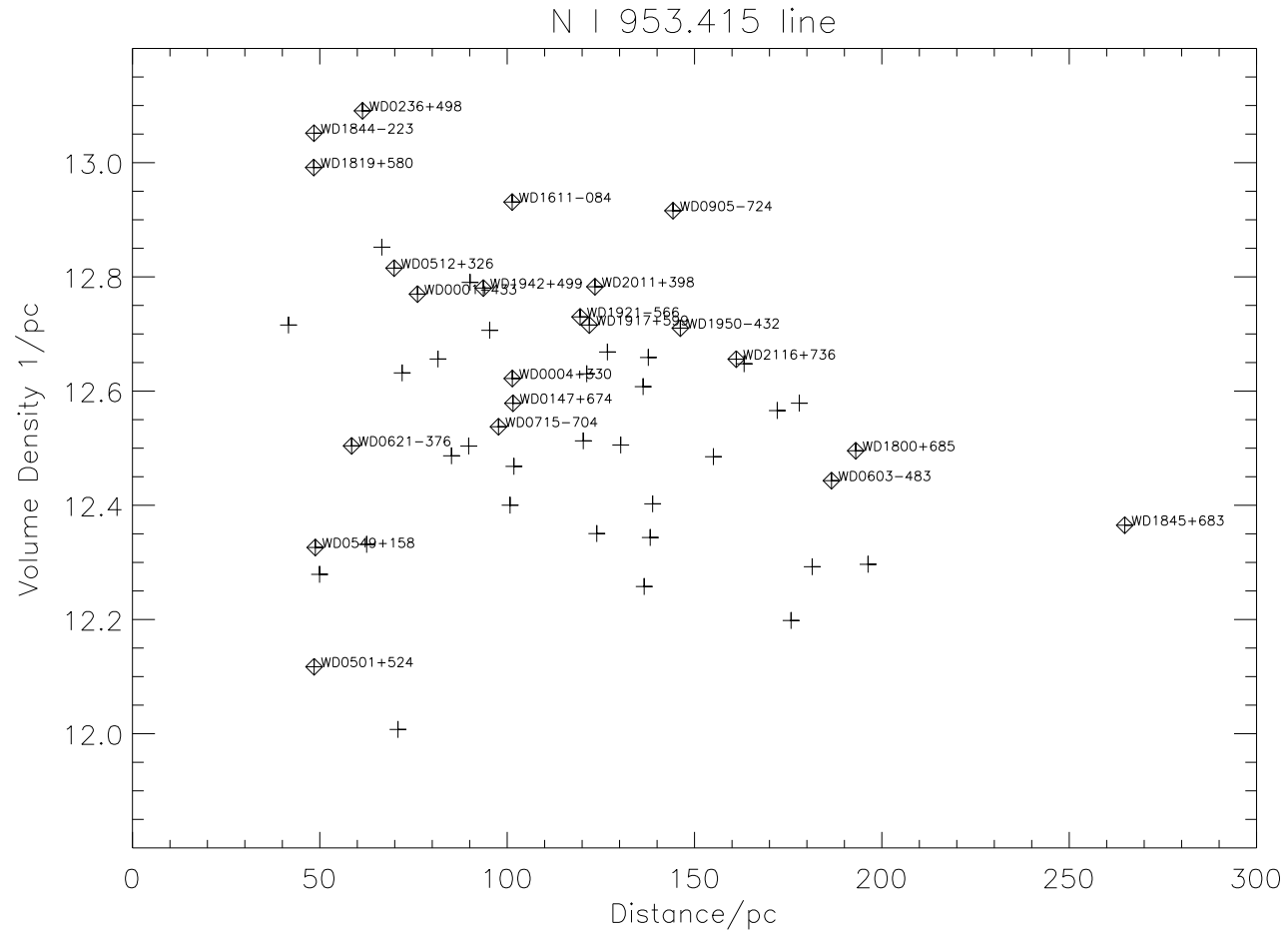


FIGURE 4.4. Low latitude stars (-30 to $+30$ degrees). Distance uncertainties are given in Table 3.1 and volume density uncertainties given individually for each line measured (see for example Table 6.13). These are not plotted here to enable the labeling of data points.

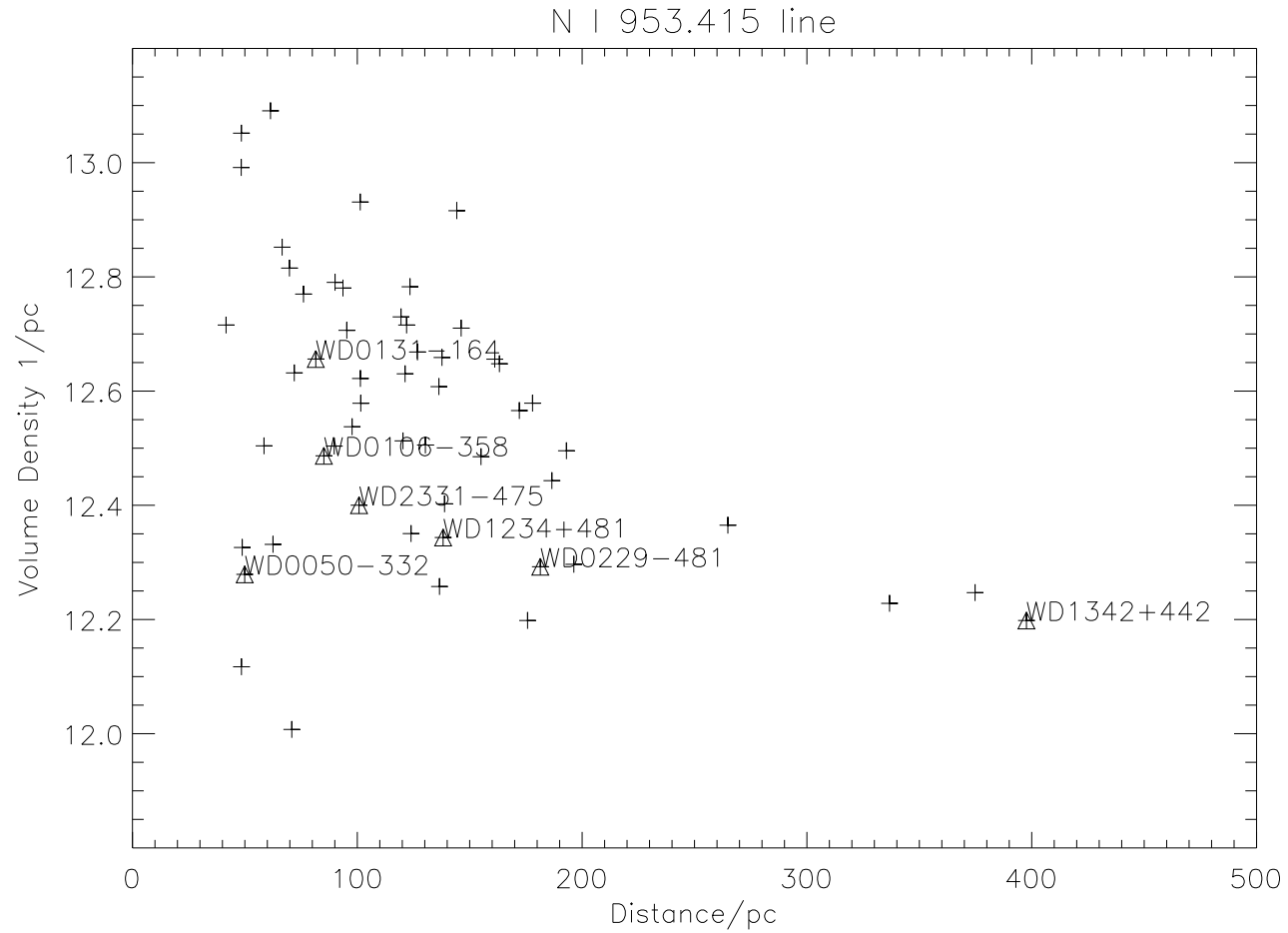


FIGURE 4.5. Polar latitude stars (-90 to -60 and 60 to 90 degrees). Distance uncertainties are given in Table 3.1 and volume density uncertainties given individually for each line measured (see for example Table 6.13). These are not plotted here to enable the labeling of data points.

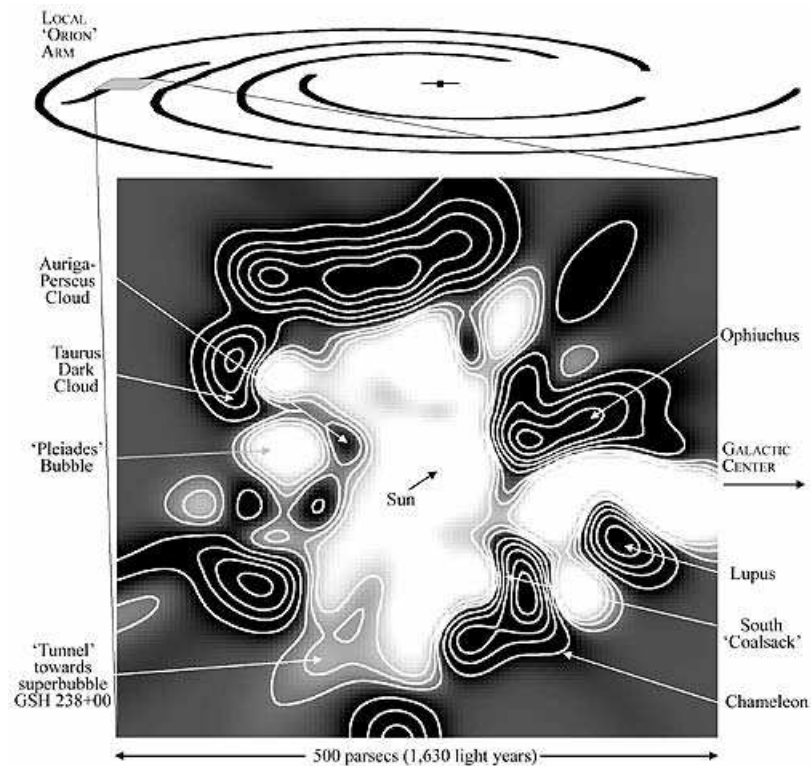


FIGURE 4.6. Lallement et al (2003) plot of cool gas in galactic latitudes. This visualization shows the density of cold interstellar gas in a lateral slice through 0 galactic latitude. Other Lallement plots used in this thesis represent slices along lines of galactic longitude and are thus planes at 90 degrees to this one.

The plots of (Lallement et al. 2003) (see Figure 4.6) provide approximate distances to the edge of the local cavity along any line of sight. In each slice the distance to the boundary can be measured with an uncertainty of several parsecs. For stars that fall between the discrete 15 degree planes, the boundary distance of the two planes either side will give, after linear interpolation, the distance to the boundary along the correct latitude. Dividing the distance of the stars in this sample by the boundary distance along each line of sight gives a scaled distance with the boundary wall at a distance 1. To show

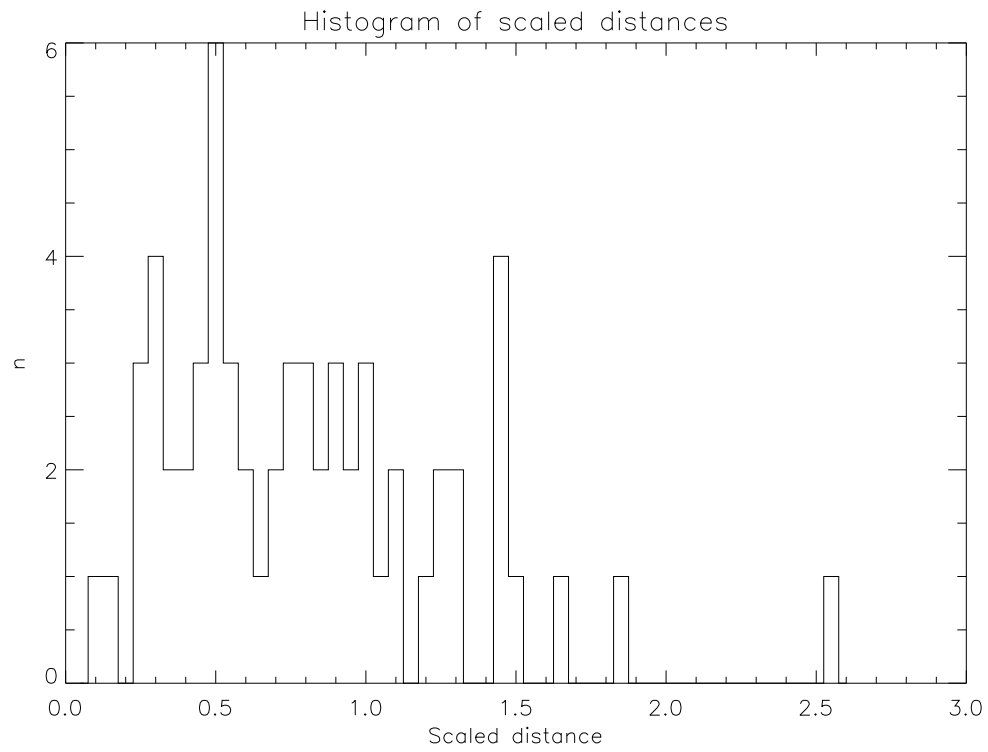


FIGURE 4.7. Histogram of scaled Lallement boundary distances

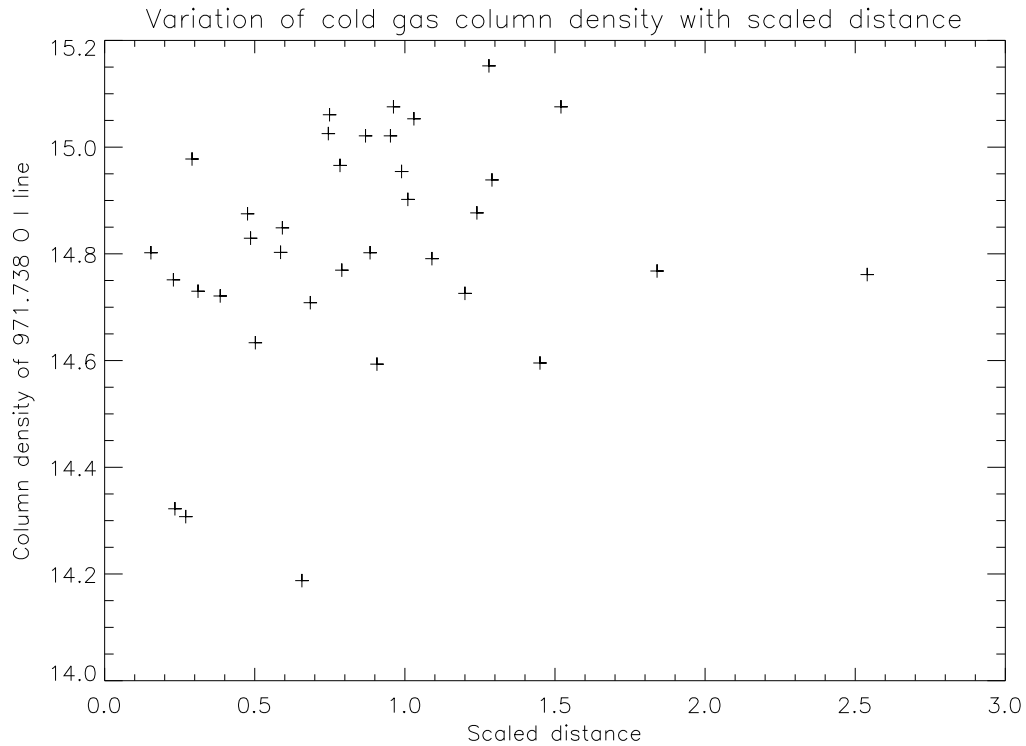


FIGURE 4.8. Amount of neutral 971.738 Å O I as a function of scaled distance

the distribution around the direction dependent boundary distance a histogram of these scaled distances is displayed in Figure 4.7.

Figure 4.8 shows the measured column densities of 971.738 Å O I compared to the scaled distances. As expected some lines of sight to stars within the cavity have a much lower column densities than those outside. Figure 4.8 also shows some stars within the cavity have a column density indicative of being outside. This is the result of compounding the uncertainty by interpolation between the 15 degree planes and also due to the heavy interpolation between the stars in the original Lallement et al. (2003) sample. It is therefore important for the consistency of this investigation that the position of a star relative to

the cavity wall is defined by the measured volume density along that line of sight rather than where the star appears in the maps of Lallement et al. (2003).

When trying to prove that O VI is detected towards more distant stars or towards those whose line of sight contain interface regions then examples can be found that agree, however, examples can be found both in agreement and out of agreement with this hypothesis. Any hypothesis could then be proven or disproven simply by the omission of evidence or by having a sample size so small or target selection so specific that only a well behaved subset of a seditious sample is studied. What is clear is that this evidence does not provide definitive proof for either the interface theory or its weaknesses. Despite this, this form of argument is the primary one used by literature up to this point. What appears to be happening is that unchecked photospheric contamination is distorting the picture. What is required is a way of identifying when contamination is effecting the result.

4.4 Velocity of the O VI line

Savage & Lehner (2006) state that the kinematical relationship between the absorption by O VI and other tracers of interstellar gas are important for evaluating the origin of the O VI. If the O VI is produced at interfaces then the O VI should share a common velocity with the cold gas. No correlation with the cold gas would indicate that the O VI is formed in bubbles, though the relative narrowness of the lines suggest that the hot gas does not occupy the entire line of sight. The final explanation, and one they miss, is that

if the O VI shares a common velocity with the background star then it probably isn't in the interstellar medium at all.

Savage & Lehner (2006) found that a large number of the $v_{OVI} - v_{CII}$ measurements have a positive offset. Their plot of v_{OVI} vs v_{CII} looks remarkably similar to their plot of v_{phot} vs v_{ism} with the O VI lines always measured at a larger velocity than the interstellar lines. Their first possible explanation given for this anomaly is that evaporative flows of hot oxygen ions are seen fleeing as the bubble expands. Alternately they suggest that the O VI is made up of multiple components, some of which have no associations with the cool gas. However, this does not necessarily explain why the offset is always positive.

The possibility that the observed O VI originated in the photosphere of the background star was not completely dismissed. Models created by Oegerle et al. (2005) indicated that the atmosphere of a star could produce O VI if it was hot enough and if the oxygen abundance was high enough. This dependence on the oxygen abundance allows the line profile of O VI to be different in two stars of similar temperature. To characterise the oxygen abundance in the star requires the measurement of other oxygen lines, where there is no chance of interstellar contribution. Although the FUSE range is rather sparse when it comes to oxygen lines the O IV $\lambda 1338.6121$, O IV $\lambda 1343.5120$ and O V $\lambda 1371.2920$, found in the IUE NEWSIPS SWP Echelle Data Set (Holberg et al. 1998), can be used for those stars that overlap both samples. Chayer et al. (2006), however, point out the impracticalities of this by showing that in order to reduce the modeled opacity in the EUV range to that observed, the abundance of oxygen in the lower O III and O IV re-

gions of the atmosphere must be set to a lower value than in the outer atmosphere. This is important for O VI as it is produced in the outermost atmosphere, whereas the O III and O IV lines are formed lower where oxygen is less abundant.

Difficulties aside, the question of whether a hot star actually lacks the O VI lines could be determined through this diagnostic technique. Care must be taken, however, since there is evidence to suggest that abundance and temperature are not the only factors that effect the strength of a photospheric line. IUE and HST data of DA white dwarfs show that high temperature species, such as N V, can appear in the photosphere of relatively cool white dwarfs (Holberg et al. 2000). What is clear is that the assumption that a high ionization species in a cool star must always be interstellar is no longer valid. This problem arises when a cooler star displays a strong O VI line. The extremes of this include the star and WD1254+223 (see Figure 4.11) which are reported to be too cool to produce O VI. WD1254+223 has no photospheric lines and very few interstellar lines due to its proximity. By fitting a single Gaussian line profile to this O VI line we can deduce a two sigma detection but upon visual inspection this line appears to be greatly influenced by a single sharp peak that could be a badly placed noise spike. Other observations of this star show a weaker line if any but these spectra are of poorer signal to noise.

Assuming that the feature in WD1254+223 is an O VI line, a photospheric origin becomes difficult to explain. The oxygen abundance could be so high that only the oxygen lines themselves could be detected above the noise. Since the $\lambda 1031.912$ O VI line has the strongest atomic oscillator strength of all the high ionisation oxygen lines the first

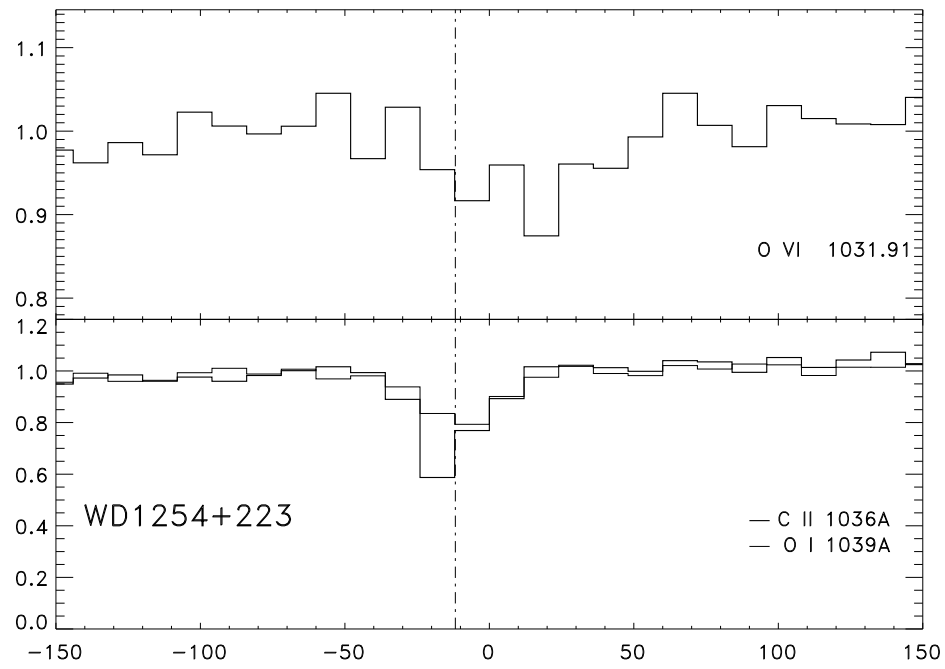


FIGURE 4.9. Plot of the O VI line profile compared to C II and O I line profile

line of oxygen to become visible would be the the $\lambda 1031.912$ O VI line. Therefore, it is physically possible to observe this line in a star that displays no other photospheric line. Another problem comes from the lack of reference lines. With no other photospheric lines it is impossible to compare the O VI line to the photospheric velocity. The point is that, when O VI is on the boundary of obscurity and there are no photospheric lines we have no way of testing whether the O VI is photospheric or not. The evidence provided by these objects is omissible since at this point in time we have no way of deciphering its root cause. This however, can not be the explanation for all the objects that show this. In this investigation these are referred to as ambiguous detections.

In those stars that do have an identifiable photospheric velocity we can test if the velocity of the O VI line follows that of the star. The fact that the average positive offset happens to be very similar to the average photospheric velocity seems a little too convenient. A test of its validity would be to closely examine stars of different photospheric velocity and observe the correlation with the velocity of the O VI line. If the positive offset phenomenon has nothing to do with the background stars then there should be no correlation with the photospheric velocities of those stars. If however the observed O VI is entirely or partially the result of photospheric O VI then a correlation is expected.

Another factor that needs attention is the strength of the O VI line. If the line is very narrow, then the velocity uncertainty will be quite high since the superposition of random noise can change the result entirely. If the line is shallow and broad the velocity uncertainty again increases. This is due to an uncertainty relating to the difficulty in exactly

locating centre and the horizontal extremities of the line. The velocity of these lines are also much more sensitive to the fitted continuum level. In previous studies it appears that the width of the line has been measured from manually locating the line's extremities. For shallow lines this process allows too much freedom in choosing where the line begins and where it ends. The measured widths will err towards the expected since the manual selection is looking for a certain result. Another problem is that a slight overestimation in the width of the line will greatly increase the equivalent width (since this is a measure of area and very sensitive to the width of the fitted Gaussian) and hence the significance of the detection. Some very shallow lines measured in previous works are reported to have a very large significance that upon visual inspection seem rather unlikely.

One further issue with this analysis is that of the false positive. If the O VI line is a combination of photospheric and interstellar contributions and if the photospheric contribution is significantly larger than the interstellar contribution then in a velocity analysis the contribution from the interstellar medium may not be visible. If one component is sometimes much stronger than the other then a selection by quality may reject all the results that contain the smaller component. If the larger peak is photospheric it is possible to reject ISM detections because the line is significantly poorer.

The analysis therefore needs to be two fold. Initially the positive offset has to be tested. To do this requires the measurement of the O VI line velocity and compare it to the photospheric velocity. If the established evaporative flow theory is correct then the positive offset will not have moved from one position to another when compared to another star

of different photospheric velocity. If a velocity shift is detected then the conclusion will be that there is at least some photospheric contribution to the line. Given that previous studies have already identified stars with suspected photospheric contribution this study will be supplemental. What it will do is examine more closely those stars where no previous photospheric contribution has been observed.

Upon quantifying the amount of stellar absorption contributing to the O VI line the following step is to quantify the ISM contribution and to find those lines of sight with an unambiguous ISM line. This can be done by searching in the cases where the photospheric contribution can be differentiated from an ISM detection. For example in those stars where the photospheric velocity is high enough to shift the photospheric O VI line far enough to allow the ISM O VI line to become visible. Measurements of the ISM column density in those stars where the ISM contribution is either distinguishable or completely absent will provide the only unambiguous measure of the amount of hot gas in the LISM. Measurement of ISM column density from those stars with a non distinguishable photospheric contribution, or an O VI line in the absence of other photospheric lines is slightly more ambiguous. Nevertheless it is still useful as an indication of the hot gas contribution.

4.5 Results of velocity analysis

A plot of the measured O VI line velocity against the average interstellar medium velocity is presented in Figure 4.10. The first thing to note is that there is indeed a positive

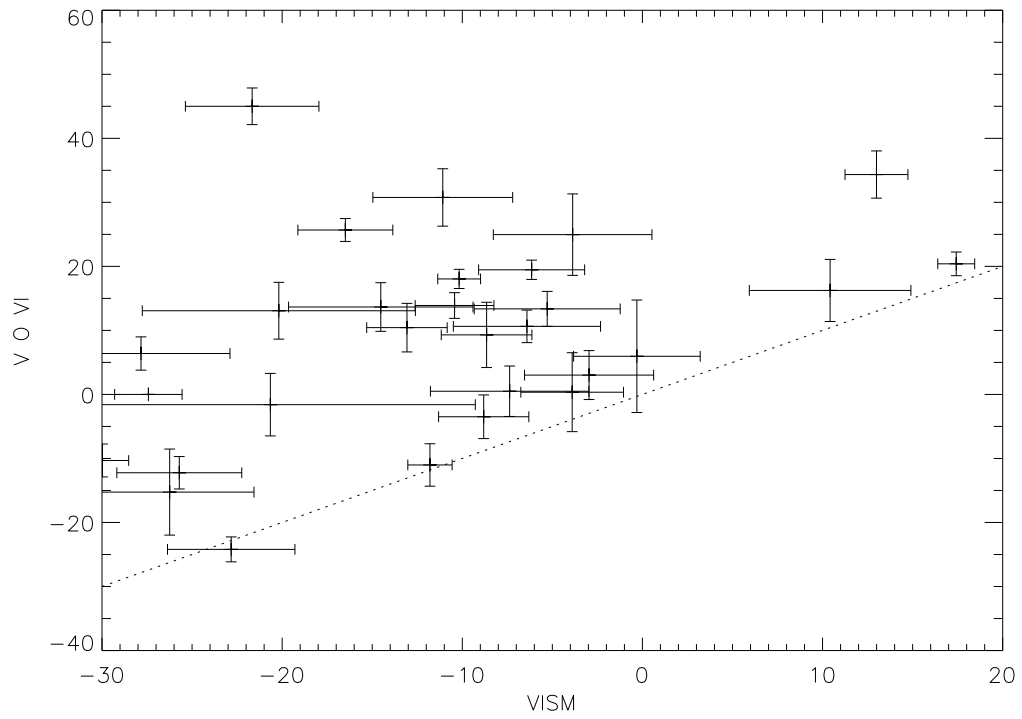


FIGURE 4.10. Velocity of the O VI line compared to the interstellar velocity. The line of $V(\text{O VI})=V(\text{ISM})$ is also plotted

offset in some detections. Conversely there is very little offset in others. On this basis we can describe the detections as falling into two categories.

4.5.1 Stars with no offset

The first category contains those stars where the O VI line does seem to have the similar velocity as the ISM in that direction. The stars WD0004+330, WD0027-636, WD0229-481, WD0232+035, WD0252-055, WD0501+524, WD1611-084, WD1950-432 and WD2331-475 all have an $v_{ISM} - v_{OVI} < 10$ km/s. To determine if these detections are interstellar requires comparing this result to the $v_{ISM} - v_{phot}$. If the detected O VI line occupies the $v_{ISM} - v_{OVI} < 10$ km/s position in a star with a $v_{ISM} - v_{phot} < 10$ km/s is clearly of no use to this investigation since both components are unresolvable. If however $v_{ISM} - v_{OVI} < 10$ km/s in a star with a $v_{ISM} - v_{phot} > 10$ km/s then it is likely that the measured line originated in the ISM. This case is the one where the photospheric lines are shifted enough to discount photospheric contamination.

4.5.2 Notes on candidate suitability

WD0004+330 is unsuitable for this analysis since v_{phot} is poorly known. The measurement is based upon a weak C III line and a Si IV line that has an odd flat bottomed profile. This star does not help this analysis. The photospheric lines of WD0027-636 are also too few to deduce anything definitive. WD0229-481 is a good example of a star with $v_{ISM} - v_{phot} > 10$ km/s and has a well defined v_{phot} . All indications show that the

feature at $\lambda 1031.9325$ originated in the interstellar medium. WD0232+035 is unusual as it has a $v_{phot} < v_{ism}$. Despite this it does have a well defined and resolved v_{phot} . The O VI line is seen at the ISM velocity for this star. In this star it is noted that very little cool gas is seen in the line of sight due to relative proximity of the star. The star WD0252-055 has a $v_{ISM} - v_{phot} < 10$ km/s and so is unsuitable. WD0501+524 also has a $v_{ISM} - v_{phot} < 10$ km/s. WD1611-084 also has a $v_{phot} < v_{ism}$ and does have a sizable O VI line at the ISM velocity though $v_{ISM} - v_{phot}$ is only just large enough to discriminate between the two. The photospheric lines of WD1950-432 are also too few to deduce anything definitive. WD2331-475 does have $v_{ISM} - v_{phot} > 10$ km/s and the O VI line is seen at the ISM velocity.

In conclusion the stars WD0229-481, WD0232+035 and WD2331-475 have an O VI line that appears unambiguously to originate in the interstellar medium. The significance of the detections is 1.5, 5.8 and 5.5 sigma detections respectively. The column densities derived for these results are 12.59 ± 0.65 , 12.73 ± 0.17 and 12.93 ± 0.17 respectively. Interestingly all three stars are high latitude stars and by comparison with and Figure 4.5 and Figure 4.6 not on the other side of an interface region.

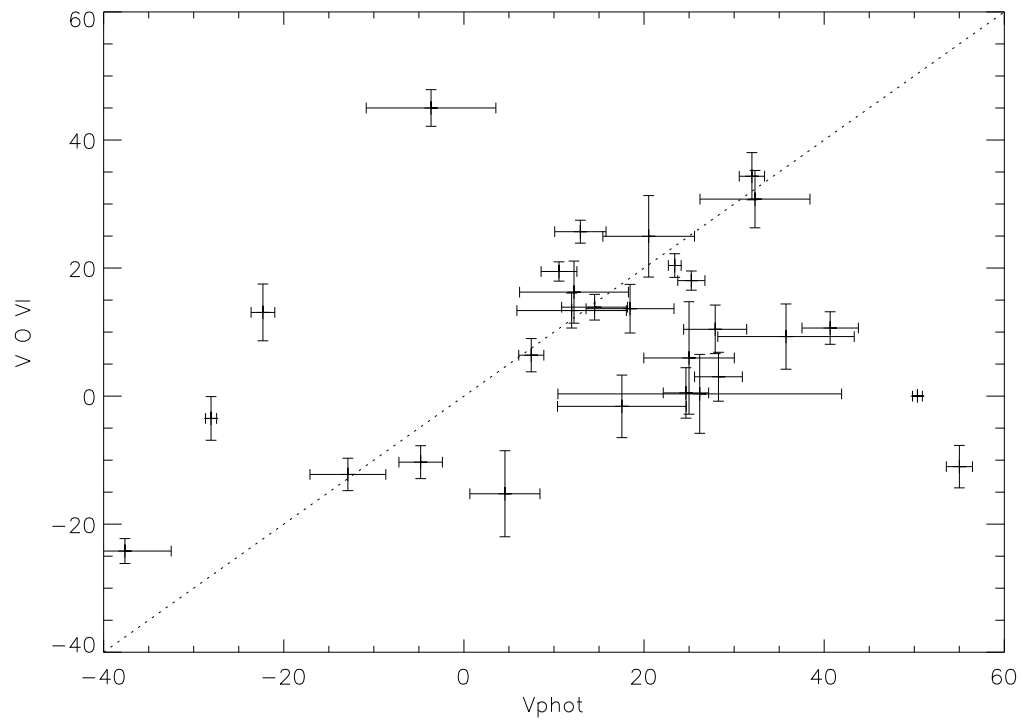


FIGURE 4.11. Velocity of the O VI line compared to the photospheric velocity

4.5.3 Stars with a positive line velocity

Looking at the second category of stars in Figure 4.10 (the positive offset stars) we can now examine the origin of the offset phenomenon. The simple question that we are trying to answer is whether the O VI detection sit at a positive velocity independent of the photospheric velocity or conversely is it dependent on the photospheric velocity. The degree of velocity offset in Figure 4.10 shows significant scatter. It appears that the v_{OVI} is largely independent of v_{ISM} . Figure 4.11 is a plot of v_{OVI} against v_{phot} and it quite clearly shows that of those stars that have a positive offset this offset has the value of the photospheric velocity of the star. This suggests that the positive velocity offset is entirely due to photospheric contamination.

4.5.4 Stars with non photospheric v_{OVI} offset

The final category that deserves attention is the four stars that have v_{OVI} in excess of their photospheric velocities. These are WD0232+035, WD1040+492, WD1611-064 and WD2111+496. The stars WD0232+035, WD1611-064 and WD2111+496 can simply be explained as those stars where $v_{phot} < v_{ism}$ and so on Figure 4.11 the positive offset of these stars show up on the other side of the line of $v_{phot} = v_{OVI}$. WD1040+492 on the other hand has a $v_{phot} > v_{ism}$ but can be explained by how poorly the photospheric velocity is known in that star.

Chapter 5

Interpretation

5.1 Hot gas

The subject of this thesis is to locate the origin of the $\lambda 1031.912$ O VI line. Since this line is used as a tracer of hot gas in the interstellar medium it is of key importance to our understanding of the state of the ISM. Previous to this work the ISM was considered to be occupied by three different phases of gas. The cold and warm phases occupy space together and form the basic building block of all stellar and planetary matter. The hot phase is produced by violent processes, such as supernova, that excite and ionise the cold phase. The interaction between the hot phase and the cold phase results in the O VI seen along the line of sights of hot local stars, i.e. white dwarfs.

According to theory, boundary or interface regions are the only places where O VI should be formed locally. The nearest boundary region to the sun is a collar of higher density cold gas that exists in the plane of the galaxy. From studies of the SXRb the cavity

in which the sun is located is drawn as an hourglass shape, with its long axis co-axial with the galactic poles (Snowden et al. 1998). These elongations coincide with gas free chimneys observed by Sfeir et al. (1999) and Welsh et al. (1999). Sensitive absorption line measurements by (Lallement et al. 2003) show that the X-ray picture is a rather averaged out view of what appears to be a complex interconnection of loops and voids. The general shape of the hour glass remains, but in the absorption line analysis the hour glass is open ended. The smooth featureless wall is replaced by a complex mix of bubbles and other disturbances. This changes our view from an isotropic bubble, to a turbulent mix of pressures and competing processes all out of equilibrium. Globally the structure resembles a tunnel through the galaxy, with its narrowest point roughly at the location of the sun.

The assumption that the local bubble is occupied by hot gas originated from the primitive picture of the local bubble being a spherical shell created by a supernova. At the time the available evidence from the SXR and from O VI lines fitted this theory. The observation of the supernova remnant called Loop 1 in soft X-rays led scientists to conclude that the ubiquitous soft X-ray background was such a shell observed from within. Now that the local bubble is considered to be one of a series of interconnecting bubbles and tunnels with a major opening toward the galactic poles the question is, should we still expect it to be full of hot gas? The density of the cavity wall is the result of the pressure from both the expansion of the local cavity and the pressure of the external environment resisting this change. In the direction of the galactic center the cavity wall is more dense due to the compression of the gas trapped between the local cavity and the Loop 1 structure. In

such a direction there is not a single interface but two.

The difficulties that arise are two fold. Firstly there is the argument that O VI is "patchy", that suggests that in some lines of sight, the thermal conditions required to produce O VI are quenched by magnetic fields (Cox & Helenius 2003). This allows for two otherwise identical lines of sight to vary significantly in O VI. The second problem is the unknown amount of photospheric O VI adding to the detection. This also has the potential to make two identical lines of sight vary significantly. Further more this contribution is dependent on both stellar temperature and oxygen abundance. This allows two stars of the same temperature to display different amounts of O VI.

A mere detection of O VI is not evidence of hot interstellar material. Every detection could be the result of, or contributed to by, a stellar O VI line. This investigation attempts to remove this ambiguity by choosing O VI detections where a stellar contribution can be ruled out. We look for stars where the photospheric lines, when present, are separated in velocity space from the interstellar material. Of an original sample of nearly 100 stars, O VI is only detected in 44 stars. The only statistical difference between the stars that have an O VI line and those stars that do not have one is that those that have one are slightly hotter than those without. For example the average temperature of those stars that show an O VI line is 47000K whereas the average temperature of those stars with no O VI line is 38000K. This difference results from the contribution of photospheric O VI in the hotter stars to the total O VI profile. Other than temperature the sample of non detections is similar to the sample of detections.

5.2 Unambiguous ISM detections

Of the original 100 stars 44 have an O VI detection and 48 have a velocity reference for the photosphere. However a star with a velocity reference for the photosphere may not have an O VI line. In some of these cases the velocity for the photosphere is known with more certainty than in others. See Table 5.1

Table 5.1: Stars with a velocity reference for the photosphere. Velocities are not corrected to any frame of reference

Name	$v_{ISM}/km/s$	$v_{phot}/km/s$
WD0001+433	-3.93	29.80
WD0004+330	-11.79	55.00
WD0027-636	-7.37	24.65
WD0041+092	-25.06	29.35
WD0050-332	-14.52	18.44
WD0106-358	-23.19	12.37
WD0111+002	-29.14	21.96
WD0131-164	-6.14	10.55
WD0226-615	-8.65	35.76
WD0229-481	-0.30	24.99
WD0232+035	-8.81	-28.07
WD0252-055	10.42	12.22
WD0501+524	17.42	23.41
WD0512+326	-3.87	20.51
WD0549+158	1.44	8.207
WD0621-376	12.99	31.97
WD0802+413	13.45	6.942
WD1019-141	-6.60	11.53
WD1021+266	-5.28	11.96
WD1029+537	-16.49	12.93
WD1040+492	-21.66	-3.65
WD1337+701	-12.05	-17.23
WD1342+442	-25.71	-12.88
WD1603+432	-51.32	22.77
WD1611-084	-22.83	-37.64
WD1634-573	-29.97	-4.80
WD1635+529	-22.54	0.17
WD1711+668	-26.33	21.26

Table 5.1

Name	$v_{ISM}/km/s$	$v_{phot}/km/s$
WD1734+742	-23.04	-2.18
WD1800+685	-35.38	-4.86
WD1819+580	-27.08	-13.74
WD1844-223	-34.25	5.04
WD1917+599	-29.34	3.06
WD1921-566	-30.10	-11.42
WD1942+499	-27.84	7.48
WD1950-432	-3.89	26.18
WD2000-561	-26.24	4.55
WD2011+398	-10.43	14.51
WD2111+498	-20.18	-22.32
WD2116+736	-17.47	-29.57
WD2124+191	-23.24	29.71
WD2146-433	-13.07	27.89
WD2211-495	-10.17	25.25
WD2257-073	-11.08	32.32
WD2309+105	-27.43	50.35
WD2321-549	-20.66	17.54
WD2331-475	-2.96	28.26
WD2350-706	-6.41	40.66

The stars WD0229-481, WD0232+035 and WD2331-475 all show an O VI line at the correct velocity for the interstellar medium (see Figures 5.1 to 5.3) whilst having a photospheric velocity both known and separated enough to rule out any photospheric contamination to the O VI line. Figure 5.9 to Figure 5.14 is a diagram of spatial position prepared by Barstow, et al (2008). This diagram shows the positions of these stars superimposed onto the data of Lallement (by private communication). Though the annotations of the diagram are difficult to read, the star WD0229-481 is plotted on the 2nd left hand diagram as the longest line of sight in the bottom left quadrant. WD0232+035 appears

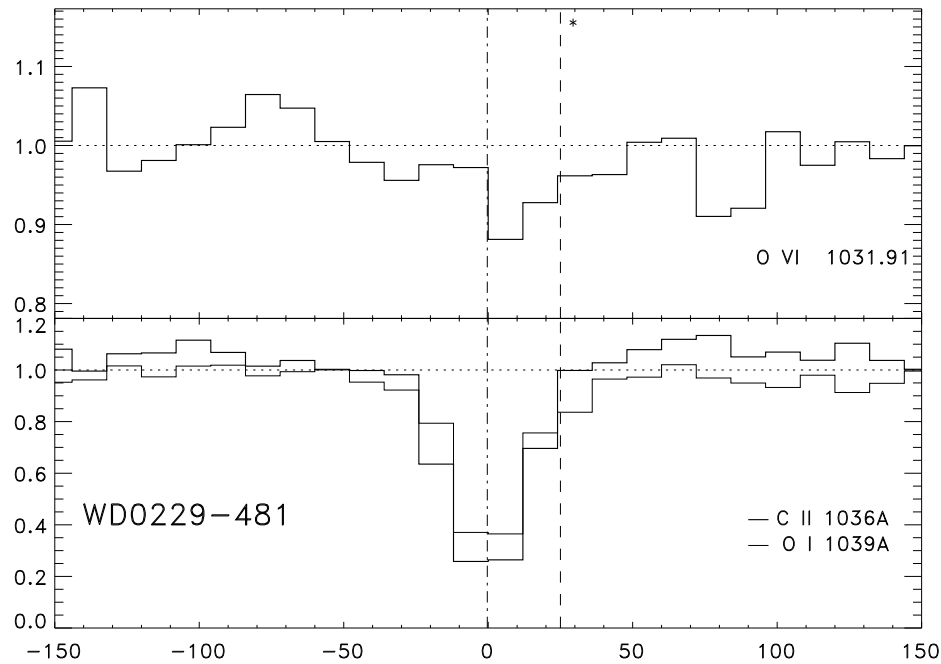


FIGURE 5.1. WD0229-481 displays an O VI line at the interstellar medium velocity. It is classed as an unambiguous interstellar detection because this spectrum has a reliably known and resolvable photospheric velocity. Plot of normalised flux against velocity in km/s

in the bottom right quadrant of the 3rd left hand diagram. WD2331-475 Appears on the same diagram in the bottom left hand quadrant. These lines of sight all fall towards the south galactic axis and do not intersect with an interface region.

This does not rule out that O VI lines could be unambiguously observed in lines of sight that do contain an interface region but to this point there is no evidence for this. It appears from this evidence, however, that the boundary wall is unimportant in the formation of O VI.

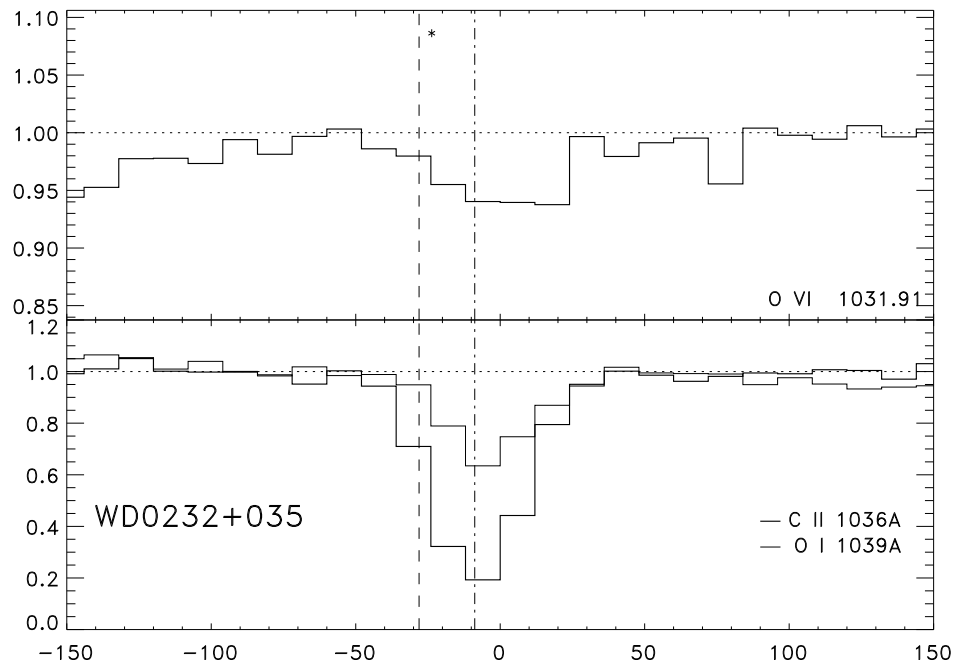


FIGURE 5.2. WD0232+035 displays an O VI line at the interstellar medium velocity. It is classed as an unambiguous interstellar detection because this spectrum has a reliably known and resolvable photospheric velocity. Plot of normalised flux against velocity in km/s

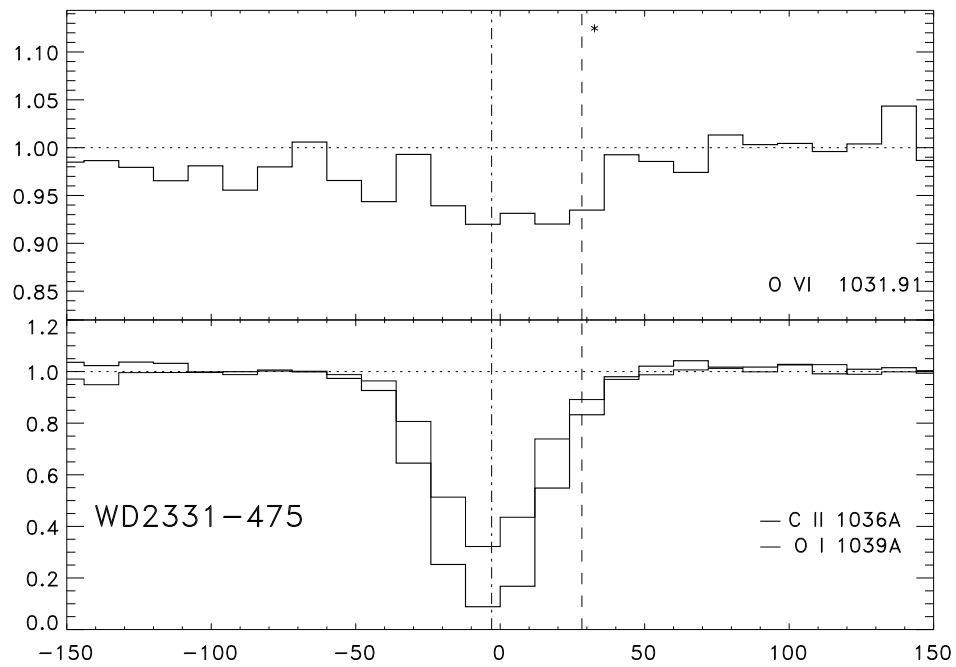


FIGURE 5.3. WD2331-475 displays an O VI line at the interstellar medium velocity. It is classed as an unambiguous interstellar detection because this spectrum has a reliably known and resolvable photospheric velocity. Plot of normalised flux against velocity in km/s

5.3 Ambiguous ISM detections

Table 5.2: Stars without a velocity reference for the photosphere

Name	$v_{ISM}/km/s$
WD0114-027	-8.018
WD0147+674	-15.47
WD0235-125	13.73
WD0236+498	-4.49
WD0310-688	36.46
WD0320-539	6.23
WD0325-857	-10.15
WD0346-011	15.29
WD0353+284	8.41
WD0354-368	8.67
WD0416+402	-0.05
WD0421+336	49.98
WD0455-282	38.66
WD0457-103	-4.99
WD0603-483	18.58
WD0659+130	-0.29
WD0715-704	-4.80
WD0809-728	-6.34
WD0830-535	9.36
WD0905-724	12.63
WD0937+505	-5.073
WD1024+326	-13.96
WD1041+580	-10.43
WD1056+516	-12.72
WD1057+719	-16.14
WD1109-225	-4.85
WD1234+481	-9.59
WD1254+223	-11.78
WD1302+597	23.87
WD1314+293	-16.13
WD1440+753	-13.73
WD1528+487	-27.33
WD1550+130	-9.89
WD1615-154	-68.31
WD1620+647	-28.82
WD1631+781	-6.90
WD1636+351	-31.08
WD1648+407	-28.66

Table 5.2

Name	$v_{ISM}/km/s$
WD1725+586	-16.60
WD1736+134	12.068
WD1845+683	-28.16
WD2004-605	-27.79
WD2014-575	-29.81
WD2020-425	-25.39
WD2043-635	-36.91
WD2123-226	50.88
WD2124-224	-28.42
WD2152-548	-3.92

Of those stars without a velocity reference for the photosphere there are stars that display O VI without displaying photospheric lines. The argument has been made that this could be the result of oxygen abundances etc but it is unlikely that this is the case for all of these stars. As a result we will treat them all as detections but refer to them as "ambiguous detections" so that we do not confuse them with WD0229-481, WD0232+035 and WD2331-475 for which we are certain of no contamination. The stars WD1725+586, WD1057+719, WD1040+492, WD1314+293 and WD1254+223 all display an O VI line in the absence of good photospheric features.

WD1725+586 is a mid latitude star about 170 parsecs away. Its position on the plots of cold gas volume density against distance makes it difficult to determine which side of the local cavity boundary it is, though it is quite likely to be on the inside. WD1057+719 is a mid latitude star about 120 parsecs away. Its position on the plots of cold gas volume density indicates that this star is within the cavity. WD1040+492 is a mid to high latitude star about 260 parsecs away. This star falls in a direction where uncertainty over the distance to the cavity wall is high. WD1314+293 is a high latitude star about 51 parsecs away. Its position on the plots of cold gas volume density indicates that this star is within the cavity. WD1254+223 is a high latitude star about 64 parsecs away. Its position on the plots of cold gas volume density indicates that this star is within the cavity. The profiles of these lines are presented in Figures 5.4 to 5.8.

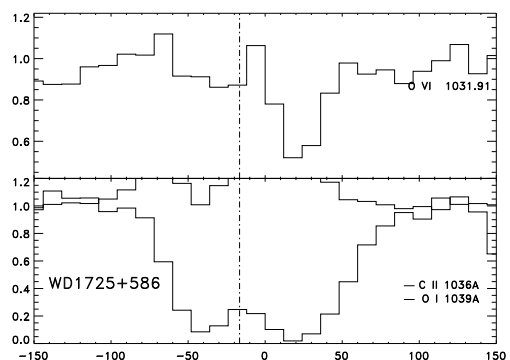


FIGURE 5.4. Plot of the O VI line profile compared to C II and O I line profile

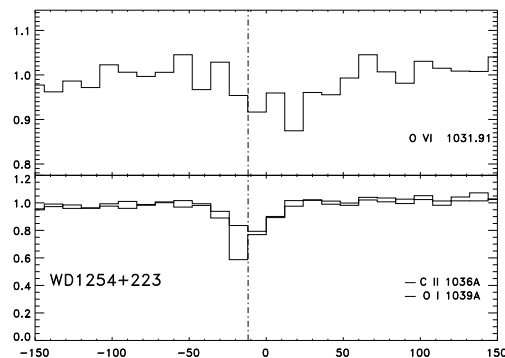


FIGURE 5.7. Plot of the O VI line profile compared to C II and O I line profile

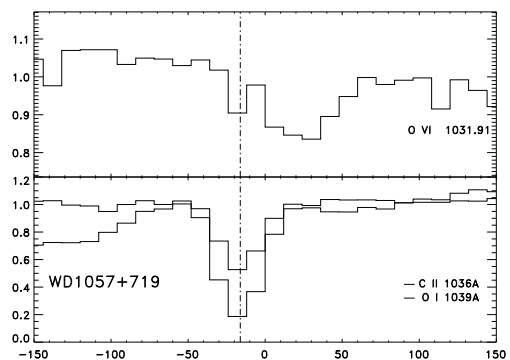


FIGURE 5.5. Plot of the O VI line profile compared to C II and O I line profile

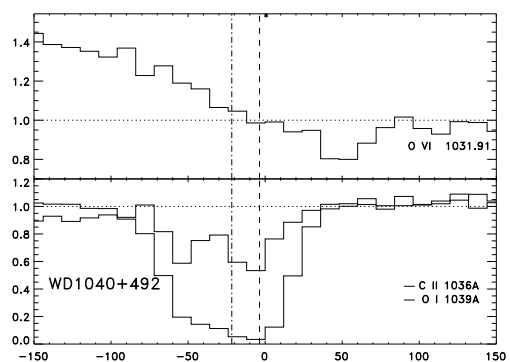


FIGURE 5.6. Plot of the O VI line profile compared to C II and O I line profile

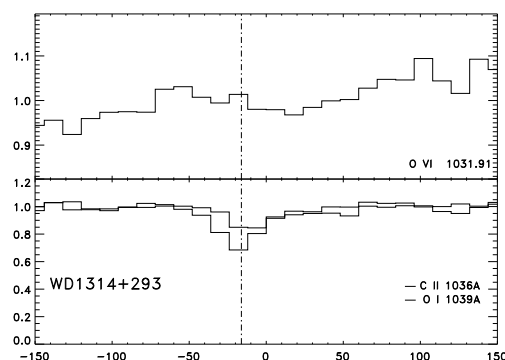


FIGURE 5.8. Plot of the O VI line profile compared to C II and O I line profile

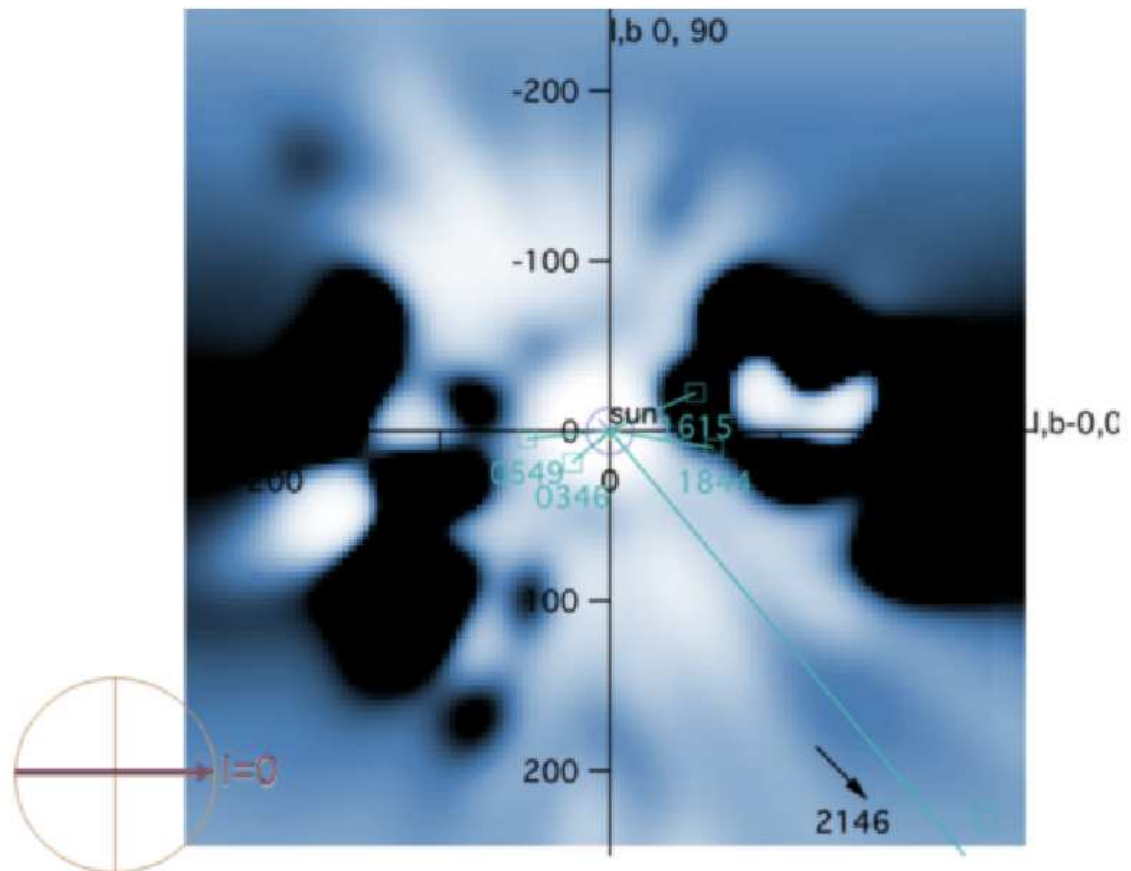


FIGURE 5.9. The position of stars in this sample compared to the cold gas phase. Dark regions represent regions larger gas density. The lighter region in the center shows the lateral extent of the local cavity. This diagram represents a slice along the 0 degree line of galactic longitude. To the right is the galactic center, with the galactic poles at the top and bottom of the plot.

Figure 5.15 shows that as the amount of hot gas increases there is generally more cold gas present as well. WD0229-481 appears, based on this rough relationship, to have an over abundance of O VI whilst WD1725+586 appears to be under abundant in O VI. An overabundance could easily be the result of stellar contamination whereas an under abundance is more likely to be a real ISM phenomenon. Most simply this under

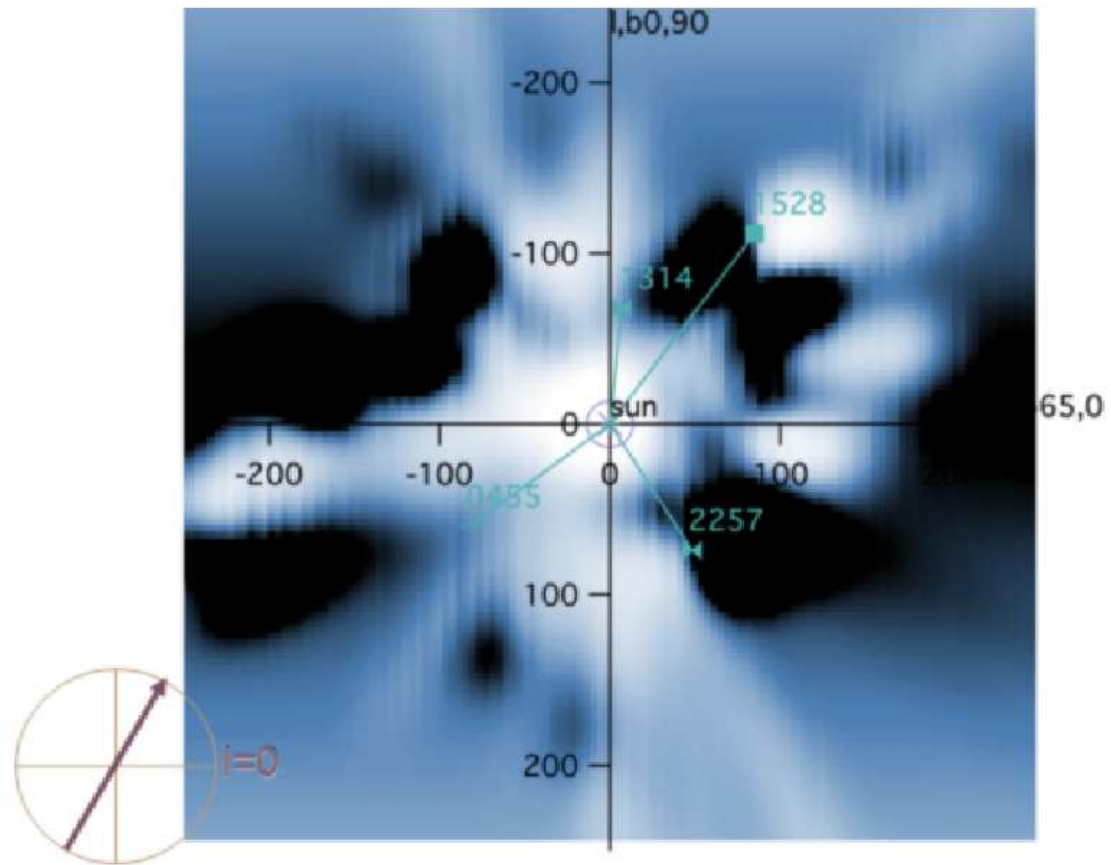


FIGURE 5.10. The position of stars in this sample compared to the cold gas phase. This diagram represents a slice along the 65 degree line of galactic longitude.

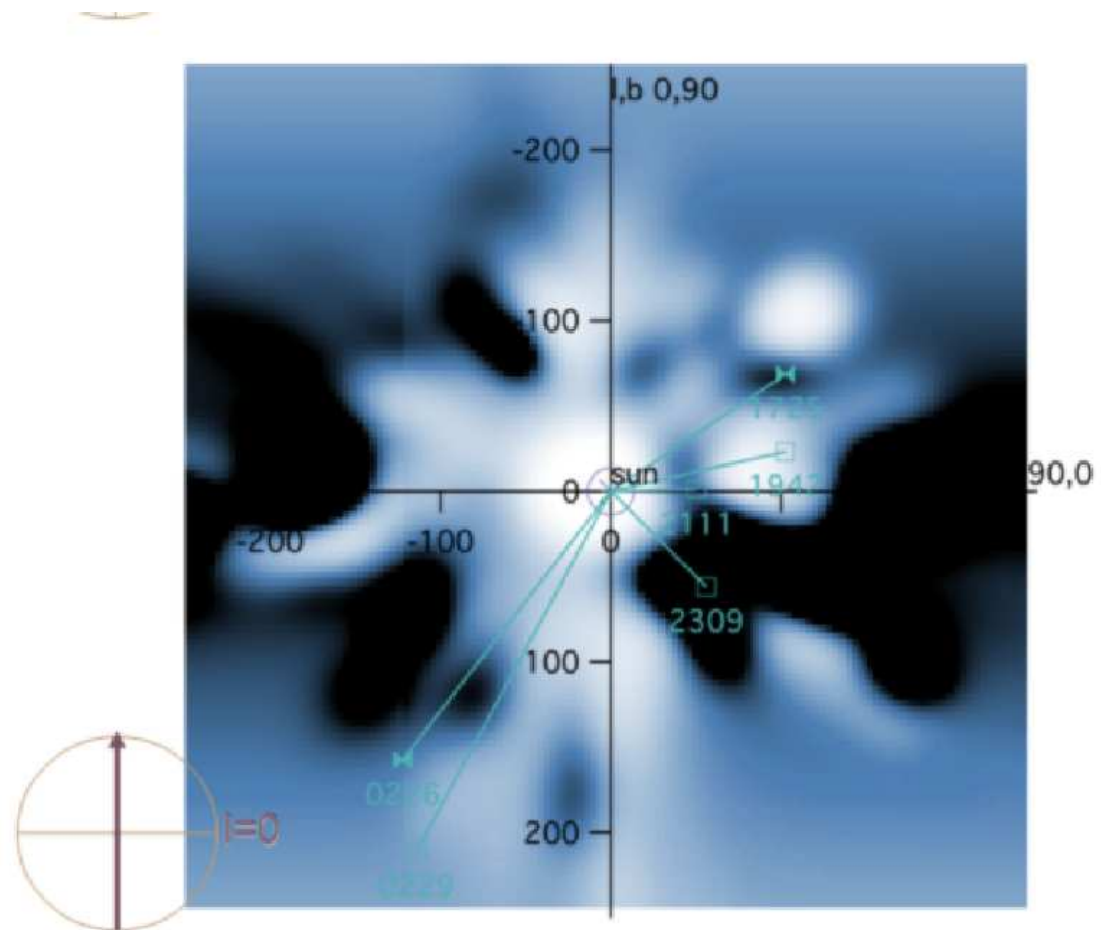


FIGURE 5.11. The position of stars in this sample compared to the cold gas phase. This diagram represents a slice along the 90 degree line of galactic longitude.

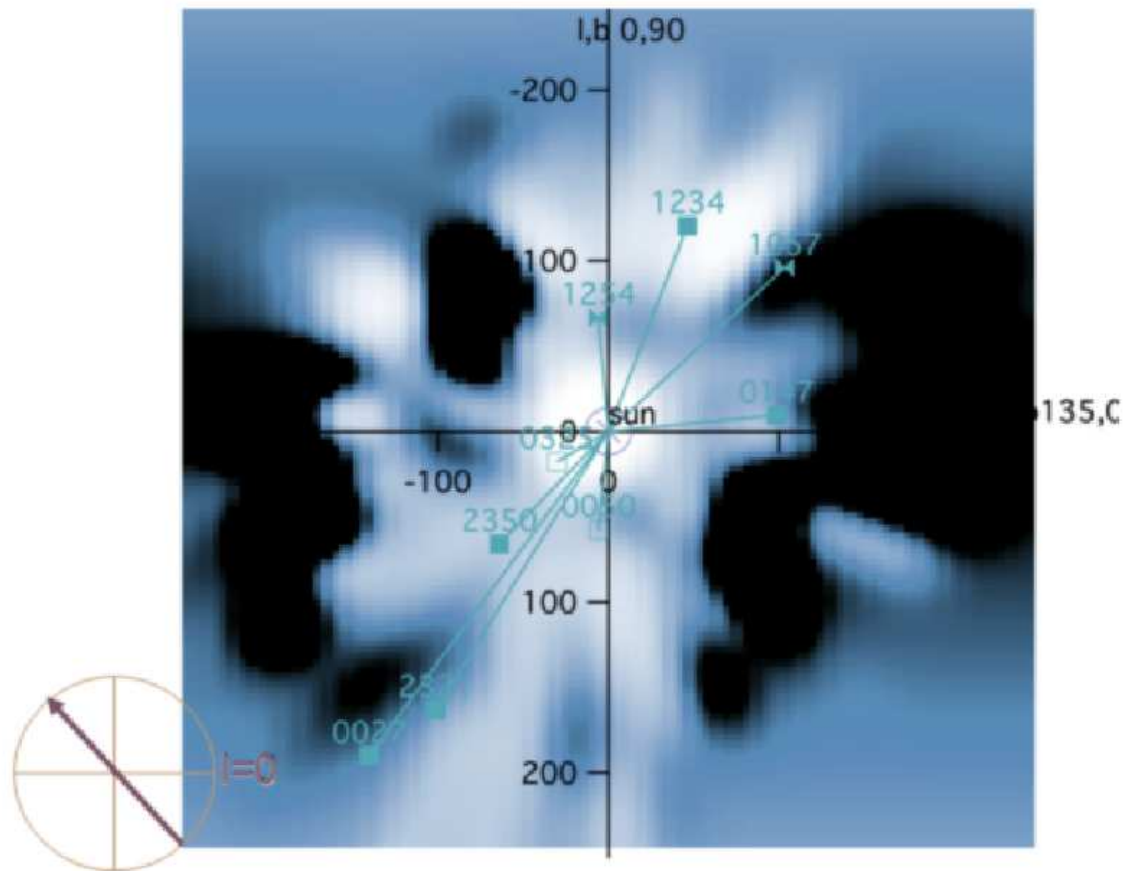


FIGURE 5.12. The position of stars in this sample compared to the cold gas phase. This diagram represents a slice along the 135 degree line of galactic longitude.

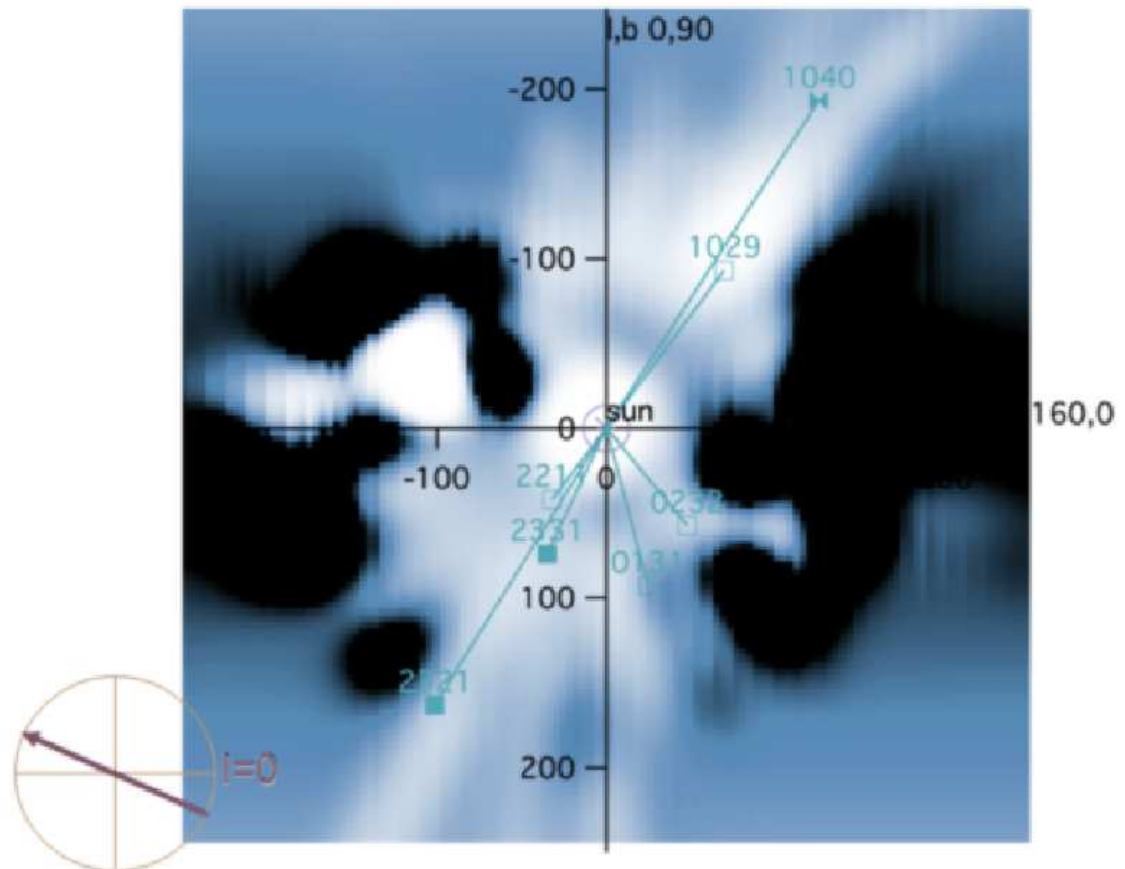


FIGURE 5.13. The position of stars in this sample compared to the cold gas phase. This diagram represents a slice along the 160 degree line of galactic longitude.

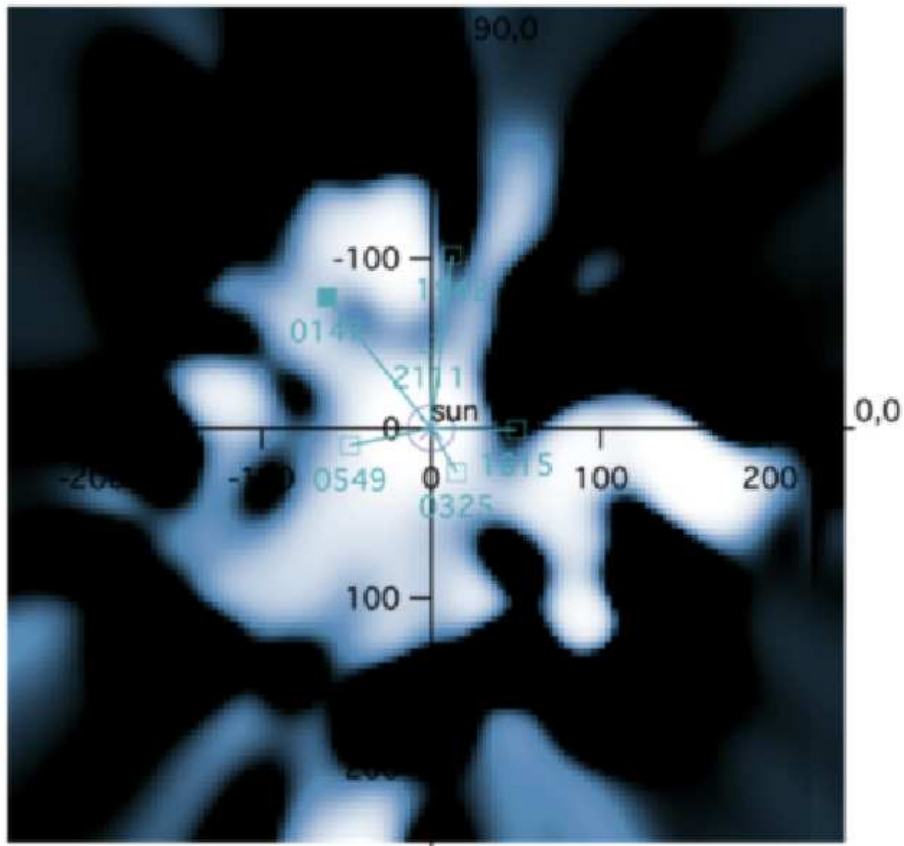


FIGURE 5.14. The position of stars in this sample compared to the cold gas phase. This diagram represents a slice along the 0 degree line of galactic latitude.

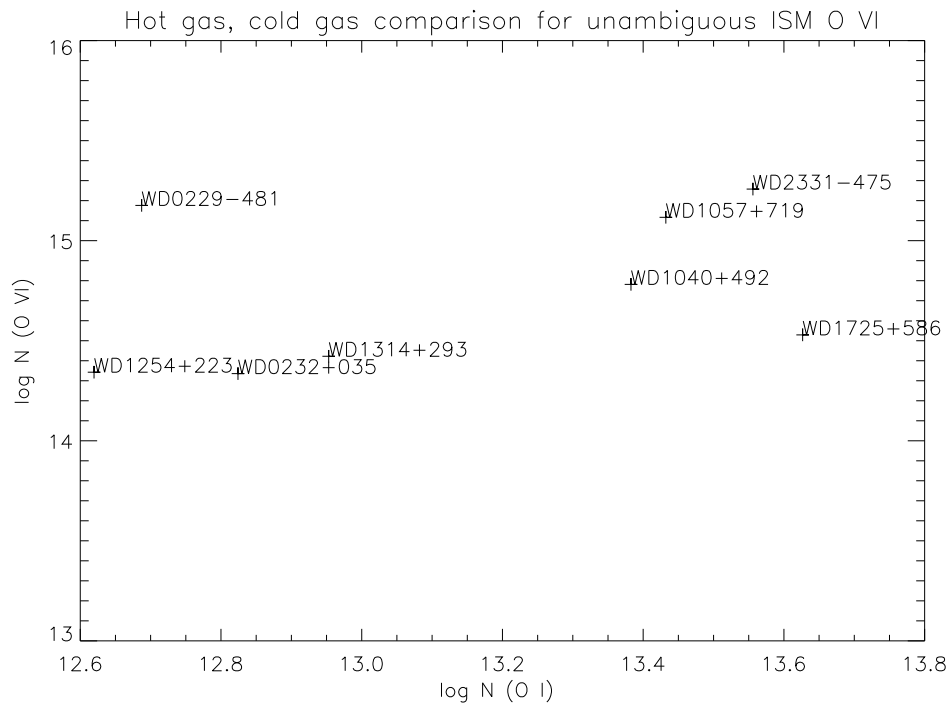


FIGURE 5.15. Comparison of the column density of O VI compared to O I for all the ISM and ambiguous ISM O VI detections.

abundant result could be a region that is both far away and in a particular line of sight with not much hot gas. This difference is the first evidence of morphological differences in the hot gas presented in this work.

5.3.1 Summary

The following tables divide the stars into three categories depending on whether ISM O VI was detected or whether the detection was ambiguous or thirdly, if no O VI was detected at all.

Table 5.3: Summary of ISM detections

Name	Detection type
WD0229-481	Detection
WD0232+035	Detection
WD1040+492	Detection
WD1057+719	Detection
WD1254+223	Detection
WD1314+293	Detection
WD1725+586	Detection
WD2331-475	Detection

Table 5.4: Summary of detections where photospheric contamination may be present

Name	Detection type
WD0004+330	Ambiguous
WD0027-636	Ambiguous
WD0050-332	Ambiguous
WD0131-164	Ambiguous
WD0147+674	Ambiguous

Table 5.4

Name	Detection type
WD0226-615	Ambiguous
WD0252-055	Ambiguous
WD0353+284	Ambiguous
WD0354-368	Ambiguous
WD0455-282	Ambiguous
WD0501+524	Ambiguous
WD0512+326	Ambiguous
WD0621-376	Ambiguous
WD0715-704	Ambiguous
WD0830-535	Ambiguous
WD1021+266	Ambiguous
WD1029+537	Ambiguous
WD1109-225	Ambiguous
WD1342+442	Ambiguous
WD1528+487	Ambiguous
WD1611-084	Ambiguous
WD1615-154	Ambiguous
WD1631+781	Ambiguous
WD1634-573	Ambiguous
WD1942+499	Ambiguous
WD1950-432	Ambiguous
WD2000-561	Ambiguous
WD2004-605	Ambiguous
WD2011+398	Ambiguous
WD2111+498	Ambiguous
WD2124-224	Ambiguous
WD2146-433	Ambiguous
WD2152-548	Ambiguous
WD2211-495	Ambiguous
WD2257-073	Ambiguous
WD2321-549	Ambiguous
WD2350-706	Ambiguous

Table 5.5: Summary of non detections

Name	Detection type
WD0001+433	Non detection
WD0041+092	Non detection

Table 5.5

Name	Detection type
WD0106-358	Non detection
WD0111+002	Non detection
WD0114-027	Non detection
WD0235-125	Non detection
WD0236+498	Non detection
WD0310-688	Non detection
WD0320-539	Non detection
WD0325-857	Non detection
WD0346-011	Non detection
WD0416+402	Non detection
WD0421+336	Non detection
WD0457-103	Non detection
WD0549+158	Non detection
WD0603-483	Non detection
WD0659+130	Non detection
WD0802+413	Non detection
WD0809-728	Non detection
WD0905-724	Non detection
WD0937+505	Non detection
WD1019-141	Non detection
WD1024+326	Non detection
WD1041+580	Non detection
WD1056+516	Non detection
WD1234+481	Non detection
WD1302+597	Non detection
WD1337+701	Non detection
WD1440+753	Non detection
WD1550+130	Non detection
WD1603+432	Non detection
WD1620+647	Non detection
WD1635+529	Non detection
WD1636+351	Non detection
WD1648+407	Non detection
WD1711+668	Non detection
WD1734+742	Non detection
WD1736+134	Non detection
WD1800+685	Non detection
WD1819+580	Non detection
WD1844-223	Non detection
WD1845+683	Non detection
WD1917+599	Non detection
WD1921-566	Non detection

Table 5.5

Name	Detection type
WD2014-575	Non detection
WD2020-425	Non detection
WD2043-635	Non detection
WD2116+736	Non detection
WD2123-226	Non detection
WD2124+191	Non detection
WD2309+105	Non detection

5.4 The connection with the SXR

One interesting commonality that the detections share is their high galactic latitude. Since the 1/4 keV soft X-ray background (SXR) is strongest in these directions and because the SXR is considered to be another tracer for hot gas it is worth comparing the distribution of the hot gas detections reported in this work with the SXR emission. The value of the 1/4 keV X-ray background in the directions of our stars is listed in Table 5.16.

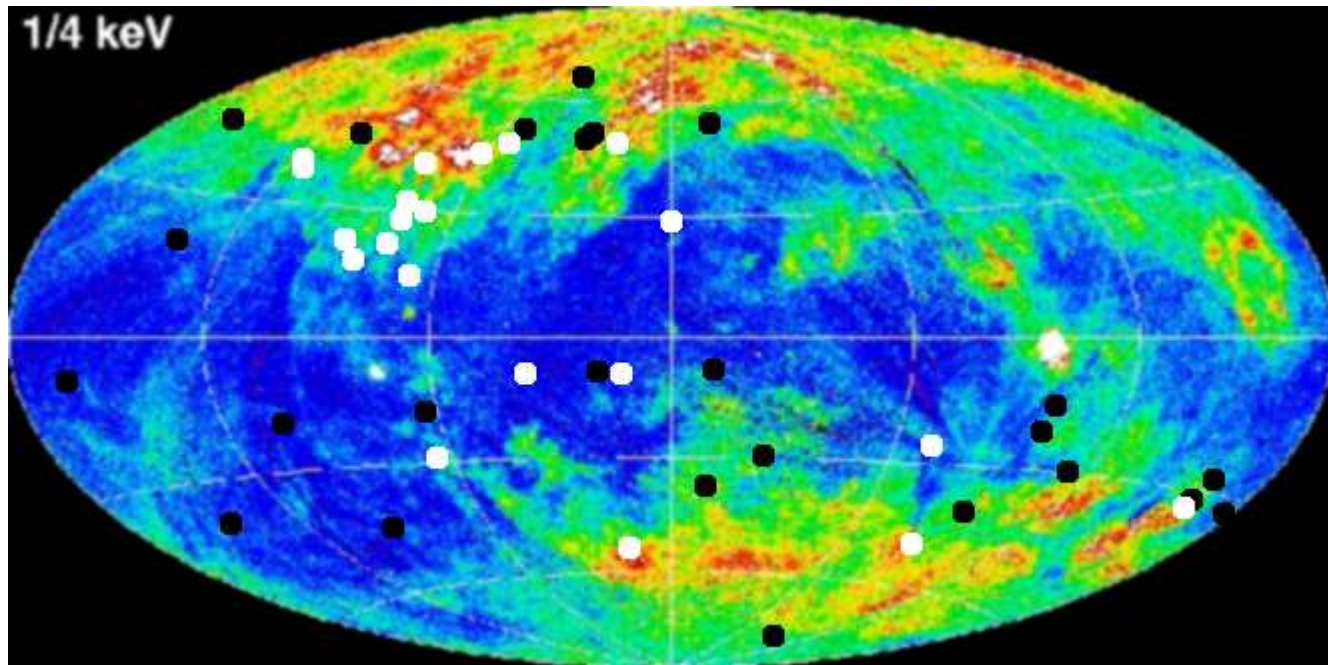


FIGURE 5.16. Non detections of O VI plotted on the 1/4 keV soft X-ray background. Black circles represent non detections within the local bubble and white circles represent non detections from beyond the local bubble.

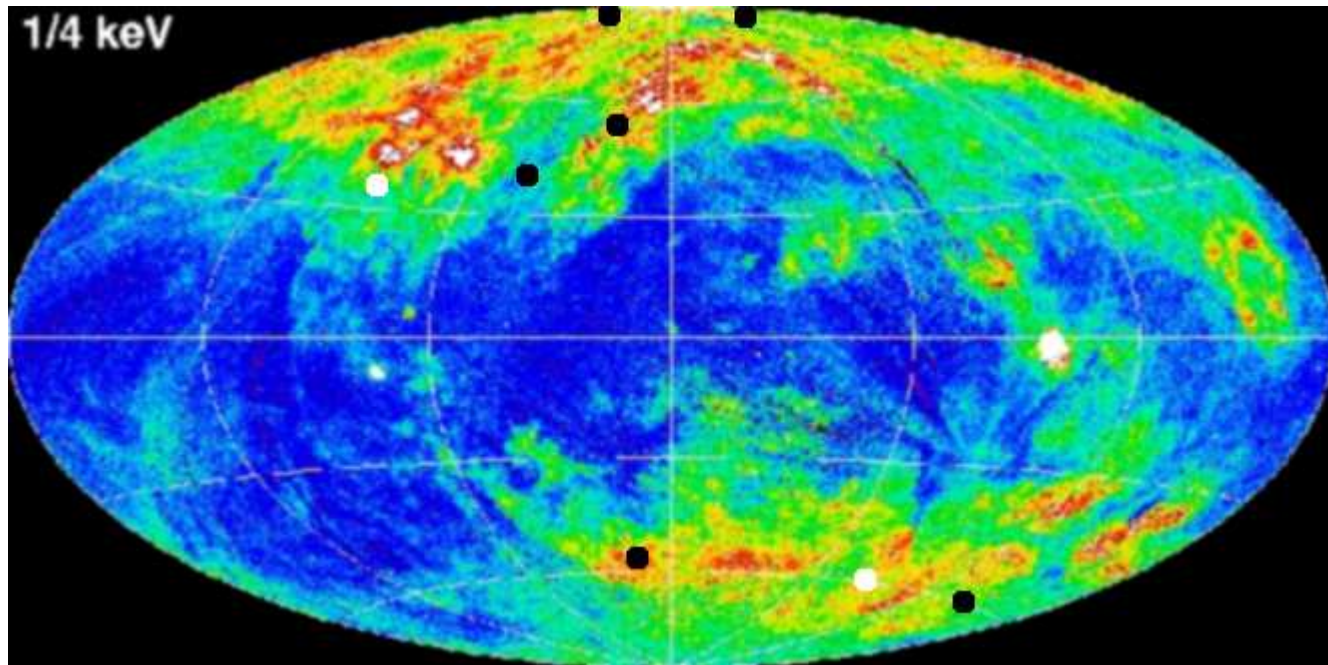


FIGURE 5.17. Detections of O VI plotted on the 1/4 keV soft X-ray background. Black circles represent detections within the local bubble and white circles represent detections from beyond the local bubble.

What is clear from Figure 5.16 is that O VI is mostly absent irrespective of where you look. In some cases it is absent beyond the bubble and in directions where the 1/4 keV soft X-ray background indicates the presence of hot gas. Within the bubble O VI is not detected in almost every part of the sky.

Figure 5.17 shows where O VI is detected. The ratio of non detections (Figure 5.16) to detections (Figure 5.17) within the bubble is approximately 4:1. Figure 5.17 also shows that there is a correlation between the location of the nearby detections and the soft X-ray background in that they are only located in regions of above average emission. This leads us to conclude that some of the hot gas structures seen in the 1/4 keV X-ray sky are within the local cavity and that this nearby hot gas component is only located towards the galactic poles.

Table 5.6: 1/4 keV X-Ray Background Combined Average Count Rate (10^{-6} counts/sec/arcmin²)

Name	SXRB	σ_{SXRB}
WD0001+433	377.4	10.5
WD0004+330	350.8	13.9
WD0027-636	954.1	25.2
WD0041+092	298.8	10.8
WD0050-332	645.2	15.1
WD0106-358	789.3	15.9
WD0111+002	411.5	12.4
WD0114-027	384.5	12.7
WD0131-164	601.7	13
WD0147+674	366.7	7.5
WD0226-615	1015.2	25.2
WD0229-481	1122.8	13.5
WD0232+035	553.7	18
WD0235-125	705.7	16.7
WD0236+498	427.2	8.8
WD0252-055	771.8	23
WD0310-688	862.3	12.7

Table 5.6

Name	SXRB	σ_{SXRB}
WD0320-539	850.6	12.6
WD0325-857	628.2	13.2
WD0346-011	689.7	13.6
WD0353+284	532.5	15.5
WD0354-368	1502.9	57.7
WD0416+402	336.4	11.7
WD0421+336	343	11.8
WD0455-282	852.7	13.8
WD0457-103	605.4	13.5
WD0501+524	300.1	10.1
WD0512+326	284.1	9.8
WD0549+158	432.2	10.3
WD0603-483	556	9.3
WD0621-376	588.8	10.1
WD0659+130	860.2	15.2
WD0715-704	485.2	9.2
WD0802+413	483.9	10.5
WD0809-728	526.9	14.3
WD0830-535	543.2	10.7
WD0905-724	470.9	13.3
WD0937+505	840.4	13.8
WD1019-141	483.4	11.5
WD1021+266	982.8	14.9
WD1024+326	1182	16.5
WD1029+537	859.7	13.7
WD1040+492	1080.4	14
WD1041+580	1056	13.9
WD1056+516	1056.2	14.4
WD1057+719	863.3	12.9
WD1109-225	626	15.2
WD1234+481	1103.5	18.2
WD1254+223	654.4	14.2
WD1302+597	1092.3	15
WD1314+293	988.6	15.2
WD1337+701	1144.3	12.5
WD1342+442	970.8	12.8
WD1440+753	717	8.7
WD1528+487	1215.8	13.8
WD1550+130	962.6	13.5
WD1603+432	1550.8	27.2
WD1611-084	328	10.9
WD1615-154	428.5	25.7

Table 5.6

Name	SXRB	σ_{SXRB}
WD1620+647	1072.6	9.2
WD1631+781	568.1	8.1
WD1634-573	441.3	17.3
WD1635+529	840	17.4
WD1636+351	873.7	12.6
WD1648+407	1231.1	14.5
WD1711+668	775.4	5.3
WD1725+586	688.3	6.6
WD1734+742	572.4	5.2
WD1736+134	389.5	8.9
WD1800+685	622.6	2.9
WD1819+580	692.8	5.8
WD1844-223	360.4	11.7
WD1845+683	576.4	5
WD1917+599	486.2	5.2
WD1921-566	722.5	33.7
WD1942+499	459.8	7.3
WD1950-432	577.2	14.9
WD2000-561	725.8	24.9
WD2004-605	868.8	28.6
WD2011+398	468.9	7.9
WD2014-575	704.2	21.5
WD2020-425	758.2	18.8
WD2043-635	657.9	21.5
WD2111+498	447.5	8.3
WD2116+736	465.2	10.2
WD2123-226	647	14.4
WD2124+191	590.3	12.2
WD2124-224	640.3	14.2
WD2146-433	1089.2	16.7
WD2152-548	1124	19.2
WD2211-495	1028.3	16.8
WD2257-073	532	15.3
WD2309+105	445	10.3
WD2321-549	1386.1	26.9
WD2331-475	949.2	28.2
WD2350-706	972.1	15

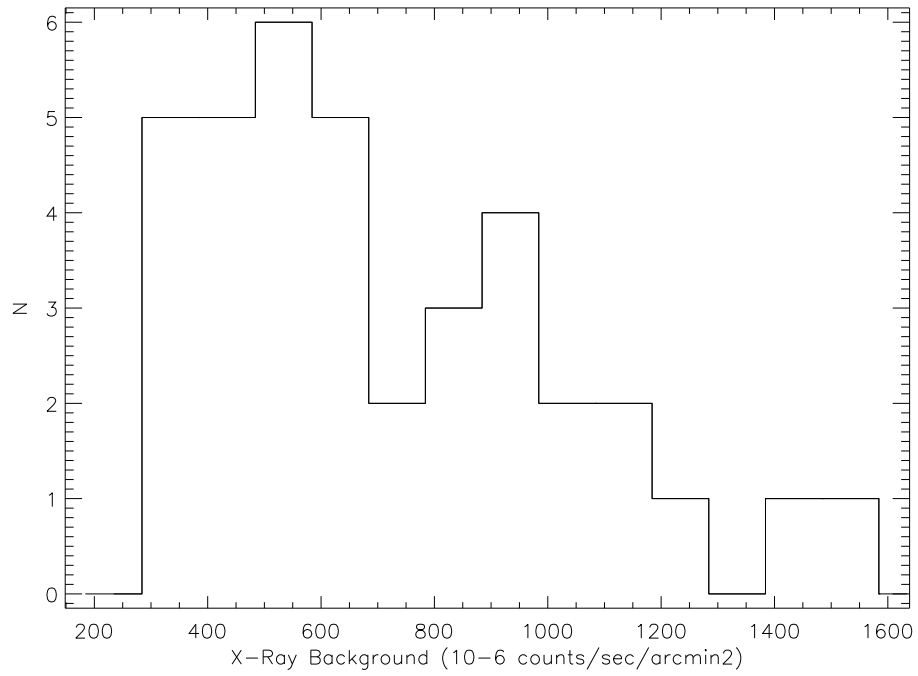


FIGURE 5.18. The 1/4 keV SXR emission histogram for non detections

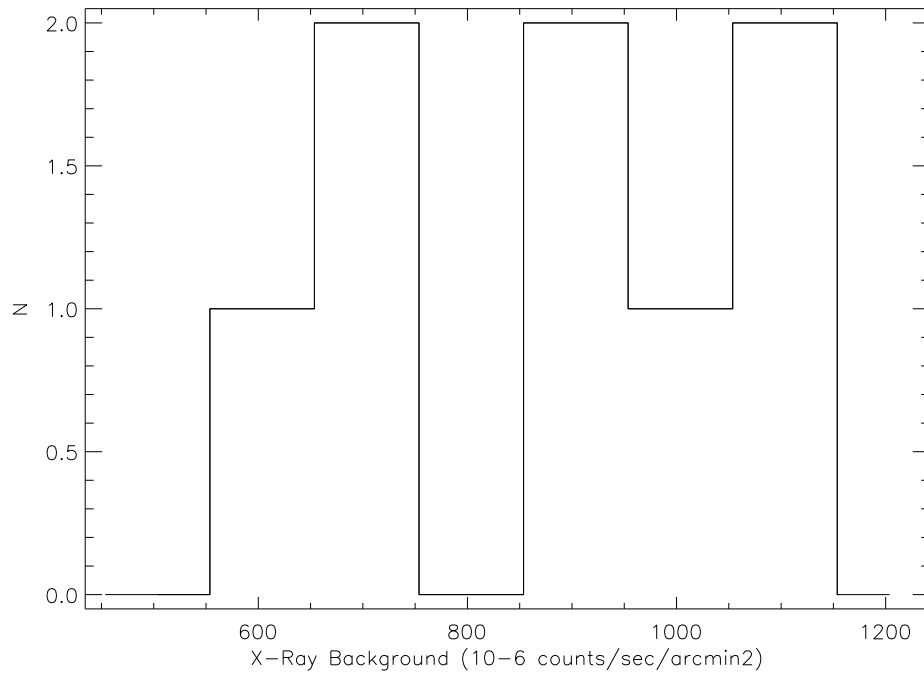


FIGURE 5.19. The 1/4 keV SXR emission histogram for detections

Using the X-Ray Background Tool at <http://heasarc.gsfc.nasa.gov> it is possible to find an X-Ray background combined average of the R1 and R2 channels of the ROSAT All-Sky Survey for the 1/4 keV band for each star in the sample. The background is calculated via the integration over area of the nearest 80 or so pixels of the ROSAT All-Sky Survey. Figure 5.18 shows that most of the non detections coincide with lower values of the SXRb and that most of the detections coincide with regions of higher SXRb (Figure 5.19). The average SXRb value is $712.0 \times 10^{-6} - +12.0 \times 10^{-6}$ counts/sec/arcmin² for the non detections and $862.6 \times 10^{-6} - +15.3 \times 10^{-6}$ counts/sec/arcmin² for the detections.

5.5 Discussion

The favored production mechanism for O VI requires a conductive interface between hot and cold gas. Historically it was supposed that the local bubble was created by a supernova and thus full of hot gas. In the locations where this gas was running into cold gas, i.e. the boundary, O VI would be produced. The observed picture is, however, quite different.

The boundary regions close to us are certainly real, cold gas measurements show a sudden increase in density when this boundary is crossed. What is not detected in these directions is the O VI that would suggest that the gas on the nearside of the cavity is hot. Studies of the SXRb reveal no emission in these galactic latitudes other than that created by solar phenomena. Towards the galactic poles the association of the non solar SXRb and the O VI is unlikely to be coincidental. This study localizes that O VI emission to

the low density chimneys.

The fact that the hot gas is observed at the interstellar velocity does suggest some coupling to the cold gas. Either that or it occupies a similar velocity coincidentally and is completely decoupled. Coincidences aside, the most probable explanation is that there is hot gas within the low density chimneys and that its interaction with the cold gas is forming O VI lines.

This new picture favours the detection of X-ray cloud shadows located along the co-axial sight-lines of the chimney, as supported by recent observations of the cloud 3C 225 (Heiles, private communication).

Though the hot gas velocity appears to be coupled with cold gas velocity there is also some evidence to suggest that the hot gas density is also coupled with the cold gas density. More hot gas does seem to be detected along longer lines of sight.

The degree of patchiness, or the scale length of the variation in density could be found from the patchiness of the SXR. It has been assumed previously that the patchiness of the SXR was due to absorbing material blocking the signal from the more distant hot gas in the galactic halo. This theory also fitted with the neutral hydrogen picture where 21cm line observations produced similar looking gas distributions. However it now seems possible that the observed patchiness in the polar SXR may be due, in part, to continuous but inhomogeneous clouds of hot gas flowing down into the galactic disk from above, and flowing up into the galactic disk from below. The correlation with the

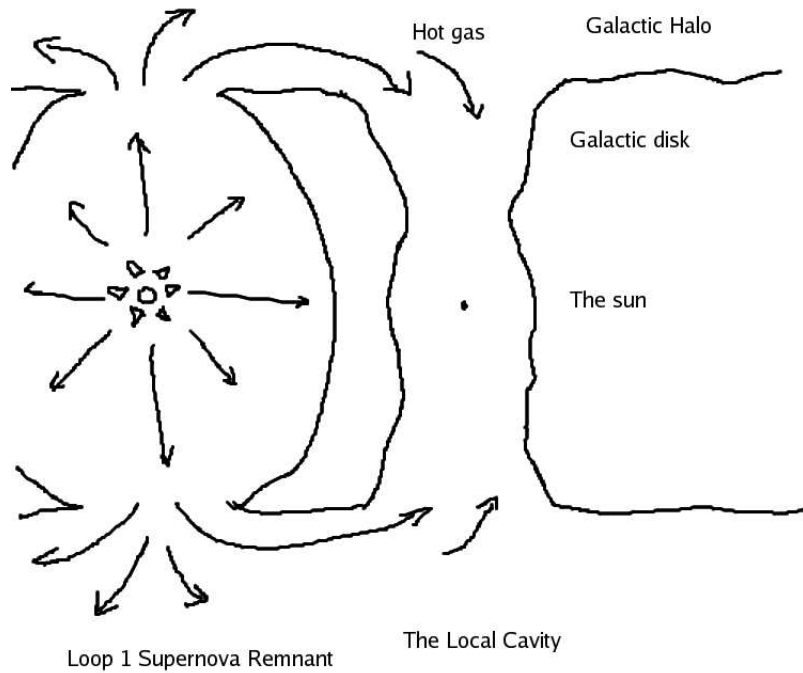


FIGURE 5.20. Diagram of the new picture of the local interstellar medium. On the left the hot gas from the Loop 1 bubble is spilling into the open ends of the local cavity.

neutral hydrogen picture, therefore, could be the result of the hot gas funneling down into the low density cavity. The patchy SXRb maybe a combination of both inhomogeneities in the hot gas and the presence of absorbing clouds. See Figure 5.20.

The non detection of O VI and 1/4 keV soft X-ray emission in the 0 to ± 30 degrees latitudes is an indication that this stream of hot gas has not yet reached our locality. Since no physical barrier is preventing the spread of the gas it must be assumed that it has just not had time to reach the galactic plane. This leads us to two definitive statements.

The new picture of the hot gas phase LISM presented in this work is different from previous pictures because of how this work examines the degree of contamination from the

background stars. Previous works have justified their limited treatment of photospheric contamination with incorrect assumptions about the Doppler shifting of the stellar O VI line and about the composition of white dwarfs. Through the correct treatment of those stars we conclude that the spatial distribution of hot gas in the LISM is very different and that the local interstellar cloud in which the solar system resides is not presently bathing in million degree gas.

5.6 Speculation

The absence of hot gas in the cavity is, therefore, largely explained with this new picture of the local interstellar medium. The presence of hot gas towards the galactic poles is the final question that will be investigated in this, the last section of this thesis.

It is possible that no singular event started the cascade, that the O VI has always been leaking into the galactic disk from above and below. Due to its slow recombination with free electrons the hot gas may simply have vanished before it is able to reach our locality. What is clear is that the hot gas is not being produced at the local boundary where the accepted theory suggests it should be.

If the presence of the hot gas is temporal, its current position is essentially a mark of how far it has reached since some time. This time could be the time since the hot gas reached the open pore that was the openings of local cavity before falling in. What event could have triggered such an inundation? Firstly, it is unlikely that the in falling material is

hot gas from the halo since halo gas has always been there and the gas we can see must have been triggered by some event to fall in. If this hot gas has always loitered around the local cavity openings it would have already inundated the cavity completely. A yet unreached portion could not exist if the hot gas has had forever to fill the void.

What is required is that this gas was produced or delivered to the openings at some discrete time. Further more the production mechanism must deliver hot gas to the south pore and the north pore at the same time, since we observe the ensuing inundation from both directions. One possible source of this hot gas is the neighboring Loop 1 bubble which at some point in the past expanded to the point where its upper and lower reaches met with the distant openings of the local cavity. Following the path of least resistance the hot gas then began its slow cascade into the cavity. This is supported by Wolleben (2007) who argue in favor of this kind of local cavity-loop 1 interaction.

Crawford et al. (2002) and Welsh et al. (2004) report that the cold gas observed in the galactic poles has a velocity of 20 to 60 km/s in our direction. Combining this velocity with our nearest detection of O VI places the earliest arrival date of the hot gas to our locality in about a million years.

Chapter 6

Appendix

6.1 Introduction

The amount of data used in this work is considerable. In order to allow future detailed examination of this work all data are included in the accompanying CD, containing a document that displays the various data used and models derived for all of the stars in the sample. In this chapter we present data for two stars, WD0501+524 and WD1314+293, as examples of the detailed analysis performed on each star, from which the summary scientific results presented in the main text were obtained.

All of these diagrams and tables are described in the main body of text. This example data is to help identify the tables and diagrams on the CD.

These two stars have been chosen as examples because WD0501+524 is a star that shows many photospheric lines and WD1314+293 is a star that does not have any photospheric lines. In the later case there are no diagrams that correspond to photospheric line profiles or velocities.

6.2 Contents

The Figure 6.1 is a completely reduced FUSE spectrum of the star. This is split into four wavelength sections to allow the details to be observed more clearly. What then follows is series of tables outlining what is known about the star. Table 6.1 displays

the values of the physical parameters obtained from a literature review of the object. Table 6.2 displays the various spectroscopic studies and identified species compiled from the literature. Finally, table 6.3 displays information on binarity. Figure 6.2 displays the Lyman line data and the fitted model spectrum. Figure 6.3 displays the confidence contours of the derived stellar parameters. Figure 6.4 is a plot of the literature derived physical parameters with this work's derived physical parameters also plotted. Figure 6.5 shows the identified ISM lines from which an average ISM line velocity is calculated. Figure 6.6 shows the identified photospheric lines from which an average photospheric line velocity is calculated. Figure 6.7 is a plot showing the distribution of line velocities for the ISM above and photosphere below. The diagram on the left shows the velocity distribution of all the measured lines and the diagram on the right only displays those lines whose velocities have gone into the average (i.e. those lines with a v similar to the centroid of the velocity distribution). The following two tables show the measured properties of those lines. The next table displays the ISM volume density measurements for the lines observed in this spectrum. The following table displays some of the deduced stellar properties, such as distance. The final diagram is that of the O VI line profile compared to that of C II and O I in the style of Savage & Lehner (2006).

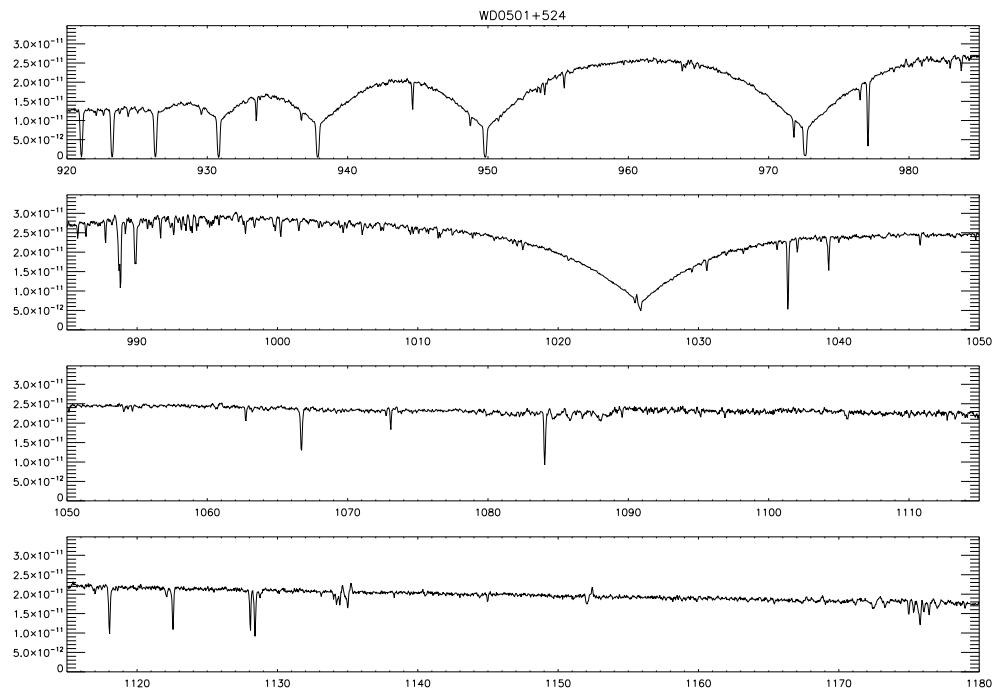


FIGURE 6.1. The processed spectrum of WD0501+524

6.2.1 WD0501+524

WD0501+524, also known as G191-B2B was first identified as a white dwarf by Greenstein (1969).

Table 6.1: Physical Parameters of WD0501+524

$Logg$	σ	T_{eff}	σ	M_o	σ	Reff
7.5				0.29		Shipman (1979)
5.95	0.04	56768	3336	0.3		Koester et al. (1979)
		59400		0.26		Guseinov et al. (1983)
7.55	0.35	62550	3520			Holberg et al. (1986)
		61170	4.83			Finley et al. (1990)
7.69		64100		0.538	0.043	Bergeron et al. (1995)
7.48	0.1	57340	1330	0.51	0.04	Marsh et al. (1997b)
7.492	0.012	61193	241	0.53	0.003	Finley et al. (1997)
7.36	0.06	61160	800	0.43	0.02	Vennes et al. (1997a)
7.57	0.05	53505	2156			Barstow et al. (2003) ^{Opt}
7.64	0.061	58152	831			Barstow et al. (2003) ^{FUSE}
7.57		58865				Lajoie & Bergeron (2007) ^{Opt}
		60680	1500			Lajoie & Bergeron (2007) ^{IUE}

Table 6.2: Line of sight to WD0501+524

Reff	Detector	Species
Cash et al. (1979)	Rocket UV	H I
Bruhweiler (1982)	Copernicus	H I
Paresce (1984)	EUV	H I, Mg II, Ti II, Na I, Fe II O VI, H_2
Jelinsky et al. (1988)	IUE	N I, Si II, C II
Bruhweiler & Cheng (1988)	IUE	H I, He I
Green et al. (1990)	EUVE	H I, He I
Kimble et al. (1991)	HUT	H I
Lilienthal & de Boer (1991)	IUE	H I
Kimble et al. (1993)	HUT	H I
Diamond et al. (1995)	ROSAT	H I
Dupuis et al. (1995)	EUVE	H I, He I
Hurwitz & Bowyer (1995)	ORFEUS	H I, C II, C* II, C III, N I N II, N III, O I
Lallement et al. (1995)	GHRIS	Fe II, Mg II
Lemoine et al. (1996)	GHRIS	H I, D I
Barstow et al. (1997)	EUVE	H I, He II
Dring et al. (1997)	GHRIS	H I, D I, Mg II, Fe II
Vidal-Madjar et al. (1998)	GHRIS	H I, D I, N I, O I, Si II Si III
Sahu et al. (1999)	GHRIS	H I, D I
Jenkins et al. (2000)	FUSE	N I, N II, N III, O I, Ar I
Redfield & Linsky (2000)	HST,EUVE,Opt	H I, Ca II
Vidal-Madjar et al. (2000)	FUSE	H I, D I, O I, N I
Lemoine et al. (2002)	FUSE	D I
Moos et al. (2002)	FUSE	D I, N I, O I
Redfield & Linsky (2002)	GHRIS	Fe II, Mg II, and Ca II
Hebrard & Moos (2003)	FUSE	H I, D I, O I
Lehner et al. (2003)	FUSE	C II, C II*, C III, N I, N II O I, Ar I, Si II, P II, Fe II Fe III, H_2
Redfield & Linsky (2004)	GHRIS	D I, C II, N I, O I Al II, Si II
Oliveira et al. (2005)	FUSE,HST	H I,O I
Oegerle et al. (2005)	FUSE	O VI
Dixon et al. (2006)	FUSE	O VI
Otte & Dixon (2006)	FUSE	O VI

Table 6.3: Binariness of WD0501+524

Reff	Notes
Giclas et al. (1972)	Proper motion companion to K dwarf
Probst (1983)	Find no IR excess
Thejll et al. (1995)	Find no IR excess
Mullally et al. (2007)	Find no IR excess

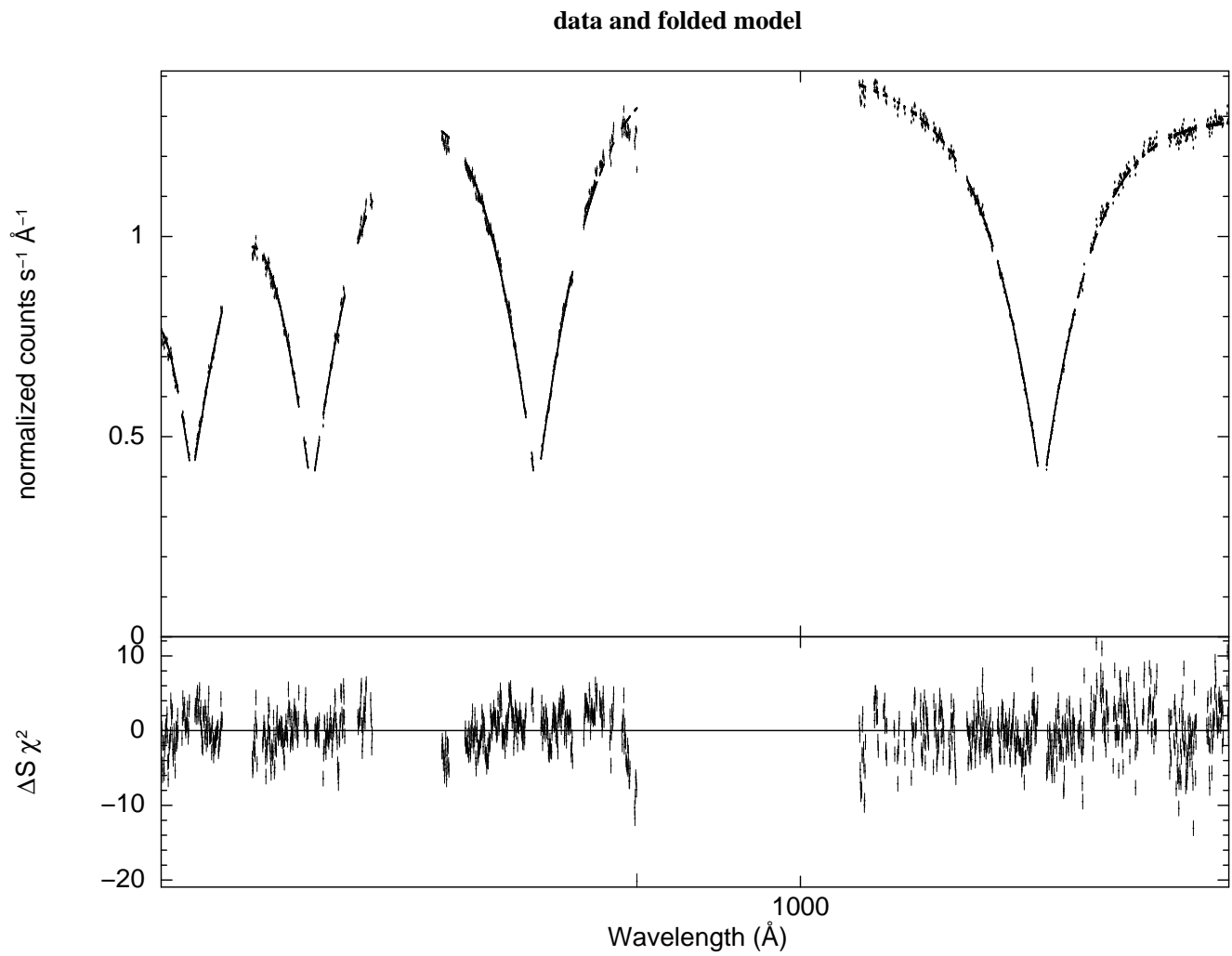


FIGURE 6.2. Data and model for WD0501+524

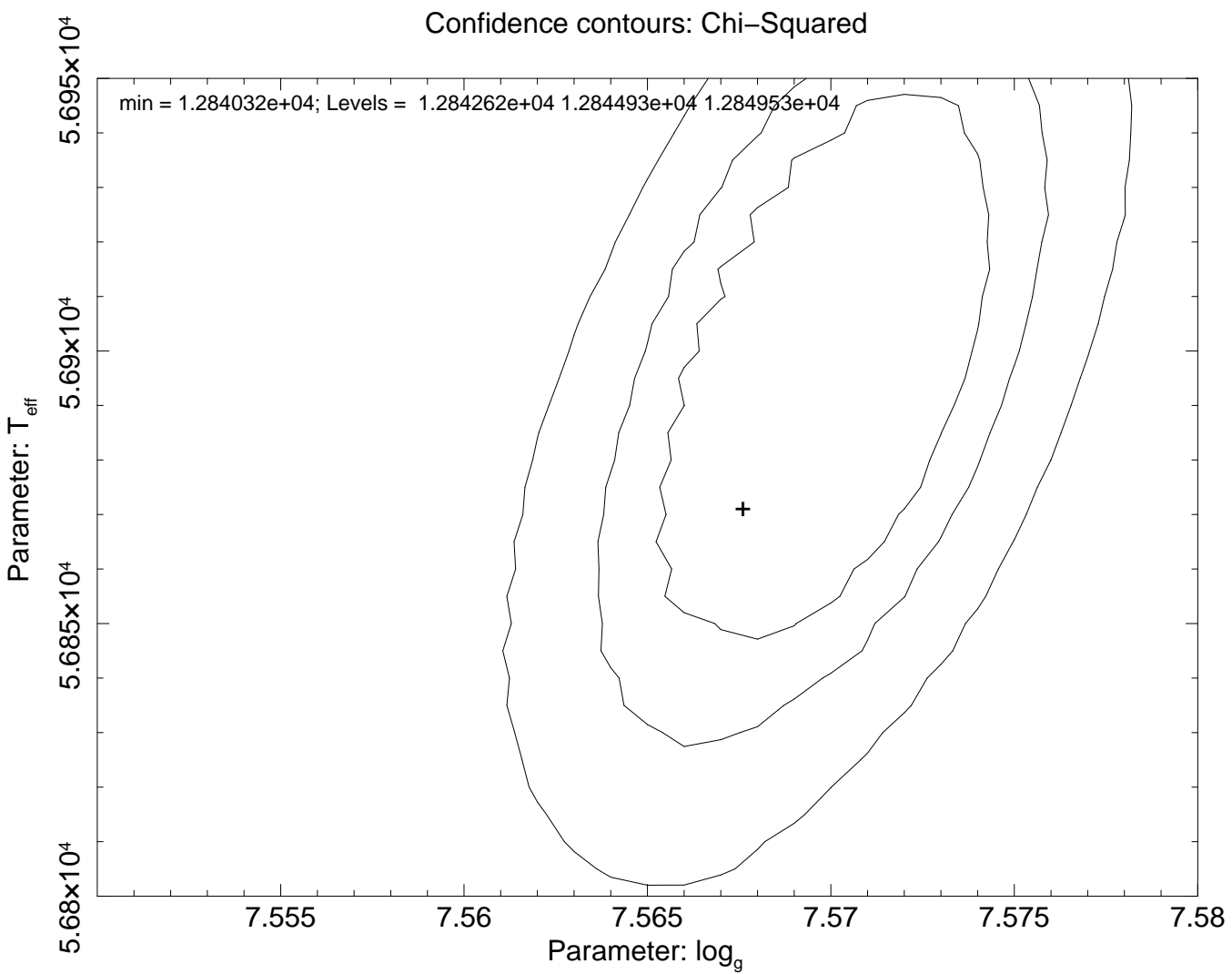


FIGURE 6.3. Confidence contours for WD0501+524

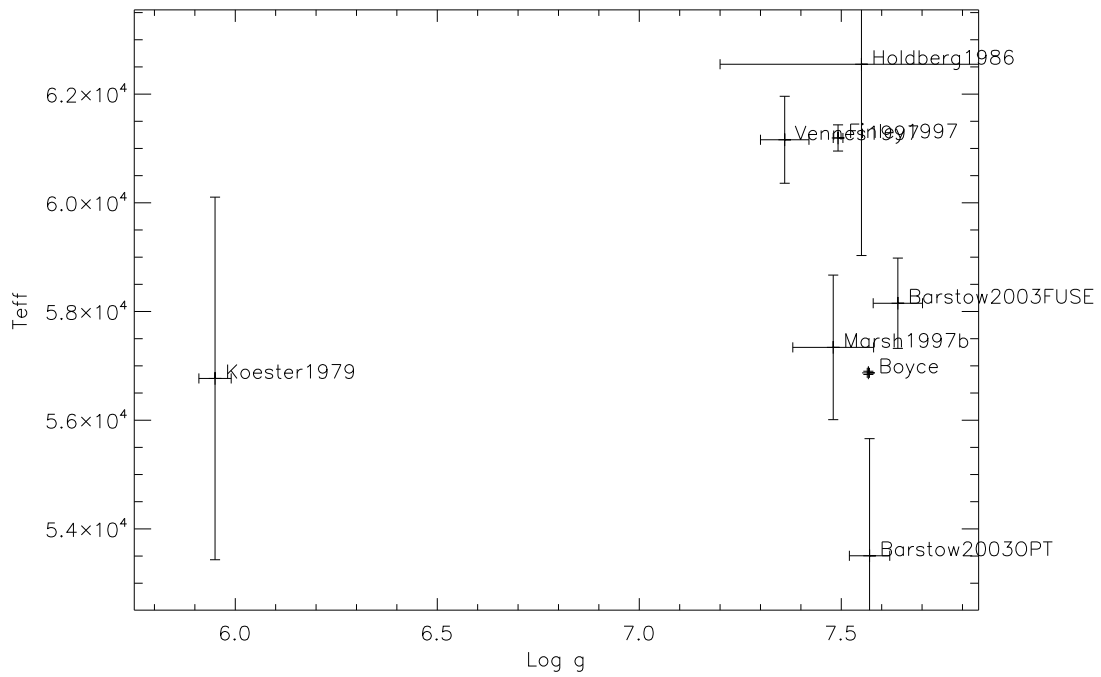


FIGURE 6.4. Literature derived physical parameters and the derived physical parameters from this work for WD0501+524. The displayed error bars on the data point from this work are small because no additional systematic uncertainties have been added to the total uncertainty.

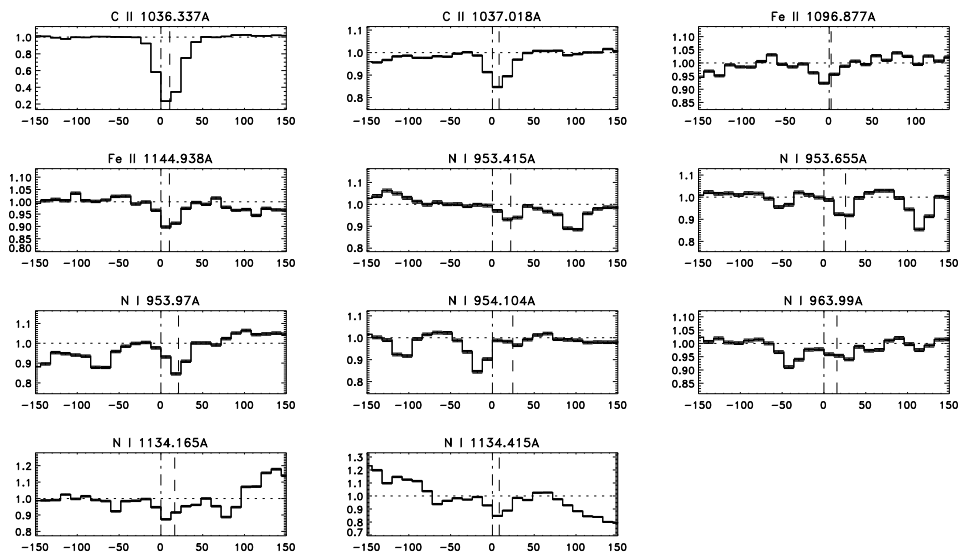


FIGURE 6.5. Identified ISM lines. Dashed line plotted at lab wavelength value.
Dotted line plotted at measured centroid

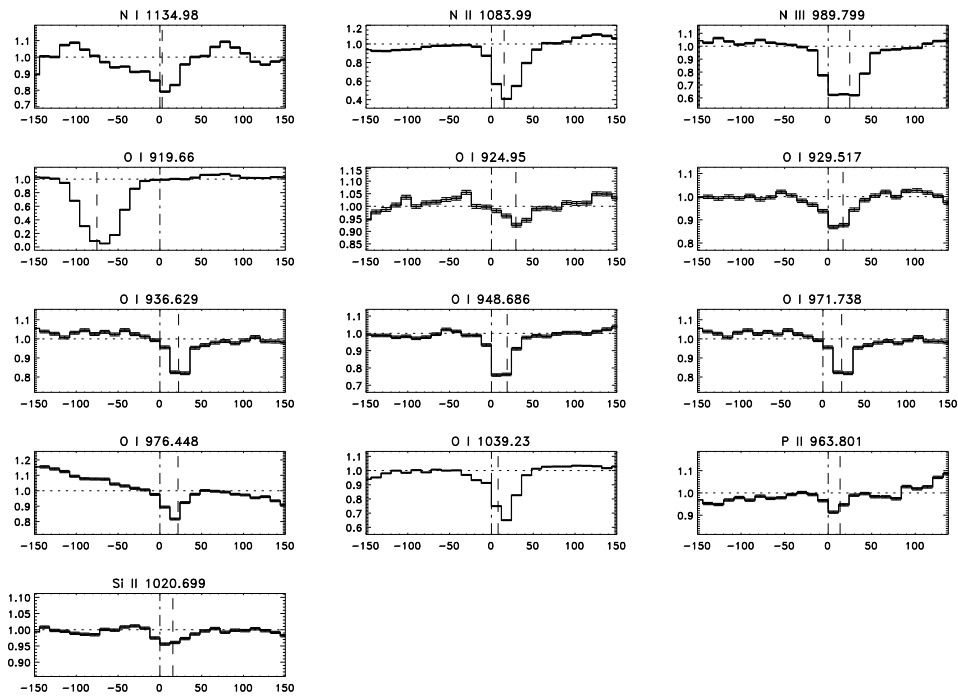


FIGURE 6.6. Identified ISM lines. Dashed line plotted at lab wavelength value. Dotted line plotted at measured centroid

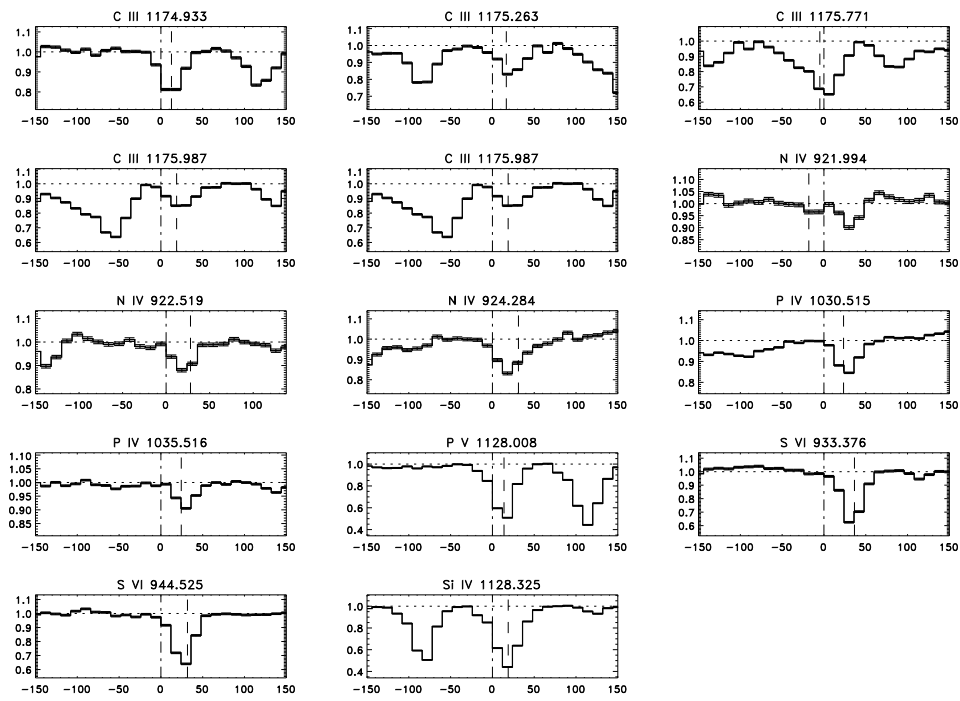


FIGURE 6.7. Identified photospheric lines. Dotted line plotted at measured centroid

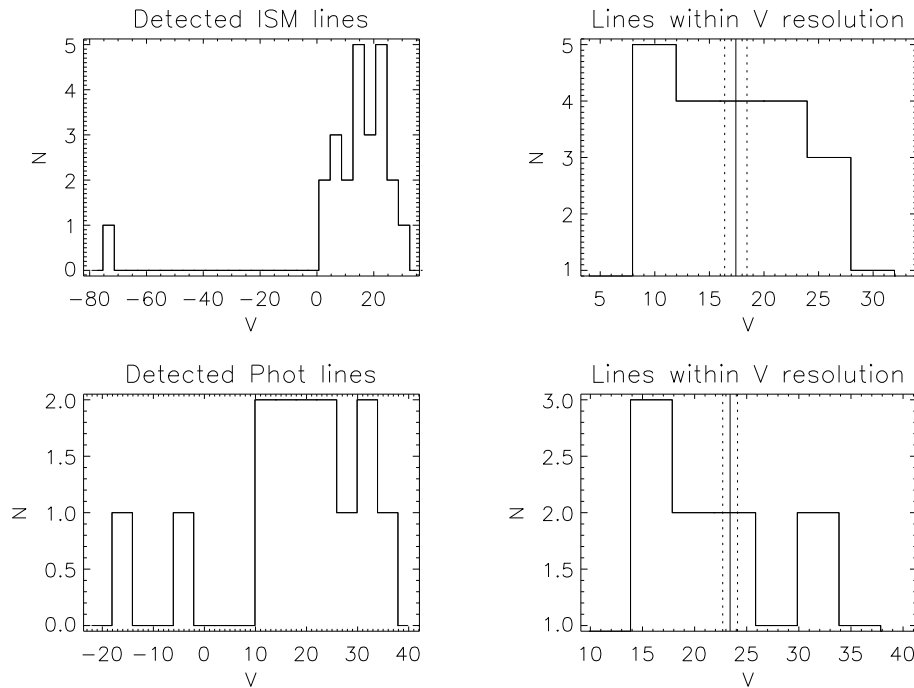


FIGURE 6.8. Plot showing the number distribution of line velocities for the detected ISM lines (above) and photospheric lines (below). The diagram on the left shows the velocity distribution of all the measured lines and the diagram on the right only displays those lines whose velocities have gone into the average (i.e. those line with a v similar to the centroid of the velocity distribution)

Table 6.4: ISM line measurements

Species	λ_o	λ_{meas}	$\sigma_{\lambda_{meas}}$	V	σ_{vel}	W	σ_W
O I	919.660	919.429	0.001	-75.328	0.216	174.930	0.940
O I	924.950	925.040	0.007	29.258	2.228	7.920	0.950
O I	929.517	929.570	0.003	17.107	1.025	16.320	0.890
O I	936.629	936.699	0.003	22.369	0.948	18.150	0.880
O I	948.686	948.746	0.002	18.844	0.647	26.410	0.880
N I	953.415	953.485	0.005	21.879	1.695	6.590	0.680
N I	953.655	953.737	0.004	25.883	1.373	7.020	0.670
N I	953.970	954.037	0.002	21.080	0.739	13.510	0.650
N I	954.104	954.182	0.010	24.375	3.261	2.900	0.670
P II	963.801	963.845	0.005	13.688	1.517	7.690	0.650
N I	963.990	964.040	0.005	15.603	1.582	7.280	0.650
N I	971.738	971.794	0.001	17.154	0.369	44.010	0.860
O I	976.448	976.519	0.004	21.663	1.143	16.280	0.830
N III	989.799	989.881	0.001	24.809	0.289	66.000	0.730
Si II	1020.699	1020.752	0.006	15.543	1.735	6.120	0.480
C II	1036.337	1036.374	0.000	10.558	0.113	88.940	0.360
C II	1037.018	1037.046	0.001	8.011	0.388	15.590	0.360
O I	1039.230	1039.258	0.001	7.958	0.307	39.250	0.430
N II	1083.990	1084.045	0.001	15.226	0.379	75.560	1.000
Fe II	1096.877	1096.885	0.004	2.269	1.122	6.970	0.490
N I	1134.165	1134.228	0.002	16.521	0.580	13.960	0.530
N I	1134.415	1134.446	0.002	8.162	0.580	14.390	0.540
N I	1134.980	1134.990	0.001	2.741	0.229	24.200	0.450
Fe II	1144.938	1144.977	0.002	10.164	0.599	10.020	0.500

Table 6.5: Photospheric line measurements

Species	λ_o	λ_{meas}	$\sigma_{\lambda_{meas}}$	V	σ_{vel}	W	σ_W
N IV	921.994	921.938	0.013	-18.100	4.089	3.150	0.880
N IV	922.519	922.605	0.004	28.007	1.452	11.800	0.900
N IV	924.284	924.380	0.004	31.121	1.361	21.710	1.070
S VI	933.376	933.490	0.002	36.542	0.659	38.040	0.910
S VI	944.525	944.625	0.001	31.790	0.454	36.930	0.730
P IV	1030.515	1030.596	0.002	23.474	0.621	15.840	0.460
P IV	1035.516	1035.600	0.002	24.385	0.711	8.650	0.370
P V	1128.008	1128.060	0.001	13.853	0.251	53.710	0.560
Si IV	1128.325	1128.396	0.001	18.909	0.236	68.770	0.590
C III	1174.933	1174.983	0.002	12.646	0.480	21.020	0.640
C III	1175.263	1175.328	0.003	16.597	0.774	20.970	0.770
	1175.771	1175.752	0.002	-4.887	0.409	64.130	0.850
C III	1175.987	1176.061	0.002	18.827	0.610	20.680	0.710
C III	1176.370	1176.425	0.003	13.968	0.702	18.440	0.710

Table 6.6: ISM volume density measurements

Species	λ_o	$\log N$	$\sigma_{\log N}$
O I	919.660	14.7844	0.0999961
O I	924.950	13.1464	1.57783
O I	929.517	13.2839	0.726478
O I	936.629	13.1209	0.638445
O I	948.686	13.0350	0.437622
N I	953.415	12.1172	1.25132
N I	953.655	11.8623	1.13321
N I	953.970	12.0192	0.580379
N I	954.104	12.2686	2.83492
P II	963.801	10.1211	0.856497
N I	963.990	12.1680	1.08758
N I	971.738	12.9715	0.259015
O I	976.448	13.0800	0.669016
Si II	1020.70	11.9111	0.935486
C II	1036.34	12.2137	0.0704330
C II	1037.02	11.4569	0.268712
O I	1039.23	12.9703	0.151754
N II	1083.99	13.1304	0.181951
Fe II	1096.88	11.6158	0.818002
N I	1134.17	12.2387	0.467360
N I	1134.42	11.9581	0.451421
N I	1134.98	12.0222	0.228943
Fe II	1144.94	11.3317	0.567367

Table 6.7: Deduced stellar properties

Property	Value
Name	WD0501+524
Teff	56840.00
Teff error	30.14
log g	7.56
log g error	0.003
Mass/solar mass	0.537
Mass error	0.001
Radius/solar radius	0.020
Radius error	5.275e-6
Eddington flux at 1000A	2.62e+10
Observed flux at 1000A	2.86e-11
Continued on next page	

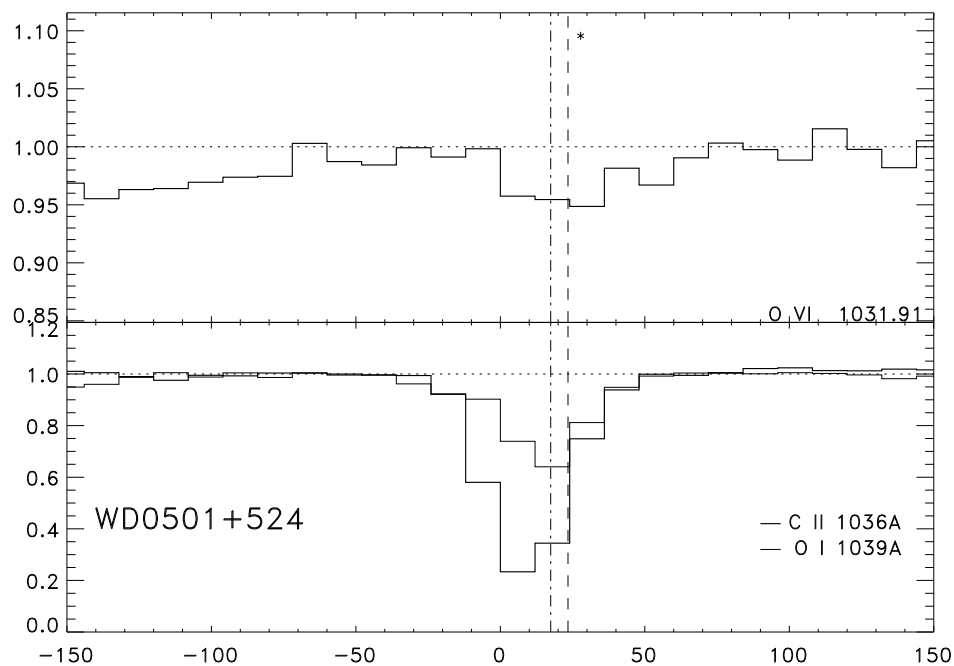
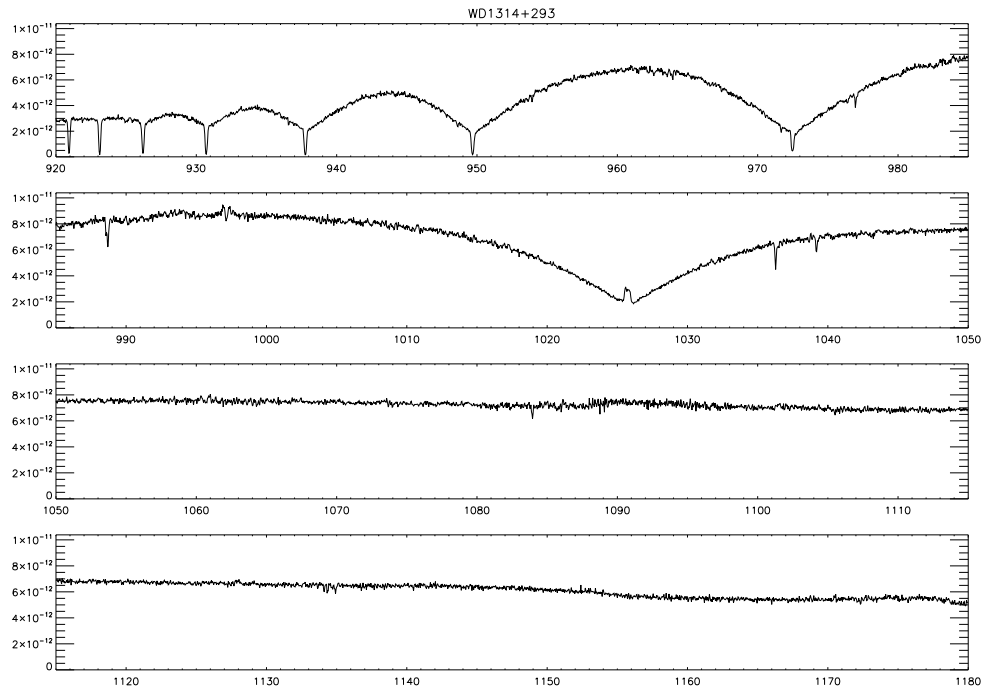


FIGURE 6.9. Plot of the O VI line profile compared to C II and O I line profile

Table 6.7 – continued from previous page

Property	value
Observed flux error	1.17e-13
Distance/parsecs	48.48
Distance error	0.20



6.2.2 WD1314+293

WD1314+293, also known as HZ43 was identified as a faint blue star by Humason & Zwicky (1947).

Table 6.8: Physical Parameters of WD1314+293

$Logg$	σ	T_{eff}	σ	M_o	σ	Reff
		60900	9000	0.59	0.32	Wesseliuss & Koester (1978)
7.9		60000		0.48		Shipman (1979)
8.33	0.18	38283	1007	0.78		Koester et al. (1979)
8.16		50000		0.88		Guseinov et al. (1983)
8.5		57500	3310			Holberg et al. (1986)
		49000	5000			Heise et al. (1988)
		59740	5910			Finley et al. (1990) ^{IUE}
		57500	3300			Finley et al. (1990) ^{Opt}
7.7		49000				Napiwotzki et al. (1993)
7.7	0.2	49000	2000	0.56	0.07	Marsh et al. (1997b)
7.986	0.045	50822	639	0.69	0.023	Finley et al. (1997)
7.85	0.07	50370	780			Barstow et al. (2001b) ^{Opt}
7.65	0.09	46100	1300			Barstow et al. (2001b) ^{HUT}
8.14	0.05	50080	290			Barstow et al. (2001b) ^{ORFEUS}
8.06		52394		0.73		Lajoie & Bergeron (2007) ^{Opt}
8.06		49785		0.73		Lajoie & Bergeron (2007) ^{IUE}

Table 6.9: Binariness of WD1314+293

Reff	Notes
Margon et al. (1976)	Wide but unresolved companion dM3.5e companion
Greenstein (1986)	Spectroscopic binary

Table 6.10: Line of sight to WD1314+293

Reff	Detector	Species
Bruhweiler (1982)	Copernicus	H I
Paresce (1984)	EUV	H I, Mg II, Ti II, Na I, Fe II
		O VI, H_2
Jelinsky et al. (1988)	IUE	N I, Si II, C II
Bruhweiler & Cheng (1988)	IUE	H I, He I
Dupuis et al. (1994)	EUVE	H I, He I
Vennes et al. (1994b)	EUVE	He II
Diamond et al. (1995)	ROSAT	H I
Vidal-Madjar et al. (1998)	GHR	H I, D I, N I, O I, Si II
		Si III
Wolff et al. (1999)	EUVE	H, He
Redfield & Linsky (2000)	HST,EUVE,Opt	H I, Ca II
Linsky et al. (2000)	EUVE	H
Kruk et al. (2000)	FUSE	H I, D I, N I, O I
Kruk et al. (2002)	FUSE	O I, N I, C II, C III, O VI,
		Si II, Ar I, Mg II, Fe II
Moos et al. (2002)	FUSE	D I, N I, O I
Redfield & Linsky (2000)	HST,EUVE,Opt	H I, Ca II
Hebrard & Moos (2003)	FUSE	H I, D I, O I
Lehner et al. (2003)	FUSE	C II, C II*, C III, N I, N II
		O I, Ar I, Si II, P II, Fe II
		Fe III, H_2
Oliveira et al. (2005)	FUSE,HST	H I, O I
Kimura et al. (2003)	FUSE	C II, NI, O I, Si II
Redfield & Linsky (2004)	GHR	D I, C II, N I, O I Al II, Si II
Oliveira et al. (2005)	FUSE,HST	H I, O I
Oegerle et al. (2005)	FUSE	O VI
Savage & Lehner (2006)	FUSE	O VI
Dixon et al. (2006)	FUSE	O VI
Oliveira et al. (2006)	FUSE	H I, D I, O I
Gnacinski & Krogulec (2006)	GHR, STIS	S II, Si II

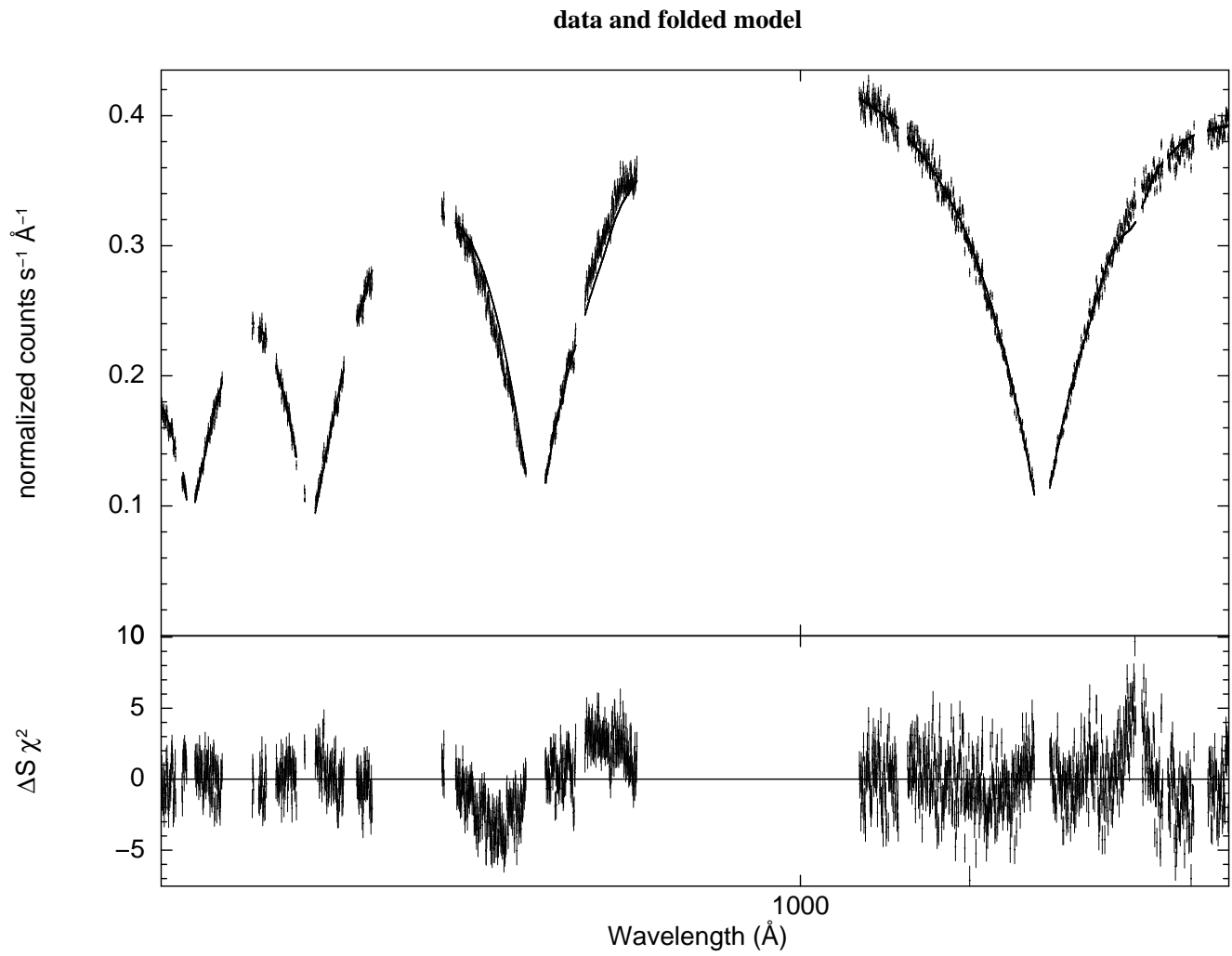


FIGURE 6.10. Data and model for WDI314+293

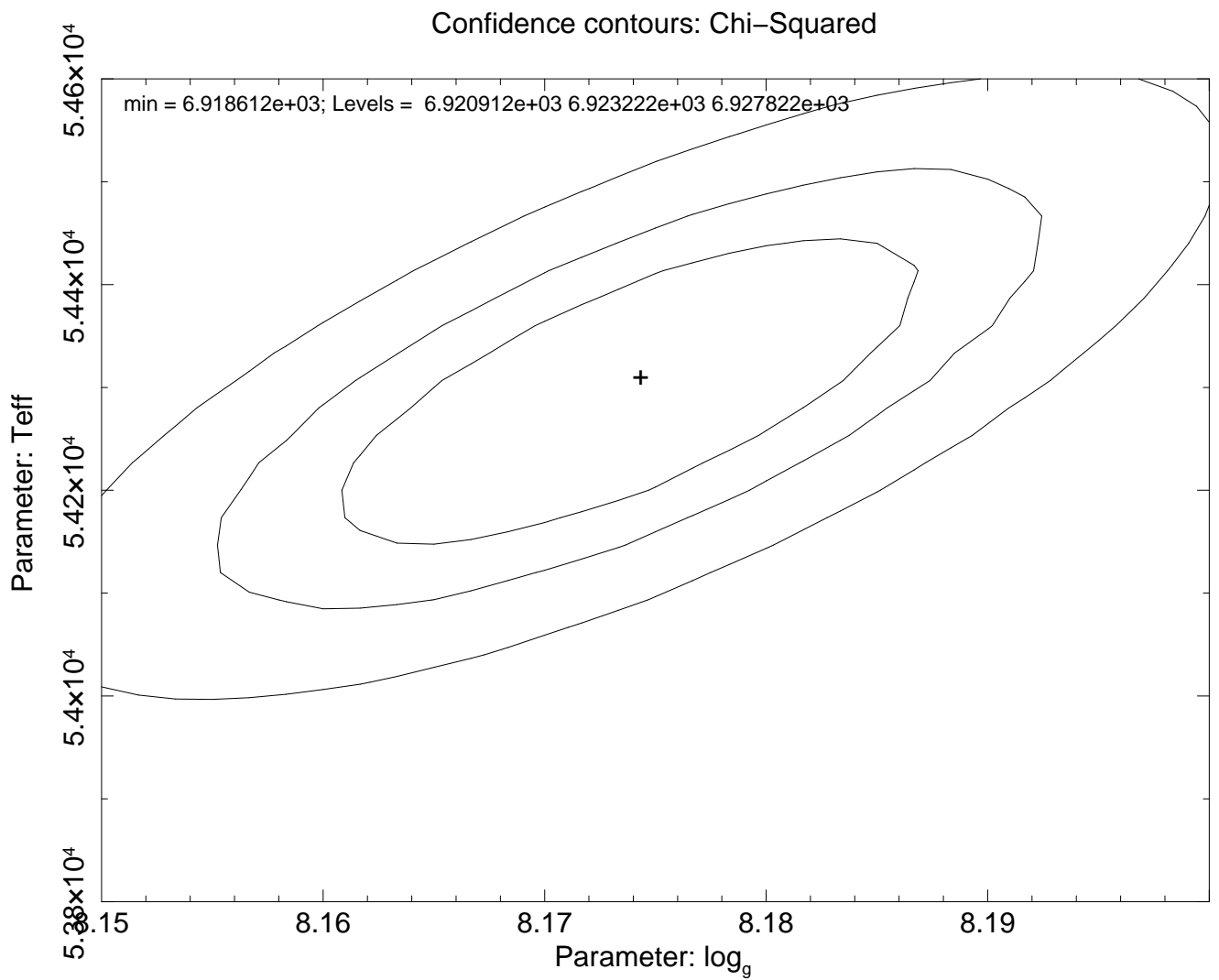


FIGURE 6.11. Confidence contours for WDI1314+293

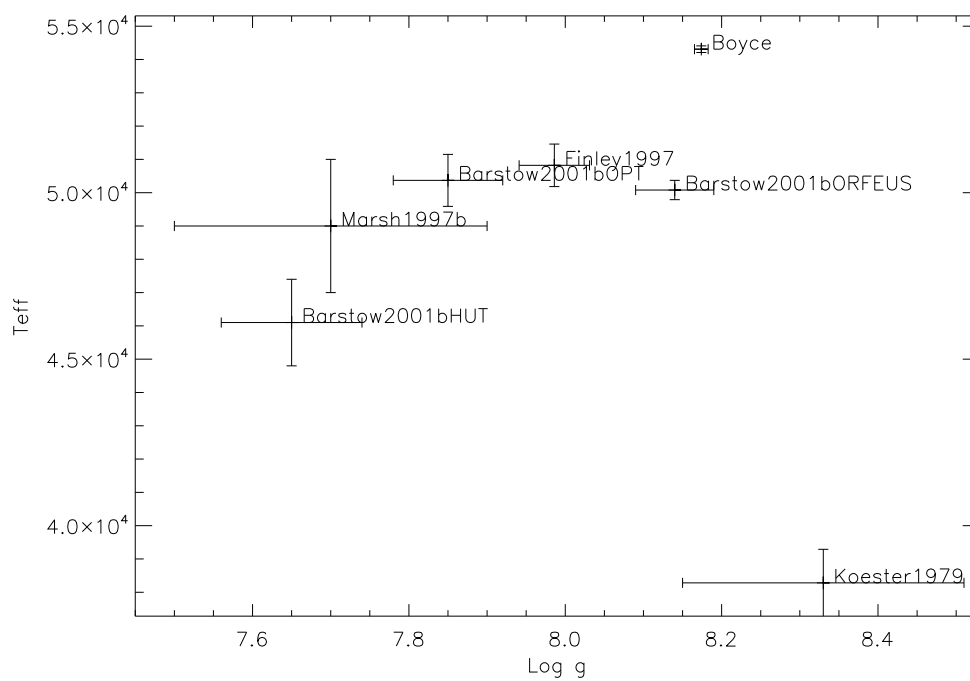


FIGURE 6.12. Literature derived physical parameters and the derived physical parameters from this work for WD1314+293. The displayed error bars on the data point from this work are small because no additional systematic uncertainties have been added to the total uncertainty.

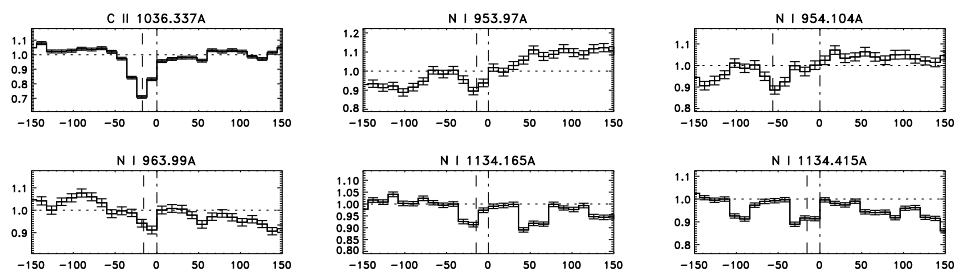


FIGURE 6.13. Identified ISM lines. Dashed line plotted at lab wavelength value. Dotted line plotted at measured centroid

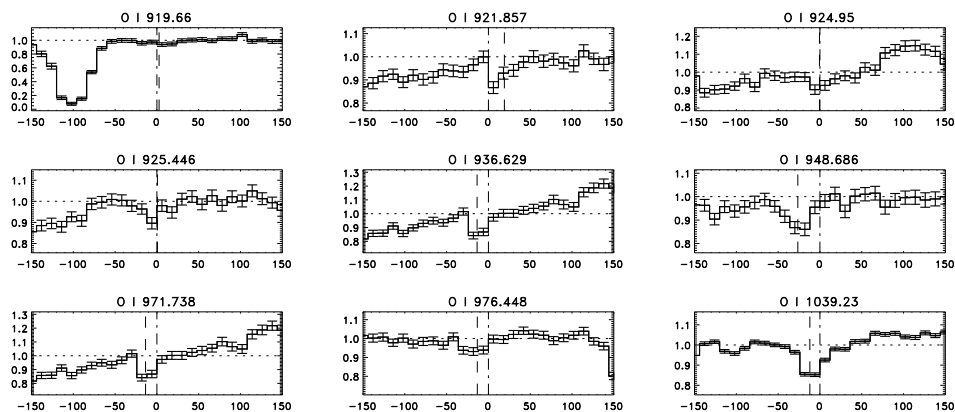


FIGURE 6.14. Identified ISM lines. Dashed line plotted at lab wavelength value.
Dotted line plotted at measured centroid

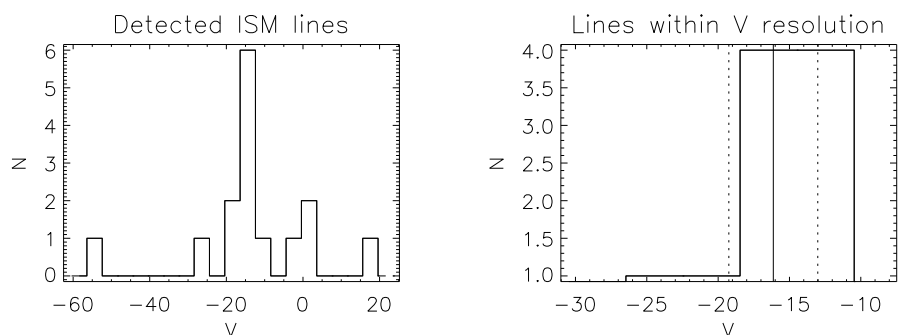


FIGURE 6.15. Plot showing the number distribution of line velocities for the detected ISM lines (above) and photospheric lines (below). The diagram on the left shows the velocity distribution of all the measured lines and the diagram on the right only displays those lines whose velocities have gone into the average (i.e. those line with a v similar to the centroid of the velocity distribution)

Table 6.11: ISM line measurements

Species	λ_o	λ_{meas}	$\sigma_{\lambda_{meas}}$	V	σ_{vel}	W	σ_W
O I	919.660	919.668	0.032	2.606	10.489	7.920	3.660
O I	921.857	921.916	0.016	19.095	5.061	11.420	3.120
O I	924.950	924.948	0.019	-0.534	6.065	10.250	3.290
O I	925.446	925.448	0.020	0.633	6.492	9.400	3.280
O I	936.629	936.587	0.011	-13.577	3.515	12.080	2.850
O I	948.686	948.602	0.014	-26.463	4.483	18.220	3.520
NI	953.970	953.925	0.014	-14.098	4.385	8.250	2.190
NI	954.104	953.924	0.011	-56.403	3.346	9.610	2.130
NI	963.990	963.939	0.014	-15.868	4.213	6.300	1.890
NI	971.738	971.677	0.010	-18.698	3.153	19.600	3.410
O I	976.448	976.405	0.020	-13.267	6.153	7.420	2.570
C II	1036.337	1036.277	0.002	-17.303	0.539	25.750	0.960
O I	1039.230	1039.188	0.005	-12.043	1.434	17.270	1.210
NI	1134.165	1134.110	0.007	-14.617	1.752	7.500	1.070
NI	1134.415	1134.357	0.006	-15.388	1.543	11.460	1.160

Table 6.12: Photospheric line measurements

Species	λ_o	λ_{meas}	$\sigma_{\lambda_{meas}}$	V	σ_{vel}	W	σ_W
	0.000	0.000	0.000	0.000	0.000	0.000	0.000

Table 6.13: ISM volume density measurements

Species	λ_o	$\log N$	$\sigma_{\log N}$
O I	919.660	13.4119	6.20008
O I	921.857	14.2196	3.88869
O I	924.950	13.2302	4.24960
O I	925.446	13.8306	4.82893
O I	936.629	12.9158	3.05123
O I	948.686	12.8455	2.48657
N I	953.970	11.7767	3.12946
N I	954.104	12.7607	2.83257
N I	963.990	12.0770	3.62606
N I	971.738	12.5919	2.19607
O I	976.448	12.7105	4.40512
C II	1036.34	11.6471	0.456696
O I	1039.23	12.5854	0.894942
N I	1134.17	11.9405	1.70968
N I	1134.42	11.8309	1.20614

Table 6.14: Deduced stellar properties

Property	Value
Name	WD1314+293
Teff	54210.00
Teff error	100.00
log g	8.17
log g error	0.009
Mass/solar mass	0.790
Mass error	0.007
Radius/solar radius	0.012
Radius error	1.278e-5
Eddington flux at 1000A	2.48e+10
Observed flux at 1000A	8.75e-12
Observed flux error	1.05e-13
Distance/parsecs	51.75
Distance error	0.63

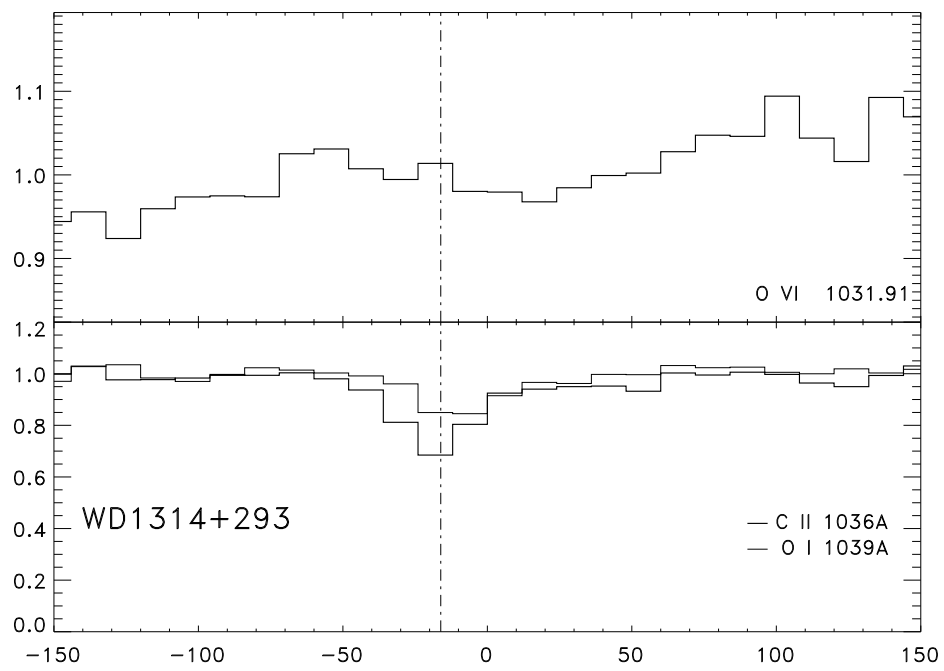


Table 6.15. Summary of the FUSE data used in this paper

Name	Observation	Name	Observation
WD0003+436J	E90305010	WD0644+375	B11902010
WD0004+330	P20411010/..20/..30/..40	RE-J0702+129	B05509010
WD0027-636	Z90302010	WD0715-703	M10507010
WD0041+092	B05507010	WD0710+74	D07101010
WD0050-332	M10101010/P20420010	WD0718-316	B05101010
WD0106-358	D02301010	WD0723-277J	D13701010
WD0114-027	B05503010	WD0802+413	Z90311010
WD0134-161	P20412010	WD0809-728	Z90312020
WD0134+833	E90305010	WD0823+317	B05302010
WD0147+674	Z90303020	WD0830-535	Z90313010
WD0209+085	C02602010	WD0905-724	A05405010
WD0214+568	U10140010	WD0937+505	Z90314010
WD0226-615	A05402010/U10621010	WD0950+139	A03411010
WD0229-481	M10504010	WD1017-138	P20415010
WD0232+035	P10405040	WD1024+263J	B05508010
WD0235-125	E56809010	WD1024+326	B05512010
WD0236+498	Z90306010	WD1032+534J	B00301010
WD0252-055	A05404040	WD1040+492	Z00401010
WD0310-688	D90703010	WD1041+580	Z90317010
WD0317-855J	A01001010	WD1056+516	B00303010
WD0320-539	D02302010	WD1057+719	Z90318010
WD0346-011	B12201020/..30/..40/..50	WD1109-225	A05401010
WD0354-368	B05511010	WD1120+439	Z90319010
WD0357+286J	B05510010	HS1136+6646	D09201020
WD0416-550	E9031501000	WD1202+608	M10523070
WD0416+402	Z90308010	WD1210+533	B05306010
WD0421+336	B05506010	WD1211+332	P20408010
WD0455-281	P10411030	WD1214+267	B05305010
WD0457-103	A05403030	WD1224+309	D07102010
WD0501+524	Coadded*	WD1234+481	M10524020
WD0505+012	B05303010	WD1253+378	B05301010
WD0512+326	A05407070	WD1254+223	M10104020
WD0549+158	P20417010	WD1302+597	C02601010
WD0603-483	Z90309010	WD1314+293	P10423010
WD0612+177	B11901010	WD1337+701	B11903010
WD0621-376	P10415010	WD1342+443	A03404020

6.3 Appendix B

Table 6.16. Summary of the FUSE data used in this paper

Name	Observation	Name	Observation
WD1440+753	Z90322010	WD2124+191	A05409090
WD1529+486	P20401010	WD2123-226	B05504010
WD1550+130	E11201010	WD2146-433	Z90339010
WD1603+432	Z90324010	WD2154+404	D07104010
REJ1614-085	B11904010	WD2152-548	M10515010
WD1615-154	P20419010	WD2153-419	Z90340010
WD1620+647	Z90325010	WD2211-491	S52308020
WD1631+781	M10528040	WD2211-495	M10303160
WD1635+529	C05002010	WD2249+585J	P25101010
WD1636+351	P20402010	WD2300-070J	A05410100
WD1650+724	E90302020	WD2309+105	P20424010
WD1648+407	Z90326010	WD2321-549	Z90342010
WD1653+778	E90316010	WD2331-475	M10517010
WD1658+441	B12202010	WD2350-706	A05408090/B12002010
WD1711+668	E90304010	WD2353+026	E56818010
WD1725+586	Z90327010		
WD1734+742	B05501010		
WD1738+668J	M10529020		
WD1921-566	B05505010		
WD1740-706	U10936030		
WD1800+685	M10530050		
WD1819+580	Z90328010		
WD1845+683	Z90329010/Z99003010		
WD1847-223	P20405010		
WD1917+599	Z90330010		
RE-J1925-56	A05411110		
WD1943+500J	Z90331010		
WD1950-432	Z90332010		
WD2000-561.1	Z90333010		
WD2004-605	P20422010		
WD2011+398	M10531020		
WD2014-575	Z90334010		
WD2020-425	Z90335010		
WD2025+554	Z90336020		
WD2032+248	B11905010		
WD2043-635	Z90337010		
WD2046+396	E56817010		
WD2111+498	M10532010		
WD2116+736	Z90338020		

Table 6.17. WD0501+524 observations

Observation	Observation
M1030401000	M1030415000
M1010202000	M1030507000
M1030515000	M1030508000
M1030519000	M1030509000
M1030603000	M1030504000
M1030604000	M1030502000
M1030517000	M1030503000
M1030516000	M1030510000
M1030513000	M1030606000
M1030514000	M1030610000
M1030511000	M1030609000
M1010201000	M1030608000
M1030506000	M1030403000
M1030412000	M1030612000
M1030413000	M1030615000
S3070101000	M1030614000
M1030409000	M1030613000
M1030408000	M1030616000
M1030407000	M1052001000
M1030405000	M1030607000
S4057604000	M1030605000

Table 6.18: Positional data of sample

Name	Distance	Reff	l(deg)	b(deg)
WD1635+529	122.5400	(Hipparcos Parallax)	-12.9400	28.6700
WD1736+134	93.6300	(Hipparcos Parallax)	37.0880	21.9897
WD2123-226	122.1000	(Hipparcos Parallax)	26.9783	-43.5887
WD0114-027				
WD0659+130				
WD0001+433			113.8958	-18.4383
WD0004+330	98.8000	Vennes et al. (1997a)	112.4803	-28.6882
WD0027-636				
WD0041+092	55	Kellett et al. (1995)		
WD0050-332	58.0000	Holberg et al. (1998)	299.1404	-84.1156
WD0106-358	95.5	Farihi et al. (2005)	280.8752	-80.8137
WD0113+002				
WD0131-164	120	Farihi et al. (2005)	167.2592	-75.1537
WD0147+674	99.0000	Savage & Lehner (2006)	128.5790	5.4420
WD0226-615	199.2000	(Hipparcos Parallax)	284.2048	-52.1567
WD0229-481	-		266.6179	-61.5914
WD0232+035	74.4000	(Hipparcos Parallax)	165.9697	-50.2699
WD0235-125			165.9697	-50.2699
WD0236+498	96.0000	Vennes et al. (1997a)	140.1523	-9.1465
WD0252-055	104.4900	(Hipparcos Parallax)	181.8555	-53.4660
WD0310-688	10.1520	(Hipparcos Parallax)	286.1960	-43.7325
WD0320-539			267.3001	-51.6355
WD0325-857			299.8575	-30.6815
WD0346-011	29.0000	Vennes et al. (1997a)	188.9534	-40.0974
WD0353+284	130.00	Vennes et al. (1997b)	165.0760	-18.6700
Continued on next page				

Table 6.18 – continued from previous page

Name	Distance	Reff	l(deg)	b(deg)
WD0354-368	400	Barstow et al. (2001a)	238.6405	-49.9773
WD0416+402	228.0000	Vennes et al. (1997a)	160.2030	-6.9504
WD0421+336	41.6700	(Hipparcos Parallax)	165.5307	-10.7472
WD0455-282				
WD0457-103	54.6700	(Hipparcos Parallax)	209.5508	-29.4078
WD0501+524	59.0000	Vennes et al. (1997a)	155.9533	7.0990
WD0512+326	25.1400	(Hipparcos Parallax)	173.2988	-3.3574
WD0549+158	49.0000	Vennes et al. (1997a)	192.0286	-5.3382
WD0603-483	178.0000	Vennes et al. (1997a)	255.7816	-27.3629
WD0621-376	78.0000	Holberg et al. (1998)	245.4061	-21.4282
WD0715-703	94.0000	Vennes et al. (1997a)	281.4000	-23.5000
WD0802+413	139.3	Farihi et al. (2005)	179.2160	30.9430
WD0809-728	121.0000	Vennes et al. (1997a)	285.8172	-20.4225
WD0830-535	82.0000	Vennes et al. (1997a)	270.1121	-8.2658
WD0905-724	139.2700	(Hipparcos Parallax)	287.8249	-16.7702
WD0937+505	218.0000	Savage & Lehner (2006)	166.9021	47.1203
WD1017-138	-	-		
WD1021+266	250.0000	Burleigh et al. (1997)	205.7172	57.2139
WD1024+326	-	-	194.5166	58.4075
WD1029+537	116.0000	Vennes et al. (1997a)	157.5135	53.2437
WD1040+492	230.0000	Vennes et al. (1997a)	162.6693	57.0087
WD1041+580	93.0000	Vennes et al. (1997a)	150.1202	52.1729
WD1056+516	-	-	156.3345	57.8174
WD1057+719	132.4	Farihi et al. (2005)	134.4790	42.9215
WD1109-225	81.5600	(Hipparcos Parallax)	274.7780	34.5360
WD1234+481	134.9	Farihi et al. (2005)	129.81	69.0086
Continued on next page				

Table 6.18 – continued from previous page

Name	Distance	Reff	l(deg)	b(deg)
WD1254+223	67.0000	Vennes et al. (1997a)	317.2548	84.7465
WD1302+597	-	-	119.8240	57.5920
WD1314+293	68.0000	Finley et al. (1997)	54.1058	84.1621
WD1337+701	24.8	Farihi et al. (2005)	117.1761	46.3094
WD1342+442	-	-	94.2960	69.9207
WD1440+753	98.0000	Vennes et al. (1997a)	114.0981	40.1163
WD1528+487	-	-	-	-
WD1550+130	-	-	23.6541	45.3389
WD1603+432	114.0000	Savage & Lehner (2006)	68.2202	47.9333
WD1611-084	93.0000	Vennes (1999)	4.2992	29.2973
WD1615-154	48.8	Farihi et al. (2005)	-	-
WD1620+647	174.0000	Savage & Lehner (2006)	96.6070	40.1640
WD1631+781	67.0000	Vennes et al. (1997a)	111.2953	33.5782
WD1636+351	115.3	Farihi et al. (2005)	56.9834	41.3968
WD1648+407	200.0000	Vennes et al. (1997a)	64.6411	39.6014
WD1711+668	-	-	97.1978	34.5669
WD1725+586	-	-	87.1717	33.8299
WD1734+742	103.0000	(Hipparcos Parallax)	105.4927	31.3534
WD1800+685	159.0000	Vennes et al. (1997a)	98.7314	29.7751
WD1819+580	-	-	86.9980	26.7632
WD1844-223	62.0000	Vennes et al. (1997a)	12.5022	-9.2474
WD1845+683	125.0000	Vennes et al. (1997a)	98.8130	25.6500
WD1917+599	-	-	-	-
WD1921-566	-	-	340.6306	-27.0091
WD1942+499	105.0000	Vennes et al. (1997a)	83.0765	12.7465
WD1950-432	140.0000	Savage & Lehner (2006)	356.5050	-29.0920
Continued on next page				

Table 6.18 – continued from previous page

Name	Distance	Reff	l(deg)	b(deg)
WD2000-561	198.0000	Savage & Lehner (2006)	341.7842	-32.2504
WD2004-605	58.0000	Vennes et al. (1997a)	336.5813	-32.8586
WD2011+398	141.0000	Vennes et al. (1997a)	77.0018	3.1835
WD2014-575	51.0000	Vennes et al. (1997a)	340.2003	-34.2481
WD2020-425	-	-	358.3597	-34.4540
WD2043-635	-	-	332.3600	-36.9200
WD2111+498	50.0000	Vennes et al. (1997a)	91.3710	1.1342
WD2116+736	177.0000	Savage & Lehner (2006)	109.3900	16.9240
WD2124+191	46.0000	Vennes et al. (1998)	70.4318	-21.9783
WD2124-224				
WD2146-433	362.0000	Savage & Lehner (2006)	357.1800	-50.1260
WD2152-548	-	-	340.5000	-48.7000
WD2211-495	53.0000	Vennes et al. (1997a)	345.7883	-52.6217
WD2257-073	88.5000	Vennes et al. (1998)	65.1744	-56.9335
WD2309+105	79.0000	Vennes et al. (1997a)	87.2625	-45.1174
WD2321-549	192.0000	Savage & Lehner (2006)	326.9080	-58.2104
WD2331-475	82.0000	Vennes et al. (1997a)	334.8358	-64.8080
WD2350-706	92.0000	Barstow et al. (2001a)	309.9147	-45.9375

Bibliography

- Adams, W. S. (1941), ‘Some Results with the COUDÉ Spectrograph of the Mount Wilson Observatory.’, *ApJ* 93, 11–+.
- Bannister, N. P., Barstow, M. A., Holberg, J. B. & Bruhweiler, F. C. (2003), ‘Circumstellar features in hot DA white dwarfs’, *MNRAS* 341, 477–495.
- Barnard, E. E. (1895), ‘On a great photographic nebula near Antares’, *Astronomische Nachrichten* 138, 211–+.
- Barrett, A. H. (1969), ‘Discovery of interstellar water vapour.’, *Comments At. Mol. Phys.*, Vol. 1, No. 5, p. 93 - 96 1, 93–96.
- Barstow, M. A., Bond, H. E., Burleigh, M. R. & Holberg, J. B. (2001a), ‘Resolving Sirius-like binaries with the Hubble Space Telescope’, *MNRAS* 322, 891–900.
- Barstow, M. A., Dobbie, P. D., Holberg, J. B., Hubeny, I. & Lanz, T. (1997), ‘Interstellar and photospheric opacity from EUV spectroscopy of DA white dwarfs’, *MNRAS* 286, 58–76.
- Barstow, M. A., Good, S. A., Burleigh, M. R., Hubeny, I., Holberg, J. B. & Levan, A. J. (2003), ‘A comparison of DA white dwarf temperatures and gravities from FUSE Lyman line and ground-based Balmer line observations’, *MNRAS* 344, 562–574.
- Barstow, M. A., Good, S. A., Holberg, J. B., Burleigh, M. R., Bannister, N. P., Hubeny, I. & Napiwotzki, R. (2002), ‘FUSE observations of PG1342+444: new insights into the nature of the hottest DA white dwarfs’, *MNRAS* 330, 425–434.
- Barstow, M. A., Holberg, J. B., Hubeny, I., Good, S. A., Levan, A. J. & Meru, F. (2001b), ‘A comparison of DA white dwarf temperatures and gravities from Lyman and Balmer line studies’, *MNRAS* 328, 211–222.
- Barstow, M. A., Wesemael, F., Holberg, J. B., Buckley, D. A. H., Stobie, R. S., Mittaz, J. P. D., Fontaine, G., Rosen, S. R., Demers, S., Lamontagne, R., Irwin, M. H., Bergeron, P., Kepler, S. O. & Vennes, S. (1994a), ‘A New Hot DA White Dwarf in a Region of Exceptionally Low HI Density’, *MNRAS* 267, 647–+.

- Bergeron, P., Liebert, J. & Fulbright, M. S. (1995), 'Masses of DA white dwarfs with gravitational redshift determinations', *ApJ* 444, 810–817.
- Bergeron, P., Saffer, R. A. & Liebert, J. (1992), 'A spectroscopic determination of the mass distribution of DA white dwarfs', *ApJ* 394, 228–247.
- Bloecker, T. (1995), 'Stellar evolution of low and intermediate-mass stars. I. Mass loss on the AGB and its consequences for stellar evolution.', *A&A* 297, 727–+.
- Bodenheimer, P., Tenorio-Tagle, G. & Yorke, H. W. (1979), 'The gas dynamics of H II regions. II - Two-dimensional axisymmetric calculations', *ApJ* 233, 85–96.
- Borkowski, K. J., Balbus, S. A. & Fristrom, C. C. (1990), 'Radiative magnetized thermal conduction fronts', *ApJ* 355, 501–517.
- Bowyer, C. S., Field, G. B. & Mack, J. F. (1968), 'Detection of an Anisotropic Soft X-Ray Background Flux', *Nature* 217, 32–+.
- Bruhweiler, F. C. (1982), The distribution of interstellar gas within 50pc of the Sun, in Y. Kondo, ed., 'Advances in Ultraviolet Astronomy', pp. 125–133.
- Bruhweiler, F. C. & Cheng, K.-P. (1988), 'The stellar radiation field and the ionization of H and He in the local interstellar medium', *ApJ* 335, 188–196.
- Burleigh, M. R., Barstow, M. A. & Fleming, T. A. (1997), 'A search for hidden white dwarfs in the ROSAT extreme ultraviolet survey', *MNRAS* 287, 381–401.
- Cash, W., Bowyer, S. & Lampton, M. (1979), 'Interstellar absorption of the extreme ultraviolet flux from two hot white dwarfs', *A&A* 80, 67–70.
- Chayer, P., Oliveira, C., Dupuis, J., Moos, H. W. & Welsh, B. Y. (2006), Probing the Atmospheres of Hot DA White Dwarfs with O VI, in G. Sonneborn, H. W. Moos & B.-G. Andersson, eds, 'Astrophysics in the Far Ultraviolet: Five Years of Discovery with FUSE', Vol. 348 of *Astronomical Society of the Pacific Conference Series*, pp. 209–+.
- Cheung, A. C., Rank, D. M., Townes, C. H., Thornton, D. D. & Welch, W. J. (1968), 'Detection of NH₃ Molecules in the Interstellar Medium by Their Microwave Emission', *Physical Review Letters* 21, 1701–1705.
- Chieze, J.-P., Pineau des Forets, G. & Flower, D. R. (1998), 'Temporal evolution of MHD shocks in the interstellar medium', *MNRAS* 295, 672–+.
- Cowie, L. L., Jenkins, E. B., Songaila, A. & York, D. G. (1979), 'O VI absorption in interstellar cloud surfaces', *ApJ* 232, 467–472.
- Cox, D. P. & Helenius, L. (2003), 'Flux-Tube Dynamics and a Model for the Origin of the Local Fluff', *ApJ* 583, 205–228.

- Crawford, I. A., Lallement, R., Price, R. J., Sfeir, D. M., Wakker, B. P. & Welsh, B. Y. (2002), ‘High-resolution observations of interstellar NaI and CaII towards the southern opening of the ‘Local Interstellar Chimney’: probing the disc-halo connection’, *MNRAS* 337, 720–730.
- Danforth, C. W., Howk, J. C., Fullerton, A. W., Blair, W. P. & Sembach, K. R. (2002), ‘An Atlas of Far Ultraviolet Spectroscopic Explorer Sight Lines toward the Magellanic Clouds’, *ApJS* 139, 81–189.
- Diamond, C. J., Jewell, S. J. & Ponman, T. J. (1995), ‘ROSAT EUV observations of DA white dwarfs and late-type stars and the structure of the local interstellar medium’, *MNRAS* 274, 589–601.
- Dixon, W. V. D., Sankrit, R. & Otte, B. (2006), ‘An Extended FUSE Survey of Diffuse O VI Emission in the Interstellar Medium’, *ApJ* 647, 328–349.
- Dixon, W. V., Sahnou, D. J., Barrett, P. E., Civeit, T., Dupuis, J., Fullerton, A. W., Godard, B., Hsu, J.-C., Kaiser, M. E., Kruk, J. W., Lacour, S., Lindler, D. J., Massa, D., Robinson, R. D., Romelfanger, M. L. & Sonnentrucker, P. (2007), ‘CalFUSE Version 3: A Data Reduction Pipeline for the Far Ultraviolet Spectroscopic Explorer’, *PASP* 119, 527–555.
- Driebe, T., Schoenberner, D., Bloeker, T. & Herwig, F. (1998), ‘The evolution of helium white dwarfs. I. The companion of the millisecond pulsar PSR J1012+5307’, *A&A* 339, 123–133.
- Dring, A. R., Linsky, J., Murthy, J., Henry, R. C., Moos, W., Vidal-Madjar, A., Audouze, J. & Landsman, W. (1997), ‘Lyman-Alpha Absorption and the D/H Ratio in the Local Interstellar Medium’, *ApJ* 488, 760–+.
- Dupree, A. K. & Raymond, J. C. (1982), ‘Discovery of highly ionized species in the ultraviolet spectrum of Feige 24’, *ApJ* 263, L63–L67.
- Dupuis, J., Chayer, P., Vennes, S., Kruk, J. W., Torres, L. M. & Sánchez, P. J. (2005), Results from a FUSE Survey of Hot White Dwarfs, in D. Koester & S. Moehler, eds, ‘14th European Workshop on White Dwarfs’, Vol. 334 of *Astronomical Society of the Pacific Conference Series*, pp. 191–+.
- Dupuis, J., Vennes, S., Bowyer, S., Pradhan, A. K. & Thejll, P. (1994), Evidence for Homogeneous Ionization of Helium in the Local Interstellar Medium from EUVE Spectroscopy of Hot DA Stars, in ‘Bulletin of the American Astronomical Society’, Vol. 26 of *Bulletin of the American Astronomical Society*, pp. 901–+.
- Dupuis, J., Vennes, S., Bowyer, S., Pradhan, A. K. & Thejll, P. (1995), ‘Hot White Dwarfs in the Local Interstellar Medium: Hydrogen and Helium Interstellar Column Densities and Stellar Effective Temperatures from Extreme-Ultraviolet Explorer Spectroscopy’, *ApJ* 455, 574–+.
- Egger, R. J. & Aschenbach, B. (1995), ‘Interaction of the Loop I supershell with the Local Hot Bubble’, *A&A* 294, L25–L28.

- Farihi, J., Becklin, E. E. & Zuckerman, B. (2005), 'Low-Luminosity Companions to White Dwarfs', *ApJS* 161, 394–428.
- Federman, S. R., Sheffer, Y., Lambert, D. L. & Smith, V. V. (2005), 'Far Ultraviolet Spectroscopic Explorer Measurements of Interstellar Fluorine', *ApJ* 619, 884–890.
- Finley, D. S., Basri, G. & Bowyer, S. (1990), 'The temperature scale of hot DA white dwarfs - Temperatures from far-ultraviolet continuum fluxes', *ApJ* 359, 483–498.
- Finley, D. S., Koester, D. & Basri, G. (1997), 'The Temperature Scale and Mass Distribution of Hot DA White Dwarfs', *ApJ* 488, 375–+.
- Fontaine, G., Brassard, P. & Bergeron, P. (2001), 'The Potential of White Dwarf Cosmochronology', *PASP* 113, 409–435.
- Friedman, S. D., Howk, J. C., Andersson, B.-G., Sembach, K. R., Ake, T. B., Roth, K., Sahnou, D. J., Savage, B. D., York, D. G., Sonneborn, G., Vidal-Madjar, A. & Wilkinson, E. (2000), 'Far Ultraviolet Spectroscopic Explorer Observations of Interstellar Gas toward the Large Magellanic Cloud Star SK -67deg05', *ApJ* 538, L39–L42.
- Froning, C. S., Long, K. S., Drew, J. E., Knigge, C. & Proga, D. (2001), 'FUSE Observations of U Geminorum during Outburst and Decline', *ApJ* 562, 963–984.
- Froning, C. S., Long, K. S. & Knigge, C. (2003), 'Accretion and Outflow in Interacting Binary Systems: Far Ultraviolet Spectroscopic Explorer Observations of the Nova-like Cataclysmic Variable UX Ursae Majoris', *ApJ* 584, 433–447.
- Giclas, H. L., Burnham, R. & Thomas, N. G. (1972), 'Proper motion survey of the south galactic pole', *Lowell Observatory Bulletin* 7, 217–254.
- Gnacinski, P. & Krogulec, M. (2006), 'Composition of the Interstellar Medium', *Acta Astronomica* 56, 373–384.
- Goldsmith, D. W., Habing, H. J. & Field, G. B. (1969), 'Thermal Properties of Interstellar Gas Heated by Cosmic Rays', *ApJ* 158, 173–+.
- Green, J., Jelinsky, P. & Bowyer, S. (1990), 'The extreme ultraviolet spectrum of G191 - B2B and the ionization of the local interstellar medium', *ApJ* 359, 499–505.
- Greenstein, J. L. (1969), 'The Lowell Suspect White Dwarfs', *ApJ* 158, 281–+.
- Greenstein, J. L. (1986), 'White Dwarfs in Wide Binaries - Part Two - Double Degenerates and Composite Spectra', *AJ* 92, 867–+.
- Greenstein, J. L., Oke, J. B. & Shipman, H. L. (1971), 'Effective Temperature, Radius, and Gravitational Redshift of Sirius B', *ApJ* 169, 563–+.
- Gundermann, E. J., Goldstein, Jr., S. J. & Lilley, A. E. (1965), 'Microwave Spectra of OH in the Direction of the Galactic Center.', *AJ* 70, 321–+.

- Guseinov, O. K., Novruzova, K. I. & Rustamov, I. S. (1983), 'Atmospheric parameters and mass distribution of DA-white dwarfs', *Ap&SS* 96, 1–23.
- Habing, H. J. (1968), 'The interstellar radiation density between 912 Å and 2400 Å', *Bull. Astron. Inst. Netherlands* 19, 421–+.
- Hartmann, D. & Burton, W. B. (1997), *Atlas of Galactic Neutral Hydrogen*, Atlas of Galactic Neutral Hydrogen, by Dap Hartmann and W. Butler Burton, pp. 243. ISBN 0521471117. Cambridge, UK: Cambridge University Press, February 1997.
- Hartmann, J. (1904), 'Investigations on the spectrum and orbit of delta Orionis.', *ApJ* 19, 268–286.
- Hebrard, G. & Moos, H. W. (2003), 'The Deuterium-to-Oxygen Ratio in the Interstellar Medium', *ApJ* 599, 297–311.
- Heger, M. L. (1918), 'Bulletin Number 326 - The occurrence of stationary D lines of sodium in the spectroscopic binaries, Beta Scorpii and delta Orionis.', *Lick Observatory Bulletin* 10, 59–63.
- Heiles, C. (1987), 'Supernovae versus models of the interstellar medium and the gaseous halo', *ApJ* 315, 555–566.
- Heise, J., Paerels, F. B. S., Bleeker, J. A. M. & Brinkman, A. C. (1988), 'The high-resolution soft X-ray spectrum of HZ 43. II - Bolometric X-ray flux, effective temperature, and radius', *ApJ* 334, 958–970.
- Herald, J. E. & Bianchi, L. (2002), 'The Binary Central Star of the Planetary Nebula A35', *ApJ* 580, 434–446.
- Hoard, D. W., Szkody, P., Froning, C. S., Long, K. S. & Knigge, C. (2003), 'Observations of the SW Sextantis Star DW Ursae Majoris with the Far Ultraviolet Spectroscopic Explorer', *AJ* 126, 2473–2486.
- Hobbs, L. M. (1974), 'A comparison of interstellar Na I, Ca II, and K I absorption.', *ApJ* 191, 381–393.
- Holberg, J. B., Barstow, M. A., Bruhweiler, F. C. & Hubeny, I. (2000), STIS Observations of the Photospheric Stratification of Heavy Elements in Hot DA White Dwarfs, in 'Bulletin of the American Astronomical Society', Vol. 32 of *Bulletin of the American Astronomical Society*, pp. 1543–+.
- Holberg, J. B., Barstow, M. A. & Sion, E. M. (1998), 'A High-Dispersion Spectroscopic Survey of the Hot White Dwarfs: The IUE NEWSIPS SWP Echelle Data Set', *ApJS* 119, 207–238.
- Holberg, J. B., Basile, J. & Wesemael, F. (1986), 'DA white dwarf effective temperatures determined from IUE Lyman-alpha profiles', *ApJ* 306, 629–641.
- Holberg, J. B. & Bergeron, P. (2006), 'Calibration of Synthetic Photometry Using DA White Dwarfs', *AJ* 132, 1221–1233.

- Holberg, J. B., Wesemael, F., Wegner, G. & Bruhweiler, F. C. (1985), 'An analysis of the bright white dwarf CD - 38 deg 10980', *ApJ* 293, 294–302.
- Hubeny, I. & Lanz, T. (1995), 'Non-LTE line-blanketed model atmospheres of hot stars. 1: Hybrid complete linearization/accelerated lambda iteration method', *ApJ* 439, 875–904.
- Huggins, W. & Miller, W. A. (1863), 'On the Spectra of Some of the Nebulae. And On the Spectra of Some of the Fixed Stars. [Abstract]', *Royal Society of London Proceedings Series I* 13, 491–493.
- Humason, M. L. & Zwicky, F. (1947), 'A Search for Faint Blue Stars.', *ApJ* 105, 85–+.
- Hurwitz, M. & Bowyer, S. (1995), 'ORFEUS Observations of G191-B2B: Neutral and Ionized Gas in the Local Interstellar Medium', *ApJ* 446, 812–+.
- Hurwitz, M., Sasseen, T. P. & Sirk, M. M. (2005), 'Observations of Diffuse Extreme-Ultraviolet Emission with the Cosmic Hot Interstellar Plasma Spectrometer (CHIPS)', *ApJ* 623, 911–916.
- Inoue, H., Koyama, K., Matsuoka, M., Ohashi, T., Tanaka, Y. & Tsunemi, H. (1979), 'Evidence of O VII emission line in diffuse soft X-rays from the N_H minimum region in Hercules', *ApJ* 227, L85–L88.
- Jelinsky, P., Bowyer, S. & Basri, G. (1988), Observations of interstellar absorption lines towards hot white dwarfs, in E. J. Rolfe, ed., 'A Decade of UV Astronomy with the IUE Satellite, Volume 2', Vol. 2, pp. 235–237.
- Jenkins, E. B. & Meloy, D. A. (1974), 'A survey with Copernicus of interstellar O VI absorption', *ApJ* 193, L121–L125.
- Jenkins, E. B., Oegerle, W. R., Gry, C., Vallerga, J., Sembach, K. R., Shelton, R. L., Fernet, R., Vidal-Madjar, A., York, D. G., Linsky, J. L., Roth, K. C., Dupree, A. K. & Edelstein, J. (2000), 'The Ionization of the Local Interstellar Medium as Revealed by Far Ultraviolet Spectroscopic Explorer Observations of N, O, and AR toward White Dwarf Stars', *ApJ* 538, L81–L85.
- Jenkins, E. B. & Shaya, E. J. (1979), 'A survey of interstellar C I - Insights on carbon abundances, UV grain albedos, and pressures in the interstellar medium', *ApJ* 231, 55–72.
- Kellett, B. J., Bromage, G. E., Brown, A., Jeffries, R. D., James, D. J., Kilkenny, D., Robb, R. M., Wonnacott, D., Lloyd, C. & Clayton, C. (1995), 'RE 0044+09: A new K dwarf rapid rotator with a white dwarf companion', *ApJ* 438, 364–375.
- Kimble, R. A., Davidsen, A. F., Blair, W. P., Bowers, C. W., Dixon, W. V. D., Durrance, S. T., Feldman, P. D., Ferguson, H. C., Henry, R. C., Kriss, G. A., Kruk, J. W., Long, K. S., Moos, H. W. & Vancura, O. (1993), 'Extreme ultraviolet observations of G191-B2B and the local interstellar medium with the Hopkins Ultraviolet Telescope', *ApJ* 404, 663–672.

- Kimble, R. A., Davidsen, A. F., Blair, W. P., Bowers, C. W., Dixon, W. V., Durrance, S. T., Feldman, P. D., Henry, R. C., Kruk, J. W., Kriss, G. A., Moos, H. W., Vancura, O., Ferguson, H. C. & Long, K. S. (1991), EUV Observations of G191-B2B and the Local ISM with the Hopkins Ultraviolet Telescope, in 'Bulletin of the American Astronomical Society', Vol. 23 of *Bulletin of the American Astronomical Society*, pp. 883–+.
- Kimura, H., Mann, I. & Jessberger, E. K. (2003), 'Elemental Abundances and Mass Densities of Dust and Gas in the Local Interstellar Cloud', *ApJ* 582, 846–858.
- Koester, D., Schulz, H. & Weidemann, V. (1979), 'Atmospheric parameters and mass distribution of DA white dwarfs', *A&A* 76, 262–275.
- Koutroumpa, D., Lallement, R., Kharchenko, V. & Dalgarno, A. (2008), 'The Solar Wind Charge-eXchange Contribution to the Local Soft X-ray Background', *Space Science Reviews* pp. 87–+.
- Kruk, J. W., Howk, J. C., André, M., Moos, H. W., Oegerle, W. R., Oliveira, C., Sembach, K. R., Chayer, P., Linsky, J. L., Wood, B. E., Ferlet, R., Hébrard, G., Lemoine, M., Vidal-Madjar, A. & Sonneborn, G. (2002), 'Abundances of Deuterium, Nitrogen, and Oxygen toward HZ 43A: Results from the FUSE Mission', *ApJS* 140, 19–36.
- Kruk, J. W., Howk, J. C., Andre, M., Moos, H. W., Oegerle, W. R., Oliveira, C., Sembach, K. R., Chayer, P., Linsky, J. L., Wood, B. E., Ferlet, R., Hebrard, G., Lemoine, M., Vidal-Madjar, A., Sonneborn, G. & FUSE Science Team (2000), D/O and D/N towards HZ 43: First FUSE Results, in 'Bulletin of the American Astronomical Society', Vol. 32 of *Bulletin of the American Astronomical Society*, pp. 1450–+.
- Kuan, Y.-J., Charnley, S. B., Huang, H.-C., Tseng, W.-L. & Kisiel, Z. (2003), 'Interstellar Glycine', *ApJ* 593, 848–867.
- Lajoie, C.-P. & Bergeron, P. (2007), 'A Comparative Study of Optical and Ultraviolet Effective Temperatures for DA White Dwarfs from the IUE Archive', *ApJ* 667, 1126–1138.
- Lallement, R. (2007), 'The Local Interstellar Medium: Peculiar or Not?', *Space Science Reviews* 130, 341–353.
- Lallement, R., Ferlet, R., Lagrange, A. M., Lemoine, M. & Vidal-Madjar, A. (1995), 'Local Cloud structure from HST-GHRS.', *A&A* 304, 461–+.
- Lallement, R., Welsh, B. Y., Vergely, J. L., Crifo, F. & Sfeir, D. (2003), '3D mapping of the dense interstellar gas around the Local Bubble', *A&A* 411, 447–464.
- Lauroesch, J. T., York, D. G., Truran, J. W. & Timmes, F. X. (2004), The Abundance of Interstellar Fluorine, in 'Bulletin of the American Astronomical Society', Vol. 36 of *Bulletin of the American Astronomical Society*, pp. 1437–+.

- Lehner, N., Gry, C., Sembach, K. R., Hébrard, G., Chayer, P., Moos, H. W., Howk, J. C. & Désert, J.-M. (2002), 'Deuterium Abundance toward WD 0621-376: Results from the FUSE Mission', *ApJS* 140, 81–89.
- Lehner, N., Jenkins, E. B., Gry, C., Moos, H. W., Chayer, P. & Lacour, S. (2003), 'Far Ultraviolet Spectroscopic Explorer Survey of the Local Interstellar Medium within 200 Parsecs', *ApJ* 595, 858–879.
- Lemoine, M., Vidal-Madjar, A., Bertin, P., Ferlet, R., Gry, C. & Lallement, R. (1996), 'The interstellar D/H ratio toward G191-B2B from GHRS observations.', *A&A* 308, 601–617.
- Lemoine, M., Vidal-Madjar, A., Hébrard, G. & and 19 co-authors (2002), 'Deuterium Abundance toward G191-B2B: Results from the FUSE Mission', *ApJS* 140, 67–80.
- Leroy, J. L. (1999), 'Interstellar dust and magnetic field at the boundaries of the Local Bubble. Analysis of polarimetric data in the light of HIPPARCOS parallaxes', *A&A* 346, 955–960.
- Lilienthal, D. & de Boer, K. S. (1991), 'Location and thickness of the nearest neutral gas cloud in the direction of Auriga-Perseus', *A&AS* 87, 471–479.
- Linsky, J. L., Redfield, S., Wood, B. E. & Piskunov, N. (2000), 'The Three-dimensional Structure of the Warm Local Interstellar Medium. I. Methodology', *ApJ* 528, 756–766.
- Margon, B., Liebert, J., Lampton, M., Spinrad, H., Bowyer, S. & Gatewood, G. (1976), 'An extrasolar extreme-ultraviolet object. II - The nature of HZ 43', *ApJ* 209, 525–535.
- Marsh, M. C., Barstow, M. A., Buckley, D. A., Burleigh, M. R., Holberg, J. B., Koester, D., O'Donoghue, D., Penny, A. J. & Sansom, A. E. (1997b), 'An EUV-selected sample of DA white dwarfs from the ROSAT All-Sky Survey - I. Optically derived stellar parameters', *MNRAS* 286, 369–383.
- McClure-Griffiths, N. M., Dickey, J. M., Gaensler, B. M. & Green, A. J. (2003), 'Loops, Drips, and Walls in the Galactic Chimney GSH 277+00+36', *ApJ* 594, 833–843.
- McKee, C. F. & Ostriker, J. P. (1977), 'A theory of the interstellar medium - Three components regulated by supernova explosions in an inhomogeneous substrate', *ApJ* 218, 148–169.
- Mebold, U. & Hills, D. L. (1975), 'The intercloud HI gas in the direction of Cassiopeia A and Cygnus A', *A&A* 42, 187–194.
- Merrill, P. W. & Wilson, O. C. (1938), 'Unidentified Interstellar Lines in the Yellow and Red', *ApJ* 87, 9–+.
- Moos, H. W., Cash, W. C., Cowie, L. L., Davidsen, A. F., Dupree, A. K., Feldman, P. D., Friedman, S. D., Green, J. C. & Green, R. F. c. (2000), 'Overview of the Far Ultraviolet Spectroscopic Explorer Mission', *ApJ* 538, L1–L6.

- Moos, H. W., Sembach, K. R., Vidal-Madjar, A., York, D. G., Friedman, S. D., Hébrard, G., Kruk, J. W., Lehner, N., Lemoine, M., Sonneborn, G., Wood, B. E., Ake, T. B., André, M., Blair, W. P., Chayer, P., Gry, C., Dupree, A. K., Ferlet, R., Feldman, P. D., Green, J. C., Howk, J. C., Hutchings, J. B., Jenkins, E. B., Linsky, J. L., Murphy, E. M., Oegerle, W. R., Oliveira, C., Roth, K., Sahnou, D. J., Savage, B. D., Shull, J. M., Tripp, T. M., Weiler, E. J., Welsh, B. Y., Wilkinson, E. & Woodgate, B. E. (2002), 'Abundances of Deuterium, Nitrogen, and Oxygen in the Local Interstellar Medium: Overview of First Results from the FUSE Mission', *ApJS* 140, 3–17.
- Morton, D. C. (1975), 'Interstellar absorption lines in the spectrum of zeta Ophiuchi', *ApJ* 197, 85–115.
- Morton, D. C. (1978), 'Interstellar absorption lines in the spectrum of Zeta Puppis', *ApJ* 222, 863–880.
- Mullally, F., Kilic, M., Reach, W. T., Kuchner, M. J., von Hippel, T., Burrows, A. & Winget, D. E. (2007), 'A Spitzer White Dwarf Infrared Survey', *ApJS* 171, 206–218.
- Napiwotzki, R., Barstow, M. A., Fleming, T., Holweger, H., Jordan, S. & Werner, K. (1993), 'Analysis of the DA white dwarf HZ 43 A and its companion star', *A&A* 278, 478–486.
- Narayan, R. (1993), The physics of pulsar scintillation., in 'Royal Society Discussion Meeting: Pulsars as physics laboratories, p. 151 - 165', pp. 151–165.
- Nozawa, T., Kozasa, T. & Habe, A. (2006), Dust Destruction In The High-velocity Shocks Driven By Supernovae In The Early Universe, in 'Bulletin of the American Astronomical Society', Vol. 38 of *Bulletin of the American Astronomical Society*, pp. 122–+.
- Oegerle, W. R., Jenkins, E. B., Shelton, R. L., Bowen, D. V. & Chayer, P. (2005), 'A Survey of O VI Absorption in the Local Interstellar Medium', *ApJ* 622, 377–389.
- Oegerle, W. R., Tripp, T. M., Sembach, K. R., Jenkins, E. B., Bowen, D. V., Cowie, L. L., Green, R. F., Kruk, J. W., Savage, B. D., Shull, J. M. & York, D. G. (2000), 'Far Ultraviolet Spectroscopic Explorer Observations of the Galactic and Intergalactic Medium toward H1821+643', *ApJ* 538, L23–L26.
- Oliveira, C. M., Dupuis, J., Chayer, P. & Moos, H. W. (2005), 'O/H in the Local Bubble', *ApJ* 625, 232–241.
- Oliveira, C. M., Moos, H. W., Chayer, P. & Kruk, J. W. (2006), 'Variations in D/H and D/O from New Far Ultraviolet Spectroscopic Explorer Observations', *ApJ* 642, 283–306.
- Otte, B. & Dixon, W. V. D. (2006), 'The Far Ultraviolet Spectroscopic Explorer Survey of O VI Emission in the Milky Way', *ApJ* 647, 312–327.

- Paresce, F. (1984), 'On the distribution of interstellar matter around the sun', *AJ* 89, 1022–1037.
- Perryman, M. A. C., Lindegren, L., Kovalevsky, J., Hoeg, E., Bastian, U., Bernacca, P. L., Cr ez e, M., Donati, F., Grenon, M., van Leeuwen, F., van der Marel, H., Mignard, F., Murray, C. A., Le Poole, R. S., Schrijver, H., Turon, C., Arenou, F., Froeschl e, M. & Petersen, C. S. (1997), 'The HIPPARCOS Catalogue', *A&A* 323, L49–L52.
- Probst, R. G. (1983), 'An infrared search for very low mass stars - JHK photometry and results for composite systems', *ApJS* 53, 335–349.
- Rand, R. J. & Kulkarni, S. R. (1989), 'The local Galactic magnetic field', *ApJ* 343, 760–772.
- Rand, R. J. & Lyne, A. G. (1994), 'New Rotation Measures of Distant Pulsars in the Inner Galaxy and Magnetic Field Reversals', *MNRAS* 268, 497–+.
- Redfield, S. & Linsky, J. L. (2000), 'The Three-dimensional Structure of the Warm Local Interstellar Medium. II. The Colorado Model of the Local Interstellar Cloud', *ApJ* 534, 825–837.
- Redfield, S. & Linsky, J. L. (2002), 'The Structure of the Local Interstellar Medium. I. High-Resolution Observations of Fe II, Mg II, and Ca II toward Stars within 100 Parsecs', *ApJS* 139, 439–465.
- Redfield, S. & Linsky, J. L. (2004), 'The Structure of the Local Interstellar Medium. II. Observations of D I, C II, N I, O I, Al II, and Si II toward Stars within 100 Parsecs', *ApJ* 602, 776–802.
- Richter, P., Savage, B. D., Wakker, B. P., Sembach, K. R. & Kalberla, P. M. W. (2001), 'The FUSE Spectrum of PG 0804+761: A Study of Atomic and Molecular Gas in the Lower Galactic Halo and Beyond', *ApJ* 549, 281–292.
- Rogerson, J. B., York, D. G., Drake, J. F., Jenkins, E. B., Morton, D. C. & Spitzer, L. (1973), 'Spectrophotometric Results from the Copernicus Satellite. III. Ionization and Composition of the Intercloud Medium', *ApJ* 181, L110+.
- Russell, H. N. (1935), 'The analysis of spectra and its application in astronomy (George Darwin Lecture, 1935)', *MNRAS* 95, 610–636.
- Sahnow, D. J., Moos, H. W., Ake, T. B. & others, . (2000), 'On-Orbit Performance of the Far Ultraviolet Spectroscopic Explorer Satellite', *ApJ* 538, L7–L11.
- Sahu, M. S., Landsman, W., Bruhweiler, F. C., Gull, T. R., Bowers, C. A., Lindler, D., Feggans, K., Barstow, M. A., Hubeny, I. & Holberg, J. B. (1999), 'The D/H Ratio in Interstellar Gas toward G191-B2B', *ApJ* 523, L159–L163.

- Sanders, W. T., Edgar, R. J., Liedahl, D. A. & Morgenthaler, J. P. (1998), The Soft X-ray Background Spectrum from DXS, *in* D. Breitschwerdt, M. J. Freyberg & J. Truemper, eds, 'IAU Colloq. 166: The Local Bubble and Beyond', Vol. 506 of *Lecture Notes in Physics*, Berlin Springer Verlag, pp. 83–90.
- Savage, B. D. & Lehner, N. (2006), 'Properties of O VI Absorption in the Local Interstellar Medium', *ApJS* 162, 134–160.
- Savage, B. D. & Sembach, K. R. (1996), 'Interstellar Abundances from Absorption-Line Observations with the Hubble Space Telescope', *ARA&A* 34, 279–330.
- Schmutzler, T. & Tscharnuter, W. M. (1993), 'Effective radiative cooling in optically thin plasmas', *A&A* 273, 318–+.
- Schnopper, H. W., Delvaile, J. P., Rocchia, R., Blondel, C., Cheron, C., Christy, J. C., Ducros, R., Koch, L. & Rothenflug, R. (1982), 'Carbon and oxygen X-ray line emission from the interstellar medium', *ApJ* 253, 131–135.
- Seaton, M. J. (1979), 'Interstellar extinction in the UV', *MNRAS* 187, 73P–76P.
- Sembach, K. R., Howk, J. C., Savage, B. D., Shull, J. M. & Oegerle, W. R. (2001), 'Far-Ultraviolet Spectroscopy of the Intergalactic and Interstellar Absorption toward 3C 273', *ApJ* 561, 573–599.
- Sfeir, D. M., Lallement, R., Crifo, F. & Welsh, B. Y. (1999), 'Mapping the contours of the Local bubble: preliminary results', *A&A* 346, 785–797.
- Shaikh, D., Zank, G. P. & Pogorelov, N. (2008), 'Self-consistent interaction of neutrals and shocks in the local interstellar medium', *ArXiv e-prints* .
- Shipman, H. L. (1979), 'Masses and radii of white-dwarf stars. III - Results for 110 hydrogen-rich and 28 helium-rich stars', *ApJ* 228, 240–256.
- Silvestri, N. M., Oswalt, T. D., Wood, M. A., Smith, J. A., Reid, I. N. & Sion, E. M. (2001), 'White Dwarfs in Common Proper Motion Binary Systems: Mass Distribution and Kinematics', *AJ* 121, 503–516.
- Slavin, J. D. (1989), 'Consequences of a conductive boundary on the local cloud. I - No dust', *ApJ* 346, 718–727.
- Smith, R. K. & Dwek, E. (1998), 'Soft X-Ray Scattering and Halos from Dust', *ApJ* 503, 831–+.
- Snow, Jr., T. P. & York, D. G. (1981), 'The detection of interstellar fluorine in the line of sight toward Delta Scorpii', *ApJ* 247, L39–L41.
- Snow, T. P., Destree, J. D. & Jensen, A. G. (2007), 'The Abundance of Interstellar Fluorine and Its Implications', *ApJ* 655, 285–298.
- Snow, T. P. & Witt, A. N. (1996), 'Interstellar Depletions Updated: Where All the Atoms Went', *ApJ* 468, L65+.

- Snowden, S. L., Egger, R., Finkbeiner, D. P., Freyberg, M. J. & Plucinsky, P. P. (1998), 'Progress on Establishing the Spatial Distribution of Material Responsible for the 1.4 keV Soft X-Ray Diffuse Background Local and Halo Components', *ApJ* 493, 715–+.
- Spitzer, Jr., L., Cochran, W. D. & Hirshfeld, A. (1974), 'Column densities of interstellar molecular hydrogen', *ApJS* 28, 373–389.
- Spitzer, L. (1978), *Physical processes in the interstellar medium*, New York Wiley-Interscience, 1978. 333 p.
- Spitzer, L. J. (1956), 'On a Possible Interstellar Galactic Corona.', *ApJ* 124, 20–+.
- Taylor, J. H. & Cordes, J. M. (1993), 'Pulsar distances and the galactic distribution of free electrons', *ApJ* 411, 674–684.
- Tenorio-Tagle, G. & Palous, J. (1987), 'Giant-scale supernova remnants - The role of differential galactic rotation and the formation of molecular clouds', *A&A* 186, 287–294.
- Thejll, P., Ulla, A. & MacDonald, J. (1995), 'Infrared flux excesses from hot subdwarfs.', *A&A* 303, 773–+.
- Vennes, S. (1999), 'Properties of Hot White Dwarfs in Extreme-Ultraviolet/Soft X-Ray Surveys', *ApJ* 525, 995–1008.
- Vennes, S., Christian, D. J., Mathioudakis, M. & Doyle, J. G. (1997b), 'An active K0 IV-V star and a hot white dwarf (EUVE J0702+129) in a wide binary.', *A&A* 318, L9–L12.
- Vennes, S., Christian, D. J. & Thorstensen, J. R. (1998), 'Hot White Dwarfs in the Extreme-Ultraviolet Explorer Survey. IV. DA White Dwarfs with Bright Companions', *ApJ* 502, 763–+.
- Vennes, S., Dupuis, J. & Bowyer, S. (1994b), Insights into the ISM and the Spectral Evolution of White Dwarfs from EUVE Observations of GD 659 and EUVE J2009-604, in 'Bulletin of the American Astronomical Society', Vol. 26 of *Bulletin of the American Astronomical Society*, pp. 1383–+.
- Vennes, S., Thejll, P. A., Galvan, R. G. & Dupuis, J. (1997a), 'Hot White Dwarfs in the Extreme Ultraviolet Explorer Survey. II. Mass Distribution, Space Density, and Population Age', *ApJ* 480, 714–+.
- Vennes, S. & Thorstensen, J. R. (1994a), 'Spectroscopic, orbital, and physical properties of the binary Feige 24 and detection of transient He II absorption in the system', *AJ* 108, 1881–1892.
- Vidal-Madjar, A., Lemoine, M., Ferlet, R., Hebrard, G., Koester, D., Audouze, J., Casse, M., Vangioni-Flam, E. & Webb, J. (1998), 'Detection of spatial variations in the (D/H) ratio in the local interstellar medium', *A&A* 338, 694–712.

- Vidal-Madjar, A., Lemoine, M., Hébrard, G., Désert, J.-M., Ferlet, R., Lecavelier des Etangs, A., André, M., Blair, W. P., Friedman, S. D., Howk, J. C., Kruk, J. W., Moos, H. W., Oegerle, W. R., Sembach, K. R., Chayer, P., Sonneborn, G. & FUSE Science Team (2000), Deuterium abundance toward G191-B2B: First FUSE result, in 'Bulletin of the American Astronomical Society', Vol. 32 of *Bulletin of the American Astronomical Society*, pp. 1450–+.
- Wada, K. & Norman, C. A. (1999), 'The Global Structure and Evolution of a Self-Gravitating Multiphase Interstellar Medium in a Galactic Disk', *ApJ* 516, L13–L16.
- Welsh, B. Y., Lallement, R. & Sallman, S. (2004), Probing the Disk-Halo Connection through the Local Interstellar Chimney, in E. J. Alfaro, E. Pérez & J. Franco, eds, 'How Does the Galaxy Work?', Vol. 315 of *Astrophysics and Space Science Library*, pp. 369–+.
- Welsh, B. Y., Sfeir, D. M., Sallmen, S. & Lallement, R. (2001), 'Far Ultraviolet Spectroscopic Explorer observations of high-velocity gas associated with the Monoceros Loop SNR', *A&A* 372, 516–526.
- Welsh, B. Y., Sfeir, D. M., Sirk, M. M. & Lallement, R. (1999), 'EUV mapping of the local interstellar medium: the Local Chimney revealed?', *A&A* 352, 308–316.
- Wesselius, P. R. & Koester, D. (1978), 'Effective temperatures of hot white dwarfs', *A&A* 70, 745–750.
- Wolff, B., Koester, D. & Lallement, R. (1999), 'Evidence for an ionization gradient in the local interstellar medium: EUVE observations of white dwarfs', *A&A* 346, 969–978.
- Wolff, B., Kruk, J. W., Koester, D., Allard, N. F., Ferlet, R. & Vidal-Madjar, A. (2001), 'FUSE observations of hot white dwarfs', *A&A* 373, 674–682.
- Wolleben, M. (2007), 'A New Model for the Loop I (North Polar Spur) Region', *ApJ* 664, 349–356.
- Wood, B. E., Linsky, J. L., Hébrard, G., Vidal-Madjar, A., Lemoine, M., Moos, H. W., Sembach, K. R. & Jenkins, E. B. (2002), 'Deuterium Abundance toward WD 1634-573: Results from the FUSE Mission', *ApJS* 140, 91–102.
- Wood, M. A. (1995), Theoretical White Dwarf Luminosity Functions: DA Models, in D. Koester & K. Werner, eds, 'White Dwarfs, Proceedings of the 9th European Workshop on White Dwarfs Held at Kiel, Germany, 29 August - 1 September 1994. Lecture Notes in Physics, Vol. 443, edited by Detlev Koester and Klaus Werner. Springer-Verlag, Berlin Heidelberg New York, 1995., p.41', pp. 41–+.
- Wright, W. H. (1918), 'Bulletin Number 332 - The ultra-violet spectrum of alpha Cygni', *Lick Observatory Bulletin* 10, 100–109.

- Yoshioka, S. & Ikeuchi, S. (1990), 'Collision of cosmological shock waves produced by explosions and formation of large-scale structures', *ApJ* 360, 352–369.